Feasibility of Perovskite Solar Cells For Space Applications

Swansea University
Prifysgol Abertawe

Declan Paul George Hughes

Department of Materials Engineering

Swansea University

Submitted to Swansea University in fulfilment of the requirements for the degree of Doctor of Philosophy

2023

Abstract

Environmental stability remains as a critical barrier for the adoption of perovskite solar cells for space applications and understanding the roles of material degradation is the key to address this challenge. The thesis investigates the stability of established perovskite solar cell architectures under mimic Low Earth Orbit (LEO) conditions.

Perovskite solar cells (PSCs) were found to have an impressive radiation hardness under 150 keV proton bombardment. At higher proton fluences, the performance degradation was found to correlate to the decrease in short circuit current density (J_{sc}). The decrease was found to be related to the degradation of the spiro-OMeTAD hole transporting layer (HTL). In mesoporous carbon-based PSCs, the proton radiation stability was found to be the highest seen under 150 keV proton bombardment. This stability was related to the thick carbon electrode.

Thermal cycling measurements revealed that the spiro-OMeTAD HTL was responsible for decreasing device performance. Raman spectroscopy exhibited a decrease in the C-C and C=C bond peak intensities, related to the degradation of the layer. This correlates to an increase in non-radiative recombination and reduced Jsc. The same measurements on a P3HT HTL showed much greater thermal stability, with improved device performance retention after heat treatment and thermal cycling.

A new thin-film encapsulation technique was also explored. Using spray coated Poly(methyl methacrylate) (PMMA), thermal and humidity stability measurements showed comparable performance to glass encapsulation. Photoluminescence (PL) measurements showed a large red-shift as a function of moisture ingress into the PSCs, and this was shown to correlate to an increase in J_{sc} and device performance.

The work presented in this thesis establishes relationships between the choice of HTL and encapsulation technique with material/device stability under mimic LEO conditions. Namely how the choice in HTL can lead to reduced proton bombardment or thermal stability, and how the encapsulation method can have an adverse effect on device performance. These are crucial for addressing the feasibility of future PSCs under mimic LEO conditions, thereby paving the way toward achieving long-term stability of PSCs for space applications.

Declaration

This work has not previously been accepted in substance for any degree and is not being concurrently submitted for any degree.

Signed: ..... DHughes. (Declan P G Hughes) ..... (Candidate)

Date: ..... 12/05/2023 .....

Statement 1

This thesis is the result of my own investigations, except where otherwise stated. Where correction services have been used, the extent and nature of the correction is clearly marked in the footnote(s). Other sources are acknowledged by footnotes giving explicit reference. A bibliography is appended.

Signed: ..... DHughes. (Declan P G Hughes) ..... (Candidate)

Date: ..... 12/05/2023 .....

Statement 2

I hereby give consent for my thesis, if accepted, to be available for photocopying and for inter-library loan, and for the title and summary to be made available to outside organisations after expiry of a bar on access approved by Swansea University.

Signed: ..... DHughes. (Declan P G Hughes) ..... (Candidate)

Date: ..... 12/05/2023 .....

Statement 3

The University's ethical procedures have been followed and, where appropriate, that ethical approval has been granted.

Signed: ..... DHughes. (Declan P G Hughes) ..... (Candidate)

Date: ..... 12/05/2023 .....

Acknowledgements

Firstly, I would like to acknowledge Airbus for funding my doctorate through the Endeavr Wales Programme. I would also like to acknowledge the EPSRC funded project EP/NO20863/1 for funding my research position at Swansea University. Further to this, I would like to thank the UK EPSRC ATIP Programme Grant EP/T028513/1 for contributions to travel, conferences and for additional funding as part of my research assistant position.

I would like to express my gratitude to Dr Wing Chung Tsoi for being a well-organised and supportive supervisor; I would also like to thank him for the opportunity to develop my knowledge further through the research assistant position within his group. Additional thanks go to Dr Jeremy Barbé. Without his mentoring and guidance during the first year of my PHD, I would not be where I am today. Moreover, I wish to thank my second supervisor and staff mentor Prof. Tristan Watson for his guidance and support through both my PHD and research assistant position. I have been very fortunate to have collaborated with many different groups (internal and external) during my PHD to whom I would also like to extend my thanks. Special thanks go to the friends I have made along the way: to Josh and Sean, for our climbing trips, beach BBQs, and for living under the same roof as me; to Michael, for our in-depth work discussions and your extensive pub quiz knowledge; to Luke, for being my office companion and all-round good friend; to the multi-office football team for making Wednesday afternoons the best time of the week. In short, I would like to thank everyone at SPECIFIC for creating an encouraging and supportive environment to work in, and for encouraging me to pursue my love of baking - many cakes and calories were had.

I am very grateful to both my family and my partner for supporting me along this seemingly endless journey. To Heather, thank you for proof-reading my many chapters; for always challenging and encouraging me to achieve my very best, and for loving me unconditionally. The final few years would have been a struggle without you. To my parents Beverly and Lee, thank you for providing me with an excellent education, financial support, and moral support along the way. Finally, to Kieran, thank you for always being there for late night discussions and laughs. I wouldn't be where I am today without all the support from everyone in my life.

Contents

List of Publications

[1] Hughes, D., Meroni, S., Barbe, J., Raptis, D., Heasman, K., Lang, F., Watson, T., Tsoi, W. (2022). Proton radiation hardness of perovskite solar cells utilizing a mesoporous carbon electrode. Proceedings of the New Generation Photovoltaics for Space. https://doi.org/10.29363/nanoge.pvspace.2022.006

[2] Barbé, J., Hughes, D., Wei, Z., Pockett, A., Lee, H. K., Heasman, K. C., Carnie, M. J., Watson, T. M., Tsoi, W. C. (2019). Radiation hardness of perovskite solar cells based on aluminium-doped zinc oxide electrode under proton irradiation. Solar RRL, 3(12), 1900219. https://doi.org/10.1002/solr.201900219

[3] Barbé, J., Pockett, A., Stoichkov, V., Hughes, D., Lee, H. K., Carnie, M., Watson, T., Tsoi, W. C. (2020). in situ investigation of perovskite solar cells' efficiency and stability in a mimic stratospheric environment for high-altitude pseudo-satellites. Journal of Materials Chemistry C, 8(5), 1715–1721. https://doi.org/10.1039/c9tc04984c

[4] Lee, H. K., Stewart, K., Hughes, D., Barbé, J., Pockett, A., Kilbride, R. C., Heasman, K. C., Wei, Z., Watson, T. M., Carnie, M. J., Kim, J.-S., Tsoi, W. C. (2022). Proton radiation hardness of organic photovoltaics: An in-depth study. Solar RRL, 6(6), 2101037. https://doi.org/10.1002/solr.202101037

[5] Li, G., Su, Z., Li, M., Lee, H. K. H., Datt, R., Hughes, D., Wang, C., Flatken, M., Köbler, H., Jerónimo-Rendon, J. J., Roy, R., Yang, F., Pascual, J., Li, Z., Tsoi, W. C., Gao, X., Wang, Z., Saliba, M., Abate, A., Structure and Performance Evolution of Perovskite Solar Cells under Extreme Temperatures. Adv. Energy Mater. 2022, 2202887. https://doi.org/10.1002/aenm.202202887

[6] Li, G., Su, Z., Canil, L., Hughes, D., Aldamasy, M. H., Dagar, J., Trofimov, S., Wang, L., Zuo, W., Jerónimo-Rendon, J. J., Byranvand, M. M., Wang, C., Zhu, R., Zhang, Z., Yang, F., Nasti, G., Naydenov, B., Tsoi, W. C., Li, Z., … Abate, A. (2023). Highly efficient P-i-N perovskite solar cells that endure temperature variations. Science, 379(6630), 399–403. https://doi.org/10.1126/science.add7331

List of Figures

List of Tables

Abbreviations

AM	Air Mass
AZO	Aluminium-doped Zinc Oxide
E_G	Band Gap
EM	Electromagnetic
EQE	External Quantum Efficiency
ETL	Electron Transporting Layer
eV	Electron-volt
FF	Fill Factor
FWHM	Full Width Half Maximum
HOMO	Highest Occupied Molecular Orbit
HTL	Hole Transporting Layer
I_{SC}	Short Circuit Current
ITO	Indium-doped Tin Oxide
J_{SC}	Short Circuit Current Density
LUMO	Lowest Unoccupied Molecular Orbit
m-CPSC	mesoporous-Carbon Perovskite Solar Cell
NIR	Near Infra-Red
PCE	Power Conversion Efficiency
PL	Photoluminescence
PSC	Perovskite Solar Cell
P3HT	Poly(3-hexylthiophene-2,5-diyl)
Spiro-OMeTAD	N2,N2,N2',N2',N7,N7,N7',N7-octakis(4-methoxyphenyl)-9,9-spirobi[9H-fluorene]-2,2,7,7-tetramine
TCO	Transparent Conducting Oxide
TPC	Transient Photocurrent
TPV	Transient Photovoltage
UV	Ultraviolet
Vis	Visible
V_{OC}	Open Circuit Voltage
XRD	X-Ray Diffraction

Chapter 1

Introduction

1.1 Introduction to Perovskite Solar Cells

1.1.1 Motivation

Several of the main issues associated with solar powered space system is the overall weight of the materials being sent and once in space, environmental stability. A solution to these issues reside within the development of efficient, stable, flexible solar cells. These traditional solar cells will need to be assessed on Earth to investigate their feasibility for space applications. Traditional solar cells are predominantly placed upon transparent, hard glass and fitted to rooftops. However, the overall thickness of the solar cells and the rigidity of the glass, contributes to the overall size and weight of the solar cells. This provides a costly challenge when distributing solar cells for space missions. Currently, most commercially available silicon (Si) solar panels weigh around 20 kg and it currently costs $2720 to send a lb of material to the ISS.[1][2] Therefore, to send a single 20 kg commercial solar cell to the International Space Station, it costs around ~$54000. This astronomical cost of transport has driven research to search for suitable low weight thin-film solar cells that are also flexible to reduce storage space. To achieve this goal, low temperature processed solar technology is required. The necessity for low temperature allows for the use of polymer based flexible substrates. An exciting candidate to meet these criteria is Perovskite Solar Cells (PSCs).

Since their inception into the world of photovoltaics in 2009, perovskite solar cells (PSCs) have quickly become a dominant topic in the field of next generation Photovoltaic (PV) research.[3] Leading the development of the third generation of solar technology, perovskite solar cells have reached a single junction performance of 25.8% Power Conversion Efficiency (PCE) in just under 14 years.[4] This unprecedented pace far surpasses the rate at which silicon was developed, and is quickly approaching the commercial single junction Si solar cell PCE of 26.7% as

shown in Figure 1.1. Here the best efficiency values for each PV technology are plotted as a function of time.

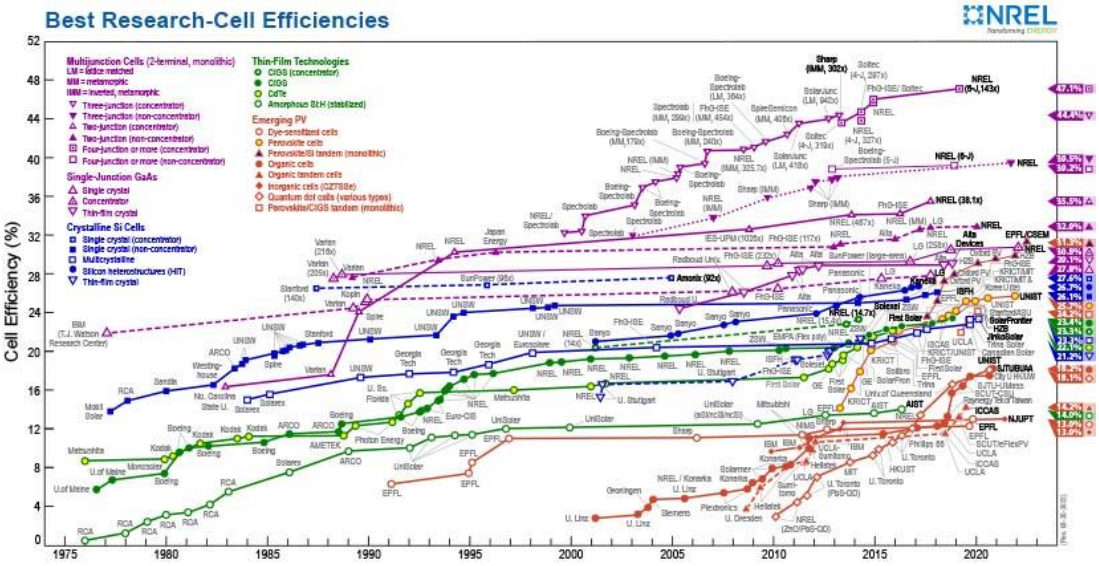

Figure 1.1: NREL efficiency tracker for different research solar technology from 1976 to 2022.[5]

For traditional Si PV, the fabrication process involves high temperature processing and therefore restricting the substrates the solar cells can be fabricated on. This means that for space PV the current technology is rigid and heavy. This large surge in performance of PSCs, the low temperature processing, and ability to be fabricated on flexible substrates has drawn attention from the aerospace sector and has placed perovskite in the spotlight for next potential replacement of space solar technology. For aerospace applications the requirements for thin film solar cells to be feasible are extensive.[6] While PSCs have been shown to exhibit High specific power, which is the measurement of power generated per unit mass of the solar cell (W/g), there are additional challenges.[7] Such challenges are High radiation tolerance, which is very important when developing space solar cells; High thermal stability as the temperature profile is different to Earths; High specific density, which is the power per unit area (kW/m^2), and the ability to combine these specifications into the manufacture of large area solar cells with integrated series interconnections onto flexible substrates.

However, PSCs are not without their drawbacks. While the PCE is continually increasing, more and more research is being pushed into maximising the stability of the devices.[8] For use in a space environment, PSCs will need to be stable under various external stimuli such as higher light intensity with increased UV; extreme temperature stability (-150 to +150 °C); high energy radiation stability, and flexion (bending) stability during initial storage. An additional factor in the measurement of device stability of PSCs is the performance of the devices in environments seen in space applications. The vacuum environment in space applications can have an adverse effect of the stability of PSCs via outgassing and defect formation.[9] Outside of device stability, an additional consideration is the scale up of perovskite solar cells to increase the device area.[10] Therefore there are multiple challenges that PSCs must overcome to be certified for use within aerospace applications. As stability seems to be the area where the most development is required, this was chosen to be the focus of this thesis.

1.1.2 Perovskite Semiconductors

Originally discovered in 1839 by Gustav Rose and named after Russian mineralogist Lev Perovski, perovskite semiconductors have been a topic of research for solar cells since their first inception in the field in 2009.[11][12] Perovskite is the name given to a crystal with the same structure as calcium titanate ($CaTiO_3$). This is more commonly denoted as the ABX_3 crystallographic structure as seen in Figure 1.2. The ABX_3 structure consists of a relatively large atomic or molecular organic cation (Type A) at the centre of the cubes. An inorganic cation (Type B) at the corner of the cubes and a relatively small halogen anion (Type X_3) at the cubes faces.

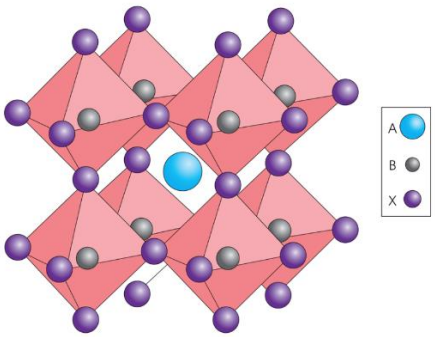

Figure 1.2 ABX_3 Crystallographic structure (Perovskite). [13]

In this structure, the type A cation is usually an alkaline earth or rare-earth element. The type B cation could be 3d, 4d, and 5d transition metal elements. This variation allows for a variety of choices for each of the A,B and X ions as seen in Table 1.1.

Table 1.1: Potential material choices for the ABX_3 perovskite structure

Perovskite Structure		
A Cation	B Cation	X_3 Cation
Organo: Methylammonium Formamidinium Cesium Rubidium	*Metal:* Lead Plumbate	*Halide:* Iodide Chloride Bromide Fluoride Astatide

While all these choices give form to the ABX_3 crystal, not every combination leads to an ideal perovskite structure. The Goldschmidt Tolerance Factor, given in equation 1.1, is an indicator for the stability and distortion of crystal structures.

$$t = \frac{r_A + r_X}{\sqrt{2}(r_B + r_X)} \tag{1.1}$$

where r_a, r_b, and r_x are the ionic radius of A, B and X respectively. For this factor, values ranging from $0.8 < t < 1.0$ are regarded as giving an ideal structure.[14]

A common perovskite composition is Methylammonium Lead Iodide (MAPI), which was used in much of the early work in the use of perovskites in solar cells.[15] However, new perovskite formulations have been developed with different stoichiometries such as triple X_3 cation Cs(FAMA)Pb(IBr).[16]

1.1.3 Working Principles of Perovskite Solar Cells

The basis of solar cells is the photo-electric effect where light of specific wavelengths can ionize electrons in a material. However, the photoelectric effect was originally explained for a metal, in which the electrons are free flowing due to the valance and conduction bands overlapping. In the case of semiconductor materials, there is a gap

between the two energy bands. In the case of a solar cell, photons excite electrons from the valance to the conduction band, therefore 'jumping' the band gap. The excitation of the electron to the conduction band creates a 'hole'. This hole possess a positive charge due to the gap left by the electron, causing a Coulomb force between the hole and electron. This attraction will force the electron to jump back down into the valence band and recombine with the hole. As incident photons will need to possess enough energy to excite the electron to the conduction band, the gap between the 2 bands is very important for efficient semiconductor performance. If the gap is large, only high energy photons will be able to excite the electrons, while a narrow band gap causes energy loss due to photons having more energy than required to excite the electrons. In the context of solar cells, this band-gap correlates with the electromagnetic (EM) spectrum and what wavelengths of light it absorbs.

The main underlying principle behind solar cells operation is the use of a P-N Junction. In the junction, the active area is the material that acts as the semiconductor. Photons interact with the electrons in the materials lattice and 'knocks' them free. This creates and electron-hole pair, also known as an exciton, which unless the coulomb force is overcome will recombine. Therefore, an electric field is required to create a current and direct the flow of electrons. This is achieved by using two different types of materials, P-Type and N-Type, which induce an internal electric field as shown in Figure 1.3.

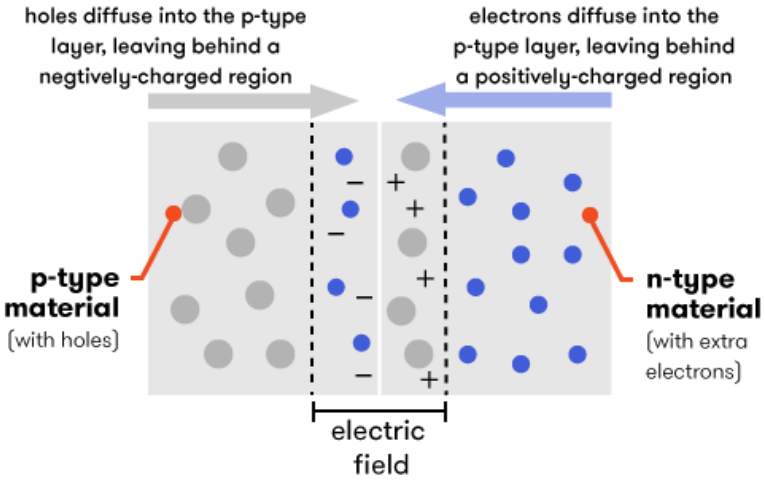

Figure 1.3: Schematic of how a P-N junction comes together and how the flow of electrons and holes occur.[17]

For a perovskite solar cell, the perovskite active layer (i) is 'sandwiched' between a p-type material and a n-type material, forming a n-i-p structure. When photons interact with the perovskite semiconductor, it creates charge carriers (electrons and holes). When these are formed in the vicinity of the electric field at the junction of the p- and n-type layers, the electric field pulls the pair apart due to the overcoming of the coulomb force creating mobile carriers. The mobility of the carriers is defined as the drift velocity of the charge carrier per unit of the electric field. Controlled by the force of the electric field, the electrons travel to the n-type side, and the holes to the p-type side . At these interfaces they are extracted and generate a current. The creation of charge carriers can also occur in areas outside of the electric field. Sometimes, these electron-hole pairs will recombine as the lack of electric field. The extra energy from this recombination is emitted as heat and reduces the overall efficiency of the cell, known as radiative loss.

1.1.4 Device Characterisation

Figure 1.4 shows a typical current density-voltage (J-V) curve for a perovskite solar cell. Determining the performance of solar cells can be achieved through important points on the graph. Where the J-V curve with the x-axis is called the open-circuit voltage (V_{oc}). This is maximum output voltage from the cell. The intersection at the y-axis is the short-circuit current density (J_{sc}) and is the maximum current density from the cell. The point of maximum output power is called the maximum power point (P_M), and the corresponding maximum power voltage and current density at this point are denoted as V_M and J_M. The blue shaded region is the maximum power output and is calculated via V_M x J_M. The fill factor (FF) is defined as the ratio between PM and the product of the V_{oc} and J_{sc}, which gives the "squareness" of the curve equation. The FF is a measure of how the device performs to an ideal device and is limited by losses such as resistive losses or charge recombination.

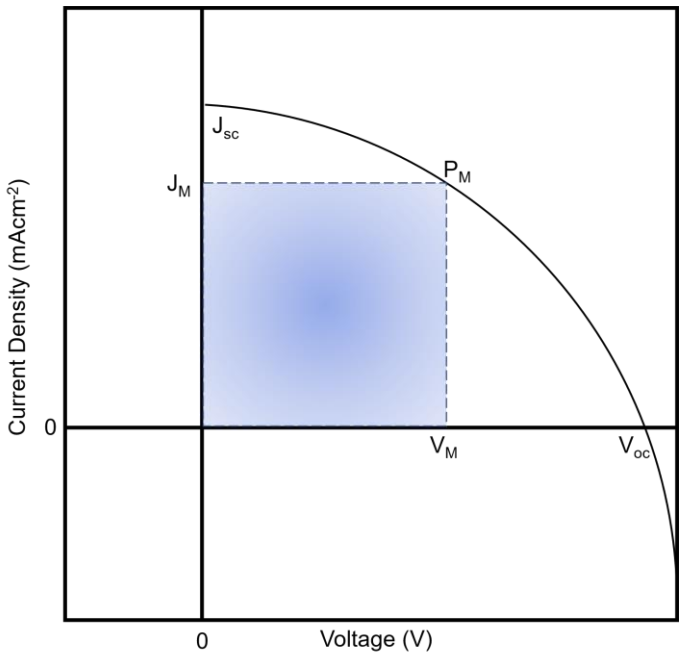

Figure 1.4 A typical J-V curve measurement for PSCs that is used to determine device characteristics.

For a solar cell, the power generated can be calculated via:

$$P = I \times V \tag{1.2}$$

The power conversion efficiency (PCE) of a solar cell is defined as the maximum power produced by the cell divided by the power of the incident light (P_{in}).

$$PCE = \frac{V_{OC} \cdot I_{SC} \cdot FF}{P_{IN}} \times 100\% \tag{1.3}$$

Where FF can be calculated via the equation:

$$FF = \frac{I_M \cdot V_M}{I_{SC} \cdot V_{OC}} \tag{1.4}$$

Converting I_{sc} to J_{sc} gives the equation

$$PCE = \frac{V_{OC} \cdot J_{SC} \cdot FF}{P_{IN}} \times 100\% \tag{1.5}$$

Resistive losses are present in perovskite solar cells. These losses can be split into two types, series resistance and shunt resistance. Series resistance (R_s) originates from the intrinsic resistances of the active layer and electrodes, but also the contact resistances between these layers.[18]. Shunt resistance (R_{sh}) is indicative of current loss within the solar cells, such as from pinholes.[18]

1.1.5 Solar Cell Architectures

1.1.5.1 Conventional Perovskite Solar Cells

PSCs are composed of multiple thin film layers. Typically, the perovskite active layer is sandwiched between two electrodes, one of which needs to be transparent so that the perovskite layer can be illuminated through the glass substrate. There are multiple perovskite formulations that can be used as the active material, but this thesis will concentrate on a triple cation perovskite active layer. Charge transport layer can be inserted between the active layer and the electrodes to improve charge transport and collection. P-type and N-type materials are used for the transport layer Figure 1.5 depicts typical perovskite device architectures.

In the perovskite device architecture, holes are transported through the Hole Transporting Layer (HTL) into the metal contacts. The electrons are transported through the Electron Transporting Layer (ETL) and are extracted in the transparent conducting electrode (TCE). When the standard structure is a stack of compact layers, it is called planar. However, the standard architecture can also utilise mesoporous layers such as mesoporous TiO_2 (m-TiO_2).[19] Another common device architecture is the inverted structure, which flips the placement of the ETL and HTL meaning that holes are extracted through the TCE and the electrons through the metal electrode. There are benefits and drawbacks to either architecture, however both are utilised extensively in the field of research.

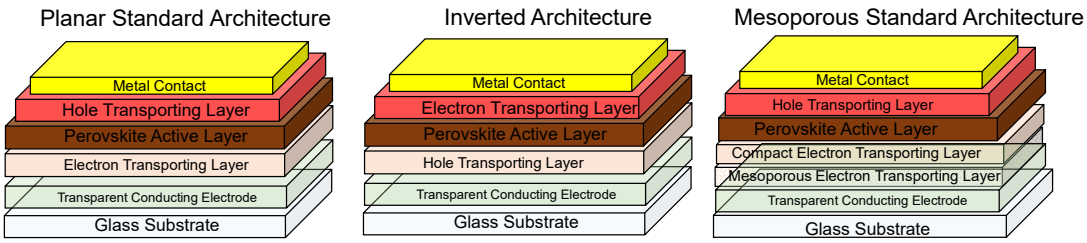

Figure 1.5 Schematic of the standard and inverted architectures used for perovskite solar cells. For the standard architecture the planar and mesoporous configurations are shown.

The standard structure offers greater operating characteristics, such as high PCE (>25%) due to higher current density, fill factor and open circuit voltage.[5] This

is due to better optimisation of the standard structures' layers, as more research has been undertaken utilising its formulation.[20] In comparison, multiple research groups have been able to break the 20% efficiency barrier when using the inverted composition, with the inverted PSC PCE hitting a record 25%.[21][22] Therefore showing that both architectures perform well when optimised. When looking at aerospace application, one disadvantage of using m-TiO_2 in the mesoporous architecture is that TiO_2 is unstable under UV radiation.[23] Under UV light stability measurement, the photocatalytic effect of the mesoporous TiO_2 layer causes decomposition of the perovskite layer, causing the formation of PbI_2 which causes defect within the perovskite layer. These defects then reduced charge extraction and device performance.

1.1.5.2 Mesoporous Carbon Stack

A relatively new field in the development of PSC, is the use of a mesoporous carbon stack architecture (m-CPSC). Utilising mesoporous techniques, the carbon stack use 3 mesoporous layers as shown in Figure 1.6. The first layer is a spray coated compact TiO2 ETL. Then a mesoporous TiO_2 ETL which is printed, followed by a mesoporous ZrO_2 layer. The ZrO_2 layer prevents the TiO_2 being in direct contact with the carbon top contact, therefore reducing pathways for the electrons and holes to easily recombine. The third layer is mesoporous carbon which is optimised for efficient charge extraction at the carbon-perovskite interface. All 3 mesoporous layer can be screen printed but are compatible with other fabrication techniques such as slot-die coating.[24] The perovskite is then introduced through infiltration into the mesoporous stack and the perovskite domain size is therefore determined by the pores within the mesoporous structure. The main drawback when looking at commercialisation is the carbon stack requires a very high sintering temperatures (~500 °C) for the layers to be properly annealed. This high temperature processing limits the carbon stack to being fabricated on glass as polymer films such as PET are unstable at higher temperatures. There has been work undertaken to speed up this process, with one experiment using NIR light to reduce the sintering time from 2 hours down to 30 seconds with an achieved PCE of 11%.[25]

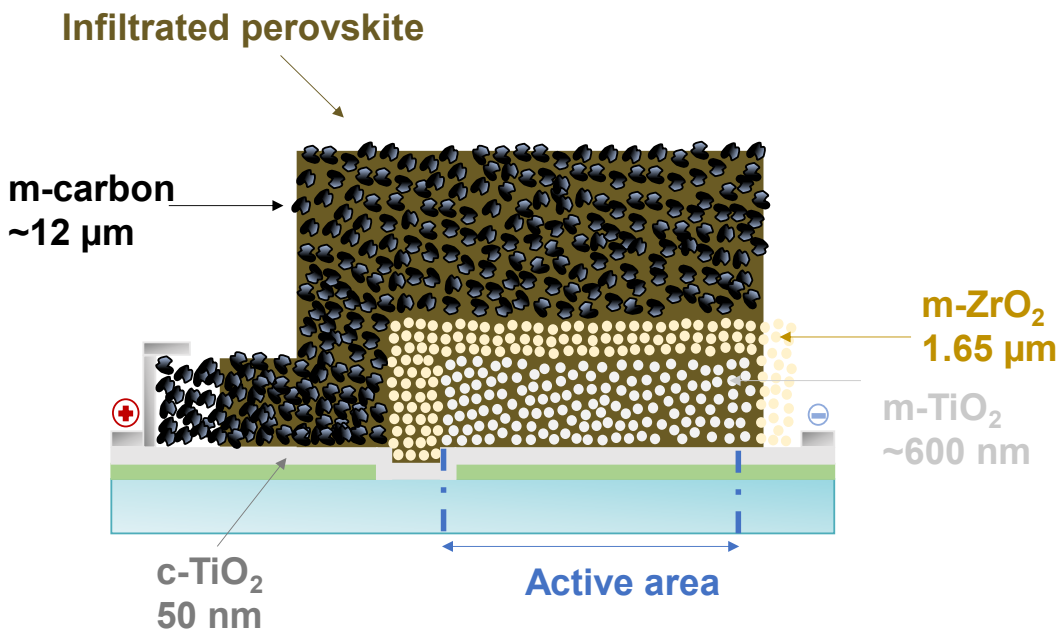

Figure 1.6 Schematic for a mesoporous carbon-based Perovskite solar cell. Each layer is labelled, with the layer thicknesses given. Adapted image.[26]

In terms of architecture performance, m-CPSC have exhibited very good stability under light soaking measurements; damp heat moisture stability testing, and high temperature testing.[27][28] The latter is due to the carbon electrode being more thermally stable in comparison to common polymer based HTLs such as spiro-OMeTAD. However, due to the thick carbon electrode m-CPSCs, the charge extraction is limited unless the devices are light soaked prior to a J-V measurement.[28] Additionally, due to the reduced charge extraction, the performance of m-CPSCs is lower compared to planar PSCs.

1.1.5.3 Tandem Devices

Tandem, coming from the Latin for 'at length', is the term given to a linearly stacked solar cell with more than one junction. Single junction solar cells have an upper limit of efficiency known as the radiative efficiency limit. It is also known as the Shockley-Queisser (SQ) limit.[29] To overcome the 33.7% SQ limit, multi-junction solar cells can be used to improve the PCE over single junction devices. Here, two different band-gap devices are linearly stacked to create a 2-terminal device. The two different active materials absorb different ranges of the EM spectrum, improving the device

performance. An example of this can be seen in Figure 1.7. The benefit of using multiple active materials, is that they can have their band gap tuned to cover more of the solar spectrum. Stacking a wide and low band gap material allows for the device to utilise the UV, visible and NIR portions of light.

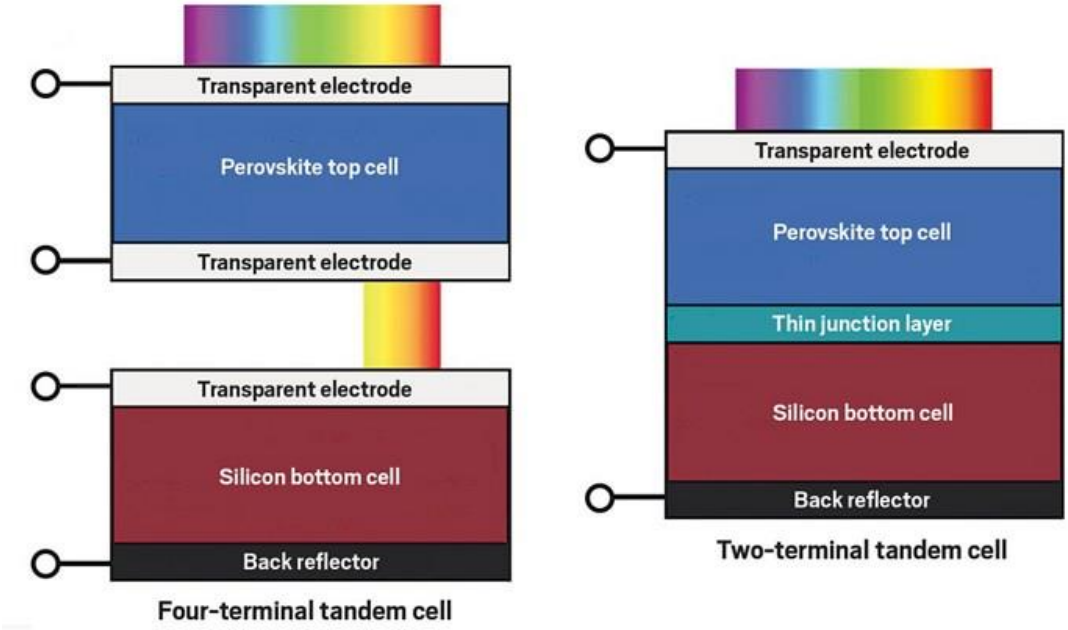

Figure 1.7 Cartoon of a two and four terminal perovskite-silicon tandem devices.[30] Perovskite tandem devices can also be fabricated without the use of Si, such as perovskite-perovskite tandems.[31]

The current record for tandem cells utilising at least one perovskite based active layer is 31.25% PCE which was developed at Helmholtz Berlin (HZB).[32] This tandem utilises a perovskite top cell and a silicon bottom cell. For a perovskite-perovskite tandem device, the record is 26.4% from Nanjing University.[33] For inorganic PV technology, the highest performing tandem solar cell is a 6 junction III-V tandem, with a PCE of 47.1%.[5] For aerospace applications, tandem perovskite solar cells will be crucial in maximising the efficiency and power output. Especially if the tandems are fabricated on thin-film substrates allowing for a much higher specific power and power density.

1.2 The Earth's Atmosphere

1.2.1 Introduction

The Earth's atmosphere is a collection of gases held around the planet due to the Earth's gravitational pull and has 5 principal layers. Each of these layers has distinct characteristics and has an interlayer between transitions known as a pause. In this section, each layer of the Earth's atmosphere and their characteristics will be explored.

1.2.2 Atmospheric Layers

Starting from the Earth's surface, the first principal layer of the Earth's atmosphere is the Troposphere. This layer begins at Earth's surface and extends up to 7-15 km depending on the position relative to the poles or the equator. This altitude variation is due to the Earth not being a perfect sphere and bulging at the equator. It is within the Troposphere that 80% of the mass of the Earth's atmosphere can be found.[34] The Troposphere consists of gaseous Nitrogen (78.084%), Oxygen (20.946%), Argon (0.9340%) and CO_2 (0.04%). The temperature of the Troposphere decreases with altitude, as the layers is heated from radiation emitted from the Earth's surface. So, the lower parcels of air are heated more than those higher up. The temperature and pressure variation within the Troposphere can be seen in Figure 1.8. Due to most of the water vapour in the atmosphere being within the Troposphere, this is where nearly all cloud formations arise and where the weather takes place.

The second principal layer is the Stratosphere. The Troposphere and Stratosphere are separated by an inter-layer called the Tropopause, which sits at an average height of 12 km. The Tropopause is a layer on constant temperature and pressure due to a constant density. The Stratosphere stretches from the Tropopause to 50km. The atmospheric pressure in the stratosphere is ~1/1000th of that at sea level (~1 mbar) and the average temperature in the Stratosphere is higher than that at the Tropopause. While the Tropopause sits at around −60 °C, the highest point of the stratosphere is closer to 0 °C.[35] This is due to the ozone layer being within the Stratosphere. As the ozone absorbs the ultraviolet light from the sun, it heats up the higher layers of the Stratosphere so there is a temperature rise with increasing

altitude. The ozone layer stretches from ~15-40km depending on the position relative to the poles or equator. The change in temperature and pressure in the Stratosphere can be seen in Figure 1.8. The highest layer of the Stratosphere is the Stratopause and is the layer gap between the Stratosphere and the Mesosphere.

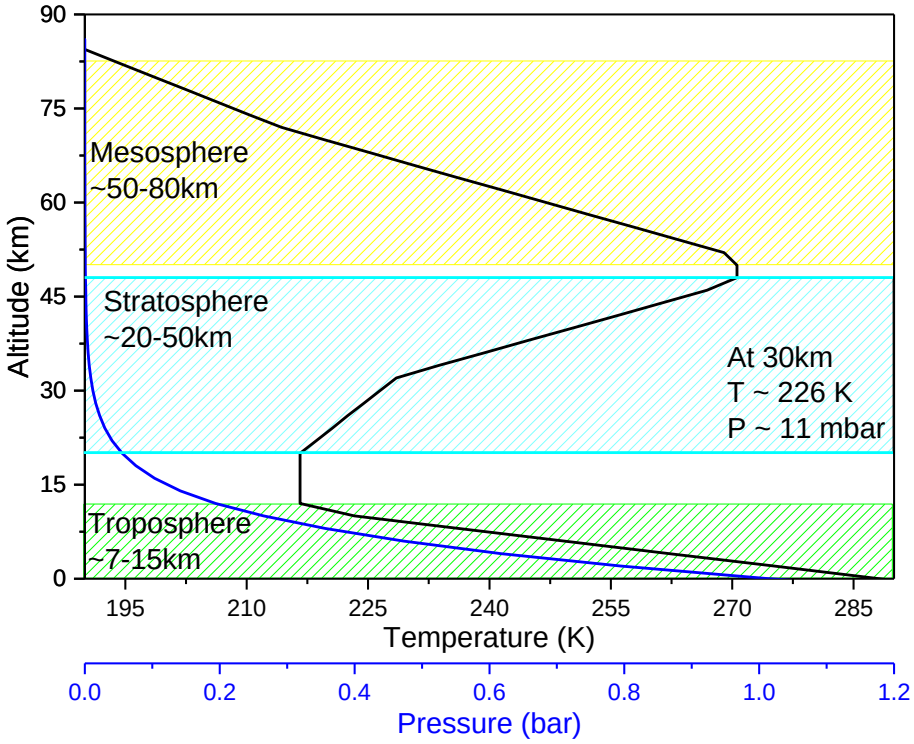

Figure 1.8 Plot of the temperature and pressure vs altitude. 30 km is signified due to this being the operating height of the Airbus Zephyr project.[36]

The third principal layer and middle segment of the Earth's atmosphere is the Mesosphere and encompasses the altitudes between 50-80km, which is from the Stratopause to the Mesopause. Here the temperature decreases with altitude and is the coldest segment of the atmosphere. Here the temperatures reaches temperatures of around −85 °C and −101 °C.[37] This decrease in temperature is due to the lower pressure and reduced solar absorption in the atmosphere. However, the mesosphere is difficult to study. Weather balloons and other aircraft cannot fly high enough, and satellites orbit above the mesosphere and are therefore unable to directly measure the layer. Since it is difficult to measure the Mesosphere directly, much about the layer is still unknown.

The fourth and second highest layer of the Earth's atmosphere is the Thermosphere. This layer spans from the Mesopause to the Thermopause or ~80km

to ~500- 1000km above the Earth's surface. This discrepancy with the outer limit of the Thermopause is due to the solar winds. At 100 km, the Kármán Line is the altitude in which 'outer space' begins.[38] This definition is accepted by the Fédération Aéronautique Internationale (FAI), who are the international standard setting organisation for aeronautics. While the Thermosphere is still part of Earth's atmosphere and phenomena such as the Aurora Borealis occurs within it, a majority of the layer is classed as space. The temperature of the Thermosphere increases with altitude due to the absorption of high energy solar radiation, which means that the Thermosphere can reach temperatures up to 1000 °C, as shown in figure 1.9. Despite all this, an object within the Thermosphere not under solar illumination will be at a low temperature. As there is an extremely low density of gas (1 particle/m^3) due to the very high vacuum (~$1x10^{-15}$ bar), the only method of heat loss is through radiative emission.[39][40] Therefore, there are very few collisions between the energized molecules and radiative heat transfer is an ineffective process. The International Space Station (ISS) sits within the Thermosphere at an altitude of 330-435 km.[41]

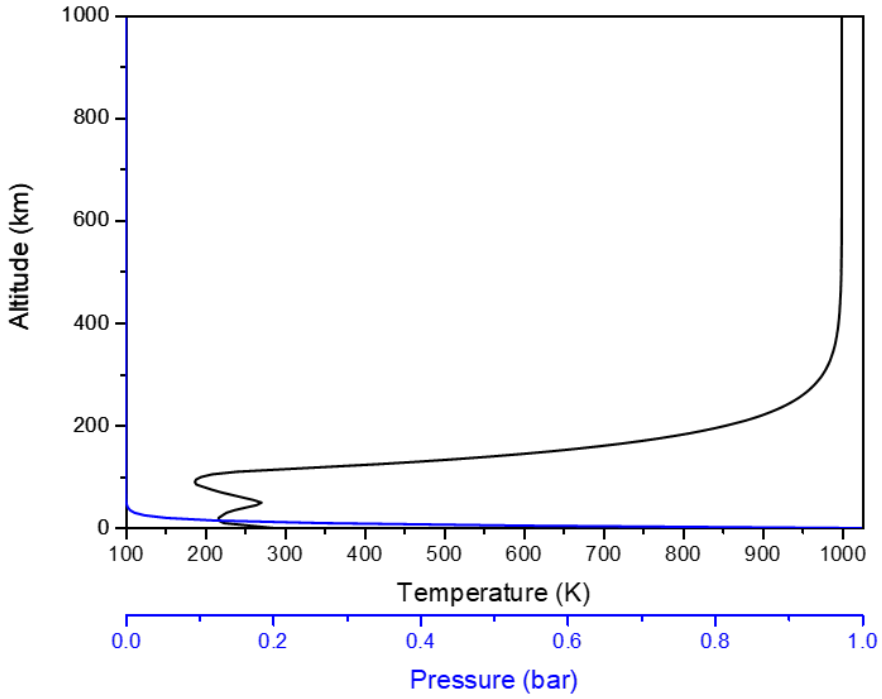

Figure 1.9 Temperature and pressure vs altitude up to a maximum altitude of 1000 km. The pressure curve does not equal 0 at higher altitudes but is ~0.

The 5th and final principal layer of the Earth's atmosphere is the Exosphere which starts at the Thermopause (700 km), also known as the Exobase, and extends up to around 10,000 km where it merges with solar winds.[42] This upper limit can also be placed at 190,000 km, as at this distance the radiation pressure from the sun is enough to overcome the effect of the Earth's gravity on a Hydrogen atom. The exobase contains extremely low densities of hydrogen, helium and several heavier molecules including nitrogen, oxygen, and carbon dioxide. The Exosphere holds most of the satellites orbiting the Earth in either a Geosynchronous (GSO) or Geostationary (GEO) orbit. The conditions within the Exosphere are further discussed in Section 1.3.1.

1.2.3 Atmospheric Solar Spectrum

The light spectrum of the sun can be best described as a blackbody, in that it absorbs nearly all incident electromagnetic radiation regardless of wavelength and can be described via the equation:

$$B_{(\lambda,T)} = \frac{2hc^2}{\lambda^5}\frac{1}{e^{hc/(\lambda K_B T)} - 1} \tag{1.6}$$

where h is Planck's constant, K_B is the Boltzmann constant, T is the temperature in Kelvins, and λ is the wavelength.

As shown in Figure 1.10, the calculated solar spectrum emitted from the sun (T=5900 K) follows the same shape as Equation 1.6. However, with atmospheric absorption the total incident power density (incident power per unit area per wavelength) varies depending on the atmospheric altitude. As shown in Figure 1.10, there are two different spectra to consider. AM1.5G and AM0 are the solar irradiance spectra relating to the Earth surface and space respectively. More details on the meaning of "AM" will be given in Section 1.2.3.1.

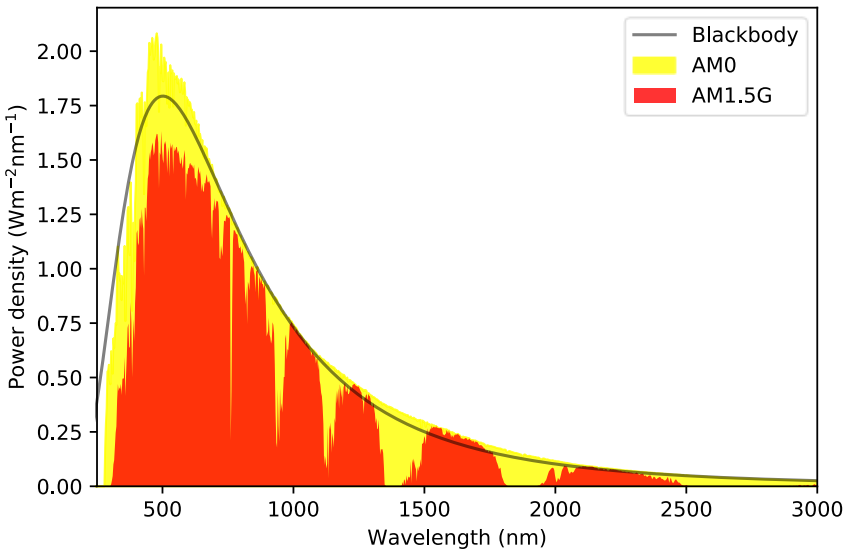

Figure 1.10 Calculated blackbody curve of the sun compared to the calculated power density of the AM1.5G and AM0 solar spectra using the Solcore python library.[43]

If you integrate under the AM0 curve for all wavelengths, you arrive at the Solar constant (1366 Wm^{-2}) which is the total irradiance arriving at the Earth.[44] This value changes depending on the distance to the sun, with the irradiance increasing as you approach the sun. As the Earth consists of multiple different atmospheric layers, the total irradiance arriving at the Earth's surface is lower than that arriving in the thermosphere. This total irradiance is affected by the atmospheric absorption of the different layers. Therefore, the solar irradiance is a function of altitude. Additionally, depending in the angle of the incident light, more absorption can occur due to the increase in distance the light must travel before reaching the surface. Therefore, the solar irradiance is also a function of the incident angle, or the zenith angle which is the apparent angle of the sun in the sky to a flat surface. The relationship between the solar irradiance and the zenith angle is known as the Air Mass.

1.2.3.1 Air Mass

As mentioned above, the solar spectrum has two different spectra that must be considered when considering solar cell operation. These being AM1.5G and AM0. Here, the Air Mass (AM) or the air mass coefficient is the optical path that light takes through the atmosphere. It can be expressed as a ratio between the path length of

the sun and the zenith angle. Mathematically, the AM can be expressed via the equation:

$$Air\ Mass(AM) = \sqrt{(r\ cos\ z)^2 + 2r + 1}\ - r\ cos\ z \tag{1.7}$$

Where Z is zenith angle and r is the ratio of the Earths radius and the effective height of the atmosphere. As the troposphere contains 80% of the Earths atmospheric mass, this effective height is taken at 15 km. While satisfactory for ground level studies, Equation 1.7 does not consider the changes in altitude, and therefore Equation 1.8 must be used to calculate the Absolute Air Mass (AM_{abs}).

$$Absolute\ Air\ Mass\ (AM_{abs}) = \frac{AM \bullet \rho_{local}}{\rho_{sea}} \tag{1.8}$$

Where ρ_{sea} is the atmospheric pressure at sea level, and ρ_{local} is the pressure at the altitude chosen. These pressure value can be found in a variety of sources.[45] Calculating AM_{abs} for a variety of different Z and altitudes can be seen in Figure 1.11.

As mentioned, there are set AM values which are designated as the standard parameters for testing.[46] AM0 is the air mass designation for no atmospheric absorption and outer space. This is the full solar spectrum, at a blackbody temperature of 5900 K, as is used when testing for space applications no attenuation of solar radiation.[47] Under AM0, the light intensity of the sun is 1366 Wm^{-2}.[48] The standardized AM coefficient is AM1.5, whose AM value corresponds to the sun at Z=48.2° and a solar power of 1000.4 Wm^{-2}. AM1.5 is calculated from the reference AM0 spectrum using different geographic and atmospheric conditions. It can be further split into 2 distinct categorises, AM1.5G and AM1.5D respectively. AM1.5G corresponds to the AM1.5 spectrum with the presence of a blue sky. The “G” comes from these conditions being known as the global spectrum. The AM1.5D (Direct) spectrum is used for concentrator measurements as the angle of incident light is reduced.[49] The AM1.5D spectrum has a solar constant of 900 Wm^{-2}.

For reporting solar cell efficiencies, Standard Test Conditions (STCs) are required and for all terrestrial applications, AM1.5G is the standard as described under standards IEC 61215/61646.[50] For aerospace conditions, AM0 is the standard spectrum as detailed in the space solar cell standard AIAA S-111A-2019.[6]

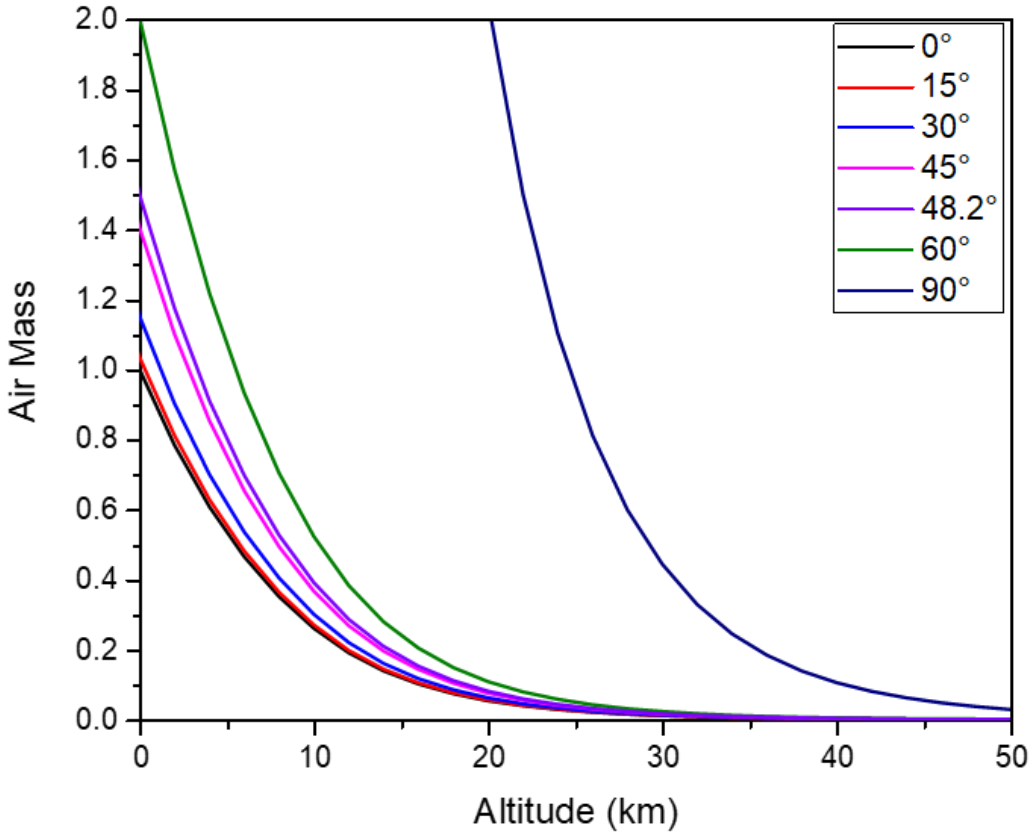

Figure 1.11 AM_{abs} as a function of different altitudes and angles following Equation 1.8.

It is worth noting that at an altitude of 30 km AM_{abs} ~0, however, the maximum solar irradiance is very close but not equal to the solar constant. It has been measured that at an altitude of 30 km the solar irradiance is 1290 Wm^{-2}.[51] This is due to the Ozone layer absorbing UVB/C as detailed in Section 1.2.2, which results in lower overall solar irradiance, even if the AM at the altitude is AM0.

1.3 Solar Cell Performance in Space Conditions

In 1958, the satellite Vanguard 1 was launched into space by the US. While this feat was over shadowed Sputnik 1 a year prior and Yuri Gagarin's famous orbital journey only 3 years later, Vanguard 1 holds a historical record as it is the first satellite to utilise solar panels.[52] Since then, satellites and orbiting bodies rely on solar cells to power their onboard systems as while batteries provide greater power, they offer much shorter lifetimes and therefore are unsuitable for long term missions and continued support. Due to this need for solar power, advancements have been made in the efficiency of solar devices along with the architectures being used. The

Vanguard 1 used silicon solar cells alongside a battery, which died in a few days of orbit. In 1958, silicon solar cells were just 4 years old and were operating at a low efficiency around 9% before reaching 14% in 1960.[53] Since their initial inception into orbital instruments, solar cells have been developed and streamlined to provide much higher efficiencies to coincide with the increasing power needs of more powerful equipment. At the current time of writing, the most used solar cells in space applications are multi-junction GaAs cells as they provide the highest efficiency as seen in Figure 1.1. The Juno mission which took place in 2011, was the first spacecraft to orbit Jupiter and at that time multi-junction GaAs cells were around 40% while the more traditional silicon devices were operating at about 25%.[5] Research has been done specifically looking at the performance of these technologies under mimic Jupiter light intensity and temperatures.[54] When it comes to choosing which type of solar cells to integrate within a satellite or spacecraft, certain conditions must be met so that the cells can perform at maximum output and the cell degradation isn't accelerated by external stimuli.

Specifically for space, the main causes for concern when adopting solar cells is the stability of the cells when experienced to thermal stress, light soaking, and high energy bombardment. Additional factors such as the flexibility of the cells and the specific power are very important. Space objects undergo large thermal stress as when objects leave the Earth's atmosphere, the reduced pressure and density of gases leads to a decrease in thermal conduction, resulting in temperatures reaching high temperatures of 128+ °c in direct sunlight and lows of -196 °c in a GEO.[55] This change in temperature can be quite a drastic transition so while devices are required to work at these temperatures, they also must be stable during this temperature cycling period. Photo-degradation is an adverse effect in which the interaction between certain layers and photons of different wavelengths leads to recombination within the active layer and therefore reduces the overall efficiency and operating conditions. This degradation can be exacerbated due to the 50% increase UV photons and high energy UV photons. High energy bombardment is an issue as due to the lack of atmosphere, objects in space are at risk to ionising radiation being emitted by various objects such as the sun or gamma-ray bursts.[56] These different types of radiation are detrimental to the operating stability of solar devices as it can cause

defects in the various layers. Therefore, efforts must be put into place to limit the damage caused.

1.3.1 Orbital Characterisation

Orbital characterisation can be split into 4 main categories: Low Earth Orbit (LEO), Medium Earth Orbit (MEO), Geosynchronous Earth Orbit (GEO), and the Solar Wind Environments which lie within the exosphere and beyond. The LEO, MEO, and GEO orbits can be seen in Figure 1.12. As all 4 of these conditions are present within the Earths Thermosphere, they all come under the AM0 solar spectrum and intensity. Additionally, due to the low particle density and therefore no atmosphere, there is the presence of high energy particles and radiation in the form of electron, protons, neutrons, and high energy photons such as X-rays and Gamma-rays.

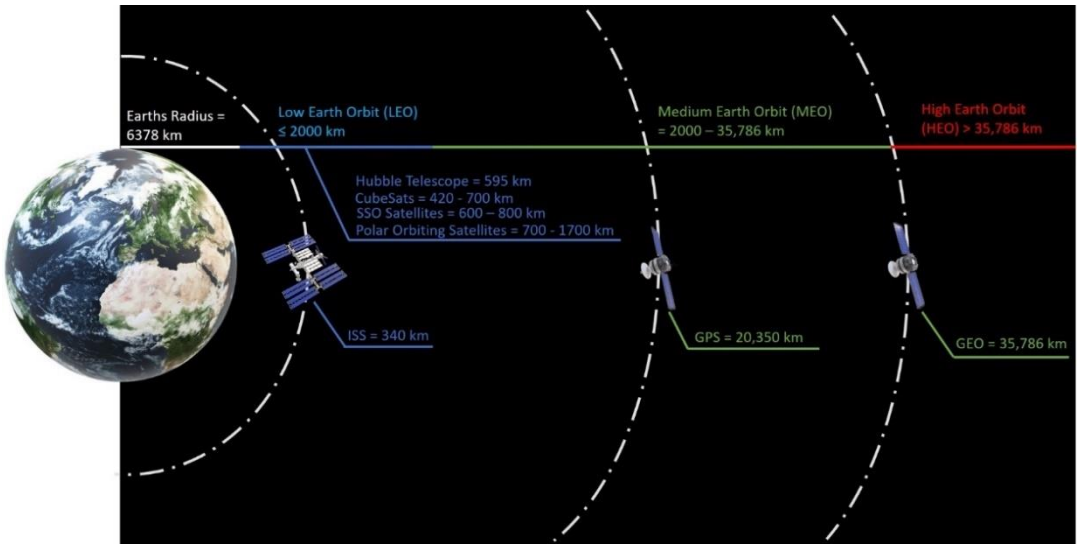

Figure 1.12 Cartoon of the different orbits found around the Earth, with applications within the Low/Medium/Geosynchronous orbits labelled.

Low Earth Orbit (LEO) is defined as any orbit between the Earth's surface and an altitude of 2000 km. The International Space Station presides at an orbit of ~340 km so is therefore in LEO.[41] The vacuum level at this altitude is $7x10^{-13}$ bar. Present in a LEO is high density Oxygen plasma (O^+) with up to 10^6 particles/cm^3 with an orbital period of around 90 minutes, with half of the orbits time being spent in the shadow of the Earth, and therefore darkness. During this time, the temperature

gradually cycles between ±100 ^{o}C in light and dark respectively. Energetic particles are also prevalent in a LEO with electrons between 40 keV to >1.6 MeV with a flux of $1x10^{6} \leq \Phi \leq 1x10^{2}$ electrons-cm^{-2}-s^{-1} from the lowest to highest energy, respectively. Protons in this same region have energies from 0.1 to >30 MeV with a flux of $1x10^{6} \leq \Phi \leq 1x10^{4}$ protons-cm^{-2}-s^{-1} from lowest to highest energy, respectively.[57] An upper limit on the electron and protons energies has not yet been discovered as it is dependent on various factors, such as solar storms like the Carrington Event. Neutrons are present in a space environment with energies MeV – TeV.[58] These neutrons come from 4 main sources; production in the atmosphere via Galactic Cosmic Radiation/Rays (GCR), which are high-energy protons and ionised atomic nuclei which move through space at nearly the speed of light. They originate from the sun, from outside of the solar system, and from distant galaxies; Earth's radiation belt (Van Allen Belts); production in the spacecraft where the high energy protons collide with the molecules in the spacecrafts materials, resulting in the formation of neutrons , and direct emission from the Sun during large Solar Particle Events (SPE), which includes Coronal Matter Ejections (CME), where the closed magnetic fields over a sunspot group cause an explosion of gas, ejecting x-rays, gamma-rays and billions of particles at speeds close to the speed of light.[57] However, measurement of the flux from these events is a current field of investigation, with a research group in Hawaii deploying a CubeSat named Neutron-1 from the ISS in 2020 to measure the flux of neutrons in LEO.[58] However, due to the Earth's magnetosphere, a LEO provides the lowest background of gamma and x-rays as the higher energy cosmic rays are attenuated by the magnetosphere. However, orbiting bodies in LEO still meet albedo higher energy photons. These are photons that are produced in the upper atmosphere (mesosphere and higher) by protons colliding with atmospheric molecules and are reflected into space. Albedo photons possess energies from 35 MeV to 10 GeV, with the lower threshold exhibiting a maximum flux of $1x10^{-2}$ photons-cm^{-2}-s^{-1} and the higher energy threshold possessing a maximum flux of $1x10^{-3}$ photons-cm^{-2}-s^{-1} .[59]

Due to the very thin atmosphere, UV radiation propagates and is denoted as vacuum UV (VUV), with 10% of the total electromagnetic radiation output from the Sun being

UV, split into UVA, UVB and UVC (400-315nm, 315-280nm and 280-100 nm respectively) and 0.1% of UV being UV below 200nm.[60] As this region of space encompasses the ISS, solar cells designed for this environment must be able to provide enough solar power to power the onboard experiments. Due to the need for high efficiency and stability in the presence of a full solar spectrum, high energy particles, and thermal cycling, GaAs III-V multi-junction cells are used as they provide the high PCE as seen in Figure 1.1. In a LEO environment, GaAs III-V cells exhibit PCE values of ~27.5% provide better proton and electron radiation stability over Si multi-junction cells.[61] Along with greater thermal and UV stability.

A medium earth orbit (MEO) in any orbit that lies between LEO and GEO (2000-35,786 km). Satellites placed in a MEO orbit have an orbital period of 12 hours, in what is known as a Semi-Synchronous Orbit (Semi-SO). MEO satellites orbit the earth at higher altitudes and therefore provide a greater coverage area for use in imaging systems and communication systems, however due to the orbital period, a constellation of satellites is needed to provide full coverage around the Earth. Most notable applications used in this orbit is the Global Positioning System (GPS) and the EUs Galileo navigational and communication satellite system. Little research into the environment in a MEO has been undertaken, therefore the flux of incident high energy particles not trapped in the Van Allen Belts is unknown.

Geosynchronous orbit (GEO) is defined as the orbit where an object will rotate with the same period as the Earth. If a satellite is placed in GEO above the equator, the satellite will remain fixed in its position relative to the Earth's surface. Therefore, an orbital period in GEO is 1 sidereal day (23 hours, 56 minutes, 4 seconds). This orbit is 35,786 km from the Earth's surface, with most communication satellites being placed here.[62] This way, an antenna on Earth can be fixed to always stay pointed towards that satellite without moving. It can also be used by weather monitoring satellites because they can continually observe specific areas to see how weather trends emerge. In a GEO orbit, there is a low-density oxygen and hydrogen plasma environment, with secondary electrons possessing energies from 1 keV to 30 keV. There are long thermal cycling times, with satellites orbiting above the equator experiencing 12 hours in the light and dark, along with bombardment from high energy particles.[63] The temperature for solar arrays in a GEO is documented to

range between -150 to +110 ^{o}C depending on the position of the object relative to the Sun, which as this altitude is the AM0 solar spectrum.[64] As a GEO is located 5.6 Earth radii (R_E) from the Earth's surface, which corresponds to the outer Van Allen belt, the radiation environment consists of high energy electrons (0.1 – 10 MeV) with a flux ~10^8 electrons/m^2/s. Like deep space missions and High Earth Orbits (HEO), which is any orbit >35,786 km, objects in a GEO also encounter Galactic cosmic rays, particles in the Solar wind, and coronal mass ejections and Solar flares. Galactic cosmic rays occur at very low flux levels, typically 1-4 particles-cm^{-2}-s^{-1}, but have high energies, with some events having particles moving close to the speed of light with energies of 1x10^{20} eV.[66] Solar Particle Events (SEPs) can release a variety of high energy particles and ions, with the composition and energies varying per event. One main source is solar flares, with typical event composed of 96.4% protons, 3.5% α-particles and 0.1% heavier ions. These particles can possess energies up to GeV/nucleon with a fluence of >1x10^9 particles-cm^{-2} and a peak flux >1x10^5 particles-cm^{-2}-s^{-1}. The timescale for these fluences is dependent on the severity of the solar storm and can range from a few minutes to several hours. Electrons in the Van Allen belt can possess energies >8 MeV with a flux of 1x10^7 electrons-cm^2-s^{-1}, while protons have energies between 0.1 & 5 MeV, with a flux of around 1x10^8 protons-cm^{-2}-s^{-1}.

As stated above, the location of a satellite within the Van Allen radiation belts is important, as it is related to the energy and fluxes of the particles trapped, so considerations must be taken when travelling through or orbiting within them. Additionally, due to the distortion of the magnetosphere from the sun's solar winds, along with the shape of the Earth's magnetic fields, the angle at which the satellite is from the Earth also affects the radiation flux. This angle is denoted as the inclination angle, with inclinations between $0^o \leq \theta \leq 30^o$ exhibiting a sharp reduction in flux, and angles $30^o \leq \theta \leq 60^o$ showing a gradual decrease before plateauing at 60^o. Above 60° the particles are not trapped and there is no belt. For a GEO, the inclination angle is 0 ^{o} as the satellites are placed in an orbit above the equator to maintain their orbital period, and to remain stationary in the reference frame of the ground observer. Figure 1.13 is a diagram of the Van Allen belts along with information regarding particle energy and flux.

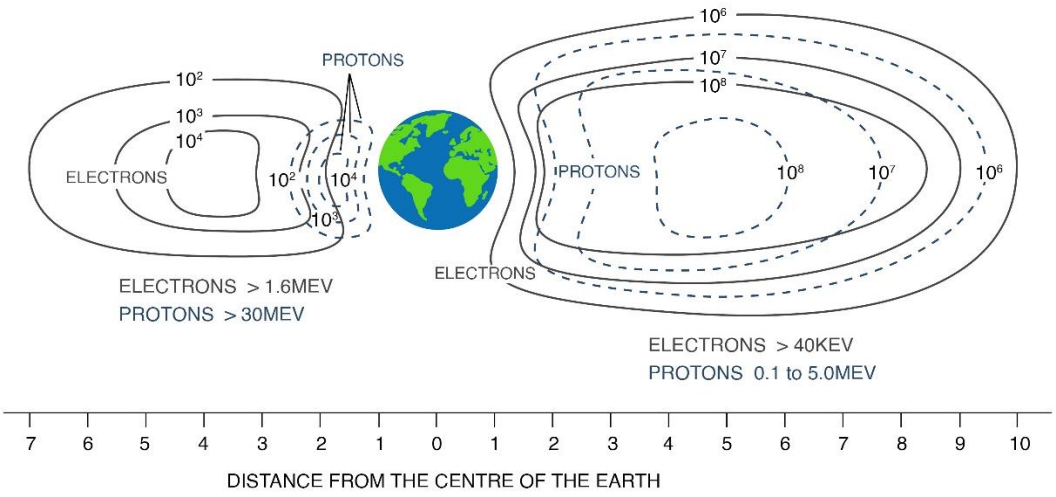

Figure 1.13 Cartoon of the Van Allen radiation belts around the Earth, with the distance range of each belt from the Earths centre measured in Earth radii. The energy values of electrons and protons in these belts are also given, along with the corresponding flux (particles/m^2/s).

These orbital characterisations can be tested within lab environments due to continued development of research technology. An example of this is the High Energy Charged Particle Radiation facility at the Marshall Space Flight Center or the Brookhaven National Laboratory.[63] Both these sites have access to high energy particle beams that allow for electrons and protons to be fired at 'targets', which can be solar cells. Ongoing research is focussed on the designing of solar cells that can cope under the constant change in temperature, extremely low pressure, flexible, have high specific power, and are also radiation robust. Currently the main solar cell technology being used is Low-Intensity Low-Temperature (LILT) cells. These cells are designed to function below -100 °C and under 50 Wm^{-2} AM0 intensity, and were used on the Rosetta mission to study the comet 67P/Churyumov-Gerasimenko.[67][68] Another type of cell that are being constantly being updated and improved are a design known as Low-Intensity High-Temperature (LIHT), with a triple-junction GaAs LIHT cells designed for the Venus environment reaching 22.7% in 2018.[69] Here the cells were taken to a light intensity of 89.4 Wm^{-2} and a temperature of 465 °C. The lower PCE compared to the highest performance III-V solar cells is due to the extreme heat limiting the V_{oc}.

1.3.2 Moisture and Humidity

While it is almost counter-intuitive to think of moisture stability when considering objects in space, the solar cells used within the power generating arrays must be fabricated on Earth and then stored before the payload is launched. This means that the solar cells may have to be held up to a year before they are put into space. During this long storage time, the solar cells should maintain their performance and remain stable. If they are not stable, and degrade, they will need to be replaced which can hinder launch schedules. Incidentally, there is research into fabricating perovskite solar cells in space to overcome this barrier using 3D printing.[70]

Moisture stability plays a strong role in the lifetime performance of solar cells, with even GaAs devices showing up to 25% degradation after 1000 hours at 85% Relative Humidity (RH).[71] Perovskite solar cells are no exception and have been shown to possess a very weak intrinsic deterrence to moisture (H_2O in the air) and O_2. It has been shown that the perovskite undergoes rapid degradation when in the presence of moisture, with PSCs undergoing a 60% decrease in PCE after 1000 hours in 60% RH.[72] This decay path can be seen for the perovskite $MAPbI_3$ in Equations 1.9 to 1.12.

$$CH_3NH_3PbI_3(s) \overset{H_2O}{\longleftrightarrow} PbI_2(s) + CH_3NH_3I(aq) \quad (1.9)$$

$$CH_3NH_3I(aq) \overset{H_2O}{\longleftrightarrow} CH_3NH_2I(aq) + HI(aq) \quad (1.10)$$

$$4HI(aq) + O_2(g) \overset{H_2O}{\longleftrightarrow} 2I_2(s) + 2H_2O(l) \quad (1.11)$$

$$2HI(aq) \overset{H_2O}{\longleftrightarrow} H_2(g) + I_2(s) \quad (1.12)$$

Where s, aq, g and l are solid, aqueous, gas and liquid respectively.[73]

Here, the main cause of instability is the presence of Methyl-ammonium (MA) Iodide which breaks down in the $MAPbI_3$ layer and leaves a solid presence of Lead Di-iodide but the MA dissolves into an aqueous solution. This degradation can also be seen in the Raman spectra of the perovskite layer, with an increase in the Raman signal for dihydrated MAPI.[74] The instability within the perovskite layer can also be seen in the charge transporting layers and therefore, requires further research into replacing these layers or adding encapsulation to reduce the interaction with oxygen and water

molecules. Encapsulation techniques such as the utilisation of transparent tape, epoxy glue and glass have been used to create an airtight seal to improve the humidity stability of PSCs.[75]

Such encapsulation provides a simpler solution to the issues regarding the stability of perovskite devices in contact with moisture for use in terrestrial settings. This post-fabrication encapsulation technique provides suitable protection and is a low-cost, short-term improvement. However, there are some present issues with this technique, as the use of glass removes the ability of flexible substrates. This restriction in flexibility and increase in weight additionally affects the devices specific power and stow volume. To reduce the overall stowage weight and allow the substrates to be flexible, encapsulation methods such as the use of thin-film flexible glass or plastic films need to be considered. Various groups have shown that moisture stability can be improved by using high-quality flexible barrier materials, such as flexible plastic films.[75] While the devices still degraded under extreme moisture testing (submerged in water) the devices showed 76% performance retention compared to the 11% retention of the unencapsulated devices. Examples of O_2 and H_2O degradation are shown in Figure 1.14.

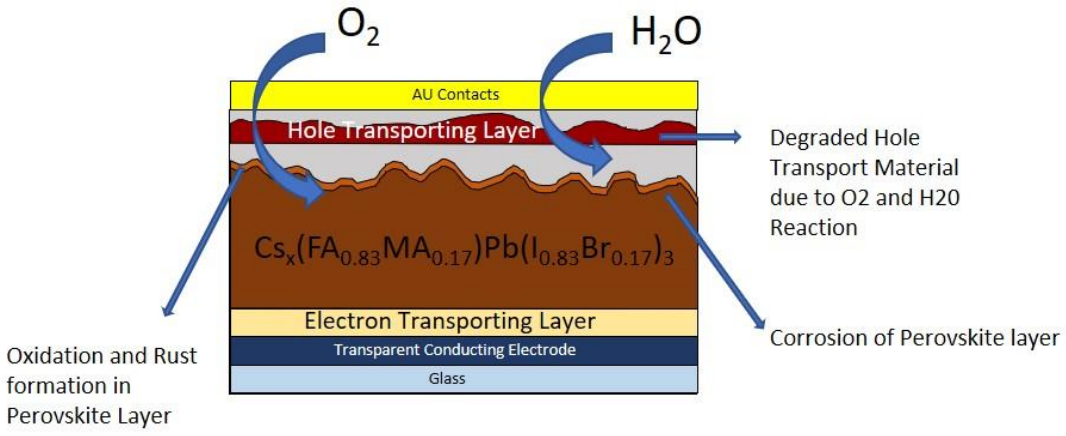

Figure 1.14 Cartoon of a conventional N-i-P perovskite solar cell utilising a triple cation perovskite active layer undergoing moisture degradation.

Composition of the active perovskite layer is another field of ongoing research to fabricate more stable layers via doping. Various attempts in improving the stability of perovskite structure have utilised cation substitution. An example of this is the use

of $FAPbI_3$ or $CsPbI_3$ as a more stable structure instead of $MAPbI_3$. However, perovskite phase changes under the moisture condition remains a critical challenge as the changes in phase reduced device performance.[76]

1.3.3 Photostability

Another issue facing the stability of perovskite solar cells, especially for space applications, is the increased degradation when under constant illumination, with the affect greatly enlarged for longer time scales.

The reduction in photostability of perovskite based solar cells is often accredited to the Ultraviolet (UV) light.[77] This decrease in performance is also dependent on the layers used when fabricating the device. An example of this is when using TiO_2 as the electron transporting layer.[78][79] This arises through the UV light being absorbed by the TiO_2, initiating a chemical degradation which increases the non-radiative recombination within the PSC. By replacing the TiO_2 layer with SnO_2, the UV stability is greatly improved and has been seen to improve PCE retention by 15% over 10 hours of UV light soaking.[80] The amount of UV radiation that the solar cells will receive is dependent on the presence of an atmosphere. the Earth receives only an overall percentage of UV light that the sun produces as seen in Figure 1.15. About ~3% of the light hitting the surface is UV when the sun is directly overhead, with the atmosphere absorbing 77% of incident UV light. Therefore 23% of the incident UV light passes through the Ozone layer and to the Earth's surface.

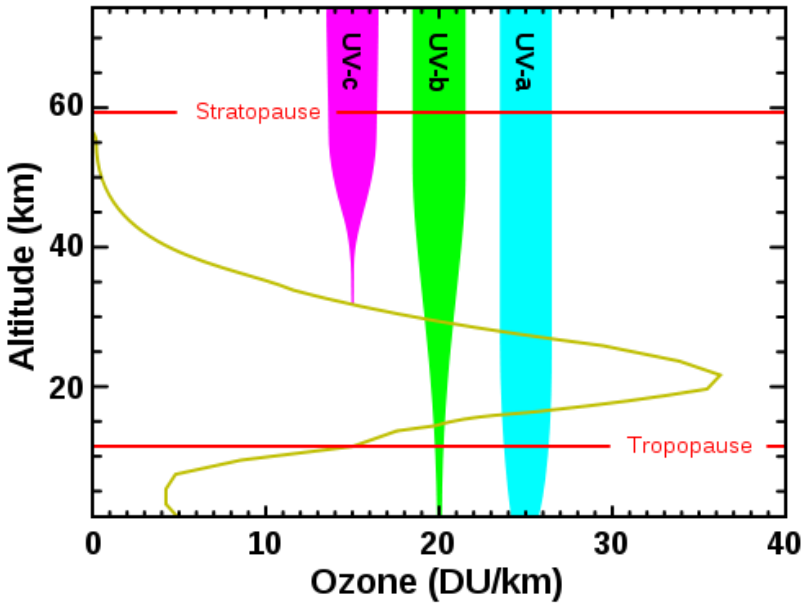

Figure 1.15 Ozone content as a function of altitude with the visual attenuation of the 3 bands of UV radiation as it encounters the layer.[81] DU stands for Dobson unit and is the unit of measurement of the amount (concentration) of a trace gas in a vertical column through the Earth's atmosphere.

While the ozone reduces the overall impact of UV on the Earth's surface, outside of the Earth's atmosphere there is no longer a protective layer and UV presides unfiltered. Therefore, solar cells within this environment are subject to increased levels of high energy, ionizing UV light. It has been shown that UVA is not the main cause of UV degradation in perovskite solar cells but is in fact the UVB and higher UV energy bands that contributing factors to the overall performance decrease.[82] SnO_2 ETL PSCs show no degradation under 370 nm UV light soaking, but the PCE degrades by 50% under 311 nm light soaking.[82]

A promising strategy to address the issues caused by UV is to convert the high energy photons into low energy photons, thereby decreasing the proportion of UV being transmitted into the perovskite layer. This can be done via the integration of down-conversion materials into the PSCs either as an ETL,HTL, or as a separate layer. A large benefit of using down-converting materials is that they not only reduce the damaging effects of UV on the devices but can also improve the PCE. One such example is the use of Eu–4,7-diphenyl-1,10-phenanthroline (Eu-complex). This layer was applied to the glass substrate to act as a down-conversion layer.[83] The layer

converts UV photons into red luminescence with an emission peak between 625 and 670 nm, with a sharp peak at about 650 nm. This improved the PSC PCE by 15.3% and improved the light stability by 20% after 10 hours.

1.3.4 Thermal Stability

Stability requirements for space solar cells are not limited to photostability, but also includes thermal stability. Solar cells that are used in orbital applications are exposed to cyclic temperature changes from very cold to very hot temperature depending on where their orbit lies. PSCs exhibit thermal instability at temperatures >150 °C (423.13 K)). This instability is affected by the organic materials/layers used within the devices, along with the intrinsic property of perovskite. More commonly used inorganic semiconductor solar cells, such GaAs, are thermally stable at temperatures >300 °C.[69] However, perovskite undergoes a temperature-dependent structural phase transition.[84] These phases can be seen in Figure 1.16.

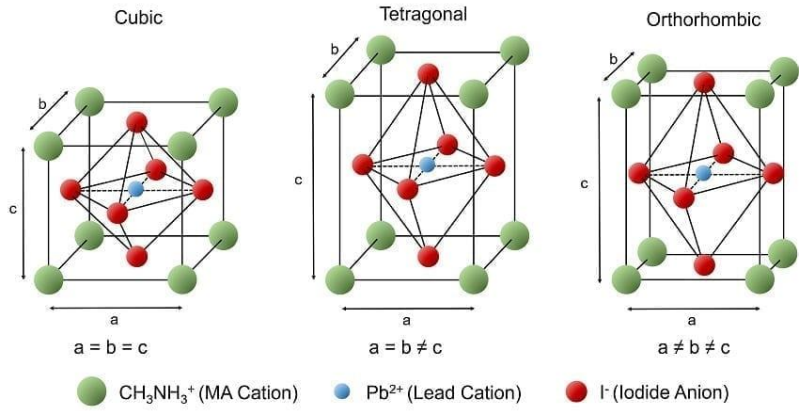

Figure 1.16 The cubic, tetragonal, and orthorhombic crystal structures of MAPI perovskite.[85]

For example, when $MAPbI_3$ reaches temperatures <163 K, it is in the orthorhombic phase (a ≠ b ≠c). However as seen in Chapter 5, this phase change is reversible. When the MAPI is at temperatures 163 K < T < 327.3 K, it remains in the tetragonal phase (a = b ≠ c). At temperatures beyond 327.3 K, $MAPbI_3$ forms a cubic phase (a = b = c). Additionally, $MAPbI_3$ perovskite has been shown to decompose under high temperatures (>100 °C), resulting in the formation of PbI_2 which can cause an increase in non-radiative recombination and trap states, reducing device performance.[86] However, the change in temperature will also affect the physical and

chemical properties of the perovskite, alongside the charge generation, recombination, and transport in perovskite-based devices.[87] Therefore, it is essential to understand how temperature affects the charge-carrier dynamics of PSCs. It has been shown that for perovskite devices under stratospheric conditions improve as the temperature decreases to a maximum PCE at -20 °C. This increase in PCE was due to the increase in the Voc and Jsc.[88] For high temperature measurements, PSCs were taken to 250 °C and a 99% decrease in PCE was observed due to the formation of PbI_2.[89] In this work the perovskite active layer was $(FAPbI_3)_{1-x}MAPb(Br_{3-y}Cl_y)_x$ showing that other perovskite formulations thermally decompose.

However, when looking at the temperature performance of PSCs, the perovskite is not the only layer that is affected by the temperature. While the perovskite experiences thermal degradation, the charge transporting layers also experience issues when they encounter extreme temperatures. An example is the HTL Spiro-OMeTAD, which has been shown to degrade under high temperatures.[90] The degradation allows for charge recombination within the perovskite film and for higher shunt resistance, resulting in decreases in performance up to 40% at 100 °C for 70 minutes.[89] Additionally, spiro-OMeTAD has a Glass Transition Temperature (T_G) of 120 °C which is the temperature at which the layer no longer acts as a solid, rigid structure but becomes a flexible, rubbery layer. This transition causes a reduction in morphological stability and the electronic properties of the layer, such as charge extraction as it can reduce the contact between the perovskite and the spiro-OMeTAD.[91] There are examples of charge transporting layers that offer superior thermal stability such as Copper(I) Thiocyanate (CuSCN) which has shown to improve the thermal stability of PSCs by 35% over spiro-OMeTAD HTL PSCs.[92]

While hot temperatures are of incredible importance when analysing solar cells stability, adequate preparation must be made to improve the cold temperature stability. In the literature, it has been shown that perovskite cells can work at temperatures <-100 °C and can even perform at temperatures as low as -193 °C.[93] However, their PCE reduced by 99%. This is good news for their inception into space applications as objects in orbit drop to very cold temperatures when not in sunlight or at extreme distances from the Sun. An example of this is Jupiter, who's

atmospheric temperature is -154 °C. Therefore, space based solar cells must be able to be stowed safely at low temperatures and not undergo degradation during time spent in the dark. This is increasingly important as there is additional thermal stress due to the cells experiencing cyclic temperature regimes. When solar cells placed within satellites orbit the Earth, they experience light and dark cycles. This subsequently means that the cells also undergo a thermal cycle from hot to cold temperatures respectively.

As high temperatures (≤150 °C) are possible in direct sunlight, any PSCs that are designed for use in a space environment must maintain their performance during operation (≤150 °C) and remain stable during the cold cycle (≥-100 °C) in the dark. They must be able to return to their initial PCE once they are in the sunlight again. It has been shown that perovskite devices effectively 'self-heal' when they spent 8 hours in the dark, with the suggestion that the effect could be seen after 60 minutes.[88] However, for an object like the ISS, the total time for a complete orbit is 90 minutes, with 45 minutes in the dark. The thermal cycle range for a satellite in LEO is further discussed in the Chapter 5 introduction, however the thermal cycling range was set to -100 ≤ T ≤ 85 °C as this encompasses the low- and high-end temperatures measured for CubeSats in LEO.

At the time of writing no work has been undertaken looking at the recovery time of very low temperature devices, and if there is any relationship between the self-healing mechanism and temperature. Incidentally, research groups have acquired real-time temperature performance of perovskite devices in a LEO, and the temperature continuously increased from 1.9 to 69.6 °C under illumination during the flight test.[93] It is desirable to track the efficiency of PSCs in a more comprehensive and real space environment.

1.3.5 Radiation Hardness

In a space environment, the presence of high energy particles such as electrons and protons, along with high energy photons such as X-rays and gamma-rays pose a threat to the stability of solar cells. While many of the high energy particles are found in space, high energy particles and photons are also present in the meso- and stratosphere in the form of secondary cosmic rays (Shown in Figure 1.17a). Secondary

cosmic rays are the by-product of proton scattering, and consist of x-rays, muons, pions, electrons, and neutrons.[94] While they are initially created in the collision event, the pions created, π + and π - , which are unstable quark anti-quark pairs, undergo weak decay into a muon and muon neutrino pair. An example of a π^+ decay is shown in figure 1.17b below.

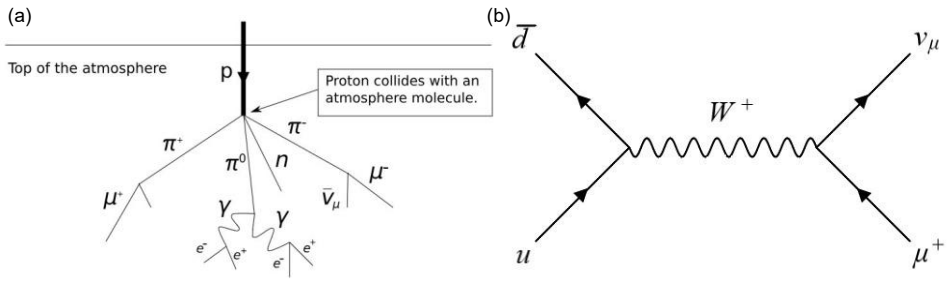

Figure 1.17 (a) Graphic detailing how primary cosmic rays (i.e., Protons) collide with air molecules such as CO_2 and scatter into secondary cosmic rays. These secondary particles then decay and scatter continuously giving various by-products.[96] (b) Feynman diagram of a Pion + decaying through the weak interaction into an anti-muon and muon neutrino pair.

However, in space the focus is more on primary cosmic rays, electrons, and gamma rays. Primary cosmic rays, such as protons and helium ions, originate mainly from intergalactic events such as supernovae light-years away and even in some cases, from our own sun through nucleosynthesis. This process takes place at the suns core. As shown in Figure 1.13, high energy particles such as protons and electrons can be trapped in the Van Allen belts and interact with orbiting bodies within the belts.

1.3.5.1 Protons and Electrons

Proton and electron radiation stability of perovskite solar cells has been an active field of investigation since 2015 when Miyasaka et al investigated the effect of 150 keV proton bombardment on standard planar PSCs.[95] Proton bombardment has been performed on PSCs with proton energies from 50 keV to 68 MeV.[95-101] In the literature, single junction PSCs are the main devices bombarded. However, Lang et al bombarded both perovskite/Si and perovskite/CIGS tandem cells with high energy protons up to 68 MeV.[96] It is shown that the perovskite/CIGS tandem outperforms

the perovskite/Si tandem by 2 orders of magnitude as the Si junction is unstable under proton irradiation and the bombardment improves the perovskite performance. On standard planar PSCs, Barbé et al have shown that under proton bombardment at 150 keV, the triple cation perovskite active layer remains stable at fluences up to $1x10^{13}$ protons/cm^2 and doesn't undergo any structural changes. However, at fluences of $1x10^{15}$ protons/cm^2 the hole transporting layer degrades, resulting in reduction and eventually negligible device performance (PCE ~0.06%).[97] The proton energy range and associated fluences for a satellite in LEO is further discussed in Chapter 2 introduction and the proton energy used in this thesis was chosen to be 150 keV. This proton energy is comparable to that found in LEO (Figure 1.13), and at distances closer to the sun. It also allows for the proton beam to interact with all layers of the standard planar PSCs (Chapter 2).

For electron bombardment, the first electron radiation study on PSCs was reported in 2015 by Miyasaka et al.[95] 1 MeV electron radiation with a maximum fluence of 1×10^{16} electrons/cm^2 was used to irradiate double cation planar PSCs. Under electron bombardment, the short-circuit current (Jsc), open-circuit voltage (Voc), and external quantum efficiency (EQE) of devices did not undergo any degradation because of the bombardment. For these devices a quartz substrate was used. This is due to soda lime glass darkening under incident radiation. When highly energetic photons (X-rays and gamma-rays) and particles bombard soda lime glass, structural defects are produced and cause a change in the electronic energy state, shifting the absorption bands of the glass. An example of this is shown in Figure 1.18.

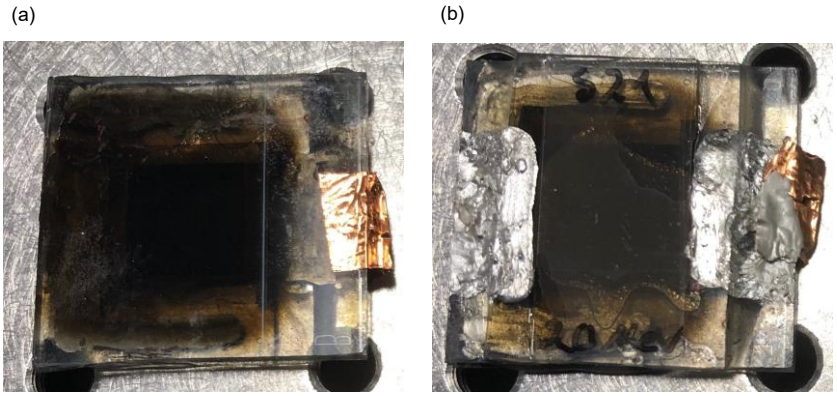

Figure 1.18 (a) 20 MeV Proton induced darkening effect on a soda lime glass substrate. (b) 20 MeV Proton induced darkening on soda lime glass encapsulation. These tests were done at a fluence of $1x10^{12}$ protons/cm^2

For orbiting systems, space-qualified glass made of ultra-thin cerium-doped glass is usually used to prevent this effect.[102] In 2018, Miyasaka performed a follow up experiment was performed looking at the effect of electron bombardment on double cation perovskite formulations.[98] It was found that standard planar PSCs with a methylammonium and Formamidinium double cation perovskite active layers can survive under accumulated dose levels up to $1x10^{16}$ electrons/cm^2 at an energy of 1 MeV. Electron bombardment induced device performance damage was found to be negligible, and no obvious degradation was observed in EQE. Therefore, PSCs should be very stable under electron bombardment.

1.3.5.2 X-Rays

Many things in space give off X-rays, such as black holes, neutron stars, the Sun. Another source of X-rays in space is the interaction of electrons with air molecules. These interactions can be split into 2 categories. Characteristic radiation, in which an incident electron will interact with a shell bound electron, causing it to be excited into free space. The hole left is filled with a higher shell electron, and this results in the release of an X-ray photon. The second interaction is Bremsstrahlung, or braking radiation, in which electrons are diverted by the nucleus of an atom. This diversion causes the electrons to release energy in the form of photons.[103] Both interactions are shown in Figure 1.19.

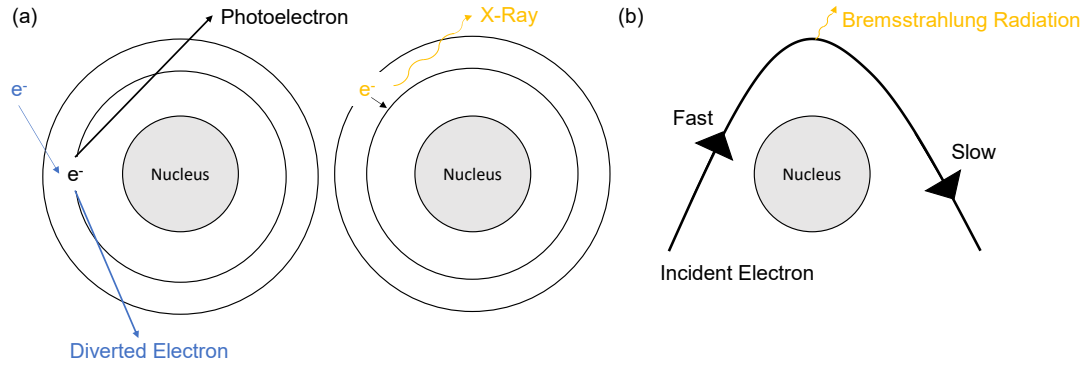

Figure 1.19 (a) Cartoon of the characteristic radiation interaction. An incident electron excites and removes an orbital electron. This shell space is then filled by a higher shell electron and emits an X-ray. (b) Cartoon of X-ray production via Bremsstrahlung.

Perovskite solar cells show promise for use as X-ray detectors. It was reported that a perovskite single crystal X-ray detector exhibited a detection efficiency of 16.4% at near zero bias under continuous X-ray irradiation up to an energy of 50 keV.[104] However, in this work no dose value is given. For the effect of X-ray radiation on PSCs, a study into the effect of X-ray exposure on perovskite films showed that perovskite films show evaporation under X-ray bombardment, reduced the material content and stoichiometry of the active layer.[105] Here the FA evaporates away under the X-ray, leaving behind PbI_2. However, little to no work has been done on the effects of X-ray bombardment on the operation of PSCs under a mimic space environment.

1.3.5.3 Gamma Rays

Lead halide perovskites have shown good performance in gamma-ray detection applications due to direct conversion of radiation into current or voltage signal.[106] Under gamma ray bombardment, It has been reported that PSCs with the structure of glass/ITO/PTAA/perovskite/C60/BCP/Cu under gamma-ray irradiation and light illumination simultaneously exhibit an 18% reduction in PCE as a result of the gamma rays after 5 hours of 1.5 krad/hr.[107] In LEO, the gamma ray dose is ~10 rad/hr.[108] Interestingly, there was evidence of a self-recovery mechanism within the devices after 1410 hr in the radiation test. The PSCs were shown to retain 96.8% of their initial PCE under continuous radiation of gamma-ray, with an accumulated dose of 2.3 Mrad or 1535 hrs (~26.5 years in LEO). The PCE stability of the PSCs surpasses that of c-Si solar cells.[107] The reported stability of PSCs is in part to the reported 'self-healing' behaviour in which gamma-ray induced generated defects within the perovskite relax, improving the FF. This allows for a recovery in efficiency loss due to early degradation induced by gamma ray radiation.

1.4 Objectives

This thesis focuses on the stability of PSCs under mimic LEO conditions. A wide range of different stability experiments are studied, along with new fabrication techniques to improve the PSCs specific power. PSCs are studied using various characterisation techniques to identify any degradation mechanisms observed while the devices were

in a controlled mimic LEO environment. Techniques such as Raman spectroscopy and photoluminescence (PL) were employed to study any chemical or optical changes in the PSCs because of thermal and humidity testing. X-ray Diffraction (XRD) measurements allowed for the investigation into the proton hardness of the perovskite active layer. Transient Photovoltage (TPV) was employed to investigate interfacial recombination between the perovskite and the HTL. An important objective for these studies is to establish relationships between the different layers within the PSC and device stability. Ultimately, the aim of this thesis is to provide insight into the feasibility of perovskite solar cells for space applications. The materials studied and the experimental methodology of techniques used are given in Chapter 2. Where applicable, device performance and statistical analysis are presented in the main text; with individual device data given in Appendix A & B for Chapter 3 & 4 respectively.

To investigate the stability of standard planar PSCs under comparable proton energy and fluence found in LEO, 150 keV proton bombardment stability of planar NIP PSCs as a function of proton fluence was extensively studied in Chapter 3. 150 keV proton bombardment was shown to cause device degradation at proton fluences $>1x10^{13}$ protons/cm^2. This degradation was shown to be a result of the spiro-OMeTAD HTL degrading under the irradiation, resulting in interfacial recombination at the perovskite/spiro-OMeTAD interface. This degradation resulting in a limiting of charge extraction, and therefore device performance. These results demonstrate that the proton stability of PSCs is dependent on the proton stability of the organic transporting layers.

In Chapter 4, the 150 keV proton stability of NIP m-CPSCs as a function of proton fluence was found to be dependent upon the thickness of the carbon electrode, correlating with the observed increase in proton bombardment stability. Based on these findings, it is proposed that a carbon electrode could be a suitable material for space-based electronics. The proton stopping power for different electrode materials was also investigated, with the proton mass stopping power of the carbon electrode being greater than that of Au, Ag, Cu, and Al. Here, it is proposed that m-CPSCs are an attractive architecture for stable space-based PSCs.

The thermal stability of planar NIP PSCs was studied in Chapter 5 to investigate how the device architecture and layers affects film and device stability during thermal cycling. The use of spiro-OMeTAD as the HTL was shown to affect device performance during 3 hours of thermal cycling between -100 and 85 °C. Low temperature stepping measurements showed that the device performance recovers after returning to room temperature, however high temperature measurements showed no recovery. By replacing the spiro-OMeTAD with P3HT, the high temperature thermal stability was greatly improved.

The J-V, thermal, and humidity stability of planar NIP PSCs utilising a thin film spray encapsulation is investigated in Chapter 6. Firstly, the effect of the encapsulation application was compared to glass and was found to offer superior PCE retention after encapsulation compared to glass encapsulated PSCs. Then a range of stability measurements were utilised to investigate the thermal, flexion and humidity stability of encapsulated PSCs. A correlation between the encapsulation thickness and humidity stability was found. This correlation can be explained by a reduction in the Water Vapour Transfer Rate (WVTR) due to the increased thickness.

Finally, all significant results from Chapters 3-6 are summarised in Chapter 7 and potential future work is discussed, such as studying the role of the ETL in the proton bombardment stability of PSCs.

REFERENCES

[1] Nocito, C., Koncar, V. (2016). Flexible photovoltaic cells embedded into textile structures. Smart Textiles and Their Applications, 401–422. https://doi.org/10.1016/b978-0-08-100574-3.00018-7

[2] Jones, H. W. (2018). Impact of lower launch cost on space life support. 2018 AIAA SPACE and Astronautics Forum and Exposition. https://doi.org/10.2514/6.2018-5286

[3] Shikoh, A. S., Polyakov, A. (2020). A quantitative analysis of the research trends in perovskite solar cells in 2009–2019. Physica Status Solidi (a), 217(23), 2000441. https://doi.org/10.1002/pssa.202000441

[4] Min, H., Lee, D. Y., Kim, J., Kim, G., Lee, K. S., Kim, J., Paik, M. J., Kim, Y. K., Kim, K. S., Kim, M. G., Shin, T. J., Il Seok, S. (2021). Perovskite solar cells with atomically coherent interlayers on SNO2 electrodes. Nature, 598(7881), 444–450. https://doi.org/10.1038/s41586-021-03964-8

[5] NREL. Best research-cell efficiency chart. NREL.gov. Retrieved May 27, 2022, from https://www.nrel.gov/pv/cell-efficiency.html

[6] AIAA. (2019). Qualification and Quality Requirements for Space Solar Cells – Amendment 1 (AIAA S-111A-2014/A1-2019). https://doi.org/10.2514/4.105852.001

[7] Hu, Y., Niu, T., Liu, Y., Zhou, Y., Xia, Y., Ran, C., Wu, Z., Song, L., Müller-Buschbaum, P., Chen, Y., Huang, W. (2021). Flexible perovskite solar cells with high power-per-weight: Progress, application, and Perspectives. ACS Energy Letters, 6(8), 2917–2943. https://doi.org/10.1021/acsenergylett.1c01193

[8] Mazumdar, S., Zhao, Y., Zhang, X. (2021). Stability of perovskite solar cells: Degradation mechanisms and remedies. Frontiers in Electronics, 2. https://doi.org/10.3389/felec.2021.712785

[9] Jiang, Y., Yang, S.-C., Jeangros, Q., Pisoni, S., Moser, T., Buecheler, S., Tiwari, A. N., Fu, F. (2020). Mitigation of vacuum and illumination-induced degradation in perovskite solar cells by structure engineering. Joule, 4(5), 1087–1103. https://doi.org/10.1016/j.joule.2020.03.017

[10] Bhati, M., Rai, R. (2018). Commercialization of large-scale perovskite solar energy technology and scaling-up issues. Perovskite Photovoltaics, 387–445. https://doi.org/10.1016/b978-0-12-812915-9.00013-7

[11] Dave Barthelmy. Perovskite Mineral Data. Retrieved November 19, 2018, from http://webmineral.com/data/Perovskite.shtml#.W_LH5Oj7RPY

[12] Kojima, A., Teshima, K., Shirai, Y., Miyasaka, T. (2009). Organometal halide perovskites as visible-light sensitizers for photovoltaic cells. Journal of the American Chemical Society, 131(17), 6050–6051. https://doi.org/10.1021/ja809598r

[13] Green, M. A., Ho-Baillie, A., Snaith, H. J. (2014). The emergence of perovskite solar cells. Nature Photonics, 8(7), 506–514. https://doi.org/10.1038/nphoton.2014.134

[14] Carsten Schinzer. Distortion of Perovskites. July 1998. Retrieved November 20, 2018, from http://www.ccp14.ac.uk/ccp/web-mirrors/pki/uni/pki/members/schinzer/stru_chem/perov/di_gold.html.

[15] Shi, Z., Jayatissa, A. (2018). Perovskites-based solar cells: A review of recent progress, materials and processing methods. Materials, 11(5), 729. https://doi.org/10.3390/ma11050729

[16] Saliba, M., Matsui, T., Seo, J.-Y., Domanski, K., Correa-Baena, J.-P., Nazeeruddin, M. K., Zakeeruddin, S. M., Tress, W., Abate, A., Hagfeldt, A., Grätzel, M. (2016). Cesium-containing triple cation perovskite solar cells: Improved stability, reproducibility and high efficiency. Energy & Environmental Science, 9(6), 1989–1997. https://doi.org/10.1039/c5ee03874j

[17] Sarah. From sunlight to electricity. Nov. 2017. Retrieved November 25, 2018, from https://www.science.org.au/curious/technology- future/solar- pv

[18] Gupta, D., Mukhopadhyay, S., Narayan, K. S. (2010). Fill factor in organic solar cells. Solar Energy Materials and Solar Cells, 94(8), 1309–1313. https://doi.org/10.1016/j.solmat.2008.06.001

[19] Hernández-Granados, A., Corpus-Mendoza, A. N., Moreno-Romero, P. M., Rodríguez-Castañeda, C. A., Pascoe-Sussoni, J. E., Castelo-González, O. A., Menchaca-Campos, E. C., Escorcia-García, J., Hu, H. (2019). Optically uniform

thin films of mesoporous tio2 for Perovskite Solar Cell Applications. Optical Materials, 88, 695–703. https://doi.org/10.1016/j.optmat.2018.12.044

[20] Sun, C. (2022). Recent progress and state-of art applications of perovskite solar cells. Highlights in Science, Engineering and Technology, 5, 141–148. https://doi.org/10.54097/hset.v5i.735

[21] Saliba, M., Correa-Baena, J.-P., Wolff, C. M., Stolterfoht, M., Phung, N., Albrecht, S., Neher, D., Abate, A. (2018). How to make over 20% efficient perovskite solar cells in regular (N–I–P) and inverted (P–I–N) architectures. Chemistry of Materials, 30(13), 4193–4201. https://doi.org/10.1021/acs.chemmater.8b00136

[22] Yang, D., Sano, T., Yaguchi, Y., Sun, H., Sasabe, H., Kido, J. (2019). Perovskite solar cells: Achieving 20% efficiency for low‐temperature‐processed inverted perovskite solar cells (adv. funct. mater. 12/2019). Advanced Functional Materials, 29(12), 1970074. https://doi.org/10.1002/adfm.201970074

[23] Lee, S.-W., Kim, S., Bae, S., Cho, K., Chung, T., Mundt, L. E., Lee, S., Park, S., Park, H., Schubert, M. C., Glunz, S. W., Ko, Y., Jun, Y., Kang, Y., Lee, H.-S., Kim, D. (2016). UV degradation and recovery of perovskite solar cells. Scientific Reports, 6(1). https://doi.org/10.1038/srep38150

[24] Khambunkoed, N., Homnan, S., Gardchareon, A., Chattrapiban, N., Songsiriritthigul, P., Wongratanaphisan, D., Ruankham, P. (2021). Fully-covered slot-die-coated zno thin films for reproducible carbon-based perovskite solar cells. Materials Science in Semiconductor Processing, 136, 106151. https://doi.org/10.1016/j.mssp.2021.106151

[25] Baker, J., Hooper, K., Meroni, S., Pockett, A., McGettrick, J., Wei, Z., Escalante, R., Oskam, G., Carnie, M., Watson, T. (2017). High throughput fabrication of mesoporous carbon perovskite solar cells. Journal of Materials Chemistry A, 5(35), 18643–18650. https://doi.org/10.1039/c7ta05674e

[26] Hughes, D., Meroni, S., Barbe, J., Raptis, D., Heasman, K., Lang, F., Watson, T., Tsoi, W. (2022). Proton radiation hardness of perovskite solar cells utilizing a mesoporous carbon electrode. Proceedings of the New Generation

Photovoltaics for Space. https://doi.org/10.29363/nanoge.pvspace.2022.006

[27] Kobayashi, E., Tsuji, R., Martineau, D., Hinsch, A., Ito, S. (2021). Light-induced performance increase of carbon-based perovskite solar module for 20-year stability. Cell Reports Physical Science, 2(12), 100648. https://doi.org/10.1016/j.xcrp.2021.100648

[28] Meroni, S. M., Worsley, C., Raptis, D., Watson, T. M. (2021). Triple-mesoscopic carbon perovskite solar cells: Materials, processing and applications. Energies, 14(2), 386. https://doi.org/10.3390/en14020386

[29] Wang, K., Zheng, L., Hou, Y., Nozariasbmarz, A., Poudel, B., Yoon, J., Ye, T., Yang, D., Pogrebnyakov, A. V., Gopalan, V., Priya, S. (2022). Overcoming shockley-queisser limit using halide perovskite platform? Joule, 6(4), 756–771. https://doi.org/10.1016/j.joule.2022.01.009

[30] Peplow, M. Perovskite progress pushes tandem solar cells closer to market. Cen.acs.org. Retrieved December 12, 2018, from https://cen.acs.org/energy/solar-power/Perovskite-progress-pushes-tandem-solar/96/i24

[31] Song, Z., Yan, Y. (2021). All perovskite tandem solar cells. Hybrid Perovskite Solar Cells, 509–539. https://doi.org/10.1002/9783527825851.ch18

[32] Bellini, E. (2022, July 7). CSEM, EPFL achieve 31.25% efficiency for tandem perovskite-silicon solar cell. pv magazine International. Retrieved September 27, 2022, from https://www.pv-magazine.com/2022/07/07/csem-epfl-achieve-31-25-efficiency-for-tandem-perovskite-silicon-solar-cell/

[33] Lin, R., Xu, J., Wei, M., Wang, Y., Qin, Z., Liu, Z., Wu, J., Xiao, K., Chen, B., Park, S. M., Chen, G., Atapattu, H. R., Graham, K. R., Xu, J., Zhu, J., Li, L., Zhang, C., Sargent, E. H., Tan, H. (2022). All-perovskite tandem solar cells with improved grain surface passivation. Nature, 603(7899), 73–78. https://doi.org/10.1038/s41586-021-04372-8

[34] Parker, S. P. (1984). McGraw-Hill Concise Encyclopedia of Science & Technology. McGraw-Hill.

[35] Quanliang, C., Lingxiao, W. (2012). Relationship of temperature variation between in the stratosphere and the troposphere. Procedia Environmental Sciences, 12, 666–671. https://doi.org/10.1016/j.proenv.2012.01.333

[36] Chmielewski, P., Wróblewski, W. (2017). Selected issues of designing and testing of a Hale-class Unmanned Aircraft. Journal of Marine Engineering & Technology, 16(4), 365–376. https://doi.org/10.1080/20464177.2017.1376371

[37] Beig, G. (2011). Long-term trends in the temperature of the mesosphere/lower Thermosphere region: 1. anthropogenic influences. Journal of Geophysical Research: Space Physics, 116(A2). https://doi.org/10.1029/2011ja016646

[38] McDowell, J. C. (2018). The edge of space: Revisiting the karman line. Acta Astronautica, 151, 668–677. https://doi.org/10.1016/j.actaastro.2018.07.003

[39] Horneck, G. (2015). Space environment. Encyclopedia of Astrobiology, 2293–2299. https://doi.org/10.1007/978-3-662-44185-5_1469

[40] Harde, H. (2013). Radiation and heat transfer in the atmosphere: A comprehensive approach on a molecular basis. International Journal of Atmospheric Sciences, 2013, 1–26. https://doi.org/10.1155/2013/503727

[41] Damjanov, K., Crouch, D. (2018). Orbital Life on the International Space Station. Space and Culture, 22(1), 77–89. https://doi.org/10.1177/1206331217752621

[42] Speight, J. G. (2020). Natural water remediation: Chemistry and technology. Butterworth-Heinemann.

[43] Alonso-Álvarez, D., Wilson, T., Pearce, P., Führer, M., Farrell, D., Ekins-Daukes, N. (2018). Solcore: A multi-scale, python-based library for modelling solar cells and semiconductor materials. Journal of Computational Electronics, 17(3), 1099–1123. https://doi.org/10.1007/s10825-018-1171-3

[44] Ångström, A. (1965). The solar constant and the temperature of the Earth. Progress in Oceanography, 3, 1–5. https://doi.org/10.1016/0079-6611(65)90004-2

[45] West, J. B. (1996). Prediction of barometric pressures at high altitudes with the use of model atmospheres. Journal of Applied Physiology, 81(4), 1850–1854. https://doi.org/10.1152/jappl.1996.81.4.1850

[46] Guo, S., Brandt, C., Andreev, T., Metwalli, E., Wang, W., Perlich, J., Müller-Buschbaum, P. (2014). First Step into space: Performance and morphological evolution of P3HT:PCBM bulk heterojunction solar cells under AM0 illumination. ACS Applied Materials & Interfaces, 6(20), 17902–17910. https://doi.org/10.1021/am504608p

[47] Otte, K., Makhova, L., Braun, A., Konovalov, I. (2006). Flexible cu(in,GA)SE2 thin-film solar cells for space application. Thin Solid Films, 511-512, 613–622. https://doi.org/10.1016/j.tsf.2005.11.068

[48] Routledge. (2013). Planning and installing photovoltaic systems: A guide for Installers, architects and engineers.

[49] Micha, D. N., Silvares Junior, R. T. (2019). The influence of solar spectrum and concentration factor on the material choice and the efficiency of multijunction solar cells. Scientific Reports, 9(1). https://doi.org/10.1038/s41598-019-56457-0

[50] Cincinnati Sub Zero. Photovoltaic Solar Testing Specifications. IEC 61646, IEC 61215 | Cincinnati Sub Zero. Retrieved April 28, 2021, from https://www.cszindustrial.com/Products/Custom-Designed-Chambers/Solar-Panel-Testing-Chamber/Solar-Testing-Specifications.aspx

[51] Kondratiev, K. Y., Nicolsky, G. A., Badinov, I. Y., Andreev, S. D. (1967). Direct solar radiation up to 30 km and stratification of attenuation components in the stratosphere. Applied Optics, 6(2), 197. https://doi.org/10.1364/ao.6.000197

[52] Perlin, J. (2002). From space to Earth: The story of solar electricity. Harvard Univ. Press.

[53] Bellis, M. (2019, July 3). The history of the First Solar Cell. ThoughtCo. Retrieved September 28, 2022, from https://www.thoughtco.com/photovoltaics-timeline-1992481

[54] Boca, A. (2019). Solar cell testing for the jupiter environment: Low irradiance, low temperature and high radiation. 2019 IEEE 46th Photovoltaic Specialists Conference (PVSC). https://doi.org/10.1109/pvsc40753.2019.8981342

[55] NASA. The NASA electronic parts and Packaging Program. Environmental Conditions for Space Flight Hardware – A Survey. Retrieved June 28, 2019, from https://nepp.nasa.gov/DocUploads/C5E0869C-0469-4D11-9FAA8012C8F52351/Environmental%20Testing%20Survey.doc

[56] Thomas, B. C., Melott, A. L., Jackman, C. H., Laird, C. M., Medvedev, M. V., Stolarski, R. S., Gehrels, N., Cannizzo, J. K., Hogan, D. P., Ejzak, L. M. (2005). Gamma‐Ray Bursts and the Earth: Exploration of atmospheric, biological, climatic, and biogeochemical effects. The Astrophysical Journal, 634(1), 509–533. https://doi.org/10.1086/496914

[57] Martinez Sierra Luz Maria. "Analysis of LEO radiation environment and its effects on spacecraft's critical electronic devices". PhD thesis. 2011.

[58] Heilbronn, L. NASA. Neutron Properties and Definitions . Retrieved August 28, 2019, from https://three.jsc.nasa.gov/articles/Heilbronn_Neutron_Supplement.pdf

[59] Nunes, M., French, L., Englert, P.A., Pilger, E.J., Yoneshige, L., Rodrigues, I., Gershom, Y.B., Imai-Hong, A., Hagi, K., Opie, C., Flynn, L., Hardgrove, C., Roebuck, B. (2019). NEUTRON-1 Mission: Low Earth Orbit Neutron Flux Detection and COSMOS Mission Operations Technology Demonstration.

[60] Harris, M. J. (2003). Spatial and temporal variability of the gamma radiation from Earth's atmosphere during a solar cycle. Journal of Geophysical Research, 108(A12). https://doi.org/10.1029/2003ja009958

[61] Vaccaro, A., Villacci, D. (2005). Performance Analysis of Low Earth Orbit Satellites for Power System Communication. Electric Power Systems Research, 73(3), 287–294. https://doi.org/10.1016/j.epsr.2004.07.011

[62] Andreev, V. M. (2005). Gaas and high-efficiency space cells. Solar Cells, 353–369. https://doi.org/10.1016/b978-185617457-2/50014-7

[63] Schneider, T. A., Vaughn, J. A., Wright, K. H., Phillips, B. S. (2015). Space environment testing of photovoltaic array systems at NASA's Marshall Space

Flight Center. 2015 IEEE 42nd Photovoltaic Specialist Conference (PVSC). https://doi.org/10.1109/pvsc.2015.7355861

[64] Kim, J., Kawasaki, T., Shikata, Y., Hosoda, S., Cho, M. (2005). Solar Array ESD ground tests in simulated Geo Environment. 43rd AIAA Aerospace Sciences Meeting and Exhibit. https://doi.org/10.2514/6.2005-483

[65] Kruk, J. W., Xapsos, M. A., Armani, N., Stauffer, C., Hirata, C. M. (2016). Radiation-induced backgrounds in astronomical instruments: Considerations for geosynchronous orbit and implications for the design of the firstwide-field instrument. Publications of the Astronomical Society of the Pacific, 128(961), 035005. https://doi.org/10.1088/1538-3873/128/961/035005

[66] Horne, R. B., Glauert, S. A., Meredith, N. P., Boscher, D., Maget, V., Heynderickx, D., Pitchford, D. (2013). Space weather impacts on satellites and forecasting the Earth's electron radiation belts with SPACECAST. Space Weather, 11(4), 169–186. https://doi.org/10.1002/swe.20023

[67] ESA. Rosetta: Frequently asked questions. Retrieved March 12, 2020, from https://www.esa.int/Science_Exploration/Space_Science/Rosetta/Frequently_asked_questions

[68] Khorenko, V., Baur, C., Siefer, G., Schachtner, M., Park, S., Boizot, B., Bourgoin, J. C., Casale, M., Campesato, R. (2017). Bol and EOL characterization of Azur 3G lilt solar cells for ESA Juice Mission. E3S Web of Conferences, 16, 03011. https://doi.org/10.1051/e3sconf/20171603011

[69] Grandidier, J., Atwater, H. A., Cutts, J. A., Kirk, A. P., Osowski, M. L., Gogna, P. K., Fan, S., Lee, M. L., Stevens, M. A., Jahelka, P., Tagliabue, G. (2018). Low-intensity high-temperature (LIHT) solar cells for Venus Atmosphere. IEEE Journal of Photovoltaics, 8(6), 1621–1626. https://doi.org/10.1109/jphotov.2018.2871333

[70] McMillon-Brown, L., Luther, J. M., Peshek, T. J. (2022). What would it take to manufacture perovskite solar cells in space? ACS Energy Letters, 7(3), 1040–1042. https://doi.org/10.1021/acsenergylett.2c00276

[71] Kim, J.-H., Choi, E. Y., Kim, B.-J., Han, E., Park, N. (2019). Stability enhancement of GaInP/GaAs/Ge Triple-junction solar cells using al2o3 moisture-barrier layer. Vacuum, 162, 47–53. https://doi.org/10.1016/j.vacuum.2019.01.022

[72] Koushik, D., Verhees, W. J., Kuang, Y., Veenstra, S., Zhang, D., Verheijen, M. A., Creatore, M., Schropp, R. E. (2017). High-efficiency humidity-stable planar perovskite solar cells based on atomic layer architecture. Energy & Environmental Science, 10(1), 91–100. https://doi.org/10.1039/c6ee02687g

[73] Cao, F., Zhang, P., Sun, H., Wang, M., Li, L. (2022). Degradation mechanism and stability improvement of formamidine-based perovskite solar cells under high humidity conditions. Nano Research. https://doi.org/10.1007/s12274-022-4524-y

[74] Hooper, K. E., Lee, H. K., Newman, M. J., Meroni, S., Baker, J., Watson, T. M., Tsoi, W. C. (2017). Probing the degradation and homogeneity of embedded perovskite semiconducting layers in photovoltaic devices by Raman spectroscopy. Physical Chemistry Chemical Physics, 19(7), 5246–5253. https://doi.org/10.1039/c6cp05123e

[75] Idígoras, J., Aparicio, F. J., Contreras-Bernal, L., Ramos-Terrón, S., Alcaire, M., Sánchez-Valencia, J. R., Borras, A., Barranco, Á., Anta, J. A. (2018). Enhancing moisture and water resistance in perovskite solar cells by encapsulation with ultrathin plasma polymers. ACS Applied Materials & Interfaces, 10(14), 11587–11594. https://doi.org/10.1021/acsami.7b17824

[76] Berhe, T. A., Su, W.-N., Chen, C.-H., Pan, C.-J., Cheng, J.-H., Chen, H.-M., Tsai, M.-C., Chen, L.-Y., Dubale, A. A., Hwang, B.-J. (2016). Organometal halide perovskite solar cells: Degradation and stability. Energy & Environmental Science, 9(2), 323–356. https://doi.org/10.1039/c5ee02733k

[77] Sun, Y., Fang, X., Ma, Z., Xu, L., Lu, Y., Yu, Q., Yuan, N., Ding, J. (2017). Enhanced UV-light stability of organometal halide perovskite solar cells with interface modification and a UV absorption layer. Journal of Materials Chemistry C, 5(34), 8682–8687. https://doi.org/10.1039/c7tc02603j

[78] Leijtens, T., Eperon, G. E., Pathak, S., Abate, A., Lee, M. M., Snaith, H. J. (2013). Overcoming ultraviolet light instability of sensitized TIO2 with Meso-superstructured organometal tri-halide perovskite solar cells. Nature Communications, 4(1). https://doi.org/10.1038/ncomms3885

[79] Wang, D., Wright, M., Elumalai, N. K., Uddin, A. (2016). Stability of perovskite solar cells. Solar Energy Materials and Solar Cells, 147, 255–275. https://doi.org/10.1016/j.solmat.2015.12.025

[80] Roose, B., Baena, J.-P. C., Gödel, K. C., Graetzel, M., Hagfeldt, A., Steiner, U., Abate, A. (2016). Mesoporous sno2 electron selective contact enables UV-stable perovskite solar cells. Nano Energy, 30, 517–522. https://doi.org/10.1016/j.nanoen.2016.10.055

[81] NASA. Solve II science implementation. NASA. Retrieved October 12, 2021, from https://cloud1.arc.nasa.gov/solveII/implement.html

[82] Farooq, A., Hossain, I. M., Moghadamzadeh, S., Schwenzer, J. A., Abzieher, T., Richards, B. S., Klampaftis, E., Paetzold, U. W. (2018). Spectral dependence of degradation under ultraviolet light in perovskite solar cells. ACS Applied Materials & Interfaces, 10(26), 21985–21990. https://doi.org/10.1021/acsami.8b03024

[83] Jiang, L., Chen, W., Zheng, J., Zhu, L., Mo, L., Li, Z., Hu, L., Hayat, T., Alsaedi, A., Zhang, C., Dai, S. (2017). Enhancing the photovoltaic performance of Perovskite Solar Cells with a down-conversion EU-Complex. ACS Applied Materials & Interfaces, 9(32), 26958–26964. https://doi.org/10.1021/acsami.7b10101

[84] Whitfield, P. S., Herron, N., Guise, W. E., Page, K., Cheng, Y. Q., Milas, I., Crawford, M. K. (2016). Structures, phase transitions and tricritical behavior of the hybrid perovskite methyl ammonium lead iodide. Scientific Reports, 6(1). https://doi.org/10.1038/srep35685

[85] Granite. (2021, December 14). Halide perovskite: Observing phase transitions in a halide perovskite. Edinburgh Instruments. Retrieved February 20, 2022, from https://www.edinst.com/phase-transitions-halide-perovskite/

[86] Kundu, S., Kelly, T. L. (2020). In situ studies of the degradation mechanisms of perovskite solar cells. EcoMat, 2(2). https://doi.org/10.1002/eom2.12025

[87] Barbé, J., Pockett, A., Stoichkov, V., Hughes, D., Lee, H. K., Carnie, M., Watson, T., Tsoi, W. C. (2020). in situ investigation of perovskite solar cells' efficiency and stability in a mimic stratospheric environment for high-altitude pseudo-satellites. Journal of Materials Chemistry C, 8(5), 1715–1721. https://doi.org/10.1039/c9tc04984c

[88] Meng, Q., Chen, Y., Xiao, Y. Y., Sun, J., Zhang, X., Han, C. B., Gao, H., Zhang, Y., Yan, H. (2020). Effect of temperature on the performance of Perovskite Solar Cells. Journal of Materials Science: Materials in Electronics, 32(10), 12784–12792. https://doi.org/10.1007/s10854-020-03029-y

[89] Jena, A. K., Numata, Y., Ikegami, M., Miyasaka, T. (2018). Role of spiro-ometad in performance deterioration of perovskite solar cells at high temperature and reuse of the perovskite films to avoid PB-waste. Journal of Materials Chemistry A, 6(5), 2219–2230. https://doi.org/10.1039/c7ta07674f

[90] Malinauskas, T., Tomkute-Luksiene, D., Sens, R., Daskeviciene, M., Send, R., Wonneberger, H., Jankauskas, V., Bruder, I., Getautis, V. (2015). Enhancing thermal stability and lifetime of solid-state dye-sensitized solar cells via molecular engineering of the Hole-transporting material Spiro-OMeTAD. ACS Applied Materials & Interfaces, 7(21), 11107–11116. https://doi.org/10.1021/am5090385

[91] Jung, M., Kim, Y. C., Jeon, N. J., Yang, W. S., Seo, J., Noh, J. H., Il-Seok, S. (2016). Thermal stability of Cuscn Hole conductor-based perovskite solar cells. ChemSusChem, 9(18), 2592–2596. https://doi.org/10.1002/cssc.201600957

[92] Zhang, H., Qiao, X., Shen, Y., Moehl, T., Zakeeruddin, S. M., Grätzel, M., Wang, M. (2015). Photovoltaic behaviour of lead methylammonium triiodide perovskite solar cells down to 80 K. Journal of Materials Chemistry A, 3(22), 11762–11767. https://doi.org/10.1039/c5ta02206a

[93] Reb, L. K., Böhmer, M., Predeschly, B., Grott, S., Weindl, C. L., Ivandekic, G. I., Guo, R., Dreißigacker, C., Gernhäuser, R., Meyer, A., Müller-Buschbaum, P. (2020). Perovskite and organic solar cells on a rocket flight. Joule, 4(9), 1880–1892. https://doi.org/10.1016/j.joule.2020.07.004

[94] Morison, I. (2008). Introduction to astronomy and cosmology. Wiley.

[95] Miyazawa, Y., Ikegami, M., Miyasaka, T., Ohshima, T., Imaizumi, M., Hirose, K. (2015). Evaluation of radiation tolerance of perovskite solar cell for use in space. 2015 IEEE 42nd Photovoltaic Specialist Conference (PVSC). https://doi.org/10.1109/pvsc.2015.7355859

[96] Lang, F., Eperon, G. E., Frohna, K., Tennyson, E. M., Al‐Ashouri, A., Kourkafas, G., Bundesmann, J., Denker, A., West, K. G., Hirst, L. C., Neitzert, H. C., Stranks, S. D. (2021). Proton‐radiation tolerant all‐perovskite multijunction solar cells. Advanced Energy Materials, 11(41), 2102246. https://doi.org/10.1002/aenm.202102246

[97] Barbé, J., Hughes, D., Wei, Z., Pockett, A., Lee, H. K., Heasman, K. C., Carnie, M. J., Watson, T. M., Tsoi, W. C. (2019). Radiation hardness of perovskite solar cells based on aluminum‐doped zinc oxide electrode under proton irradiation. Solar RRL, 3(12), 1900219. https://doi.org/10.1002/solr.201900219

[98] Miyazawa, Y., Ikegami, M., Chen, H.-W., Ohshima, T., Imaizumi, M., Hirose, K., Miyasaka, T. (2018). Tolerance of perovskite solar cell to high-energy particle irradiations in space environment. IScience, 2, 148–155. https://doi.org/10.1016/j.isci.2018.03.020

[99] Durant, B. K., Afshari, H., Singh, S., Rout, B., Eperon, G. E., Sellers, I. R. (2021). Tolerance of perovskite solar cells to targeted proton irradiation and electronic ionization induced healing. ACS Energy Letters, 6(7), 2362–2368. https://doi.org/10.1021/acsenergylett.1c00756

[100] Brus, V. V., Lang, F., Bundesmann, J., Seidel, S., Denker, A., Rech, B., Landi, G., Neitzert, H. C., Rappich, J., Nickel, N. H. (2017). Defect dynamics in Proton irradiated $CH_3NH_3PbI_3$ Perovskite Solar Cells. Advanced Electronic Materials, 3(2), 1600438. https://doi.org/10.1002/aelm.201600438

[101] Luo, P., Sun, X.-Y., Li, Y., Yang, L., Shao, W.-Z., Zhen, L., Xu, C.-Y. (2021). Correlation between structural evolution and device performance of $CH_3NH_3PbI_3$ Solar cells under proton irradiation. ACS Applied Energy Materials, 4(12), 13504–13515. https://doi.org/10.1021/acsaem.1c01958

[102] Henson, T. D., Torrington, G. K. (2001). . Inorganic Optical Materials III. https://doi.org/10.1117/12.446894

[103] Tan, D., Heaton, B. (1994). Bremsstrahlung intensity and spectrum—theoretical deduction and discussion. Applied Radiation and Isotopes, 45(11), 1101–1111. https://doi.org/10.1016/0969-8043(94)90190-2

[104] Wei, H., Fang, Y., Mulligan, P., Chuirazzi, W., Fang, H.-H., Wang, C., Ecker, B. R., Gao, Y., Loi, M. A., Cao, L., Huang, J. (2016). Sensitive X-ray detectors made of methylammonium lead tribromide perovskite single crystals. Nature Photonics, 10(5), 333–339. https://doi.org/10.1038/nphoton.2016.41

[105] Svanström, S., García Fernández, A., Sloboda, T., Jacobsson, T. J., Rensmo, H., Cappel, U. B. (2021). X-ray stability and degradation mechanism of lead halide perovskites and lead halides. Physical Chemistry Chemical Physics, 23(21), 12479–12489. https://doi.org/10.1039/d1cp01443a

[106] Liu, F., Wu, R., Wei, J., Nie, W., Mohite, A. D., Brovelli, S., Manna, L., Li, H. (2022). Recent progress in halide perovskite radiation detectors for gamma-ray spectroscopy. ACS Energy Letters, 7(3), 1066–1085. https://doi.org/10.1021/acsenergylett.2c00031

[107] Yang, S., Xu, Z., Xue, S., Kandlakunta, P., Cao, L., Huang, J. (2018). Organohalide lead perovskites: More stable than glass under gamma‐ray radiation. Advanced Materials, 31(4), 1805547. https://doi.org/10.1002/adma.201805547

[108] Onorato, G., Di Schiavi, E., Di Cunto, F. (2020). Understanding the effects of Deep Space Radiation on nervous system: The role of Genetically Tractable Experimental Models. Frontiers in Physics, 8. https://doi.org/10.3389/fphy.2020.00362

Chapter 2

Experimental Methodology and Simulations

2.1 Materials

The perovskite precursor materials used in this thesis were purchased from Tokyo Chemical Company (TCI), Sigma Aldrich and Dyesol. The precursor characteristics are outlined in Table 2.1.

Table 2.1 Perovskite precursor purities and molecular weights

Material	Purity (%)	Molecular Weight (g/mol)
Lead Iodide (PbI_2)	>98.0	461.01
Lead Bromide ($PbBr_2$)	>98.0	367.01
Methylammonium Bromide (MABr)	>99.99	111.97
Formamidinium Iodide (FAI)	>99.99	171.97
Cesium Iodide (CsI)	99.999	259.81

The hole transporting layer materials were purchased from Sigma Aldrich and Ossila. They are shown in table 2.2. The molecular structure and full chemical name are shown in Figure 2.1.

Table 2.2 HTL precursor purities and molecular weights

Material	Purity (%)	Molecular Weight (g/mol)
Spiro-OMeTAD	99.0	1225.43
FK209	98.0	1503.17
4-TbP	>98.0	135.21
LI-TFSI	99.99	287.08
P3HT	97.6	60150

Spiro-OMeTAD

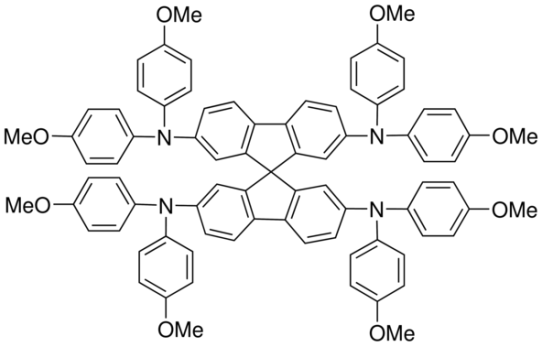

$N^2,N^2,N^{2'},N^{2'},N^7,N^7,N^{7'},N^{7'}$-octakis(4-methoxyphenyl)-9,9′-spirobi[9H-fluorene]-2,2′,7,7′-tetramine

P3HT

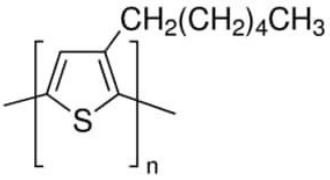

Poly(3-hexylthiophene-2,5-diyl)

Figure 2.1 Molecular structure and full chemical name of the HTL materials. Images taken from the Sigma Aldrich Website.[1][2]

The solvents chlorobenzene (CB), Dimethylformamide (DMF) and dimethyl sulfoxide (DMSO) were purchased from Sigma Aldrich. SnO_2 nanoparticles in colloidal suspension were purchased from Alfa Aesar.

2.2 Device Fabrication

2.2.1 Standard Device Design

The completed perovskite device is shown in Figure 2.2, where the glass substrate is 25 x 25 mm^2. The cells have 1 pixel with an active area of 1 cm^2, and 5 cells with an active area of 0.15 cm^2. Most devices studied were fabricated following the standard planar architecture: ITO glass (~100 nm)/tin oxide (SnO_2) (~25 nm)/triple cation perovskite (~400 nm)/spiro-OMeTAD (~75 nm)/gold (Au) (~100 nm). The ITO glass used was pre-patterned with two ITO stripes with a sheet resistance of 15 Ω/□.

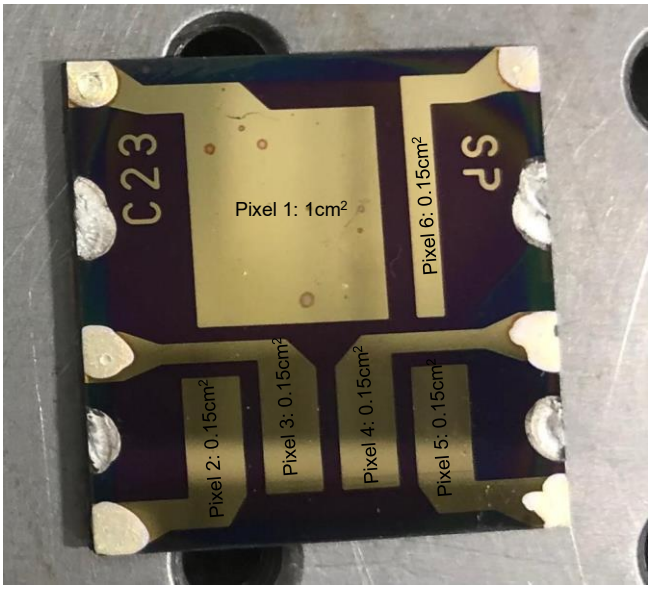

Figure 2.2 The commonly used PSC throughout this thesis after fabrication with the pixel layout labelled.

Firstly, the ITO glass substrates were scrubbed with Hellmanex detergent and a toothbrush. They were then sonicated in Hellmanex for 5 minutes, de-ionized (DI) water three times for 5 minutes, twice in acetone for 5 minutes and once in IPA for 5 minutes. The devices were then dried using a N_2 gun and placed into an O_2 plasma cleaner for 5 minutes under O_2 plasma at ~0.4 mbar. The SnO_2 nanoparticle (NP) solution was prepared by mixing the SnO_2 NPs in colloidal suspension and DI water in a 6.5:1 (V:V) ratio. This solution was sonicated for 30 minutes, and then mechanical vibrated to decrease the likelihood of NP agglomeration. The SnO_2 NP precursor layer was spin coated onto the ITO substrate in air at 3000 rpm, with 3000 rpm/s acceleration for 30s. Two stripes of the SnO_2 NP precursor were then wiped off with DI water using a cotton bud to expose the ITO contacts, and then the film was annealed at 150 °C on a hotplate for 30 minutes to form SnO_2 (25 nm). The perovskite solution was fabricated by mixing 507mg PbI_2, 22 mg MABr, 73 mg $PbBr_2$ and 172 mg FAI. These were dissolved in a mixture of DMF:DMSO in an 8:2 (V:V) ratio for 1 hour, before adding 52 µl of 320 mg/ml of CsI in DMSO. The final stoichiometric formulation of the triple cation is $Cs_{0.05}(FA_{0.83}MA_{0.17})Pb(I_{0.83}Br_{0.17})_3$. The solution was then spin coated in a dry nitrogen filled glovebox using 2 spin speeds (1000 rpm for 10s & 6000 rpm for 20s) via the anti-solvent method with chlorobenzene (CB) to give a layer thickness of 450 nm. The spiro-OMeTAD solution was prepared by mixing 90

mg spiro-OMeTAD, 10 µl FK209 (300 mg/ml in acetonitrile), 19 µl Li-TFSI (520 mg/ml in CB) and 34 µl 4-tBP. This was dissolved in 1 ml of CB. The Spiro-OMeTAD solution spin coated onto the devices at 4000 rpm, with a ramp speed of 2000 rpm/s for 20s to give a layer thickness of 100 nm. Finally, 100 nm of Au were thermally evaporated to complete the devices. Devices were encapsulated with Kapton tape, UV cured epoxy and glass unless otherwise stated. There were 8 devices made per batch, each with 4 pixels measured per sample (0.15 cm^2), giving a total of 32 J-V measurements per batch.

2.2.2 Aluminium-doped Zinc Oxide TCO

In chapter 3, quartz is used to offset the transparency reduction that soda lime glass encounters under high energy proton bombardment. These quartz samples are un-patterned, so aluminium-doped zinc oxide was used for the transparent conducting oxide (TCO). Additionally, AZO was chosen due to its low cost, non-toxicity, and non-reliance on rare earth elements.[3] The quartz substrates (UV grade fused silica glass) were purchased from Kintec. The quartz was cleaned via the same method as described in Section 2.2.1. The AZO was then radio-frequency (RF) sputtered by Dr. Zhengfei Wei (Swansea University) using a Moorfield Nanolab 60 sputtering system with power density of 2.46 W/cm^2. The sheet resistance of deposited AZO is 23-25 Ω/□ and the layer thickness was measured to be ~700 nm. The devices were then fabricated following the same procedures as Section 2.2.1.

2.2.3 Mesoporous Carbon Perovskite Solar Cells

In Chapter 4, mesoporous carbon perovskite solar cells (m-CPSCs) were used to investigate the radiation hardness of HTL free PSCs. The M-CPSCs were fabricated by Dr. Simone Meroni and Dr. Dimitrios Raptis (Swansea University). The Fluorine-doped Tin Oxide (FTO) substrate was initially patterned with a Nb:YVO4 laser (532 nm), then cleaned with a solution of Hellmanex (2%, deionized water), rinsed with acetone, IPA, and finally plasma cleaned in an O_2 atmosphere for 5 min. A compact TiO_2 blocking layer was sprayed with a solution of 10% Titanium di-isopropoxide bis (acetylacetonate) (TAA, 75% in IPA, Sigma-Aldrich) on the FTO substrate, which was kept at 300 °C on a hot plate. After the deposition of C-TiO_2 (~50 nm), the

mesoporous TiO_2 paste was diluted 1:1 by weight in terpineol (95%, Sigma-Aldrich), screen-printed and sintered at 550 °C (~600 nm). Next, the mesoporous ZrO_2 (Solaronix) and carbon paste (Gwent electronic materials) were sequentially screen-printed and each annealed at 400 °C (~1.65 µm and ~12 µm respectively). MAPI-AVA perovskite precursor solution (0.439 g PbI_2 (99%, Sigma-Aldrich), 0.1514 g MAI (CH_3NH_3I, anhydrous, Dyesol) and 0.0067 g 5-ammonium valeric acid iodide (5-AVAI, Dyesol) in 1 ml γ-Butyrolactone (Sigma Aldrich)) was then drop cast (15 µl) onto the cooled stack. Devices were left in air for 10 min to allow the solution to percolate through the stack, before annealing in an oven for 1 hr at 50 °C. The finished cells were then exposed to a standard 70% relative humidity process at 40 °C for 24 hrs to induce a recrystallisation and then dried under vacuum before measuring. Each m-CPSC has an active area of 1 cm^2 and were made in batches of ~10 devices. A cartoon of the m-CPSC architecture is shown in Figure 2.3, along with each layer and its effective thickness labelled.

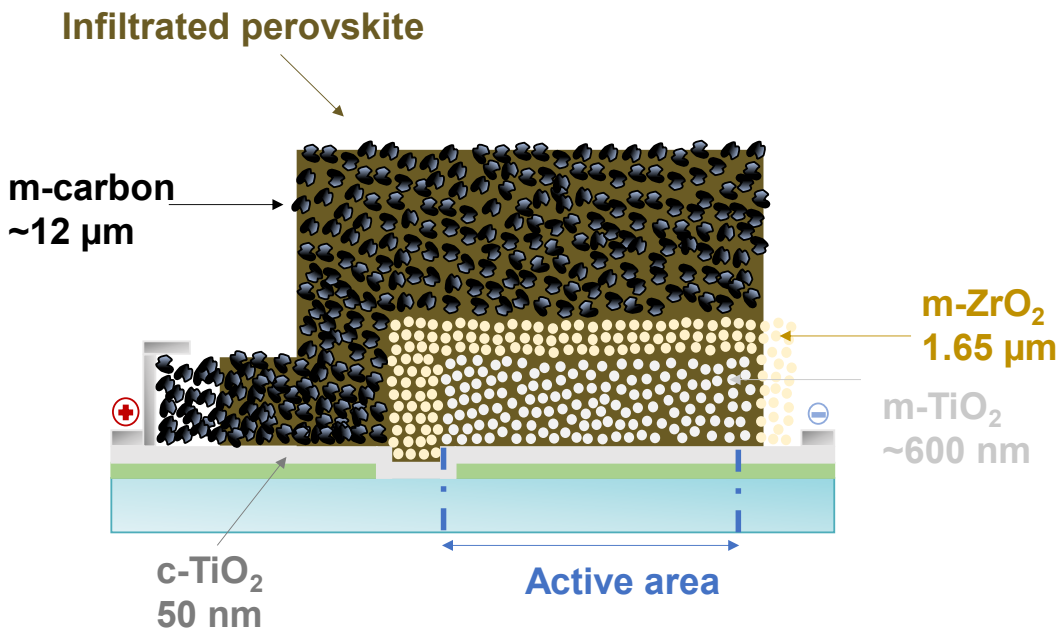

Figure 2.3 Device architecture of the mesoporous-carbon based perovskite solar cells (m-CPSC).

2.3 Optical Characterisation

2.3.1 UV-VIS NIR Absorbance Spectroscopy

UV-VIS-NIR Absorption Spectroscopy is an optical characterisation technique that measures the absorption of light by films or solutions in the UV, visible and near infra-red ranges (200 - 1000 nm). This technique allows for the characterisation of any electronic or morphological properties from the absorbance and transmission spectra. A reduction in the transmittance of glass after energy bombardment indicates a change in the lattice structure and modification to the absorbance bands.[4] There are 3 processes that can occur when light interacts with a sample. They are reflectance, absorbance, and transmittance. These 3 processes can be split further, as not all light is reflected or transmitted at the same angle. These processes are shown in Figure 2.4. When incident light is reflected, it can be reflected at different angles. When the angle is 0°, the light is mirror reflected and this is known as Surface Reflectance (R_S). If the light is reflected across many different angles, this is called Diffuse Reflectance (R_D). In the case of transmittance, when the transmitted light is travelling in the same direction as the incident light and is parallel, this is known as Collimated Transmittance (T_C). However, light that is scattered within the sample, may transmit at different angles. When the light is transmitted across many different angles, this is known as Diffuse Transmittance (T_D).

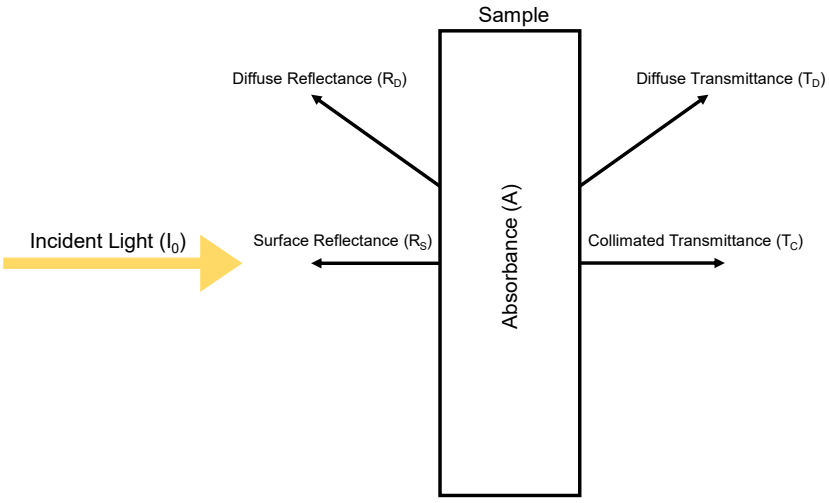

Figure 2.4 Cartoon schematic to show how an incident beam of light is absorbed (A), reflected (R), or transmitted (T) through a sample.

The relationship between these interactions are shown in Equation 2.1

$$I_0 = A + R + T = A + R_S + R_D + T_C + T_D \quad (2.1)$$

Experimental measurements are described in terms of transmittance, which is the ratio of the light intensity between the incident light from the source (I_0) and the transmitted light incident after it has passed through the sample (I). The UV-Vis spectrometer has a 100% transmittance calibration that calibrates the initial light intensity at each wavelength. Therefore, the difference between the initial calibrated and measured intensity is the transmittance:

$$Transmittance\ (T) = \frac{I}{I_0} \quad (2.2)$$

The relationship between the transmittance and the absorbance is given by:

$$Absorbance\ (A) = -\log_{10} T \quad (2.3)$$

In this thesis, the UV–VIS transmittance experiments were undertaken to compare the changes in transmittance for quartz/AZO after proton bombardment using a UV/Vis/NIR spectrometer (Lambda 750; PerkinElmer) with an integrating sphere in the range of 180–1000 nm with 1 nm steps. The same measurements were performed for PMMA/PET samples to look at the PMMA transparency. For diffuse reflectance measurements, samples with structure quartz/perovskite/gold were placed within the integrating sphere with the quartz substrate facing the light beam. This structure was used to investigate the optical reflectance as the samples are opaque due to the Au. Therefore, it can be assumed that there is no transmittance through the sample and following Equation 2.1, any changes in the perovskite absorbance would appear in the reflectance spectra.

2.3.2 Photoluminescence Spectroscopy

When light interacts with an electron in a low energy state, the electron can be excited to a higher energy state via absorption. Luminescence is the emission of a photon as an electron undergoes a transition from this excited electronic state to a

lower unoccupied electronic state via spontaneous emission. When the excitation of an electron is caused by the absorption of optical electromagnetic waves, the luminescence is called photoluminescence (PL). PL spectroscopy involves using a beam of light to excite electrons in molecules, causing them to emit light via fluorescence, phosphorescence, or a combination of both.

The working principle of PL spectroscopy is illustrated in Figure 2.5. Incident light passes through a monochromator to select a particular excitation wavelength. The sample absorbs the excitation light, and the resultant PL from the sample passes through another monochromator into a photodetector. The PL spectrum (PL vs wavelength) is obtained by measuring the emission passing through the grating of the final monochromator.[5]

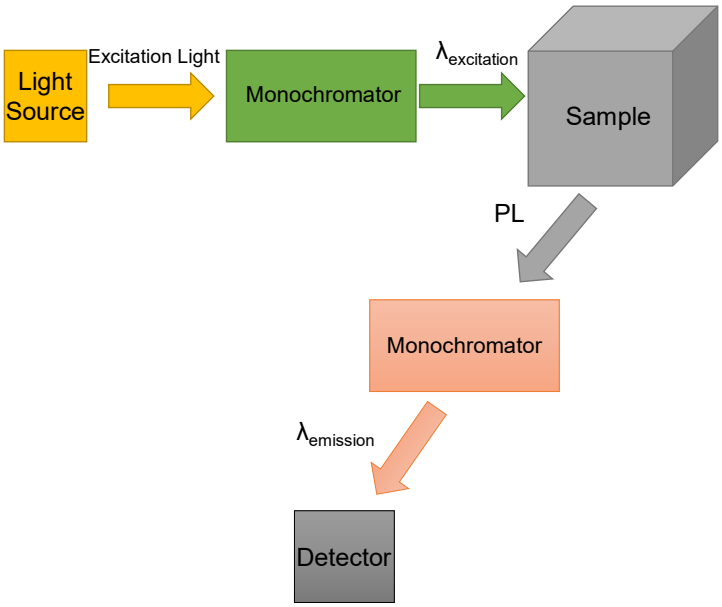

Figure 2.5 Cartoon schematic of a photoluminescence (PL) concept.

PL spectroscopy has a variety of different uses when probing PSCs and the perovskite active layer. PL spectroscopy can be used to probe the charge generation and charge extraction of perovskite devices, with the PL reducing if there is improved charge extraction and increasing if there is an increase in recombination.[6][7]

PL measurements were performed with a Renishaw inVia Raman system (Renishaw plc., Wotton-Under-Edge, UK) in backscattering configuration. Unless otherwise stated, a 532-nm laser and 50x objective were used (NA 0.50, spot size ~1 µm). For the PL measurements in this thesis, a laser power of 300 nW and an

acquisition time of 1s were used. For the creation of the PL maps seen in Chapters 3-6, the PL was measured at multiple points over an area of ~1600 μm^2, and these points were then averaged to give the final PL spectrum.

2.4 Chemical/Structural Characterisation

2.4.1 Raman Spectroscopy

Raman spectroscopy is a spectroscopic technique that uses the interaction of light with matter to probe a material's molecular structure. Raman spectroscopy yields information about molecular vibrations and provides multiple characteristics of the specific vibrations. When photon interact with a molecule and a scattered with the same energy, this is described as elastic scattering, also known as Rayleigh scattering. A small number of these photons, approximately 1 photon in 10 million will scatter at a different frequency than the incident photon.[8] This process is called inelastic scattering, or the Raman effect.

Raman scattering is described by quantum mechanics. When photons interact with a molecule, the molecule may be excited to a virtual energy state at a higher energy. At this higher energy virtual state, there are 3 different outcomes. The first outcome is not Raman scattering but Rayleigh scattering. This occurs when there is no energy change between the incident and emitted photon as the light is elastically scattered. The second and third outcome occur when the molecule relaxes to a vibrational energy level that is different than the initial energy state, emitting a photon of different energy. The Raman shift is calculated by taking the difference between the energy of the initial incident photon and the energy of the resultant scattered photon. The shift is normally given in wavenumber (cm^{-1}) which is defined as the number of waves per unit distance. To calculate the wavenumber, take the photon energy (E) which is directly proportional to the frequency ($E = h\nu$), and the frequency (ν) which is inversely proportional to the wavelength ($\nu = c\lambda^{-1}$). As frequency is the number of waves per second, the wavenumber is $\tilde{\nu} = \nu/c$, and therefore $\tilde{\nu} = \lambda^{-1}$. When the energy of the scattered photon is less than the initial incident photon, the scattering is called Stokes scattering. Additionally, anti-stokes scattering is when the molecule relaxes to a final energy state at a lower energy than

the initial energy state. This occurs when the molecule is already in a vibrationally excited state prior to the incident photon and is therefore excited to a virtual state at a higher or equal energy level. An example of Rayleigh and Raman scattering can be seen in Figure 2.6.

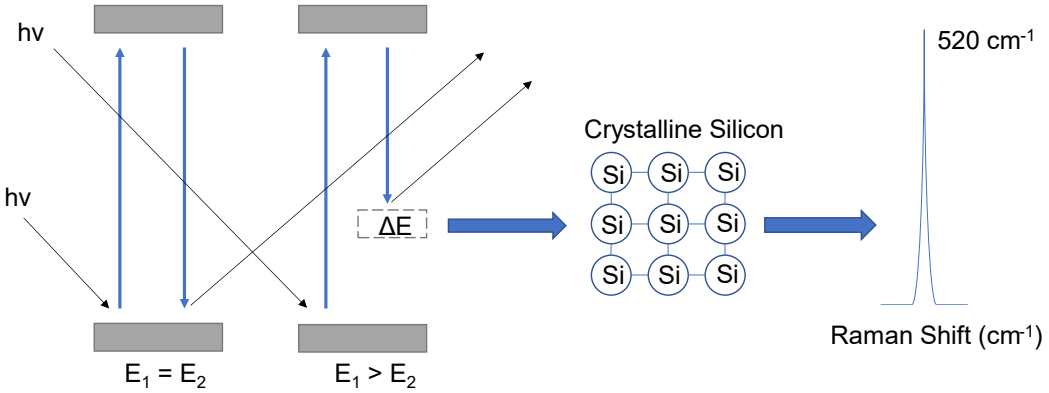

Figure 2.6 Cartoon of how incident light can result the Rayleigh scatting (E_1=E_2) and how it can result in molecular excitation to a higher energy state (ΔE) and produces a sharp peak at 520 cm^{-1} when measuring crystalline silicon due to the stokes scattering.

Raman spectroscopy has many uses when probing PSCs, especially looking at how the molecular/chemical structure changes under external stimuli such as humidity.[9] Additionally, for polymers transparent to the excitation wavelength, the intensity of the Raman spectra can be used to estimate the thickness of the layer.[10] Raman and PL measurements were performed with a Renishaw inVia Raman system (Renishaw plc., Wotton-Under-Edge, UK) in backscattering configuration. A 532-nm laser and 50x objective were used (NA 0.50, spot size ~1 µm). For Raman measurements, a laser power of 150 µW and acquisition time of 10 s were used to measure a map of points over an area of ~1600μm^2, which were also averaged to give an accurate representation of the measured spectra.

2.4.3 X-Ray Diffraction

X-Ray Diffraction (XRD) is a technique that allows for the crystallographic structure of a material to be probed. By irradiating a material with X-rays, you can measure the intensity of the scattered X-rays as a function of scattering angle.

XRD is very useful for yielding information on how the measured structure deviates from the ideal one, owing to internal stresses and defects.[11] This is very useful when looking at any changes in the crystalline structure of perovskite because of high energy radiation.[6] The atoms scatter incident X-rays through interaction with the atoms' electrons, which produces a scattering pattern (spherical waves) in all directions. In most directions, destructive interference dominates as the waves cancel each other out. However, in a few specific directions they add constructively as determined by Bragg's law:

$$2d \sin\theta = n\lambda \quad (2.4)$$

Where d is the spacing between diffracting planes, θ is the incident angle of X-ray, n is an integer, and λ is the X-ray beam wavelength. The distance between planes of atoms, also known as the lattice spacing (d), gives rise to the diffraction peaks. Each peak corresponds to a d-spacing. Therefore, if there is a change in the lattice spacing there will be change scattering angle and the peak intensity.

XRD measurements were performed using a Bruker D8 Discover instrument with a Cu-Kα beam (wavelength 0.15418 nm) at 40 kV and 40 mA, scan parameters of 1.3 s per step at 0.02° of 2θ step size. All measurements were performed on samples with structure quartz/perovskite/gold, so that the perovskite crystalline structure was measured through the gold layer. The XRD measurements in Chapter 3 were performed by Dr. Jérémy Barbé at Swansea University.

2.5 Thickness Measurements

The thickness measurements were taken using the Alpha Step D-500 stylus profilometer (KLA Tencor). For the measurements in Chapter 6, the stylus force was set to 5 mg, and the height range was set at 10 µm and 100 µm depending on the measurement. For each sample, 3 measurements were taken at different locations and the software included with the profilometer automatically calculates the average and standard deviation of the measured thicknesses.

2.6 Electrical Characterisation

2.6.1 Current Density-voltage Device Characterisation

The current density (J) vs voltage (V) curves (J-V) were obtained using a Newport 92193A-1000 solar simulator, providing AM1.5G illumination. The intensity of the solar radiation at AM1.5G was calibrated and measured using a silicon photodiode with a KG5 window. The KG5 window reduces the <300nm UV and >900nm IR intensity to better match the spectral response of the PSCs (~300-800 nm). For AM0 calibration, an AM0 filter from Newport was coupled with a certified 1 cm^2 GaAs cell to match the solar intensity to the measured GaAs AM0 J_{sc}. A Keithley 2400 331 source meter was used to apply an external bias and a computer using a LabView programme recorded the current density as a function of applied voltage. This programme automatically calculates the V_{oc}, J_{sc}, FF and PCE for the measured pixel.

2.6.2 External Quantum Efficiency

External quantum efficiency (EQE) is defined as the percentage of charge carriers extracted with respect to the number of incident photons that illuminate the sample. This is calculated as a function of photon wavelength. The AM1.5G J_{sc} can be calculated from the EQE spectra via Equation 2.5

$$J_{sc} = \int qS(\lambda)F(\lambda)d\lambda \qquad (2.5)$$

Where q is the electronic charge, S is the EQE response, and F is the AM1.5G spectra. Both S and F are functions of wavelength, and therefore must be integrated over all measured wavelengths. Equation 2.5 can also be used to calculate the AM0 J_{sc} by changing F to the AM0 spectrum. The EQE measurements in this thesis used a QEX10 Quantum Efficiency Measurement System calibrated with a NIST-certified Si cell from PV Measurements. A xenon-quartz tungsten halogen light source, which contains a broad range of wavelengths, is passed through a monochromator to get a range of monochromated light at different wavelengths. This light beam illuminates the solar cell and the photocurrent generated is recorded as a function of wavelength. The measurements can be taken under DC mode, or under an AC mode for more sensitive measurements by using a light chopper with a variable frequency. EQE is a very useful measurement that can assess device performance, including losses from reduced charge generation and charge extraction.[12] It can also be used alongside reflectance spectroscopy to calculate the Internal Quantum Efficiency (IQE).[13]

2.6.3 Thermal Stability Measurements

The thermal stability measurements seen in Chapter 5 & 6 The thermal measurement set-up consists of 5 principal components, the Pfeiffer vacuum pump, the Linkam controller, the Linkam liquid nitrogen pump, a Liquid Nitrogen (LN_2) Dewar and the Linkam vacuum chamber. The components are connected as shown in Figure 2.7

The Pfeiffer vacuum pump is a rough oil pump that can reach vacuum levels of ~$9x10^{-2}$ mbar. The vacuum level in space is ~$1x10^{-15}$ bar however this is not a reachable pressure outside of high vacuum cold atom labs where they reach pressures of ~$1x10^{-14}$ bar.[14] Therefore the measurements taken under mimic LEO conditions are at a pressure of ~$9x10^{-2}$ mbar. The Linkam controller connects to a computer to run the Linkam control software. This software allows the user to control the vacuum level, the temperature of the stage, the pumping rate for LN_2 and set-up thermal ramps. To monitor the conditions, the controller is connected to the Linkam pump, a Pfeiffer vacuum gauge, and a thermocouple.

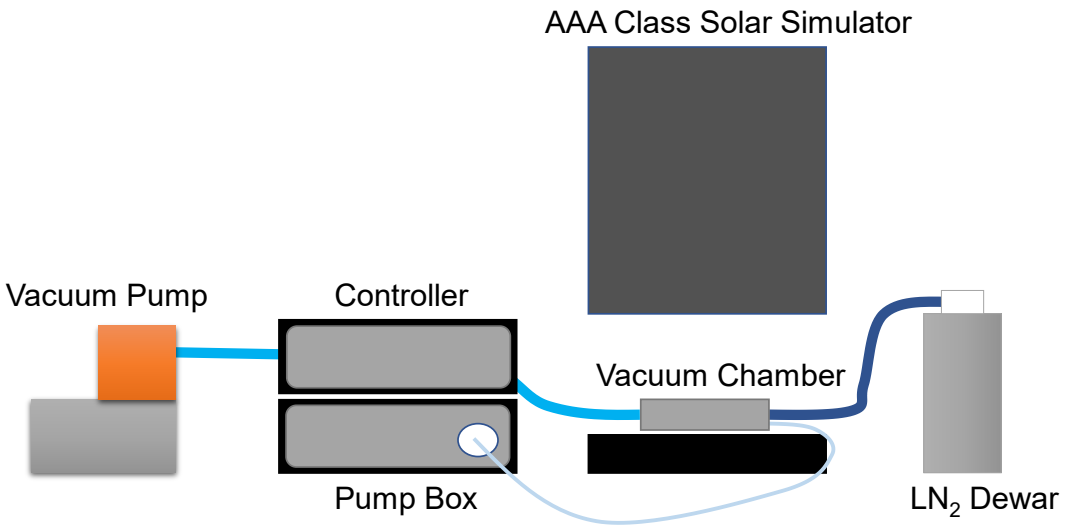

Figure 2.7 Cartoon set-up of the thermal stability measurement arrangement. The LN_2 Dewar and vacuum pump connect directly to the chamber, along with the Linkam LN_2 pump box.

The Linkam pump connects to the Linkam vacuum chamber in tandem with the 3L LN_2 Dewar to pull through the LN_2 to cool the sample stage. The pump also has

a small rubber pipe connection that attaches to the top of the vacuum chamber and blows N_2 gas to remove any condensation build-up on the glass window due to the low temperatures. The sample stage also contains a heater that allows for heating. The set-up allows for a maximum temperature change of 30°C/min.

The Linkam vacuum chamber contains the main electrical connections that allow for device measurements while the devices are under mimic conditions. The outside view of the chamber can be seen in Figure 2.8. Externally, the chamber has 2 large connector ports that attach to the vacuum pump tubing and the Pfeiffer vacuum gauge. This allows for the chamber to be pumped down to ~$9x10^{-2}$ mbar and for the vacuum level to be measured. The stage has 2 small connector ports for the Linkam pump and the LN2 Dewar. The Linkam pump uses a female connection to connect to the stage while the Dewar uses a male. The stage is verified to be able to be controlled to temperatures 350°C > T >-196 °C. On the opposite side of the vacuum chamber is 4 BNC male connections. These ports are connected to a series of pins that can be manoeuvred to connect to the electrodes of the PSCs and allow for device measurements. The vacuum stage also has a lid with a counter-clockwise (CCW) thread that screws into place. This lid has a 1 cm diameter circular window (0.79 cm^2) which allows for the light from the solar sim to enter the chamber. There are also several grooves in the lid for a hose to be attached. This hose blows air to stop condensation forming on the glass window when at cold temperatures.

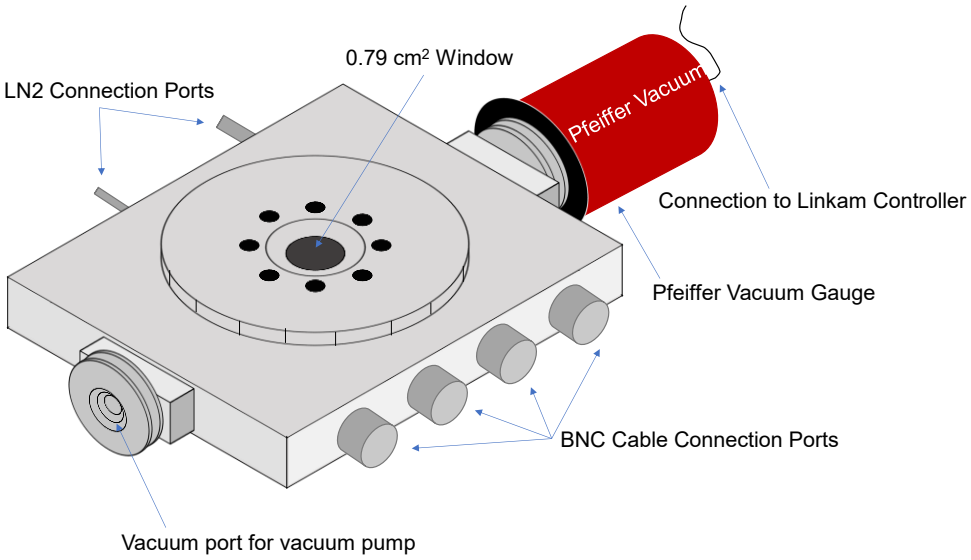

Figure 2.8 Cartoon of the Linkam vacuum stage. The main components are labelled, and the Pfeiffer vacuum gauge has been included as it is a major component.

All thermal cycling measurements shown in Chapter 5 and 6 were repeated several times to confirm the measured trends and improve the reliability.

2.6.4 Humidity Stability Measurements

The humidity measurements in Chapter 6 were performed using a Linkam RH95 Humidity Controller to control the Relative Humidity (%RH) of a stage. The %RH can be set between 5-95% and has a fixed ramp rate of ~7 % RH/min. The controller can also dry the stage using a recycling desiccant system to reduce the %RH. As shown in Figure 2.9, the humidity set-up consists of three pieces. The humidity stage, the humidity controller, and the water bottle. The humidity stage is very similar to the vacuum stage; however, the vacuum connection ports are no longer there, and there is an additional connection port next to the LN_2 connection ports for the liquid bottle to connect to. The liquid bottle is a thick beaker with a maximum fill limit of 150 ml. The lid of this bottle is attached to a metal heating coil that evaporates the water inside the bottle to create the humidity level inside the stage. This is achieved by a transfer tube that is attached to the lid and connects to the humidity stage via a CCW screw port next to the LN_2 ports. Once the lid and bottle are assembled, they are connected to the main controller via a CCW screw fitting which is tightened to secure the bottle.

The main humidity controller controls the humidity level within the chamber via a touchscreen on the front of the main body. This means the humidity controller does not need to connect to a computer to run. On the touchscreen, the current temperature and humidity level of the stage is displayed, along with the humidity level the stage has been set to. The humidity level is measured via humidity sensor inside the stage which is connected to the back of the controller unit.

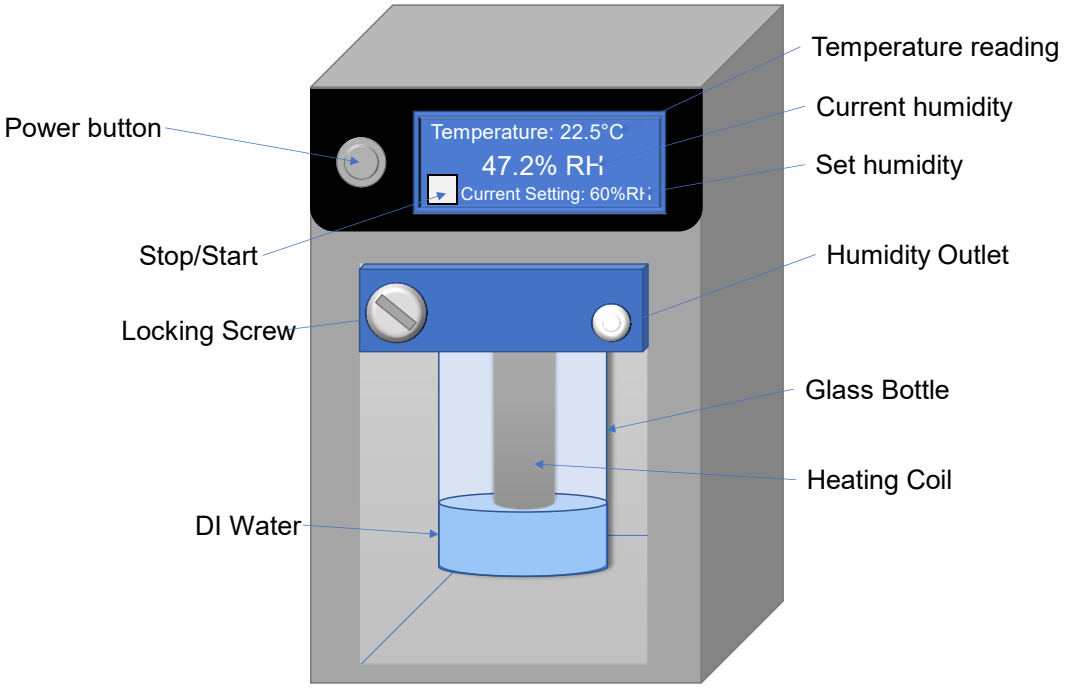

Figure 2.9 Cartoon diagram of the humidity controller used for the humidity measurements. The touchscreen displays all the relevant information about the stage.

2.6.5 Transient Lifetime Measurements

Transient lifetime measurements probe the decay of light generated charge carriers over time after the samples are briefly illuminated by a light source. The illumination is a short pulse, normally in the order of ns, and the decay of the carrier density with time is measured. When looking at solar cells, the photogenerated charges are extracted at the electrodes, resulting in a current. This current is detected by an oscilloscope in form of voltage across a resistor. A cartoon of this process is shown in Figure 2.10. Transient Photocurrent (TPC) is a transient lifetime measurement of charge carriers, where the solar cell is held at short circuit conditions (where the voltage is 0 V). The short light pulse causes a build-up of carriers at the electrode, who then decay after the pulse. In comparison, Transient Photovoltage (TPV) measurements are a transient lifetime measurement of charge carriers where the solar cell is kept at open circuit. For TPV measurements the solar cells are kept under steady-state illumination to give the steady-state voltage. The light source is then pulsed to generate an induced voltage, and the decay of this induced voltage back to the steady-state is measured.[15] The longer the minority carrier lifetime the more

slowly the carrier's decay. Both TPV and TPC can yield information about extractable charges, charge recombination and charge carrier density.[6][15] TPV measurements can be seen in Chapter 3, where they are used to probe degradation in PSCs after 150 keV proton bombardment.

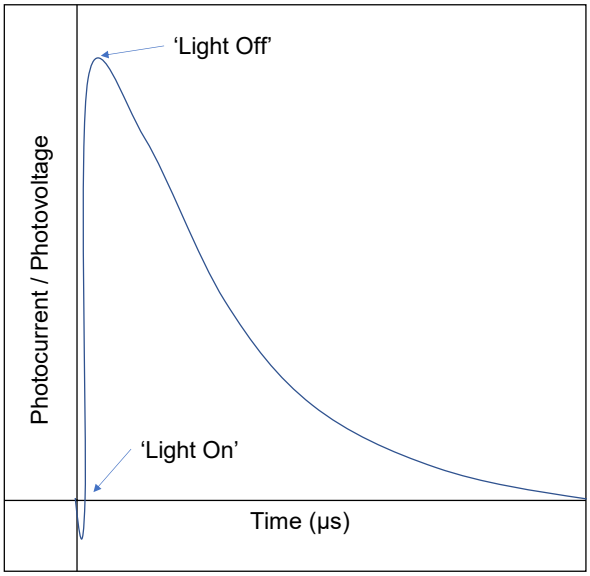

Figure 2.10 Cartoon plot of the photocurrent/photovoltage response when an excitation light source is switched on (Light On), and the exponential decay in measured photocurrent/photovoltage when the light source is switched off (Light Off).

The TPV and TPC measurements were performed by Dr. Adam Pockett and Dr. Suzzanne Thomas at Swansea University. TPV measurements were performed using a commercially available transient measurement system (Automatic Research GmbH). This system uses a 635-nm red laser diode driven by a waveform generator (Keysight 33500B) to give a 500-ns pulse length. The steady-state illumination was provided by a white LED with its intensity calibrated to generate the same device photocurrent as measured using the solar simulator—this intensity is referred to as "1 sun equivalent." An intensity range was then calibrated using a silicon photodiode, so the induced voltage is easily resolved. In Chapter 3 and 5, transient responses were captured by a digital storage oscilloscope (Keysight DSOX2024A). The device under test was held at open circuit by a custom-built voltage follower (1.5 TΩ input impedance). TPC measurements were performed using the same set-up as the TPV, however the white LED was removed to keep the PSCs at short circuit conditions. A

current amplifier (Femto DHPCA-100) was used to amplify the photocurrent signal to reduce signal noise.

2.7 Proton Energy Bombardment and Simulation

2.7.1 Proton Energy and Fluence

In a space environment, the proton energy range can vary greatly depending on the location. The same can be said of the fluence and proton flux. Proton fluence is described as the total number of incident protons per unit area and proton flux is the total number of protons per unit area per unit time. Also described as the time derivative of the proton fluence, proton flux ($\dot{\Phi}$) takes the form:

$$\dot{\Phi} = \frac{d\Phi}{dt} \tag{2.9}$$

where Φ is the proton fluence and is defined as

$$\Phi = \frac{dN}{dA} \tag{2.10}$$

where N is the number of protons and A is the area.

Data from NASAs Electron, Proton, and Alpha-particle Monitor (EPAM) is shown in Figure 2.11. The EPAM experiment is orbiting Lagrange Point 1 (L1), which is 0.5 Astronomical Units (A.U) from the Earth. 1 A.U is the distance between the Earth and the Sun. It is shown that at L1, that protons with energies 115-185 keV have a flux of $1x10^{10}$ protons/cm^{2}s. This equates to a fluence of $1x10^{15}$ protons/cm^2 after 1 day (84600 s) in orbit at L1. While for a LEO, the same proton fluence is equivalent to ~10,000 years depending on the orbiting angle to the equator.

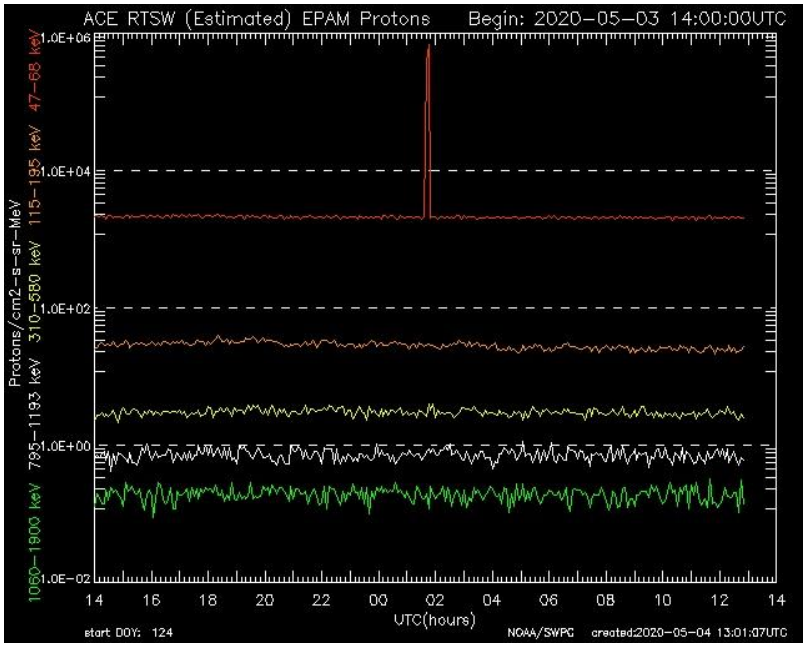

Figure 2.11 Plot of EPAM data over 24 hours for the flux of protons with energy from 47 - 1900 keV. This data highlights the decrease in flux as proton energy increases.[16]

Due to the difference in fluence between L1 and LEO, the radiation environment can be very different depending on the orbit and thus the application. Therefore, it is a logical choice to choose an energy that has a fluence significant to the application, such as a LEO satellite, but also of high enough energy to penetrate the perovskite solar cells to properly assess their radiation hardness. Radiation hardness testing for Si and GaAs solar cells have also been performed at 150 keV, allowing for a comparison between the PSCs and currently used PV technology.[17][18] For this reason, 150 keV protons were chosen for the experiments in Chapters 3 & 4.

2.7.2 Ion Implantation

Ion implantation is a low-temperature process by which ions of an element are accelerated into a solid target. The collision between the accelerated ion and the solid target can change the physical, chemical, or electrical properties of the target. An Ion implantation experimental set-up typically consists of an ion source, where the desired ions are produced, an accelerator, where the ions are electrostatically accelerated to a high energy, and a target chamber, where the ions are incident on the target. An example of an ion implanter can be seen in Figure 2.12 Therefore, ion implantation can be considered a particular case of particle radiation. Each incident

ion is typically a single atom or molecule, and thus the actual amount of material implanted in the target is the integral over time of the ion current (rate of flow of ions). The currents supplied by implants are typically small (μA), and thus longer implantation times are needed to achieve a higher ion fluence.[19]

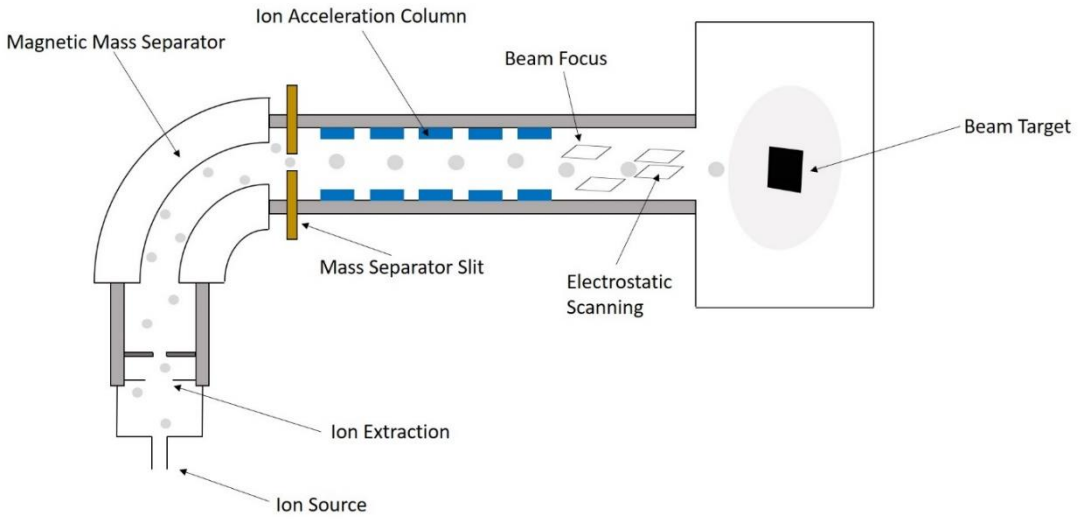

Figure 2.12 Cartoon of an ion implantation set-up. Ions pass through the extraction slit, into the magnetic mass separator and slit, before being accelerated by the acceleration column into the beam focus and then into the target.

As ion implantation uses a beam of excited ions to bombard a target, the attenuation of this ion beam by the sample is related to the flux and interaction cross section. If a beam of particles enters a material of total thickness z, the exponential attenuation of the ion beam is given by

$$\dot{\Phi} = \dot{\Phi}_0 e^{-n\sigma z} \qquad (2.11)$$

where σ is the total cross section, n is the number density of scattering events, and $\dot{\Phi}_0$ is the initial flux. Therefore, the further into a sample the beam travels the larger the attenuation will be, before the ions come to a stop within the material. For the bombardment experiments shown in Chapters 3 & 4, the ion implantation was performed at the Surrey Ion Beam Centre in UK, by Dr. Keith Heasman. The reference (not irradiated) samples were sent together with the irradiated samples to the Surrey Ion Beam Centre. All the samples were packed in N_2 atmosphere in the dark during traveling. The reference samples were exposed to air when the other samples were

also exposed to air just before proton irradiation and during the travel back to Swansea. For the bombardment sample loading, the perovskite cells were mounted directly onto 4-in support plates that were inserted into a carousel wheel in the sample chamber. Silver paste was applied to allow charges to be conducted to the back of the samples and in the holder plate to avoid charge accumulation. Samples were loaded in a 7°/0° tilt/twist orientation to the incident beam and implanted under vacuum (2.3 ± 0.2 x 10^{-6} mbar). For the bombardment in Chapter 3, the samples were placed to receive direct impact of the protons, with the back contact (gold electrode) facing the proton source. Indeed, the quartz substrate was thick enough to shield the cells from proton irradiation, so that it would be impossible to measure the effect of proton irradiation on the perovskite layer if the quartz was facing the proton source. For the bombardment in Chapter 4, the sample were placed so the carbon electrode was facing the proton source and would receive the full impact on the protons. A Danfysik 1090 low-energy high-current implanter was used to implant 150 keV protons into the samples (from the gold side). The fluence rate was controlled to 3 x 10^{10} $cm^{-2}s$ for fluence 10^{12} protons/cm^2 and 3 x 10^{11} $cm^{-2}s$ for fluences 10^{13} to 10^{15} protons/cm^2.

2.7.3 Stopping Range in Matter Simulation

Stopping Range in Matter (SRIM) is a collection of programs that allow for the calculation of incident particle attenuation in a material (stopping power) with a range of ions (up to 2 GeV/amu) into targets made of matter using a quantum mechanical treatment of ion-atom interactions.[20] This calculation uses a Monte Carlo statistical algorithm to calculate collisions within the target, and then averaging the collision results. During the ion-atom collisions, the ion and atom have a screened Coulomb collision, including exchange and correlation interactions between the overlapping electron shells. The ion has long range interactions creating electron excitations and plasmons within the target. These are described by including a description of the target's collective electronic structure and interatomic bond structure when the calculation is setup.

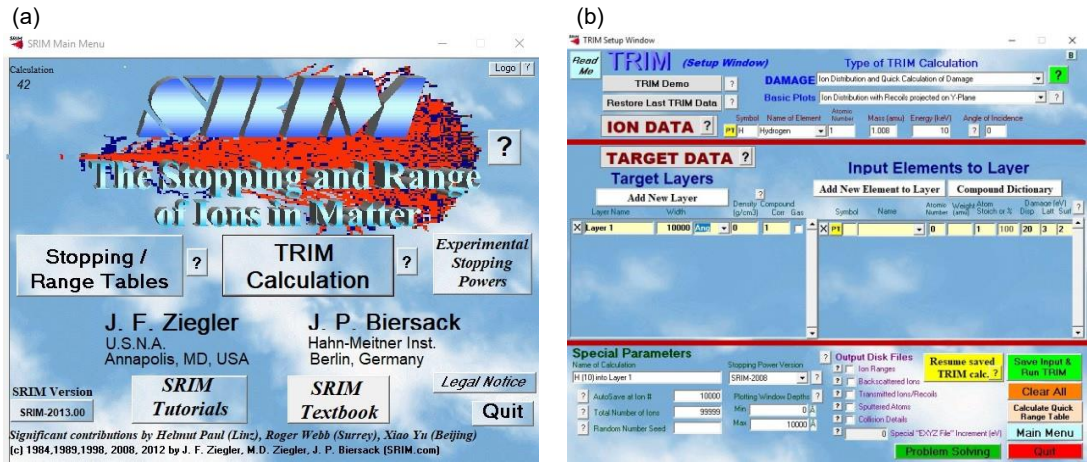

Figure 2.13 (a) Main function menu of SRIM, with the options for TRIM and the compound table. (b) Main screen of TRIM with the target layer construction dialog box (left) and the elemental composition of the layers (right).

For the proton bombardment simulation shown in Chapters 3-6, the SRIM package Transport of Ions in Matter (TRIM) was used. TRIM allows for the creation of targets comprised of up to 8 different layers. TRIM also allows for these layers to consist of compounds. Within the TRIM menu screen, the ion which is being used to bombard the target can be selected and the energy of the incident ions can also be chosen. For all simulation work done within this thesis, the ion used to bombard was hydrogen (H^+ which is a proton) and the bulk of the simulation work, the ion energy was set 150 keV. A variety of different data can be obtained from TRIM simulation such as the penetration depth, the ionisation of electrons, and generated ionic vacancies. These results can be plotted within the programme itself or exported for analysis.

2.7.3 Bethe-Bloch Python Simulation code

Python code written by me was used to solve the Bethe-Bloch equation as seen in Chapter 4. Here I used the python libraries Math, Matplotlib, Numpy, os, time, Scipy and MySQL to develop a self-plotting program that also outputted the results as a txt file to plot the data in the OriginPro® plotting software. The full code for calculating the density independent (mass) stopping power is given below. For the stopping power, the term (1/(rho * 0.001)) is removed from the calculation of De_Dx.

```
import math as ma
import numpy as np
import mysql.connector
import matplotlib.patches as mpatches
import matplotlib.pyplot as plt
import os
import time
import scipy.constants as sci

def frange(start, end=None, inc=None):
    "A range function, that does accept float increments..."

    if end == None:
        end = start + 0.0
        start = 0.0

    if inc == None:
        inc = 1.0

    L = []
    while 1:
        next = start + len(L) * inc
        if inc > 0 and next >= end:
            break
        elif inc < 0 and next <= end:
            break
        L.append(next)

    return L

M_P = 938.3 #MeV
M_e = 9.11E-31 #kg
m_e = M_e
N_A = 6.022E26 #molescules/mol
e_0 = 8.854E-12 #Cm/J
c = 3.0E8 #m/s
m_P = 1.67E-27 #kg
e = 1
Kc = 1/(4*ma.pi*e_0)
a_0 = 5.29E-11
V_0 = sci.hbar/(2*ma.pi*m_e*a_0)

mydb = mysql.connector.connect(
  host="localhost",
  user="root",
  password="Password",
  database="Bethe_Bloch"
)

while True:
    try:
        Time = int(input('How Many Elements Do you Wish To Bombard?
' ))
    except:
        print("Please enter a number")
        continue
    else:
```

```
        Ele = []
        Timet = []
        break

for t in range(0,Time):
    Choice = input("Enter Element to bombard ")

    Ele.append(Choice.strip())

for z in range(0,len(Ele)):

    mycursor = mydb.cursor()
    mycursor.execute("SELECT * FROM elemental_data WHERE Element='"
+ Ele[z] + "'")
    myresult = mycursor.fetchall()

    count0 = time.time()

    mm = float(myresult[0][1]) #kg/kmol
    ne = float(myresult[0][2]) #electrons/molecule
    rho = float(myresult[0][3]) #kg/m3 & for mesoporous Carbon
    I = float(myresult[0][4])

    x1=[]
    y1=[]

    for i in np.arange(0.001,10000,0.001):

        Ke = i

        x1.append(i)

        A = (Ke/M_P)
        A_s = ma.sqrt(2*Ke*6.242E-19/M_P)

        Beta = (1-(1/(1+A)**2))**0.5

        Z = ne
        n = (N_A*ne*rho)/mm

        v_P = (c**2 - c**2 *(1/(1+A))**2)**0.5

        De_1 = (Kc**2)*(((4*ma.pi*n*(1.0)**2)*(1.60E-
19)**4)/((M_e*v_P**2)))

        De_2 = ma.log(((2*M_e*v_P**2)/ 1.6E-19)/(I*(1 - Beta**2))) -
Beta**2


        De_Dx = ((1/(rho*0.001))*(De_1*De_2)*6.242e+10)
        if De_Dx >=0:
            y1.append(De_Dx)
        else:
            x1.remove(i)
            continue

    results = [x1,y1]
```

```
    if os.path.exists(""+Ele[z]+".txt"):
        os.remove(""+Ele[z]+".txt")
    else:
        with open(""+Ele[z]+"_Proton.txt", "w") as file:
            file.write("Proton Energy (MeV)\tStopping Power
(MeV/cm)\n")
            for x in zip(*results):
                file.write("{0}\t{1}\n".format(*x))

    plt.plot(x1,y1, label=''+ Ele[z] +'')
    count1 = time.time()
    Totalt = count1 - count0
    Timet.append(Totalt)
    print(str(Ele[z]) + " completed in " + str(Totalt) + " seconds")
    t+=1

print("Total time taken = " + str(sum(Timet)) + "seconds")
plt.ylabel('dE/dx (MeV•$cm^2$/g)')
plt.xlabel('Proton Energy (MeV)')
plt.yscale('log')
plt.legend(loc="upper right")
plt.xscale('log')
plt.show()
```

References

[1] Spiro-MeOTAD 99 HPLC 207739-72-8. 99 HPLC 207739-72-8. Retrieved November 15, 2018, from https://www.sigmaaldrich.com/GB/en/product/aldrich/792071?gclid=Cj0KCQjwguGYBhDRARIsAHgRm48tg92lgqVQFpyzdgfaVb2A-fCdyj26jxzd6qoVlYSdZ4QKl-2741kaAtFyEALw_wcB

[2] Poly(3-hexylthiophene-2,5-diyl). Poly(3-hexylthiophene-2,5-diyl) - P3HT. (n.d.). Retrieved July 8, 2021, from https://www.sigmaaldrich.com/GB/en/substance/poly3hexylthiophene25diyl12345156074985

[3] Ravichandran, K., Jabena Begum, N., Snega, S., & Sakthivel, B. (2014). Properties of sprayed aluminum-doped zinc oxide films—a review. Materials and Manufacturing Processes, 31(11), 1411–1423. https://doi.org/10.1080/10426914.2014.930961

[4] Bishay, A. (1970). Radiation induced color centers in multicomponent glasses. Journal of Non-Crystalline Solids, 3(1), 54–114. https://doi.org/10.1016/0022-3093(70)90106-7

[5] L. Prodi and A. Credi, “Spectrofluorimetry,” in The Exploration of Supramolecular Systems and Nanostructures by Photochemical Techniques, pp. 97–129, Springer, Dordrecht, 2012.

[6] Barbé, J., Hughes, D., Wei, Z., Pockett, A., Lee, H. K., Heasman, K. C., Carnie, M. J., Watson, T. M., Tsoi, W. C. (2019). Radiation hardness of perovskite solar cells based on aluminum‐doped zinc oxide electrode under proton irradiation. Solar RRL, 3(12), 1900219. https://doi.org/10.1002/solr.201900219

[7] Tumen-Ulzii, G., Qin, C., Matsushima, T., Leyden, M.R., Balijipalli, U., Klotz, D. and Adachi, C. (2020), Understanding the Degradation of Spiro-OMeTAD-Based Perovskite Solar Cells at High Temperature. Sol. RRL, 4: 2000305. https://doi.org/10.1002/solr.202000305

[8] Bumbrah, G. S., & Sharma, R. M. (2016). Raman spectroscopy – basic principle, instrumentation, and selected applications for the characterization of drugs of abuse. Egyptian Journal of Forensic Sciences, 6(3), 209–215, https://doi.org/10.1016/j.ejfs.2015.06.001

[9] Hooper, K. E., Lee, H. K., Newman, M. J., Meroni, S., Baker, J., Watson, T. M., Tsoi, W. C. (2017). Probing the degradation and homogeneity of embedded perovskite semiconducting layers in photovoltaic devices by Raman spectroscopy. Physical Chemistry Chemical Physics, 19(7), 5246–5253. https://doi.org/10.1039/c6cp05123e

[10] Liszka, B. M., Lenferink, A. T., Witkamp, G.-J., Otto, C. (2015). Raman micro-spectroscopy for quantitative thickness measurement of nanometer thin polymer films. Journal of Raman Spectroscopy, 46(12), 1230–1234. https://doi.org/10.1002/jrs.4749

[11] Dolabella, S., Borzì, A., Dommann, A., Neels, A., Lattice Strain and Defects Analysis in Nanostructured Semiconductor Materials and Devices by High-Resolution X-Ray Diffraction: Theoretical and Practical Aspects. Small Methods 2022, 6, 2100932. https://doi.org/10.1002/smtd.202100932

[12] Miyazawa, Y., Ikegami, M., Chen, H.-W., Ohshima, T., Imaizumi, M., Hirose, K., Miyasaka, T. (2018). Tolerance of perovskite solar cell to high-energy particle irradiations in space environment. IScience, 3, 86. https://doi.org/10.1016/j.isci.2018.04.023

[13] Thouti, E., Sharma, A. K., Sardana, S. K., Komarala, V. K. (2014). Internal quantum efficiency analysis of plasmonic textured silicon solar cells: Surface plasmon resonance and off-resonance effects. Journal of Physics D: Applied Physics, 47(42), 425101. https://doi.org/10.1088/0022-3727/47/42/425101

[14] Elliott, E. R., Krutzik, M. C., Williams, J. R., Thompson, R. J., Aveline, D. C. (2018). NASA's Cold atom lab (cal): System development and ground test status. Npj Microgravity, 4(1). https://doi.org/10.1038/s41526-018-0049-9

[15] Sandberg, O. J., Tvingstedt, K., Meredith, P., Armin, A. (2019). Theoretical perspective on transient photovoltage and charge extraction techniques. The Journal of Physical Chemistry C, 123(23), 14261–14271. https://doi.org/10.1021/acs.jpcc.9b03133

[16] ACE real-time Solar Wind. ACE Real-Time Solar Wind | NOAA / NWS Space Weather Prediction Center. (n.d.). Retrieved May 21, 2019, from https://www.swpc.noaa.gov/products/ace-real-time-solar-wind

[17] Ohshima, T., Sato, S.-ichiro, Nakamura, T., Imaizumi, M., Sugaya, T., Matsubara, K., Niki, S., Takeda, A., Okano, Y. (2013). Electrical performance degradation of gaas solar cells with InGaAs quantum dot layers due to proton irradiation. 2013 IEEE 39th Photovoltaic Specialists Conference (PVSC). https://doi.org/10.1109/pvsc.2013.6745049

[18] Hu, Zhengu., He, Shiyu., Yang, Dezhuang. (n.d.). Radiation effects of protons and electrons on backfield silicon solar cells. PROTECTION OF MATERIALS AND STRUCTURES FROM THE SPACE ENVIRONMENT, 1–8. https://doi.org/10.1007/1-4020-4319-8_1

[19] El-Kareh, B. (1995). Ion Implantation. Fundamentals of Semiconductor Processing Technology, 353–466. https://doi.org/10.1007/978-1-4615-2209-6_6

[20] Ziegler, J. F. (2001). S R I M. JFZ IBM-Web page 001. Retrieved April 15, 2019, from http://www.srim.org/SRIM/SRIMINTRO.htm

Chapter 3

The Effect of 150 keV Proton Bombardment on Perovskite Solar Cells Utilising an Aluminium-doped Zinc Oxide Transparent Conducting Oxide

3.1 Introduction

As detailed in Section (1.3.5), high energy particles pose a threat to the operational performance of electronic devices and semi-conductors. Therefore, the stability of PSCs under particle bombardment is crucial to the study of feasibility for space applications. The most common technique to ensure high stability on Earth is the use of encapsulation to protect the metal contact side of the device (the side which is in contact with the air). However, the presence of additional hazards and external stimuli found in space create an environment that conventional substrates and encapsulation techniques struggle to adapt to. An example of this is the use of space qualified glass as a device substrate; this is required to reduce the creation of colour centres within the substrate which is caused by high energy particle bombardment. Alternatively, if high stability can be achieved without the use of encapsulation, a solid foundation for PCS would be established for use in space. The removal of a thick, solid encapsulation layer allows for a lower overall device weight which is an important factor in space payloads. This will allow for further research to focus on improving overall device efficiency. To demonstrate this stability, directed proton bombardment through the electrode is utilised to probe the PSCs active area while leaving the quartz substrate untouched.

The aim of this chapter is to expand on current research into the particle stability of perovskite devices by utilising a new TCO known as Aluminium-doped Tin Oxide (AZO). Here, the results of a 150 keV proton bombardment into the metal

electrode are presented along with additional characterisation of the device structure and a record PCE for AZO PSCS. It is demonstrated that PSCs can withstand proton irradiation up to $1x10^{13}$ protons/cm^2 without significant loss in efficiency. From $1x10^{14}$ protons/cm^2 , a decrease in short-circuit current of PSCs is observed, which is consistent with interfacial degradation due to deterioration of the Spiro-OMeTAD hole transport layer during proton irradiation. The structural and optical properties of perovskite remain unchanged up to high fluence levels. The results in this chapter have been published in SolarRRL.[1]

3.2 Results & Discussion

3.2.1 Proton Penetration Depth

Simulations of the proton beam's penetration depth were completed using SRIM and are shown in Figure 3.1. The goal of this work was to probe the radiation hardness of the triple cation perovskite and to characterise any changes in PV performance. To achieve this, the protons must have enough energy to pass through the device and stop close to or in the active area. Simulations of the 150 keV beam into the quartz substrate showed that the incident protons are unable to pass through the 1.5 µm thick substrate and stop within the quartz at a depth of 230 nm. Therefore, to investigate the stability of the perovskite devices, the devices would need to be bombarded through the Au electrode. This allowed for protons to stop within the Spiro-OMeTAD HTL; the perovskite active area; the SnO_2 ETL, and the AZO TCO. This in turn allowed for the investigation into the device stability without the presence of an encapsulating layer.

(a) (b)

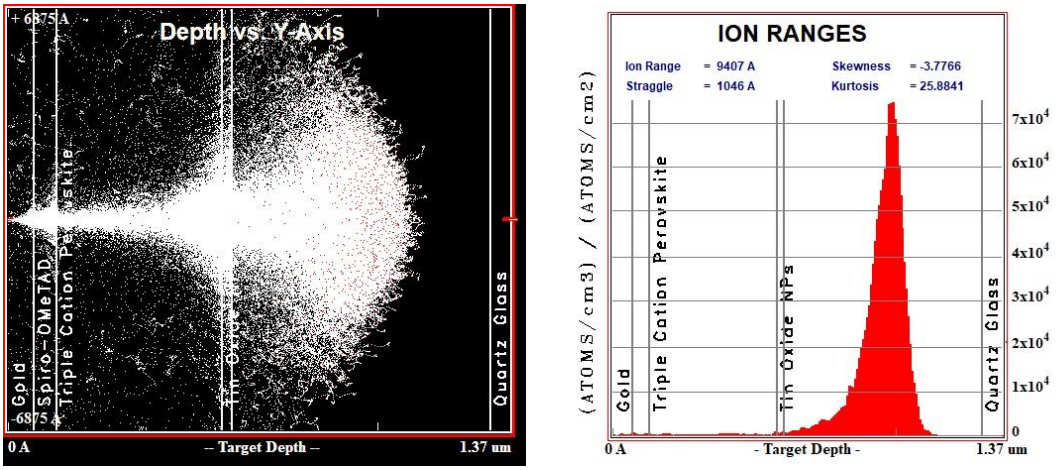

Figure 3.1 a) SRIM generated proton depth calculation at 150 keV incident on the Au electrode b) Histogram of proton stopping depth in relation to device layers.

From the simulations performed, most protons stop within the AZO layer. This indicates that the TCO is also critical to the stability of perovskite solar cells. This significant stopping power is attributed to the AZO's thickness. At ~700 nm thick, (thicker than the active layer ~450 nm) it stops the protons from reaching the quartz substrate. As the validity of the quartz's radiation hardness is yet to be determined, the thick AZO layer guarantees that colour centres would be unable to form if the quartz were to underperform as a stable substrate. In addition, a significant fraction of protons collide with atoms in the perovskite layer near the SnO_2 interface, as well as in the Spiro HTL. This allows for an investigation into the effect of proton irradiation not only in TCO, but also in the active layer and charge extraction layers as well.

3.2.2 Pre-Bombardment Device Performance

A total of 10 devices were fabricated with the AZO TCO. Using the pixel design as seen in Section 2.1.1, each device had 4 measured pixels resulting in up to 40 PV parameter measurements; this improved the reproducibility of the device performance before and after bombardment. The range of PCE values obtained and the device structure used are shown in Figure 3.2a. The J–V curves under 1 Sun AM1.5G and AM0 illumination for the champion cell are presented in Figure 3.2b. A table of the Voc, FF, and Jsc values obtained are shown in Table A.1.

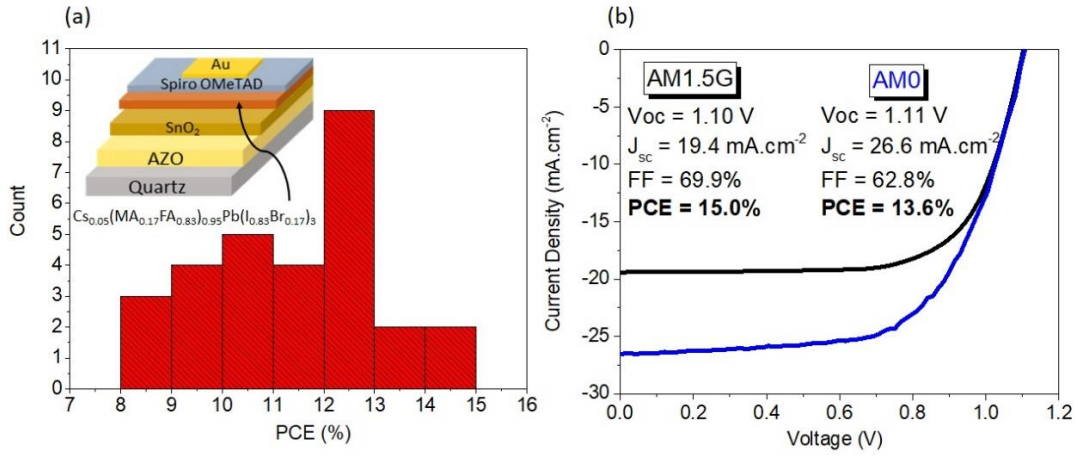

Figure 3.2 a) Histogram of PCE for perovskite solar cells with structure quartz/AZO/SnO_2/$Cs_{0.05}(MA_{0.17}FA_{0.83})_{0.95}Pb(I_{0.83}Br_{0.17})_3$/Spiro/Au. b) J–V curves under 1 Sun AM1.5G and AM0 illumination for the champion cell.

As illustrated in Figure 3.2a, the PCE of the cells under 1 sun AM1.5G illumination vary between 8% and 15%, with the dominant PCE being 12-13%. The average Voc across all devices is ~1.1 V, the average FF is 54.19%, and the average Jsc is 18.41 $mAcm^{-2}$. At the time of the manuscript's publication, the champion cell with a PCE of 14.95% outperforms previous works on perovskite solar cells fabricated on AZO by an almost 3% increase in absolute efficiency.[2-5] The champion PCE under 1 sun AM0 illumination reached up to 13.6%, with a Voc of 1.11V, FF of 62.8%, and an increased Jsc of 26.6 $mAcm^{-2}$. The increase in Jsc is due to the increased solar intensity (1367 W/m^2), as they are proportional. Due to the rather large range of PCEs obtained, it was decided to select one device with a pixel of PCE <11% and partner this with one sample with a PCE >11%. This pairing allowed for an investigation into the effect of PCE on proton stability, as well as control samples which were not exposed to any bombardment. Additional samples were also made to look at the effect of proton irradiation on bare quartz, AZO on quartz and perovskite on quartz. This allowed for an investigation into the reported radiation hardness of quartz as compared to glass, the stability of AZO for use as a TCO in space applications, and to solely probe the radiation hardness of the perovskite layer. The different samples also act as a control to help understand the origin of a degradation that might occur within the device structure.

3.2.3 Post-Bombardment Device Performance

As the devices travelled to the Ion Beam Centre in Surrey and were kept under N2 in the dark before irradiation was carried out. The devices were then kept for a week under dark air before they could be remeasured after irradiation. To compare the percentage change in device performance, the device's remaining factor (RF) performance than individual pixel PV parameters. The RF was calculated by dividing the PV parameters after proton irradiation by the PV parameters before proton irradiation. This was done for each fluence under both 1 Sun AM1.5G and AM0 solar intensity. The External Quantum Efficiency (EQE) was also measured, to allow for a comparison between the measured Jsc and the EQE. Both the AM1.5G RF and EQE are presented in Figure 3.3. The AM0 J-V RF figure can be found in Figure A.2.

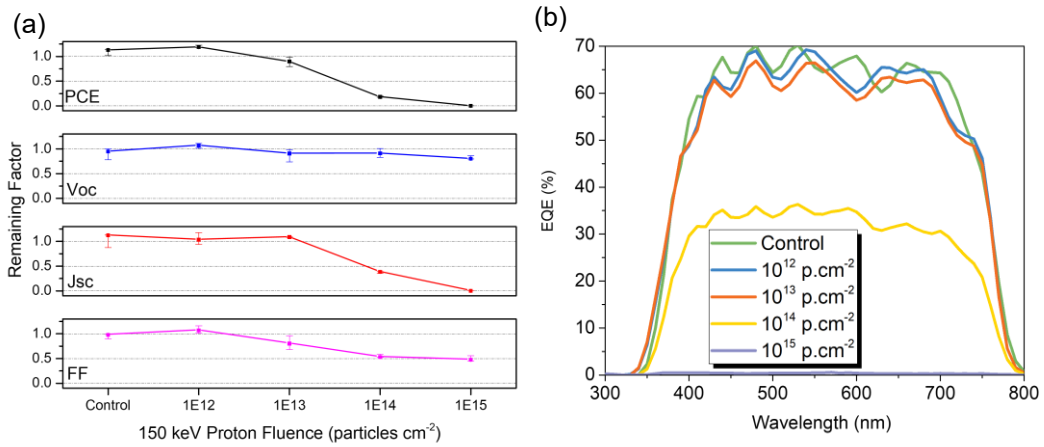

Figure 3.3 a) Changes of photovoltaic characteristics (J_{sc}, FF, V_{oc}, and PCE) of perovskite solar cells under AM1.5G illumination as a function of proton fluence. Averaged values measured for a total of ~6 different pixels for each fluence. b) EQE for representative devices as a function of proton fluence.

Compared to the control samples, there is a slight increase in the measured PCE at $1x10^{12}$ protons/cm^2 fluence, with a PCE RF ~1.18 and a small decrease at $1x10^{13}$ protons/cm^2 with a PCE RF ~0.9. As move towards the higher fluences such as $1x10^{14}$ protons/cm^2, a prominent decrease was observed and the PCE RF reduced to 0.2. This decline in performance was due to the observed decrease in Jsc (RF ~0.38) and FF (RF ~0.53), while the Voc remained almost constant. At $1x10^{15}$ protons/cm^2 this decrease was exacerbated with a very low current (RF ~$6x10^{-4}$), indicating the

cells were highly degraded with a PCE RF ~$3x10^{-4}$. However, due to the presence of a non-negligible V_{oc} RF of 0.8, the results suggest that the perovskite layer itself was not significantly degraded. Whereas the decrease in FF and J_{sc} could be explained by a deterioration of charge extraction properties due to the degradation of Spiro-OMeTAD or/and SnO_2 interlayers.

Miyasawa et al. measured non-uniform spectral response of photocurrent of $FAMAPb(IBr)_3$ cells after the samples underwent proton irradiation at a fluence of $1x10^{14}$ protons/cm^2. This was attributed to the degradation of the active layer.[6] In this work, the uniform reduction in the EQE spectrum, coupled with the change in PV parameters, is indicative of a deterioration in charge extraction rather than charge generation properties. This points out the crucial role of charge extraction layers in the degradation of solar cells during irradiation. At $1x10^{15}$ protons/cm^2, the measured EQE was almost non-existent, with a PCE of ~1%, and barely visible in Figure. 3.4b. From these measurements, PSCs utilising Spiro-OMeTAD as the HTL can be exposed to a radiation level up to $1x10^{13}$ protons/cm^2 without being significantly degraded. By comparison, the V_{oc} and J_{sc} of Si solar cells exposed to 150 keV protons decreased by 40% and 10%, respectively, at $1x10^{13}$ protons/cm^2.[7] In addition, investigations have demonstrated that GaAs solar cells exposed to 150 keV protons started to degrade at a radiation dose as low as $1x10^{10}$ protons/cm^2 and the remaining factor for the maximum power (P_{max}) decreased to 0.2 at $1x10^{12}$ protons/cm^2.[8] In the case of the AZO PSCs, a P_{max} remaining factor of 0.2 was reached only at $1x10^{14}$ protons/cm^2, showing that PSCs have at least two orders of magnitude higher tolerance to proton irradiation than GaAs solar cells. While the measured radiation stability is greater than more commonly used PV technologies, further characterisation needed to be undertaken to understand and detail the underlying mechanisms responsible for the degradation in the device's performance at $1x10^{14\text{-}15}$ protons/cm^2.

To help distinguish which layer could be the most probable cause, SRIM was used to calculate the energy loss and generated vaccancies in each layer. The results are shown in Figure 3.4.

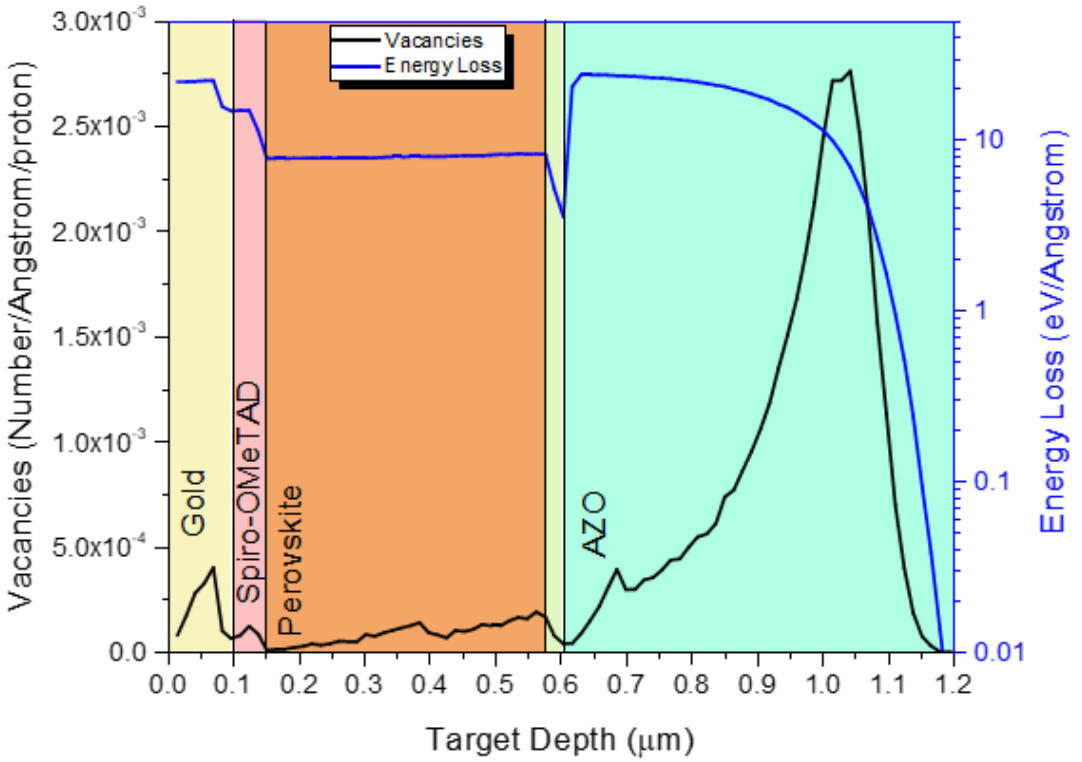

Figure 3.4 SRIM calculated generated vacancies (black) and energy loss due to ionisation of electrons (blue) in each layer as a function of target depth. Colours used for visual reference only.

The energy loss and generated vacancy plots follow a similar trend through each of the layers. Vacancies are generated when an incident ion collides with an atom and has enough energy to break the molecular bonds of the atoms in the materials structure. These Vacancies will eventually relax and return to the molecular structure. Spiro-OMeTAD exhibits greater vacancies generated and a higher energy loss when compared to the SnO_2 ETL, however the main peaks for vacancy generated appear in the Au and AZO electrodes. Therefore, a combination of different non-destructive techniques were used to probe the full degradation mechanisms in the PSCs and perovskite films after proton irradiation, thus giving a better understanding of the possible degradation in individual layers within the device stack.

3.2.4 Gold Metal Electrode Sheet Resistance

The first layer to be investigated was the Au metal electrode as this is the face through which the incident protons penetrated the device. As shown in Figure 3.4

the gold electrode exhibits strong proton stopping properties, as shown by the high proton energy loss, which is attributed to the density (19.3 kg/m^3) and thickness of the layer (~100 nm). As Au does not undergo nuclear transmutation until an energy of ~5 MeV, protons with energy 150 keV are unlikely to cause atomic changes in the Au electrode.[9] Additionally, through the SRIM simulation in Figure 3.4, there is a spike in vacancies close to the Au/Spiro-OMeTAD interface. At a fluence of $1x10^{12}$ protons/cm^2, the number of vacancies is calculated to be $2.75x10^{12}$/cm^2. This number increases to $2.75x10^{15}$/cm^2 at a fluence of $1x0^{15}$ protons/cm^2. It has been shown that under proton implantation, the generated vacancies in the Au Face Centred Cubic (FCC) lattice will relax back to their nearest neighbour and maintain the same structure. This relaxation however can result in a change in lattice parameters, like the lattice constant, which can affect the conductivity.[10] This suggests that any changes may be in the in the Au electrodes electronic properties.

To investigate how the proton bombardment affected the conductivity of the Au electrode, sheet resistance measurement were performed on Au evaporated onto quartz substrates and proton bombarded at the same energy and fluence as the PSC. The sheet resistance was measured a total of 3 times and across different areas. These values and the average values are shown in Table 3.1.

Table 3.1 Sheet resistance measurements of the gold electrodes for the bombarded devices and the mean values for each fluence.

	Sheet Resistance (Ω/□)				
	Reference	$1x10^{12}$ protons/cm^2	$1x10^{13}$ protons/cm^2	$1x10^{14}$ protons/cm^2	$1x10^{15}$ protons/cm^2
Reading 1	3.01	12.06	9.266	7.021	5.432
Reading 2	2.99	12.89	9.742	7.213	5.513
Reading 3	2.97	13.86	10.81	7.089	7.021
Mean Value	2.99	12.93	9.94	7.11	5.99

From the mean values, there is a 432% increase in sheet resistance after proton bombardment at a fluence of $1x10^{12}$ protons/cm^2. However, as the proton fluence

increases, there is a 64% decrease in sheet resistance. While the changes in the lattice constant due to vacancy relaxation in the FCC structure could explain the decrease sheet resistance from $1x10^{12}$ to $1x10^{15}$ protons/cm^2, the reason behind the increase in sheet resistance between the control and $1x10^{12}$ proton/cm^2 device is unknown and would require further study. Due to this decrease, it is highly unlikely the gold electrode contributes to the decrease in devices performance at high proton fluences. The PV parameters of the $1x10^{12}$ protons/cm^2 devices increase (PCE RF ~1.18) compared to the control devices, while the sheet resistance increases by 432%. This indicates that this is no observed correlation between the Au sheet resistance and the JV parameters shown in Figure 3.4. As the change in the sheet resistance of the gold electrode does not directly affect PV performance, additional studies were needed to pinpoint the exact cause of the device degradation.

3.2.5 Aluminium-doped Zinc Oxide Transparent Conducting Oxide

From the measured changes in the Au electrical conductivuty suggesting that the gold electrode did not contribute towards the decrease in device performance, the next layer investigated was the AZO layer as most of the incident protons stopped within the TCO. To investigate the reported superior radiation stability, the optical transmittance of bombarded bare quartz and AZO/quartz were measured. The reasoning behind this was to study if there is any change in the optical transmittance. A change is optical properties may imply a change in electrical properties as well. An example is a small change in transmittance can have a considerable effect on a devices J_{sc} as it is directly proportional to the light intensity, which will be reduced if there is a decrease in optical transmittance

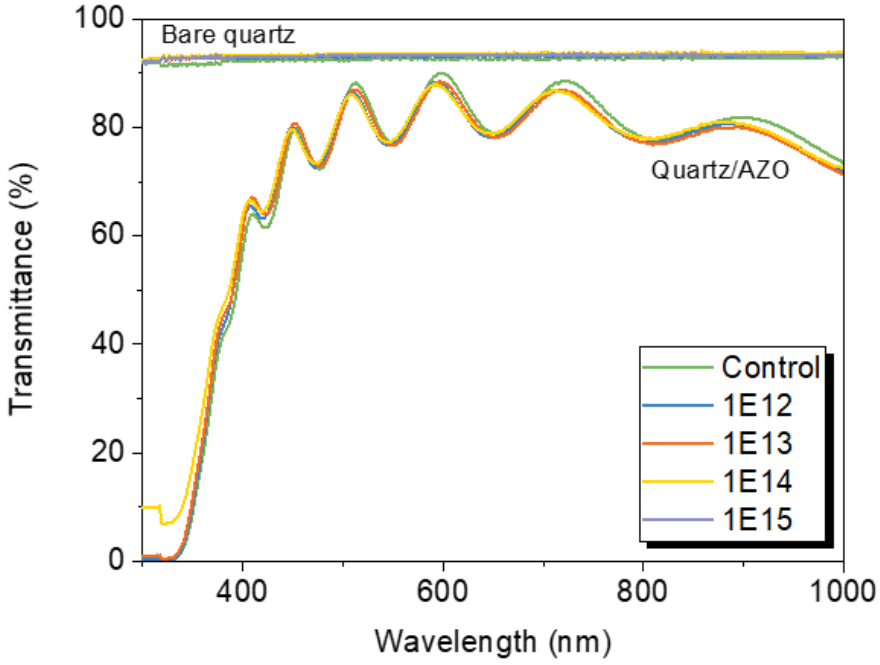

Figure 3.5 Optical transmittance spectra of bare quartz and quartz/AZO substrates after protons bombardment with various fluences.

As shown in Figure 3.5, the optical properties of AZO/quartz remain unchanged after proton irradiation up to a fluence of $1x10^{15}$ protons/cm^2, which is a clear indication that AZO can withstand very high proton irradiation without undergoing optical changes and damage. Incidentally, comparing Figure 3.4b and Figure 3.5, the ripple-like-shape seen in the EQE follows a similar pattern to the optical transmittance of the AZO. The measured optical transmittance of the bare quartz also remains unchanged, confirming the proton radiation hardness of the substrates with relatively low energy protons.

As the AZO/quartz were also bombarded with a sample at each fluence, the sheet resistance was also measured for these samples. The results are shown in Table 3.2.

Table 3.2 Sheet resistance measurements of AZO/quartz for a reference device and the bombarded devices, with the mean values for each fluence.

	Sheet Resistance (Ω/□)				
	Reference	$1x10^{12}$ protons/cm^2	$1x10^{13}$ protons/cm^2	$1x10^{14}$ protons/cm^2	$1x10^{15}$ protons/cm^2
Reading 1	13.68	42.79	38.95	38.01	37.56
Reading 2	15.34	42.41	37.79	38.55	38.06
Reading 3	17.41	42.76	39.96	37.57	38.23
Mean Value	15.48	42.65	38.90	38.04	37.95

Table 3.3 shows a similar trend as the Au electrode. Here it is shown that there is a 275% increase in sheet resistance at a fluence of $1x10^{12}$ protons/cm^2. Again however, this decrease does not correspond to any change in the PV parameters as the $1x10^{12}$ protons/cm^2 samples show an increase in performance (PCE RF ~1.18) while also exhibiting an increase in gold and AZO sheet resistance. It is possible that these changes in AZO sheet resistance do not affect the PCE considerably as the devices are small area (6.25 cm^2) but could cause issues at larger scales. Therefore, it is suggested that the electrical changes in the gold and AZO layers do not contribute to the decrease in device performance, and that the AZO optical transmittance shows very good proton stability, even up to $1x10^{15}$ protons/cm^2. The reasoning behind this increase and decrease trend is not known, and unlike for the Au electrode, the AZO structure is not FCC. Therefore, additional future characterisation will be needed to understand the changes in conductivity.

3.2.6 Triple Cation Perovskite Active Layer

As both the gold and AZO electrode showed good radiation hardness, the next layer to be considered was the perovskite itself. While previously it has been mentioned that due to the consistent V_{oc} values, it was highly unlikely that the perovskite layer had undergone any significant degradation. However, it was also important to verify if the perovskite had undergone any degradation e.g. on its structural and optical

properties. This would allow for a discussion into the radiation hardness of the perovskite itself. This investigation into the radiation hardness of the perovskite was achieved using X-ray diffraction (XRD), reflectance spectra measurements and photoluminescence (PL) measurements.

XRD was performed on perovskite films deposited on quartz substrates with a gold top electrode evaporated on-top (quartz/perovskite/Au). The XRD spectra of the samples exposed to irradiation of 10^{14} and 10^{15} protons/cm^2 are shown in Figure 3.6 and are compared to a non-irradiated control sample.

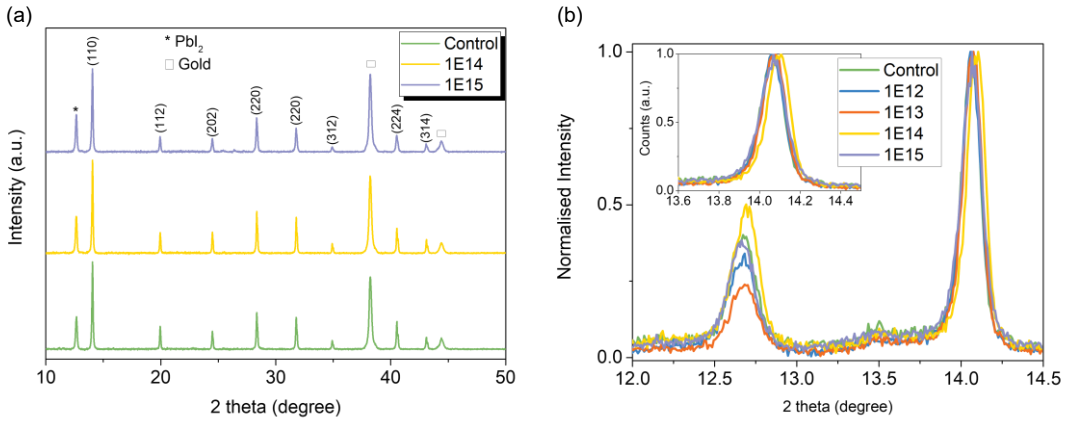

Figure 3.6 a) X-ray diffraction spectra of bare perovskite films on quartz with a gold electrode, without proton irradiation and after proton irradiation with fluences 10^{14} and 10^{15} protons/cm^2. b) Normalized XRD spectra centred at the perovskite peak (110) and the PbI2 peak. Insert of (110) perovskite peak at 14.1°.

For all samples, a peak is visible at an angle of 12.7° and is attributed to PbI_2. This peak could arise due to the 5% PbI_2 excess used in the precursor solution and/or any environmental degradation as the samples were measured more than 40 days after their initial fabrication. There are 3 perovskite peaks visible in the XRD spectra. These are labelled 100, 220, and 220 at an angle of 14.1, 28,4, and 31.8° respectively.[11] The normalized XRD spectra shown in Figure 3.6b shows a good overlap of the perovskite peak (110) between the control and all fluences. However, for the PbI_2 peak, there is no clear trend as a function of fluence which does not support clear degradation as a function of proton fluence. Additionally, the ratio of the PbI_2 peak between the control and 1x10^{15} protons/cm^2 devices are similar. Therefore, this indicates no consideration degradation of the crystalline structure of

the triple cation perovskite film due to the proton irradiation even at 10^{15} protons/cm^2. This was a desirable result as it signifies the impressive low energy proton irradiation stability of triple cation perovskite.

The optical reflectance spectra of the perovskite films on quartz with gold electrode are shown in Figure 3.7. The measurements were made through the quartz substrate. Optical reflectance was used due to the samples being opaque. Therefore, it can be assumed that there is no transmittance through the sample, and following Kirchhoff's Law, any changes in the perovskite absorbance would appear in the reflectance spectra.

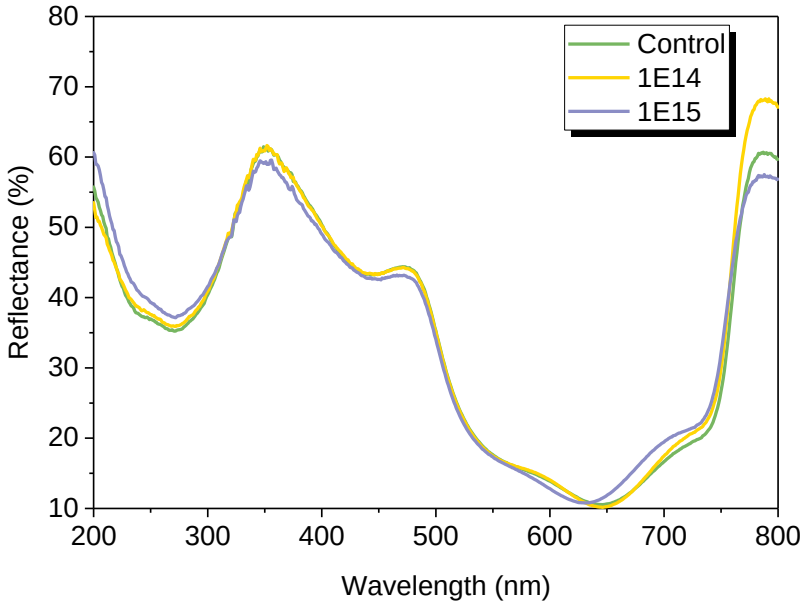

Figure 3.7 Diffuse reflectance spectra measured with an integrating sphere for perovskite films deposited on quartz, with a gold electrode, without irradiation and after irradiation with fluences 10^{14} and 10^{15} protons/cm^2.

As seen in the EQE spectra, the perovskite band edge is clearly visible at 740-775 nm for all three samples and all the spectra in the range of 200-775 nm are very similar. The difference in intensity above 775 nm are not related to perovskite and could be due to variations in the thickness of the gold electrode. We note however that the sample irradiated with $1x10^{15}$ protons/cm^2 has a slightly different spectral shape in the range 650-700 nm and 200-300 nm. This could suggest that perovskite has undergone some degradation at $1x10^{15}$ protons/cm^2, although it may not fully explain the strong PCE drop measured for this sample at the proton fluence.

The final set of measurements performed on the perovskite active layer was Photoluminescence and was used to investigate the radiation hardness of the perovskite active layer in terms of its photo-physical/chemical properties. Here the spectra were measured through the quartz substrate to probe the perovskite active layer. The averaged PL spectra of the full device stack as a function of proton irradiation is shown in Figure 3.8. The PL mapping as a function of proton fluence can be found in Figure A.1.

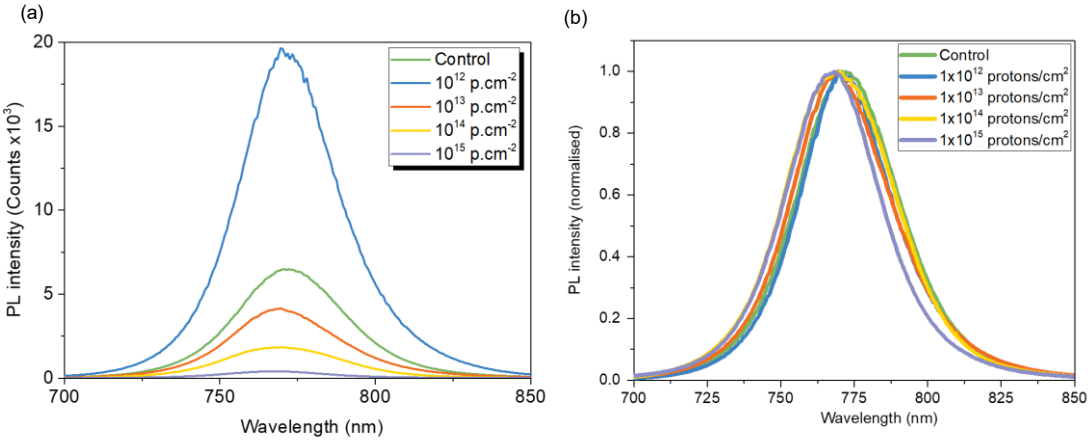

Figure 3.8 a) PL intensity of perovskite solar cells as a function of protons fluence. b) Normalised PL as a function of proton fluence.

The PL intensity undergoes almost more than a threefold increase in magnitude after irradiation with 1x10^{12} protons/cm^2 as compared to the control sample. This could be correlated to the slight increase in PCE after irradiation as observed with the 1x10^{12} protons/cm^2 devices and suggested that the performance of PSCs could be improved after 150 keV proton irradiation with a low fluence. However, the PL intensity begins to decrease at 1x10^{13} protons/cm^2, with the PL for the 1x10^{15} protons/cm^2 device exhibiting a very low signal in comparison. Here, the continuous decrease of the PL intensity is in excellent agreement with the observed decrease in PV performance.

PL intensity can also be indicative of the quality of the perovskite bulk or layer interfaces with the perovskite active area. Deep trap states formed in the perovskite bulk can induce non-radiative recombination and therefore quench the PL.[12][13] Additionally, a defective interface due to degradation of either the electron or hole

extraction layers can also quench the PL if carriers are lost to non-radiative recombination due to the reduced charge extraction.[14][15] Therefore, the origin of the decrease in PL could be due to degradation of one of the transporting layers. Spiro-OMeTAD is an organic polymer, and traditionally exhibit low radiation stability.[16] Therefore, characterising any changes in the optical or chemical properties of the spiro-OMeTAD HTL would be important in understanding the changes in device performance.

3.2.7 Spiro-OMeTAD Hole Transporting Layer

Through a variety of different measurement techniques, the degradation within the device stack which caused the drop in performance has been attributed to the Spiro or SnO2 layer. Additional characterisation was needed to find out which of the two layers had undergone the most significant degradation. This was achieved using Raman spectroscopy mapping as organic materials normally give a strong Raman response. As the Raman intensity can be sensitive to measurement conditions, such as the focus of the excitation laser, the normalized Raman spectra as a function of proton fluence are shown in Figure 3.9. The averaged spectra were obtained by averaging out 100 spectra obtained from the Raman mapping. The raw Raman spectra are shown in Figure A.3. To add additional confirmation of the results, at least two samples were measured for each fluence.

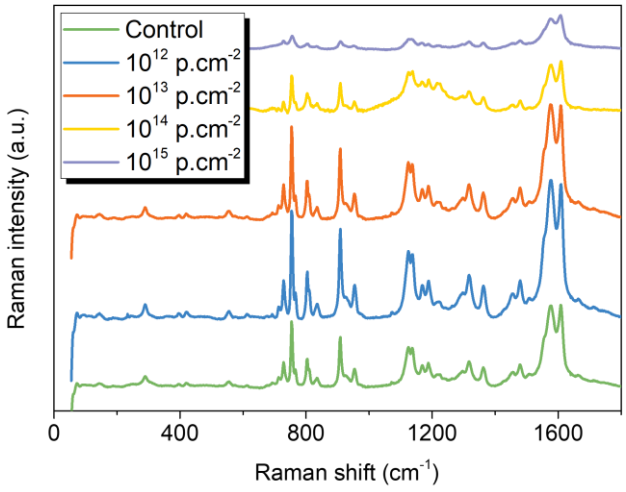

Figure 3.9 Raman spectra of perovskite solar cells measured through the Spiro-OMeTAD HTL (outside the gold electrodes) as a function of protons fluence.

While the overall spectral shape of the Raman spectra is similar when comparing between proton fluences and the control devices, the peak intensity is attenuated as the proton fluence is increased, especially at $1x10^{14}$ and $1x10^{15}$ protons/cm^2. There is strong intensity reduction at the peaks around 755 and 914 cm^{-1}, however the largest reduction in Raman intensity is found at the peaks around 1600 cm^{-1}. These peaks are attributed to the C=C vibrational modes and variation in these modes can affect organic semiconductors more significantly.[17]

This decrease in the Raman signal for higher fluences correlates well with the degradation of cells performance after proton irradiation and indicates that the loss in PCE at $1x10^{14}$ and $1x10^{15}$ protons/cm^2 is highly likely due to degradation of the Spiro-OMeTAD HTL. It has already been shown in literature that Spiro-OMeTAD is very sensitive to temperature, such that it can begin to degrade at 60^{o}C, and undergoes strong thermal degradation at 100°C.[18] However, even with the reported low temperature stability, it is highly unlikely that the temperature raised sufficiently high enough such that degradation would occur during the implantation, even for the highest protons fluence. The proton beam used a low power density of 15 mW/cm^2 for irradiation, and along with that, the samples were clipped down onto a heat sink to limit the temperature rise. Therefore, it is reasonable that the degradation present in the Spiro-OMeTAD layer is a result of the proton irradiation.

3.2.8 TPV and Charge Carrier Density Measurements

Using optical reflectance and XRD measurements, it has been shown that the perovskite active layer remains stable, even at $1x10^{15}$ protons/cm^2. In contrast, Raman spectroscopy and PL measurements have shown that the spiro-OMeTAD HTL undergoes degradation at proton fluences of $1x10^{14}$ and $1x10^{15}$. To further understand how the degradation of the spiro-OMeTAD HTL affected device mechanics such as carrier lifetime and density, transient photovoltage (TPV) and charge carrier density measurements were performed. These techniques are detailed in Chapter 2. The results of these measurements can be seen in Figure 3.10.

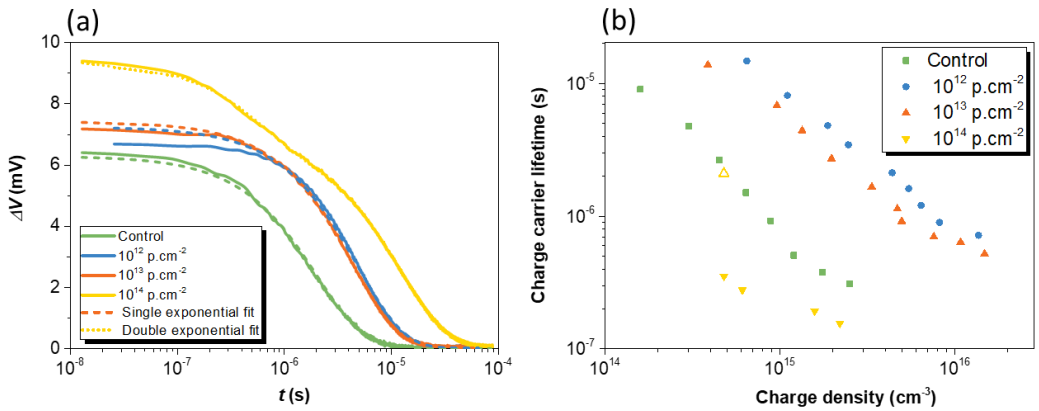

Figure 3.10 (a) Change in voltage (ΔV) as a function of time (TPV decays) for each sample at 0.1 sun equivalent (100 W/m^2) light intensity (5000 K white LED). (b) Charge carrier lifetime versus charge carrier density as a function of proton fluence. The open triangle represents the slower time constant obtained from the double exponential fitting at 1x10^{14} protons/cm^2.

For devices with one dominant charge recombination mechanism, the perturbed V_{oc} decays back to a ΔV returns to 0 (steady state) with a single exponential time constant.[19][20] This behaviour was observed for the control devices and the irradiated samples up to a fluence of 1x10^{13} protons/cm^2, indicating that bulk charge recombination in the perovskite layer is the dominating mechanism for low proton doses, as shown in Figure 3.11a. When examining the higher fluences, the 1x10^{14} protons/cm^2 devices have additional process observed at short times (<1 µs) and these result in double exponential fitting being required at that fluence at light intensities below 0.25 sun. This double exponential behaviour for the faster recombination process has been linked to the presence of interfacial recombination, either at the ETL or HTL contacts.[21-23] Therefore, from the observed degradation of the Spiro-OMeTAD under Raman spectroscopy, the faster time constant can be attributed to recombination at the perovskite/Spiro interface for these devices. However, for the 1x10^{15} protons/cm^2 device, it was not possible to obtain a stable V_{oc} when using the standard TPV technique as these devices were highly degraded. However, evidence of fast interfacial recombination was observed in the form of a negative transient deflection in response to a 1 sun equivalent laser pulse as shown

in Figure 3.11. 1 Sun intensity was used due to the very low response from the TPV measurements. This observation has also been observed in other work.[24-26]

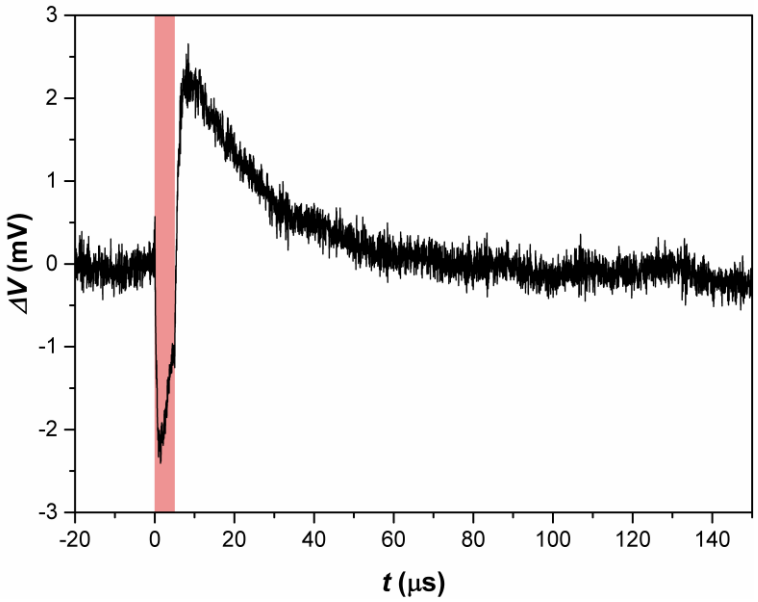

Figure 3.11 TPV response for device bombarded with $1x10^{15}$ protons/cm^2 measured at 1 Sun equivalent intensity. Laser pulse (red shaded region) induces a rapid negative deflection (decrease in V_{oc}) in the TPV response which is indicative of a fast interfacial recombination.

The charge density measurements shown in Figure 3.10b were calculated using the differential capacitance method.[27] As seen, the proton bombardment with $1x10^{12}$ and $1x10^{13}$ protons/cm^2 resulted in a significant increase in charge density. The increase from 10^{15} cm^{-3} in the controls to 10^{16} cm^{-3} is attributed to the formation of trap states within the perovskite bulk. Shallow traps states will correspond to an increase in carrier lifetime, as seen in the $1x10^{12}$ proton/cm^2 devices compared to the control at the same charge carrier densities, while the formation of deeper traps would likely act as recombination centres and cause a decrease in carrier lifetime. Literature such as Lang et al. have also observed this apparent decrease in the rate of recombination because of proton bombardment induced defect formation and the resulting longer carrier lifetimes.[28] This was explained by an efficient trapping/de-trapping of minority charge carriers in radiation-induced trap states without major impact on device performance. At $1x10^{14}$ protons/cm^2, the observed additional fast interfacial recombination significantly reduced the carrier lifetime to 10^{-6} – 10^{-7} s

from ~10^{-5} for the control device. However, the calculated slower time constant obtained from the double exponential fitting is in the same range as the lifetimes calculated for the control devices, suggesting that there could be some degradation to the bulk perovskite, however the interfacial recombination dominates. This is consistent with the main source of the performance loss at $1x10^{14}$ protons/cm^2 being the degradation of the Spiro-OMeTAD interface, while trap states formed in the perovskite layer do not affect the performance significantly.

3.3 Conclusion

This chapter finds that the proton radiation stability of planar N-i-P PSCs with an AZO TCO is heavily reliant on the radiation hardness of the HTL, as shown by the degradation of the spiro-OMeTAD at fluences >$1x10^{13}$ protons/cm^2. Using SRIM, it was found that the bulk number of incident protons will stop within the AZO TCO layer, signifying the importance of having a radiation stable TCO within a full device stack. However, as all layers were subject to proton irradiation, each layer was characterised to determine radiation stability. The initial PV measurements of the AZO PSCs before bombardment were presented with a champion 1 Sun AM1.5G PCE of 15% and champion 1 Sun AM0 PCE of 13.6% being achieved. The AZO device PCEs ranged from 8-15% under 1 Sun AM1.5G. It is shown through remaining factor values that the PSCs exhibit a high tolerance to 150 keV proton radiation, up to a fluence of $1x10^{13}$ protons/cm^2. In comparison, Si and GaAs solar cells are known to be destroyed or highly deteriorated at this proton energy and fluence. However, as the proton fluence increases to $1x10^{14}$ and $1x10^{15}$ protons/cm^2, the devices undergo a sharp decline in performance. This chapter finds that the degradation of the Spiro-OMeTAD HTL during proton irradiation results in an increase in interfacial recombination at the spiro/perovskite interface hindering charge extraction properties. This reduction in charge extraction correlates well with the observed decrease in the Jsc and the observed degradation in the spiro-OMeTAD Raman spectra and PL intensity. XRD, optical reflectance, and PL measurements found that the structural and optical properties of perovskite remain intact up to high fluence levels, which correlates with the very stable Voc and can be concluded as being radiation stable under 150 keV proton bombardment. However, the TPV measurements indicate an increase in

charge carrier density and lifetime from $1x10^{12}$ protons/cm^2. This is explained through the formation of proton radiation-induced shallow trap states in the perovskite bulk. It is thought that these trap states release charge carriers efficiently and do not affect the performance of the cells for low fluence levels. Sheet resistance measurements were taken for both irradiated gold and AZO, however the observed increased in these measurements do not contribute to any change in device performance as shown with the $1x10^{12}$ protons/cm2 sample. Additionally, optical transmittance measurements show that the optical properties of quartz and AZO/quartz substrates remain unchanged, even after irradiation up to $1x10^{15}$ protons/cm^2. It was not possible to measure any potential degradation of the SnO_2 ETL after proton irradiation due to the very thin (~25 nm) SnO_2 layer being insensitive to many of the techniques used in this work such as PL or Raman spectroscopy. Optical transmittance and reflectance measurements were performed; however, the results were inconclusive. Future work will be necessary to determine the role of SnO_2 ETL in the performance loss due to proton irradiation. Overall, the findings in this chapter highlight both decent PCE and good stability against proton irradiation. A deeper scientific understanding on the interfacial degradation due to proton irradiation is also found. These results can be useful for the development of future high PCE perovskite solar cells with ultra-high stability against proton irradiation.

REFERENCES

[1] Barbé, J., Hughes, D., Wei, Z., Pockett, A., Lee, H. K., Heasman, K. C., Carnie, M. J., Watson, T. M., Tsoi, W. C. (2019). Radiation hardness of perovskite solar cells based on aluminum-doped zinc oxide electrode under proton irradiation. Solar RRL, 3(12), 1900219. https://doi.org/10.1002/solr.201900219

[2] Dou, B., Miller, E. M., Christians, J. A., Sanehira, E. M., Klein, T. R., Barnes, F. S., Shaheen, S. E., Garner, S. M., Ghosh, S., Mallick, A., Basak, D., van Hest, M. F. (2017). High-performance flexible perovskite solar cells on Ultrathin Glass: Implications of the TCO. The Journal of Physical Chemistry Letters, 8(19), 4960–4966. https://doi.org/10.1021/acs.jpclett.7b02128

[3] Zhao, X., Shen, H., Zhang, Y., Li, X., Zhao, X., Tai, M., Li, J., Li, J., Li, X., Lin, H. (2016). Aluminum-doped zinc oxide as highly stable electron collection layer for perovskite solar cells. ACS Applied Materials Interfaces, 8(12), 7826–7833. https://doi.org/10.1021/acsami.6b00520

[4] La Ferrara, V., De Maria, A., Rametta, G., Della Noce, M., Mercaldo, L. V., Borriello, C., Bruno, A., Delli Veneri, P. (2017). ZnO nanorods/azo photoanode for perovskite solar cells fabricated in ambient air. Materials Research Express, 4(8), 085025. https://doi.org/10.1088/2053-1591/aa7fcd

[5] Dang, T.-V., Pammi, S. V. N., Choi, J., Yoon, S.-G. (2017). Utilization of azo/au/azo multilayer electrodes instead of FTO for perovskite solar cells. Solar Energy Materials and Solar Cells, 163, 58–65. https://doi.org/10.1016/j.solmat.2017.01.008

[6] Miyazawa, Y., Ikegami, M., Miyasaka, T., Ohshima, T., Imaizumi, M., & Hirose, K. (2015). Evaluation of radiation tolerance of perovskite solar cell for use in space. 2015 IEEE 42nd Photovoltaic Specialist Conference (PVSC). https://doi.org/10.1109/pvsc.2015.7355859

[7] Hu, Z., He, S., Yang, D. (2006). Radiation effects of protons and electrons on backfield silicon solar cells. PROTECTION OF MATERIALS AND STRUCTURES FROM THE SPACE ENVIRONMENT, 1–8. https://doi.org/10.1007/1-4020-4319-8_1

[8] Ohshima, T., Sato, S.-ichiro, Nakamura, T., Imaizumi, M., Sugaya, T., Matsubara, K., Niki, S., Takeda, A., Okano, Y. (2013). Electrical performance degradation of gaas solar cells with InGaAs quantum dot layers due to proton irradiation. 2013 IEEE 39th Photovoltaic Specialists Conference (PVSC). https://doi.org/10.1109/pvsc.2013.6745049

[9] Elmaghraby, E. K., Hassan, K. F., Omara, H., Saleh, Z. A. (2010). Production of the mercury-197 through proton induced reaction on gold. Applied Radiation and Isotopes, 68(9), 1694–1698. https://doi.org/10.1016/j.apradiso.2010.04.009

[10] Nguyen, K. T., Hiep Vuong, V., Nguyen, T. N., Nguyen, T. T., Yamamoto, T., Hoang, N. N. (2021). Unusual hydrogen implanted gold with lattice contraction at increased hydrogen content. Nature Communications, 12(1). https://doi.org/10.1038/s41467-021-21842-9

[11] Wei, X., Zhang, M., Liu, X., Chen, F., Lei, X., Liu, H., Meng, F., Zeng, H., Yang, S. and Liu, J. (2018), Semitransparent $CH_3NH_3PbI_3$ Films Achieved by Solvent Engineering for Annealing- and Electron Transport Layer-Free Planar Perovskite Solar Cells. Sol. RRL, 2: 1700222. https://doi.org/10.1002/solr.201700222

[12] Tian, Y., Peter, M., Unger, E., Abdellah, M., Zheng, K., Pullerits, T., Yartsev, A., Sundström, V., Scheblykin, I. G. (2015). Mechanistic insights into perovskite photoluminescence enhancement: Light curing with oxygen can boost yield thousandfold. Physical Chemistry Chemical Physics, 17(38), 24978–24987. https://doi.org/10.1039/c5cp04410c

[13] deQuilettes, D. W., Zhang, W., Burlakov, V. M., Graham, D. J., Leijtens, T., Osherov, A., Bulović, V., Snaith, H. J., Ginger, D. S., Stranks, S. D. (2016). Photo-induced halide redistribution in organic–inorganic perovskite films. Nature Communications, 7(1). https://doi.org/10.1038/ncomms11683

[14] Eperon, G. E., Moerman, D., Ginger, D. S. (2016). Anticorrelation between local photoluminescence and photocurrent suggests variability in contact to active layer in perovskite solar cells. ACS Nano, 10(11), 10258–10266. https://doi.org/10.1021/acsnano.6b05825

[15] Lakhiani, H., Dunlop, T., De Rossi, F., Dimitrov, S., Kerremans, R., Charbonneau, C., Watson, T., Barbé, J., Tsoi, W. C. (2019). Variations of infiltration and electronic contact in mesoscopic perovskite solar cells revealed by high-Resolution Multi-mapping techniques. Advanced Functional Materials, 29(25), 1900885. https://doi.org/10.1002/adfm.201900885

[16] Lee, H.K.H., Stewart, K., Hughes, D., Barbé, J., Pockett, A., Kilbride, R.C., Heasman, K.C., Wei, Z., Watson, T.M., Carnie, M.J., Kim, J., Tsoi, W.C. (2022). Proton Radiation Hardness of Organic Photovoltaics: An In-Depth Study. Sol. RRL, 6: 2101037. https://doi.org/10.1002/solr.202101037

[17] Köhler, A., Bässler, H. (2015). The Electronic Structure of Organic Semiconductors. In Electronic Processes in Organic Semiconductors (eds A. Köhler and H. Bässler). https://doi.org/10.1002/9783527685172.ch1

[18] Miyazawa, Y., Ikegami, M., Chen, H.-W., Ohshima, T., Imaizumi, M., Hirose, K., Miyasaka, T. (2018). Tolerance of perovskite solar cell to high-energy particle irradiations in space environment. IScience, 2, 148–155. https://doi.org/10.1016/j.isci.2018.03.020

[19] Contreras-Bernal, L., Salado, M., Todinova, A., Calio, L., Ahmad, S., Idígoras, J., Anta, J. A. (2017). Origin and whereabouts of recombination in perovskite solar cells. The Journal of Physical Chemistry C, 121(18), 9705–9713. https://doi.org/10.1021/acs.jpcc.7b01206

[20] Correa-Baena, J.-P., Turren-Cruz, S.-H., Tress, W., Hagfeldt, A., Aranda, C., Shooshtari, L., Bisquert, J., Guerrero, A. (2017). Changes from bulk to surface recombination mechanisms between pristine and cycled perovskite solar cells. ACS Energy Letters, 2(3), 681–688. https://doi.org/10.1021/acsenergylett.7b00059

[21] Carnie, M. J., Charbonneau, C., Davies, M. L., Regan, B. O., Worsley, D. A., Watson, T. M. (2014). Performance enhancement of solution processed perovskite solar cells incorporating functionalized silica nanoparticles. J. Mater. Chem. A, 2(40), 17077–17084. https://doi.org/10.1039/c4ta03387f

[22] Montcada, N. F., Marín-Beloqui, J. M., Cambarau, W., Jiménez-López, J., Cabau, L., Cho, K. T., Nazeeruddin, M. K., Palomares, E. (2016). Analysis of photoinduced carrier recombination kinetics in flat and mesoporous lead perovskite solar cells. ACS Energy Letters, 2(1), 182–187. https://doi.org/10.1021/acsenergylett.6b00600

[23] O'Regan, B. C., Barnes, P. R., Li, X., Law, C., Palomares, E., & Marin-Beloqui, J. M. (2015). Optoelectronic studies of methylammonium lead iodide perovskite solar cells with mesoporous TiO_2: Separation of electronic and chemical charge storage, understanding two recombination lifetimes, and the evolution of band offsets during J-V hysteresis. Journal of the American Chemical Society, 137(15), 5087–5099. https://doi.org/10.1021/jacs.5b00761

[24] Pockett, A., Carnie, M. J. (2017). Ionic influences on recombination in perovskite solar cells. ACS Energy Letters, 2(7), 1683–1689. https://doi.org/10.1021/acsenergylett.7b00490

[25] Calado, P., Telford, A. M., Bryant, D., Li, X., Nelson, J., O'Regan, B. C., Barnes, P. R. F. (2016). Evidence for ion migration in hybrid perovskite solar cells with minimal hysteresis. Nature Communications, 7(1). https://doi.org/10.1038/ncomms13831

[26] Pockett, A., Raptis, D., Meroni, S. M., Baker, J., Watson, T., Carnie, M. (2019). Origin of exceptionally slow light soaking effect in mesoporous carbon perovskite solar cells with Ava additive. The Journal of Physical Chemistry C, 123(18), 11414–11421. https://doi.org/10.1021/acs.jpcc.9b01058

[27] Shuttle, C. G., O'Regan, B., Ballantyne, A. M., Nelson, J., Bradley, D. D., de Mello, J., Durrant, J. R. (2008). Experimental determination of the rate law for charge carrier decay in a polythiophene: Fullerene Solar Cell. Applied Physics Letters, 92(9), 093311. https://doi.org/10.1063/1.2891871

[28] Lang, F., Jošt, M., Bundesmann, J., Denker, A., Albrecht, S., Landi, G., Neitzert, H.-C., Rappich, J., Nickel, N. H. (2019). Efficient minority carrier detrapping mediating the radiation hardness of triple-cation perovskite solar cells under proton irradiation. Energy Environmental Science, 12(5), 1634–1647. https://doi.org/10.1039/c9ee00077a

Chapter 4

Radiation Stability of Mesoporous Carbon-Based Perovskite Solar Cells Under 150 keV Proton Bombardment

4.1 Introduction

The stability of PSCs under particle bombardment is paramount in the study of feasibility for space applications. In the last chapter, it was discussed that high energy particles pose a threat to the performance of electronic devices. Whilst the stability of the devices under 150 keV proton bombardment significantly surpassed that of regular satellite PV, the 150 keV proton irradiation of planar n-i-p PSCs using AZO electrode caused degradation to the HTL layer at fluences higher than $1x10^{13}$ protons/cm^2; this degradation caused interfacial recombination which lowered device performance to almost inoperable at $1x10^{15}$ protons/cm^2. There remains two possible solutions to the degradation issue. Firstly, the use of encapsulation materials (see Chapter 6) would allow for the continued use of Spiro-OMeTAD devices; this would create a radiation stable baseline which could lead to the use of more efficient architectures such as tandem cells. Secondly, removing the HTL altogether would remove the layer that is most susceptible to proton radiation induced degradation. This chapter expands on the removal of the HTL, investigating the particle stability of perovskite devices by utilising the robust HTL free architecture of mesoporous carbon perovskite solar cells (m-CPSCs). As shown in Chapter 2, the m-CPSC have a thick (~400 nm) carbon electrode that also acts as a self-encapsulation which could potentially block incident protons. This chapter presents the results of a 150 keV proton bombardment into the mesoporous carbon electrode-based PSCs. Non-destructive optical characterisation techniques including Raman spectroscopy and PL were used for additional characterisation. It was found that the m-CPSCs are stable

under 150 keV proton bombardment at a fluence of $1x10^{15}$ protons/cm2. The results in this chapter have been published in Energy Technology.[1]

4.2 Results and Discussion

4.2.1 Before Proton Bombardment

The m-CPSCs devices used within this chapter are detailed in Chapter 2. They have an active area of 1 cm^2 with a 0.49 cm^2 mask being used during the JV measurements. This relatively large active area and mask size were chosen as they are more appropriate to test the devices scalability. The mask size was chosen to reduce the effect on inconsistencies at the external edges of the printing, which can affect the measured device performance. There has been a detailed investigation into the effect of mask size to m-CPSC performance.[2] The reverse J–V curves under AM1.5G and AM0 illumination for the champion cell are shown in Figure 4.2. The device parameters for the champion cells under 1 sun AM1.5G and 1 sun AM0 illumination are also shown.

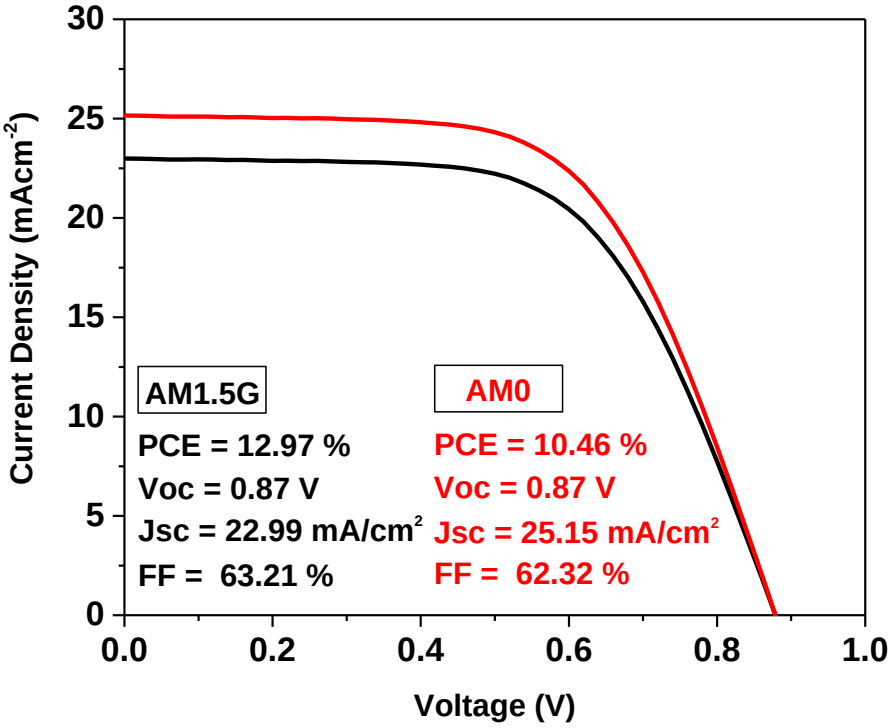

Figure. 4.2 J-V curves under 1 sun AM1.5G (Black) and 1 sun AM0 illumination (Red) for the champion cell.

As seen before in Chapter 3, the variation in performance between the AM1.5G measurement and AM0 measurement is the reduced PCE and increased Jsc. The champion performance at AM1.5G is ~13% PCE, with a Voc of 0.87 V, a Jsc of 22.99 $mAcm^{-2}$, and FF of 63.21%. The PCE decreases by 19% to 10.46% and the Jsc increases by 9% to 25.15 $mAcm^{-2}$. The variation in device performance between AM1.5G and AM0 is expected and has been shown in Chapter 3. However, here the Jsc does not increase by a factor of 1.36 as seen before. This could be due to the slow response time of the carbon devices as the carbon electrode has high series resistance (R_S) and therefore need to be light soaked (kept under light) for 3 minutes before measuring. The histogram of the device PCE for AM1.5G and AM0 can be seen in Figure 4.3.

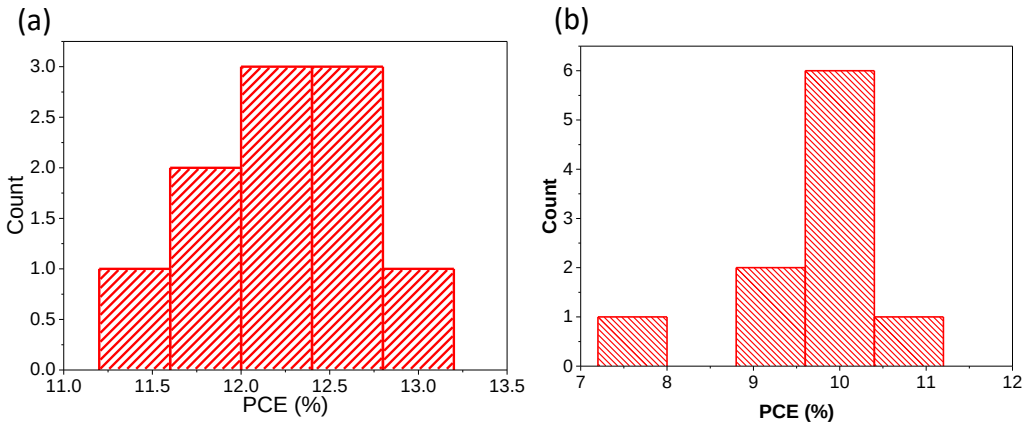

Figure 4.3 a) Histogram of PCE under 1 sun AM1.5G illumination b) Histogram of PCE under 1 sun AM0 illumination.

From Figure 4.3a, the dominant PCE value under AM1.5G is between 12-12.75%, however the PCE spread is narrow as the full PCE range is between 11-13%. This is regarded as narrow when compared to the PCE range in Chapter 3, which was 8-15%. When the same devices were measured under AM0, the dominant PCE is much more prominent at ~10%. In comparison to other work in the literature, the lower measured PCE here can overshadow the stability of the devices.[3] However, as mentioned above, the cause of this reduced PCE is the high series resistance of the carbon electrode. Since publication, the current average PCE is now ~15% and new techniques such as including grids within the electrode have improved

conductivity.[4] The m-CPSC is still in development and therefore higher PCEs could be seen in the future with better optimisation of the device layers.

4.2.2 Proton Bombardment Simulation

As seen similarly in Chapter 3, two samples were chosen for each proton fluence. Some devices were not exposed to proton irradiation but subjected to the same atmospheric conditions to serve as control samples. All irradiated samples were bombarded through the carbon electrode with 150 keV protons with fluences ranging from $1x10^{12}$ to $1x10^{15}$ protons/cm^2. All samples were kept under N_2 in the dark before irradiation was carried out, and then kept for a week under dark air after bombardment, before they were returned from the Surrey Ion Beam Centre and remeasured at Swansea University.

Utilising the same investigation methods as seen in Chapter 3, SRIM simulations were used to simulate the incident proton beam stopping range. However, additional measures would be needed to properly simulate the mesoporous nature of the device stack. The previous uses of SRIM, such as seen before in Section 3.2.1, consider the cases where the layers are planar in n-i-p devices. Therefore, each of these layers are compact. In the case of the m-CPSC, there are multiple mesoporous layers, each infiltrated with MAPI-AVA perovskite. Therefore, a new method of calculating the density for each layer is required. Here we consider volume fractions, which are given via the equation:

$$\varphi_i = \frac{V_i}{\sum_j V_j} \tag{4.1}$$

Where φ_i is the volume fraction of material i, V_i is the volume of material i in cm^3 and the denominator is the summation of the volumes of all materials within the layer. A caveat is made in which it is assumed that the perovskite is fully infiltrated within the layers, and that there is a defined boundary between each of the layers as SRIM does not consider roughness. Through thickness measurements, the volume of each layer is known (shown in Chapter 2). Using this equation, and the knowledge that the summation of all φ_i is equal to 1, the total density within a layer is calculated via:

$$\rho_{Total} = \sum_{i} \varphi_i \rho_i \tag{4.2}$$

Where ρ_i is the density of material i. The use of Equations 4.1 & 4.2 allows for a more accurate estimate of the true density of the mesoporous layers with infiltrated perovskite. The results from the SRIM simulations are shown in Figure 4.4.

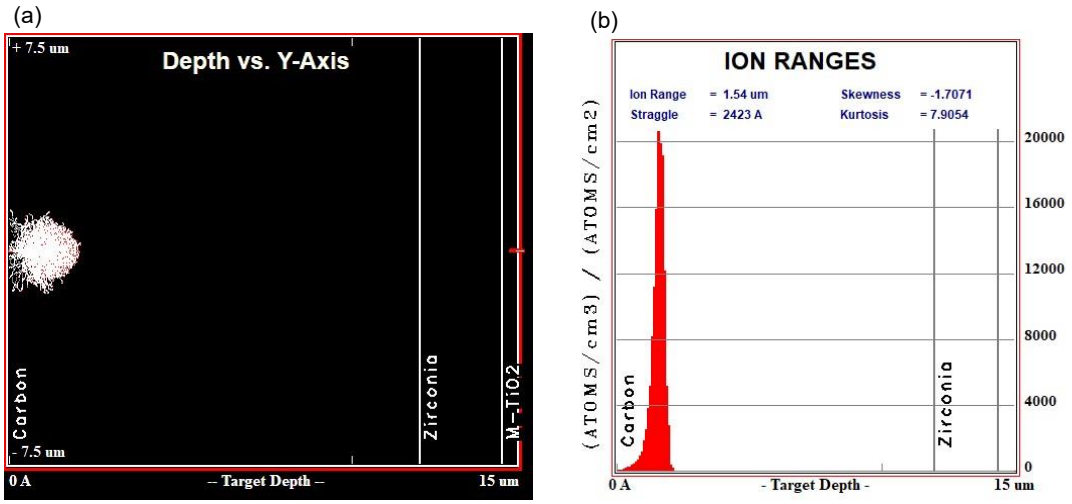

Figure 4.4 a) SRIM generated proton depth calculation at 150 keV incident on the mesoporous carbon electrode b) Histogram of proton stopping depth in relation to device layers.

From the SRIM simulations in Figure 4.4, the protons are stopped within the carbon electrode at a maximum calculated target depth of ~1.54 µm. The bulk of the protons are stopped at a range of ~1.27 µm, which is ~9% the total thickness of the carbon electrode. Therefore, the most likely area of potential degradation is the carbon electrode and the "capping layer" of perovskite material. However, to properly assess the radiation stability of the m-CPSCs, the active layer will also need to be investigated.

4.2.3 J-V Performance After Bombardment

The devices were measured after the 150 keV proton bombardment under AM1.5G and AM0, and the Remaining Factor (RF) values were calculated as seen in Chapter 3. The RF values for the PV parameters (PCE, V_{oc}, J_{sc}, and FF) under 1 Sun AM0 illumination after proton irradiation are shown in Figure 4.4. The RF values under

AM1.5G are found in Figure B.1 as the AM0 values are more relevant for space applications.

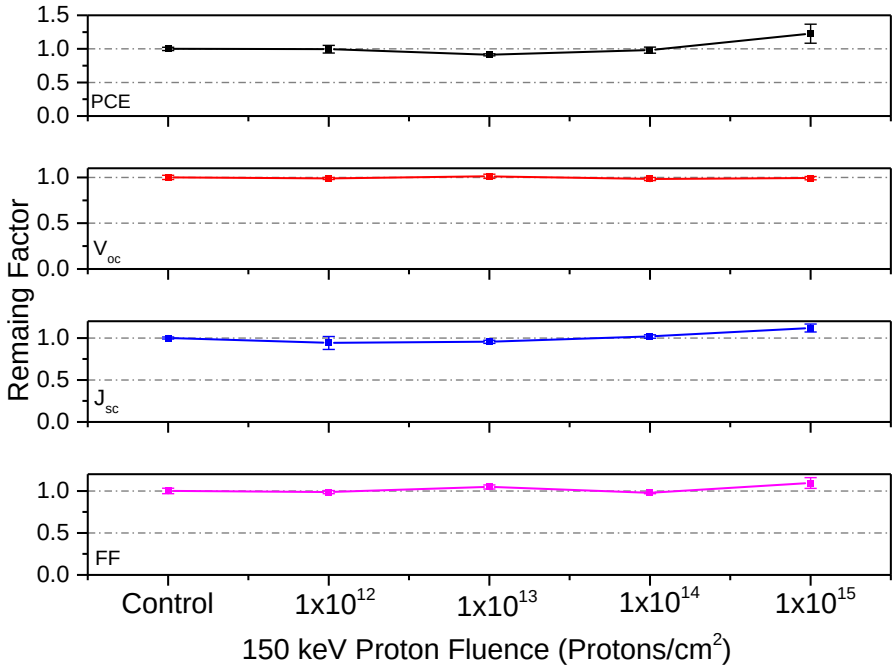

Figure 4.5 Remaining Factor of PCE, V_{oc}, J_{sc}, and FF (under 1 sun AM0 illumination) versus proton fluence of m-CPSC (including the control device). The data points are the average values at each fluence, and the error bars represent the range of values.

Interestingly in Figure 4.5, the PCE, V_{oc}, J_{sc}, and FF all remained close to a remaining factor of 1.0. There is a 6% decrease in the Jsc RF at $1x10^{12}$ protons/cm^2, however due to the stable Voc (RF ~0.99) and FF (RF ~0.99), the PCE remains stable with a RF ~0.99. Additionally, there is a decrease in PCE at 1x1013 protons/cm2, with a PCE RF ~0.91. There is an observed increase in PCE at $1x10^{15}$ protons/cm^2, with the PCE RF reaching ~1.2. This increase is due to J-V parameter variation after bombardment for one device at $1x10^{15}$ protons/cm^2 as seen in the device parameter table in Table B.1. Due to the parameters remaining consistent, even at $1x10^{15}$ protons/cm^2, it is suggested that the devices were not degraded under 150 keV proton irradiation. To further show the stability of the m-CPSCs, the JV curves and EQE spectra as a function of proton fluence are shown in Figure 4.6a and 4.6b respectively.

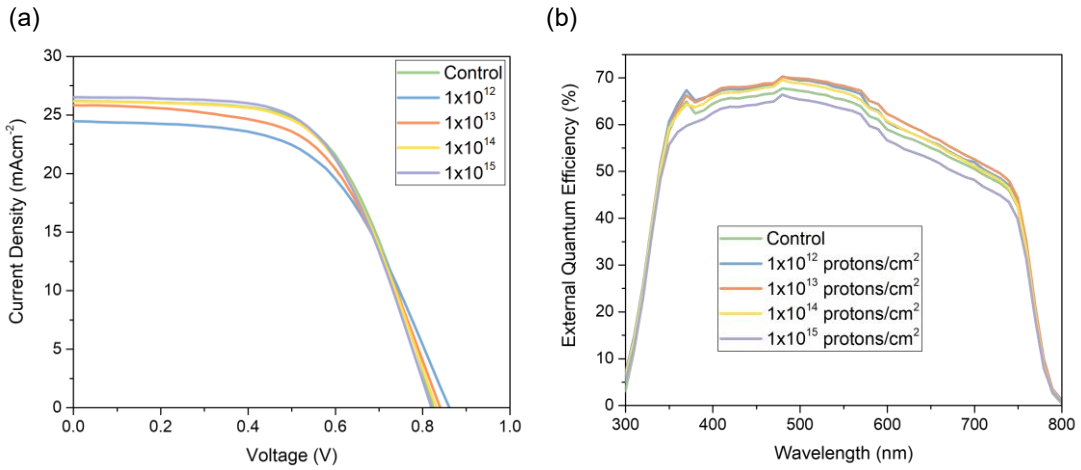

Figure 4.5 a) Reverse J-V curves under 1 sun AM0 illumination for the m-CPSCs as a function of proton fluence. (b) Measured EQE spectra as a function of proton fluence.

The J-V curves in Figure 4.5a follow the observed RF trend, with the $1x10^{12}$ protons/cm^2 devices exhibiting a 7% decrease in Jsc compared to the control, and all devices displaying a good overlap of V_{oc} values around ~0.84 V. Overall there is no visible degradation of the JV curve shape as a function of proton fluence, which correlates well with the stable device parameters.

When comparing the EQE spectra as a function of proton fluence in Figure 4.5b, the same trend observed in the J-V curves is also exhibited. There is a 4% decrease in area under the curve for the $1x10^{12}$ protons/cm^2 device when compared to the control. However, as the fluence increases this is good overlap and is a therefore in fair agreement with the stable J_{sc} RF. In other works looking at comparable irradiation conditions, Miyasaka et al showed that there was a non-uniform spectral response of photocurrent in $FAMAPb(IBr)_3$ cells after proton irradiation at fluence of $1x10^{14}$ protons/cm^2 which they attributed to degradation of the active layer.[5] In the last chapter, it was showed that a uniform reduction in the EQE spectrum was indicative of a deterioration in charge extraction properties rather than charge generation properties suggesting a degradation of the Spiro-OMeTAD HTL properties. Here, no significant change in EQE across the proton fluences is observed. Therefore, it is inferred that there is no degradation of the active layer, the TiO_2 ETL, or a change in charge extraction properties of the mesoporous carbon electrode because of the proton bombardment.

Therefore, from the JV measurements it is shown that screen printed PSCs utilising a mesoporous carbon electrode can be exposed to a radiation level up to $1x10^{15}$ protons/cm^2 at 150 keV without being significantly degraded. By comparison, the V_{oc} and J_{sc} of Si solar cells exposed to 150 keV protons decreased by >40% and 10%, respectively, at $1x10^{13}$ protons/cm^2.[6] At this same proton energy, GaAs solar cells exhibit a ~40% decrease in PCE at a fluence of $1x10^{11}$ protons/cm^2.[7] In Chapter 3, planar PSCs fabricated with an Au electrode, triple cation perovskite, and Spiro-OMeTAD HTL were stable up to $1x10^{13}$ protons/cm^2 when exposed to 150 keV protons. At a fluence of $1x10^{15}$ protons/cm^2 the devices were completely degraded due to interfacial recombination at the perovskite/HTL interface. Furthermore, 100 keV proton bombardment on flexible inverted PSCs show an initial ~20% performance decrease at $1x10^{13}$ protons/cm^2 due an increase in series resistance and a decrease in shunt resistance by the generation of recombination centres and trap centres due to the irradiation.[8] Therefore, at this proton energy range, screen printed m-CPSCs exhibit the greatest stability against 150 keV proton irradiation.

4.2.4 Spectroscopic Study

4.2.4.1 Probing Through the Glass Substrate

As the m-CPSCs exhibit superior proton stopping power and stability, experimental issues arise as there is no degradation to probe and investigate. Therefore, work was undertaken to try and explain why the m-CPSCs have high radiation stability. Like the previous chapter, this involved using non-destructive techniques such as Raman and PL to investigate why the PSCs remain stable, and if there are any micro-changes in the carbon electrode as from the SRIM simulation all the protons stop within it. Due to the mesoporous nature of the CPSCs, micro-Raman and PL mapping was used to study the homogeneity of the device layers and to take an average spectrum for comparison. The mapping results for the control sample is shown in Figure B.2 as a showcase on how the roughness of the mesoporous layers affect the Raman signal. As m-CPSCs are unencapsulated, the use of Raman and PL was useful to also probe the effect of storage and transport as these cells were under air for ~2 weeks during

the experimental time and travel time before were remeasured. The Raman and PL measurements were performed on the same area.

The averaged Raman spectra as a function of proton fluence is shown in Figure 4.6a, with the normalised spectra shown in Figure 4.6b. The Raman spectra through the glass substrate shows three distinct peaks.

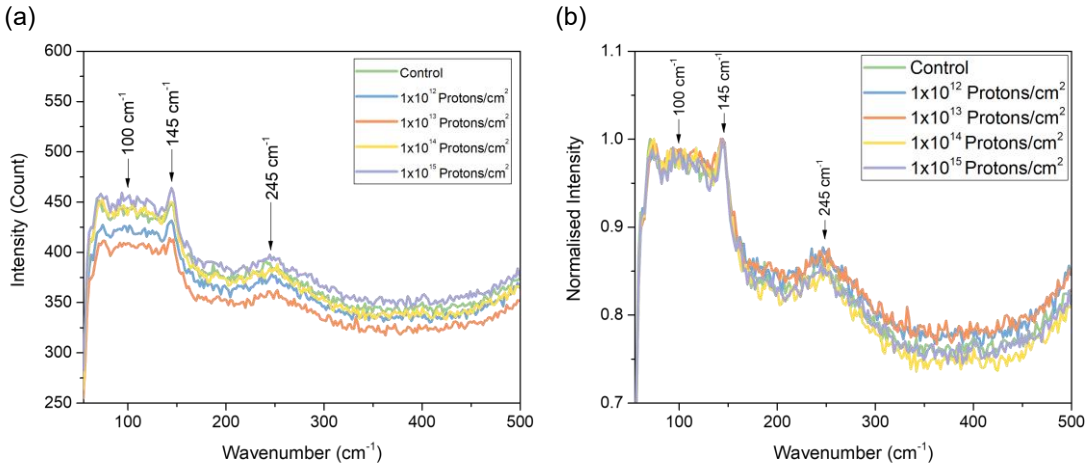

Figure 4.6 a) Raman spectra of perovskite solar cells measured between 50 and 500 cm^{-1} through the glass substrate as a function of proton fluence. b) Normalised Raman spectra of perovskite solar cells measured between 50 and 500 cm^{-1} through the glass substrate as a function of proton fluence.

The first peak being a wide peak at ~100 cm^{-1} is associated with the vibrations of the Pb-I cage.[9] The vibrational modes for PbI_2 are in the vicinity of 96 cm^{-1}, 106 cm^{-1}, and 113 cm^{-1}. The presence of these three modes could explain why the peak at 100cm^{-1} is broad. The second peak is at 145 cm^{-1}, is attributed to the anatase phase of the TiO_2 ETL used in the devices, and the third peak at 245 cm^{-1} is related to a methylammonium (MA) torsional mode.[10] There is no conclusive trend in the Raman peak intensity, which could be due to the mesoporous nature of the device structure. Therefore, it should be more accurate to normalize the Raman spectra to account for the inhomogeneity. The normalised Raman spectra is shown in Figure 4.6b and has been normalized to the peak at 145 cm^{-1}. The spectra at 145 cm^{-1} overlap each other excellently, consistent with no degradation in the TiO_2 chemical structure. There is also no considerable change in the peak position or FWHM at 100

cm^{-1} and 245 cm^{-1}, which is consistent with no degradation on the perovskite structure.

Alongside the Raman measurements, micro-PL mapping of the full device stack before and after the proton irradiation was also measured through the glass substrate. This was an additional method used to look at the stability (regarding to optical properties) and device homogeneity. The PL mapping is shown in Figure B.3 while the averaged PL spectra as a function of proton fluence is shown in Figure 4.7a, with the normalised spectra shown in Figure 4.7b.

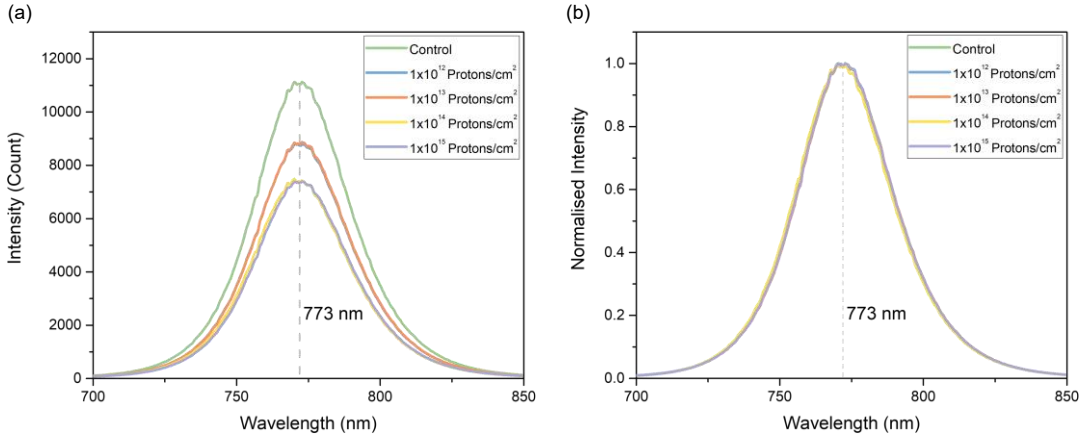

Figure 4.7 a) PL spectra of perovskite solar cells as a function of proton fluence. b) normalised PL spectra of perovskite solar cells as a function of proton fluence.

As shown In Figure 4.7, the PL intensity peak is centred at 773nm which is attributed to the perovskite. The PL signal undergoes a decrease in intensity as a function of proton fluence, however there is an overlap of intensity between $1x10^{12}$ and $1x10^{13}$ protons/cm^2, and $1x10^{14}$ and $1x10^{15}$ protons/cm^2. The $1x10^{14}$ and $1x10^{15}$ protons/cm^2 samples present the lowest PL intensity as compared to the reference sample. However, the decrease in PL intensity as a function of proton fluence is not in agreement with the stability of J-V performance as seen previously. As the mesoporous carbon electrode should block all protons, the decrease in intensity could be due to air/humidity, but not affect the PCE. Another cause could be the variation in homogeneity of the active area and therefore PL intensity. The PL mapping after bombardments (Figure B.3) shows variations in the PL intensity, with a maximum variation of 11,000 counts for the $1x10^{14}$ protons/cm^2 device. To reduce the effect of inhomogeneity, the normalised PL data a function of proton fluences

was compared, as shown in Figure 4.7b, and showed no considerable shift in peak position or change in FWHM. The observed excellent PL spectral overlap is consistent with no considerable degradation of the PL properties, and further suggests that the change in PL intensity is due to the inhomogeneity caused be the mesoporous nature of the active area. The consistency in the normalised PL indicates that there is no change in the optical properties or phase separation in the perovskite as observed for mixed FAMAPb(Br)$_3$ based devices.[11]

While it is strongly suggested that the reduction in the PL intensity as a function of proton fluence is due to the mesoporous active area, PL intensity can be indicative of the quality of the bulk perovskite layer or extraction layer interfaces. Deep trap states formed in the perovskite bulk can induce nonradiative recombination and quench the PL. In full device stacks, defective interfaces of the HTL and ETL, due to degradation, can also quench the PL due to an increase of nonradiative recombination. Taking the assumption that the absorbance is similar across all fluences as they are non-/slightly degraded, the Photoluminescence Quantum Yield (PLQY) can be estimated to investigate the change in the Quasi-Fermi level splitting (QFLS). By estimating the QFLS, the implied changes in the V_{oc} can be calculated as they scale logarithmically on the PLQY. The estimated QFLS from the PL can be calculated using Equation 4.1:

$$QFLS_{PL} = QFLS_{RAD} + K_B T \cdot \ln(PLQY) \tag{4.3}$$

Where $QFLS_{RAD}$ is the radiative QFLS, K_B is the Boltzmann constant, and T is the temperature in Kelvins.[12] Assuming that $QFLS_{RAD}$ is the same or similar for all samples, The change in $QFLS_{PL}$ ($\Delta QFLS_{PL}$) is given by Equation 4.2:

$$\Delta QFLS_{PL} = K_B T \cdot \ln\left(\frac{PLQY_{before}}{PLQY_{after}}\right) \tag{4.4}$$

Approximating the PLQY to the PL intensity, the 43% difference in PL intensity between the control and 1x10^{14} or 1x10^{15} protons/cm^2 sample leads to a $\Delta QFLS_{PL}$ and calculated V_{oc} loss of ~12 meV. Therefore, the estimation of the QFLS shows that the decrease in PL intensity is not contradicting the measured J-V stability.

4.2.4.2 Probing Through the Carbon Electrode

As the active layer was shown to be stable and undergo little to no degradation, the next layer to probe was the mesoporous carbon electrode. The SRIM simulations performed showed that the protons should stop ≤1.5 µm within the electrode, meaning any potential structural changes because of the proton bombardment would most likely occur within the electrode. Illumination was applied to the mesoporous carbon electrode to probe any structural and optical changes in the perovskite embedded within the mesoporous carbon layer at a depth ~2 µm.[13] This perovskite is described as a "capping layer" as it is not within the active area and does not contact the TiO_2 ETL.

Raman mapping was used to investigate any structural changes in the perovskite capping layer and mesoporous carbon electrode. Due to the roughness of the carbon electrode, the non-normalised data was deemed unreliable to draw any conclusions from, so the normalised Raman spectra was used to investigate any changes within the capping perovskite and carbon electrode. The non-normalised data is shown in Figure B.4. The normalised Raman spectra measured through the carbon electrode as a function of proton fluence are shown in Figure 4.8.

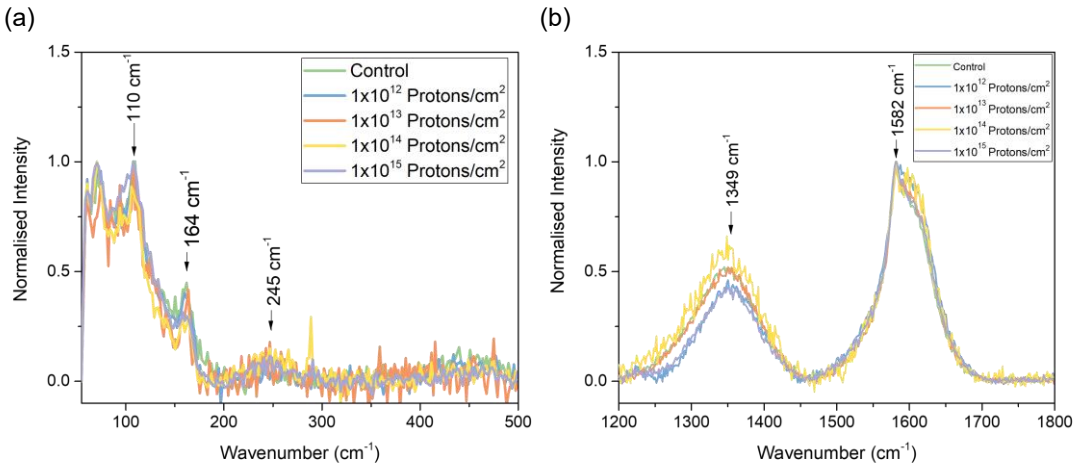

Figure 4.8 Normalised Raman spectra of the perovskite solar cells a) 50 and 500 cm^{-1} as a function of proton fluence b) 1200 and 1750 cm^{-1} as a function of proton fluence.

Figure 4.8a shows the perovskite Raman signal, while Figure 4.8b shows the Raman signal from the mesoporous carbon electrode. In comparison to the Raman measurements taken from the glass side, the overall perovskite Raman signal is weaker due to the increase in light scattering from the meso-porous carbon

electrode. Therefore, it is particularly better to focus on the normalised Raman data. Figure 4.8a has been normalised to the relatively sharp peak at 110 cm^{-1} and there are three observed Raman peaks at 110 cm^{-1} 164 cm^{-1}, 245 cm^{-1} respectively. The peaks at 110 cm^{-1} and 164 cm^{-1} are attributed to the formation of dihydrated MAPI.[14] Both peaks are more prominent with increasing humidity level, indicating the presence of moisture in the capping layer of perovskite. The broad peak at 245 cm^{-1} is again attributed to MA cation torsional modes. For each of the three peaks, however, there is no trend between the relative peak intensity and proton fluence, suggesting that the amount of moisture present in each device is random.

Figure 4.8b shows the normalized Raman intensity in the range of 1200-1750 cm^{-1} where there are two clear peaks at 1349 and 1582 cm^{-1}. These peaks are assigned to the D and G bands of carbon respectively. The D peak is only visible in sp^2 hybridized carbon systems and arises due to the defects in the layer. The more defects that are present in the carbon layer, the higher the Raman intensity of the D-band relative to the G-band.[15][16] The G peak is due to stretching of the C-C bond in graphitic materials which can be used to investigate any modification to the structure and is common to all sp^2 carbon systems. In Figure 4.8b, which has been normalised to the G-band, there is very good overlap at the 1582 cm^{-1} peak. This overlap suggests that there is no considerable change in structure of the carbon because of the proton bombardment. While there is some variation in D-band intensity, there is no trend as a function of proton fluence. Here it is suggested that the variation in the carbon domain size across the samples is responsible for the variation in the measured D intensity. To further support this hypothesis, the intensity ratio of the D (I_G) and G (I_D) peaks was calculated for the control, $1x10^{12}$, and $1x10^{15}$ protons/cm^2 samples and are shown in Figure 4.9. $1x10^{12}$ and $1x10^{15}$ protons/cm^2 samples were chosen to compare any changes between the control and irradiated samples, along with any changes as a function of increasing proton fluence.

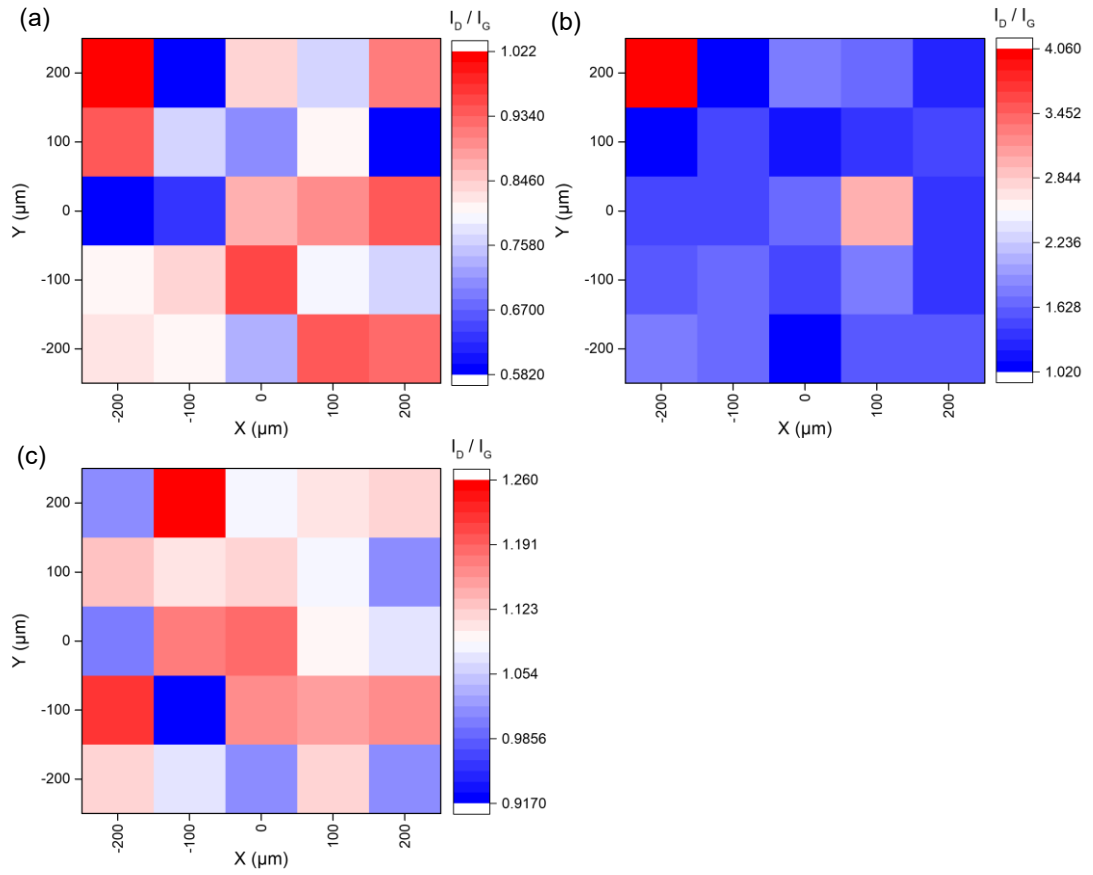

Figure 4.9 Mapped ratio of the Raman intensity of the carbon D and G peaks (I_D/I_G). a) Control device b) 1x10^{12} protons/cm^2 c) 1x10^{15} protons/cm^2.

As seen in Figure 4.9, there is variation in I_D/I_G across the irradiated samples. Across the measurement area (~0.16 mm^2) there is no conclusive trend as a function of proton fluence. The average ID/IG is 0.8, 1.6, and 1.1 for the control, 1x10^{12}, and 1x10^{15} protons/cm^2 samples respectively. The increase in ID/IG for the 1x10^{12} and 1x10^{15} protons/cm2 samples suggests that there is an increase in defects within the carbon electrode because of the proton bombardment. In the case of the 1x10^{12} protons/cm^2 sample, the increase in I_D/I_G could explain the measured decrease in Jsc as the defects could potentially affect the conductivity of the carbon electrode. However, this is not concluded here and would require further work.

Alongside Raman spectroscopy measurements, PL mapping was also performed through the carbon electrode. These measurements were performed alongside the Raman measurements and are therefore from the same 0.16 mm^2 area. The averaged and normalised PL peaks are shown in Figure 4.10 as a function

of proton fluence. The peaks positions are labelled for the normalised PL peaks to show the shift in peak position.

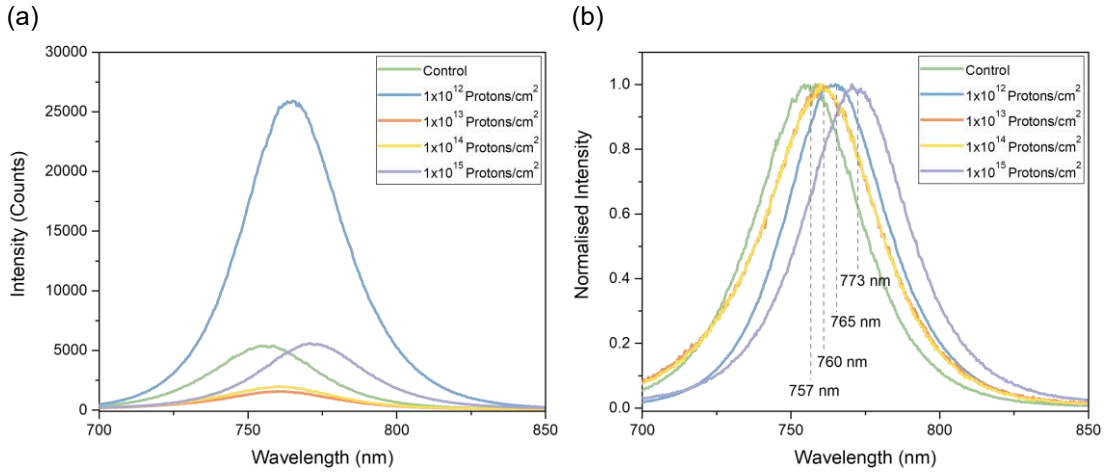

Figure 4.10 a) Averaged PL spectra as a function of proton fluence b) Normalised averaged PL spectra as a function of proton fluence.

In Figure 4.10a, the PL peak for the $1x10^{12}$ protons/cm^2 sample exhibits a ~490% increase in intensity compared with the control device. This increase in PL intensity could be related to the increase in defects within the $1x10^{12}$ protons/cm2 m-CPSC as the poor conductivity of the carbon will lead to increased recombination and reduced charge extraction. There is also a clear shift in peak position between the different samples, which is easier to distinguish using the normalised data shown in Figure 4.10b. Here there is a clear shift in the PL peak wavelength between the samples under different proton fluences and the control sample. In comparison to the PL measurements taken through the glass substrate (Figure 4.7), the control PL peak has a centre value of 757 nm which is blue shifted by 16 nm. The direct cause for the shift in PL position is unknown. Here, it is hypothesised that the blue shift seen here is due to the polydisperse nature of the carbon/perovskite capping layer, with a similar effect having been observed in other work.[17] However, there is also an observed red shift between the control sample and the bombarded devices. The control, $1x10^{12}$, $1x10^{13}$, $1x10^{14}$, and $1x10^{15}$ protons/cm^2 devices have centre values of 757, 765, 760, 760, and 773 nm respectively. The measured change in PL centre value is independent from proton fluence, suggesting that the change is not due to the proton bombardment. However, as the cells are unencapsulated the carbon

electrode and perovskite “capping” layer is in contact with moisture in the air. Moisture induced changes in perovskite has been shown to cause a red shift in the PL peak position.[18] As the perovskite in the “capping” layer is close to the carbon surface, it would encounter more moisture than the more embedded perovskite active area and therefore would exhibit a larger shift in PL peak position. With this hypothesis in mind, the observed shift follows no trend, indicating that the amount of moisture that encounters the perovskite “capping” layer is random and could be related to the formation of the mesoporous structure. Overall, the measured blue-shift of the perovskite PL position through the carbon electrode could be due the counter effect of random variation of polydisperse nature of the layer, and/or the pressence of humidity at the top carbon surface causes a PL red shift in the perovskite “capping“ layer. Furhter work will be needed to investigate this trend. Importantly, the ‘capping’ layer of perovskite/m-carbon is not involved in device functionality, hence the variation in PL intesnity and oberved shift does not affect the PCE of the m-CPSCs.

4.2.5 Electrode Proton Bombardment Simulations

To understand why the perovskite in the meso-carbon devices exhibits superior proton bombardment stability against other device structures using metal electrodes, simulations were performed to compare the proton stopping power of the carbon electrode and compare it to other commonly used metal alternatives. The idea was that the simulations should provide a better understanding of the penetration depth of the proton beam into the materials and how the choice of electrode affects the proton stability. Two different simulation packages were used, the first being The Stopping and Range of Ions in Matter (SRIM) and its sister programme, Transport of Ions in Matter (TRIM). This package was used to calculate the lower proton energy (150 keV) stopping range. The second package used was a self-written python code to solve the Bethe-Bloch equation for the different electrodes across a much wider range of energies as this allows us to assess the stopping power not just for the proton energy used in this experiment but at energies you would also find in LEO.

The electrode materials that were simulated using both SRIM and python were mesoporous carbon, Silver (Ag), Gold (Au), Aluminium (Al) & Copper (Cu).

4.2.5.1 SRIM Target Depth Simulations

Figure 4.11 shows the energy loss at 150 keV, as a function of target depth, for the electrode materials. Here, target depth is a measure of how far into a material a proton will travel before it comes to rest. This is sometimes also called the shield thickness. As we are looking at the energy loss during travel through matter, the results of the SRIM simulation are presented as Bragg curves. As $E_{loss} \propto V^{-2}$, a peak is formed as the protons reach their minimum velocity, which is called the Bragg peak, however due to the low energy in this work they are not well defined as seen in other work looking at higher energies.[19]

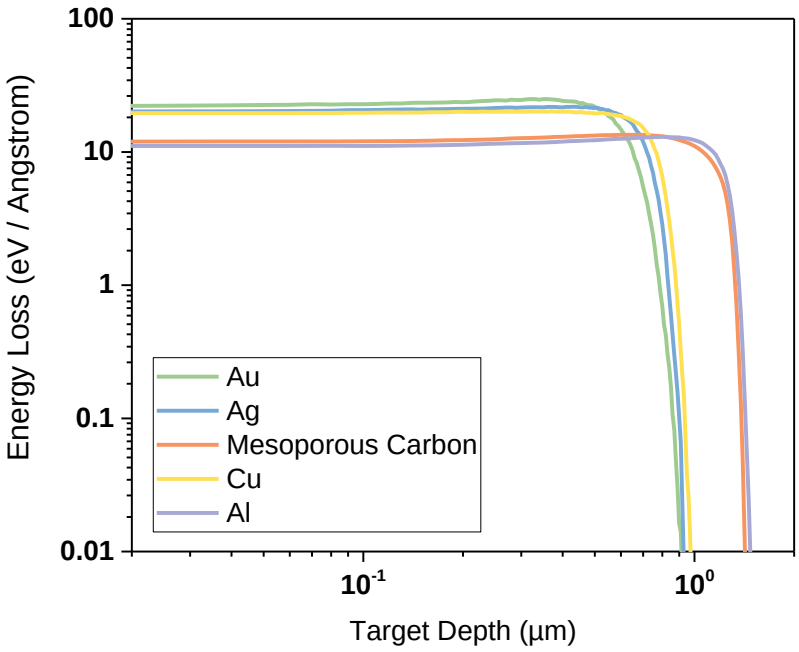

Figure 4.11 Log-log plot of 150 keV proton energy loss due to ionisation in the electrodes as a function of electrode thickness (Target Depth).

From this plot, Au and Ag possess the shortest target depth (highest stopping power) with 150 keV protons, with protons completely stopped at a target depth of ~920 nm and therefore can be regarded as the best metal electrode for stopping 150keV protons from those investigated here. Cu has a simulated target depth of ~980 nm and Al has a depth of ~1.34 µm. For mesoporous carbon, protons stop at a

target depth of ~1.3 µm. At a proton energy of 150 keV, the protons have enough energy to cause ionisation in each of the materials. For example, Comparing Au and mesoporous carbon, the electronic configuration of Au is $[Xe]4f^{14}5d^{10}6s^{1}$ with an ionisation energy of 888 $kJmol^{-1}$, while mesoporous carbon has an electronic configuration of $[He]2s^{2}2p^{2}$ and an ionisation energy of 1086.1 $kJmol^{-1}$. Only considering the ionisation energy, the mesoporous carbon should have a lower target depth in comparison to Au as the incident protons should lose more energy through ionisation. Therefore, from the SRIM simulations, the main cause of the variation in target depth is the density and atomic mass of the different electrodes. Au has a density of 19.3 g/cc, which is 10.7x greater than mesoporous carbon's 1.8 g/cc. Looking at the atomic mass, 1g of Au contains $1.18x10^{26}$ atoms, while 1g of C contains $5.01x10^{22}$ atoms, meaning that there are ~$2.35x10^{3}$ more atoms in the gold electrode than the carbon. This would result in increased proton collisions within the material, resulting in more energy loss through ionisation and a reduced target depth. Although mesoporous carbon has lower proton stopping power than most of the electrodes, the target depth is very similar to that shown in Figure 4.4, meaning that the inclusion of the infiltrated perovskite does not affect the proton stopping power of the carbon electrode. This finding shows that the mesoporous carbon electrode is responsible for the superior proton stability of the devices with 150 keV proton even at 1 x 10^{15} protons/cm^{2}.

A noteable result from the SRIM simulation results is that the mechanisms that lead to the good device performance also play a crucial role in proton radiation stability. For effective electrode conductivity in the m-CPSC architecture, the carbon layer is required to be thick (~12 µm). Therefore, the device design already incorporates impressive proton radiation shielding. On the other hand, for other common metal electrodes simulated here such as Au, the required thickness of the metal to stop the 150 keV protons is ~9.2x thicker than the electrodes used for the planar PSCs in this thesis (~100 nm). The simulations show that a significant increase in the metal thickness could stop the 150keV protons, but it could be challenging, expensive, and time consuming to achieve that thickness using a thermal evaporation approach. However, these simulations only consider a single proton energy, which is

not indicative of the environment found in LEO. Therefore, additional simulations were required to investigate the stopping power over a larger energy range.

4.2.5.2 Bethe-Bloch Stopping Power Simulations

To gain insight on the proton stopping power at higher proton energy, proton stopping power of the electrodes was also simulated up to 100 GeV proton energy. This is because of the wider range of energies that are present in a LEO and beyond, so the stopping power at higher energies would also need to be investigated. This was achieved using the Bethe-Bloch equation to solve the stopping power for each material from 100 keV to 100 GeV. For this package, python simulation code of the Bethe-Bloch equation was self-written and used. The results of this simulation allowed for the calculation of dE/dx, the energy deposited per unit length. From this value the minimum layer thickness to achieve sufficient shielding can be calculated for any given proton energy. SRIM was used previously due to there being caveats at lower energies, which are dicussed later. The derivation is as follows.

Given a particle with charge Z and velocity v that is moving in a medium of constant electron density, a free electron located at a distance *x* in the medium and a perpendicular distance *b* from the charged particles path (impact parameter) will experience a force

$$F = -K_c \frac{Ze^2}{r^2} = |eE| = \left(e\left(E_\perp^2 + E_\parallel^2\right)\right)^{\frac{1}{2}} \quad (4.5)$$

Where K_c is equal to $(1/4\pi\varepsilon_0)^2$, with ε_0 being the permittivity of free space. The distance between the charge particle and the free electron is denoted as r, e is the electron charge, and E is the electric field. The electric field has a transversal and parallel component denoted as $E_\perp + E_\parallel$ respectively. The kinetic energy transfer (T_e) from the proton to the electron is given by Equation 4.6:

$$T_e = K_c \frac{2Z^2e^4}{m_e b^2 v^2} \quad (4.6)$$

Here m_e is the mass of an electron (9.11×10^{-31} kg). Equation 4.6 can be used as the estimate energy transfer to all electrons with the same *b*. If n_e is the electron density, the number of electrons with impact parameter *b* to a differential change *b* + *db*, with

a differential distance *dx* along the incident ion trajectory is $2\pi n_e b$dbdx. Using this term and Equation 4.6, the total energy transfer (energy loss) can be integrated as:

$$-\frac{dE}{dx} = 2\pi T_e n_e b db dx = K_c^2 \frac{4\pi n_e Z^2 e^4}{m_e v^2} \int \left(\frac{db}{b}\right) \tag{4.7}$$

To integrate over b, there are limits that must be put in place. At b = 0 the energy loss must tend towards ∞ due to the 1/*b* term. Therefore, as Equation 4.6 has a $1/b^2$ relation, the minimum impact parameter (b_{min}) gives rise to the maximum kinetic energy (T_{max}). The calculated T_{max} is shown in Equation 4.8:

$$T_{max} = 2m_e v^2 \tag{4.8}$$

$$when\ b_{min} = k_c \frac{Z^2 e^4}{m_e v^2} \tag{4.9}$$

Now considering atomically bound electrons, especially those in the outer orbitals, there is a mean excitation energy (I) that can be defined for each element. This constant is the required T_e to either excite or ionise bound electrons. As electronic stopping occurs through interactions with the electrons via excitation or ionisation, energy transfers with energy less than the ionisation constant are forbidden as electronic stopping will not occur, and nuclear stopping dominates (collisions with nuclei) before the particle stops. Therefore, any impact parameters that would lead to $T_e < I$ will not contribute. This means that there is a maximum *b*, b_{max}, which occurs at $T_e = I$ as shown in Equation 4.10 and is the upper limit of the impact parameter.

$$I = K_c^2 \frac{2Z^2 e^4}{m_e b_{max}^2 v^2} \tag{4.10}$$

$$where\ b_{max} = K_c \frac{Ze^2}{v} \left(\frac{2}{m_e I}\right)^{\frac{1}{2}} \tag{4.11}$$

Using both b_{min} and b_{max} as the limits of the integral in equation 4.7, and applying quantum mechanical corrections, the Bethe-Bloch equation is:

$$-\frac{dE}{dx} = \left(\frac{1}{4\pi\varepsilon_0}\right)^2 \frac{4\pi n_e Z^2 e^4}{m_e v^2} \ln\left[\frac{2m_e v^2}{I(1-\beta^2)}\right] - \beta^2 \tag{4.12}$$

Where dE/dx is the stopping power of a given element and Z being the atomic number of the bombarded material. m_e is the mass of the electron. β is the relativistic velocity ratio (V/c) of the incident protons; n_e is the electron density of the target and I is the mean excitation energy of the bombarded element, which can be calculated empirically via Equation 4.13:

$$I \approx 9.1Z\left(1 + 1.9Z^{-2/3}\right)eV \tag{4.13}$$

V is the velocity of the incident protons and is calculated from the relativistic kinetic energy $K_e = (\gamma - 1)mc^2$, where γ is $1/\sqrt{1 - V^2/c^2}$.

For the electrode materials investigated the mean excitation energy has been found experimentally, so Equation 4.13 is included to complete the derivation but was not used for the simulations. Figure 4.12 shows the stopping power as a function of proton energy derived from the Bethe-Bloch equation for several common metal electrodes in semiconductors and solar cells.

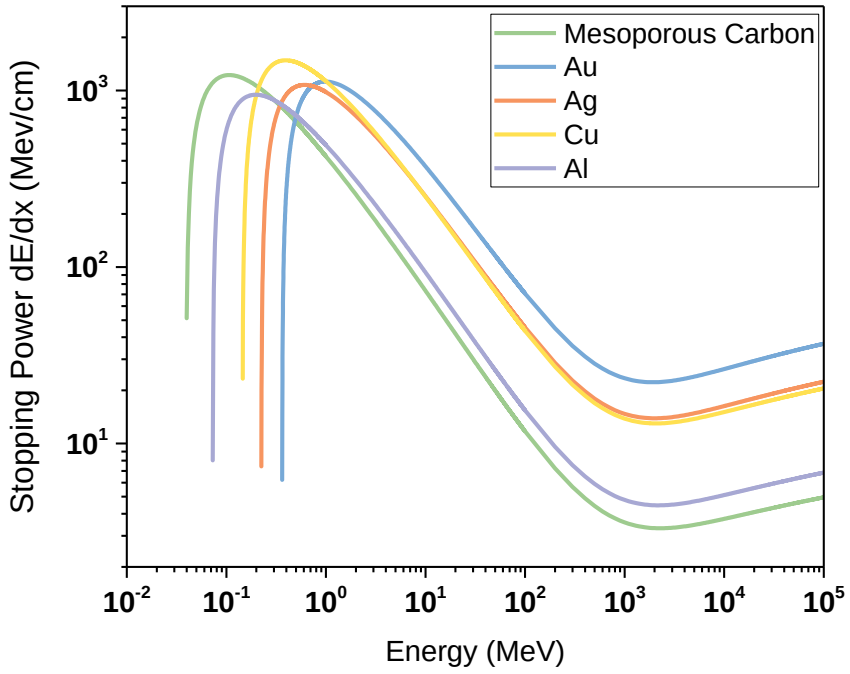

Figure 4.12 Bethe-Bloch calculated proton stopping power as a function of proton energy of different electrode materials.

Equation 4.12, and therefore the line-shape, scales with both Z^2 and V^{-2}. The shift in the peak stopping power is due to the different Z and n_e values for each

element. The maximum energy loss is when the incident proton energy is sufficient that electronic stopping dominates over nuclear stopping, and is the dominant energy loss mechanism. As the proton energy, and therefore velocity increases, the V^{-2} term dominates and causes as decrease in stopping power. This decrease reaches a minium value at β~0.96 before the logarithmic term begins to dominate and the stopping power begins to increase before plateauing at β=1 (V=c). Comparing the Bethe-Bloch simulations results to SRIM's, at 150 keV the mesoporous-carbon has a stopping power of 1166 MeV/cm. Therefore, a layer with a thickness of at least of 1.29 µm will stop the incident protons. This is in agreement with SRIM, including the similarity in stopping power between Al and mesoporous carbon for proton energies <1 MeV. However, when looking at higher energy levels >200 keV, the stopping power of mesoporous carbon is much lower that of Cu, Ag, and Au. At a protons energy of 10 MeV, the stopping power of mesoporous carbon is 73.40 MeV/cm. This means a layer thickness of at least 1.36 mm is needed. For Au, the required layer thickness is 269 µm. Both Ag and Cu have a similar stopping power of 251.84 and 250.45 MeV/cm respectively. This results in a Ag and Cu layer thickness of 396 and 399 µm respectively. In LEO, protons with energy 10 Mev are present in the Van Allen Belt with a flux of $3.96x10^{12}$ protons/cm^2/year.[20] For protons with energy 150 keV, the proton flux is ~$3.154x10^{11}$ protons/cm2/year, meaning that a fluence of $1x10^{15}$ protons/cm^2 is ~10,000 years in LEO.[21] Therefore, a mesoporous carbon layer needs to be ~5x thicker than that of an Au layer and ~3.4x thicker than a Ag and Cu layer. However, this raises another topic of consideration, the viability of evaporating metal electrodes with a layer thickness of ≥269 µm compared with printing a 1.36mm mesoporous carbon layer.

It is worth noting that while the Bethe-Bloch equation allows for simulations of a much larger energy range, there are shortcomings. These are more apparent when looking at energies <1 MeV for different materials. Here it is clear that the stopping power diverges to 0 as the proton energy tends towards 100 keV. This decrease is due to the Bethe-Bloch equation having a lower band cut-off energy parameter, whose value depends on the material being bombarded. The physical meaning behind this parameter is related to the minimum ionisation threshold energy, as the Bethe-Bloch equation assumes the protons are always ionised. There

are two solutions to solve this and improve the package, and they are to use the Lindhard-Scharff approximation or empirical data. The issue of using empirical data is that for compunds such as MAPI-AVA, there has been no investigation into the mean excitation energy and thus there is no empirical data to work from. This means that the version of Equation 4.13 designed for compounds will need to be used, which adds a layer of discrepency. This is given via:

$$I_{compound} \approx exp\left(\frac{1}{n}\sum_{i} n_i Z_i \ln I_i\right) \tag{4.14}$$

Where n is the total number of electrons per unit volume, n_i is the electron density of material i, Zi is the atomic number of material i, and I_i is the mean excitation energy of material i. The first solution considers the use of the Lindhard-Scharff-Schiøtt (LSS) approximation, which considers much lower ion energies (~1-90 keV) and therefore nuclear stopping interactions.[22] When considering the case of proton bombardment, the LSS approximation can written in the form:

$$S = 8\pi e^2 a_0 N \frac{Z_2}{\left(1 + Z_2^{2/3}\right)^{3/2}}\left(\frac{V_P}{V_0}\right) \tag{4.15}$$

Where a_0 and V_0 are the Bohr radius ($5.29\text{x}10^{-11}$ m) and Bohr velocity ($2.18\text{x}10^{6}$ m/s) respectively. V_p is the proton velocity and N is the electronic number density. In the LSS region, the stopping power is proportional to the incident proton velocity. As nuclear stopping and therefore LLS dominates at lower energies, the protons are non-relativistic ($\beta << c$) which gives the stopping-energy relationship $S \propto V \propto E^{1/2}$.

Due to the complexity of combining LSS with Bethe-Bloch, the approximation was not used in this work; however, other publications regarding attenuation of charge particles and ion implantation in different mediums have fully assessed the stopping power across a range of energies.[23] Additionally, an open-source database comprised by the National Institute of Standards and Technology (NIST) allows for the simulation of proton bombardment into a variety of different elements for a range of energies through their PSTAR tool.[24] These simulations use both empirical data and the full LSS + Bethe-Bloch + modifications for the results. These modifications are the shell-corrections, the Barkas correction, and the density-effect

correction.[25-27] However, NIST calculates what is referred to as the mass-stopping power of an element rather than stopping power defined previously. The mass-stopping-power is the density independent stopping power. This version of stopping power uses units of MeV•cm^2•g^{-1} and is calculated via:

$$\frac{S}{\rho} = -\frac{1}{\rho}\frac{dE}{dx} \tag{4.16}$$

Where S is the stopping power, ρ is the density of the target material and S/ρ is the mass-stopping-power. The reason for using the mass-stopping power is that when a substance is compared in gaseous and solid form, the stopping powers of the two states are very different due to the different densities. Therefore, dividing the stopping power (MeV/cm) by the density (g/cm^3) of the material to obtain the mass stopping power (MeVcm^2/g) means that the result depends only very little on the density of the material. The results from the PSTAR simulation are shown in Figure 4.13 and further shows the proton stopping power of mesoporous carbon. The mass stopping power line shape follows the same trend as the stopping power, however the stopping power no longer diverges to 0 at longer energy values as the nuclear stopping contribution has been included.

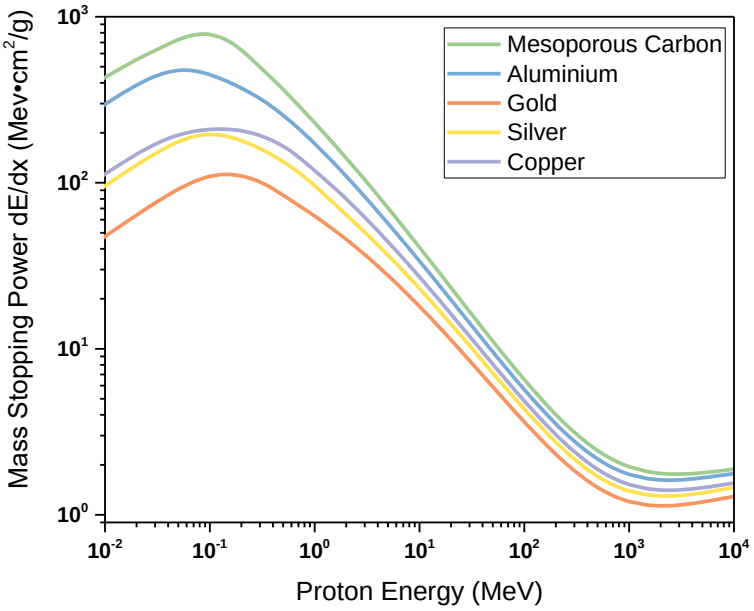

Figure 4.13 Plot of mass-stopping poweras a function of proton energy for different metal electrodes compared against mesoporous carbon. This was plotted using open source data from PSTAR.[24]

In Figure 4.13, it is shown that mesoporous carbon possess the highest mass stopping power out of all the materials simulated, with Au exhibiting the lowest. This shows that for the results in Figure 4.12, the high stopping power of Au is due to its higher density compared to the other electrode materials. Incidentally, it also suggests that a compact carbon layer would provide better proton stopping power than the mesoporous electrode due to the increase in density (ρ ~ 2.2 g/cc). The variation in mass stopping power between Cu and Ag is small, which is also seen in Figure 4.12. Therefore, Ag and Cu electrodes appear to offer similar proton stopping power. Overall, the simulations further supports the notion that a compact or mesoporous carbon electrode has potential in space applications due to the simulated high stopping power under proton bombardment.

4.3 Conclusion

This chapter finds that screen-printed perovskite solar cells with a mesoporous carbon electrode have a very high tolerance to 150 keV proton irradiation, even up to a proton fluence of $1x10^{15}$ protons/cm^2. Using SRIM, it was found that the bulk number of incident protons will stop within the carbon electrode at a target depth of ~1.27 µm. It is shown through remaining factor values that the m-CPSCs exhibit a high tolerance to 150 keV proton radiation, up to a fluence of $1x10^{15}$ protons/cm^2 which is equal to 10,000 years in LEO. In comparison, Si and GaAs solar cells are known to be destroyed or highly deteriorated at this proton energy and fluence. Proton fluences ≥$1x10^{14}$ protons/cm^2 have also been shown to degrade the Spiro-OMeTAD HTL in planar PSCs.

To investigate any changes in the structure or optical properties of the active area and carbon electrode, Raman spectroscopy and PL measurements were performed. PL measurements through the glass substrate were consistent with no phase separation of the perovskite, and the Raman shows no considerable degradation of the perovskite embedded in the mesoporous and compact TiO_2 layer. An estimate of the QFLS showed that the 49% increase in PL intensity at $1x10^{12}$ protons/cm^2 compared to the control sample only results in a 12 meV difference in Voc. Raman spectroscopy of the carbon electrode showed the formation of dihydrated MAPI with peaks at 110 and 164 cm^{-1}. The carbon G-peak position

remains unchanged as a function of proton fluence, indicating no change in the chemical structure of the carbon electrode. The ratio of the carbon D and G peaks (I_D/I_G) showed that the variation in the D peaks varies across devices and the measurement area, indicating the variation in D-peak intensity is due to the mesoporous nature of the carbon electrode. Additionally, I_D/I_G was much higher in the $1x10^{12}$ protons/cm^2 device, indicating an increase in defects in the carbon which could be the cause in the decrease Jsc and increased PL intensity. This will need to be investigated in future work. PL measurements taken from the carbon electrode showed a significant blue and red shift in PL peak values across fluences. The shift is attributed to the competing mechanisms of moisture ingress into the perovskite "capping" layer and the polydisperse nature of the perovskite. Importantly, the presence of moisture does not affect the device performance as the degraded region is not within the PV active area. This strongly indicates that the devices would be stable when in storage before a payload launch.

SRIM and Bethe-Bloch simulations showed that the origin of the superior proton stability is due to the thickness of the carbon electrode rather than the proton stopping power of the material itself. Data analysis of PSTAR simulations showed that of the electrodes considered, mesoporous carbon exhibits the highest mass stopping power. This suggests that a compact carbon electrode would provide better proton stopping power over a mesoporous one due to the increased density. However, this would need to be confirmed experimentally in further work.

Overall, the findings of this chapter show that m-PSCs possess high radiation stability and could have attractive potential for space applications. However, there are still issues to overcome for m-CPSCs before they can begin to be considered as a replacement for the currently used PV technology. Issues such as lower PCE compared to planar PSCs and the increased difficulty of fabrication on flexible substrates due to the high temperature (~500 °C) fabrication processes limit m-CPSCs specific power.

References

[1] Hughes, D., Meroni, S.M.P., Barbé, J., Raptis, D., Lee, H.K.H., Heasman, K.C., Lang, F., Watson, T.M. and Tsoi, W.C. (2021), Proton Radiation Hardness of Perovskite Solar Cells Utilizing a Mesoporous Carbon Electrode. Energy Technol., 9: 2100928. https://doi.org/10.1002/ente.202100928

[2] Tong, C., Ji, W., Li, D., Mei, A., Hu, Y., Rong, Y., Han, H. (2019). Modeling the edge effect for measuring the performance of mesoscopic solar cells with shading masks. Journal of Materials Chemistry A, 7(18), 10942–10948. https://doi.org/10.1039/c9ta02459j

[3] Meroni, S. M., Worsley, C., Raptis, D., Watson, T. M. (2021). Triple-mesoscopic carbon perovskite solar cells: Materials, processing, and applications. Energies, 14(2), 386. https://doi.org/10.3390/en14020386

[4] Raptis, D., Stoichkov, V., Meroni, S. M. P., Pockett, A., Worsley, C. A., Carnie, M., Worsley, D. A., Watson, T. (2020). Enhancing fully printable mesoscopic perovskite solar cell performance using integrated metallic grids to improve carbon electrode conductivity. Current Applied Physics, 20(5), 619–627. https://doi.org/10.1016/j.cap.2020.02.009

[5] Miyazawa, Y., Ikegami, M., Miyasaka, T., Ohshima, T., Imaizumi, M., Hirose, K. (2015). Evaluation of radiation tolerance of perovskite solar cell for use in space. 2015 IEEE 42nd Photovoltaic Specialist Conference (PVSC). https://doi.org/10.1109/pvsc.2015.7355859

[6] Burgess, R. M., Chen, W. S., Devaney, W. E., Doyle, D. H., Kim, N. P., Stanbery, B. J. (1988). Electron and proton radiation effects on gaas and Cuinse/sub 2/ thin film solar cells. Conference Record of the Twentieth IEEE Photovoltaic Specialists Conference. https://doi.org/10.1109/pvsc.1988.105835

[7] Li, S. S., Weng-Lyang, W., Pan-Wei, L., Loo, R. Y., Kamath, G. S., Knechtli, R. C. (1980). Deep-level defects, recombination mechanisms, and their correlation to the performance of low-energy proton-irradiated algaas—gaas solar cells. IEEE Transactions on Electron Devices, 27(4), 857–864. https://doi.org/10.1109/t-ed.1980.19947

[8] Malinkiewicz, O., Imaizumi, M., Sapkota, S. B., Ohshima, T., Öz, S. (2020). Radiation effects on the performance of flexible perovskite solar cells for space applications. Emergent Materials, 3(1), 9–14. https://doi.org/10.1007/s42247-020-00071-8

[9] Pistor, P., Ruiz, A., Cabot, A. et al. Advanced Raman Spectroscopy of Methylammonium Lead Iodide: Development of a Non-destructive Characterisation Methodology. Sci Rep 6, 35973 (2016). https://doi.org/10.1038/srep35973

[10] Pérez-Osorio, M. A., Lin, Q., Phillips, R. T., Milot, R. L., Herz, L. M., Johnston, M. B., Giustino, F. (2018). Raman spectrum of the organic–inorganic halide perovskite $CH_3NH_3PbI_3$ From first principles and high-resolution low-temperature Raman measurements. The Journal of Physical Chemistry C, 122(38), 21703–21717. https://doi.org/10.1021/acs.jpcc.8b04669

[11] Miyazawa, Y., Ikegami, M., Chen, H.-W., Ohshima, T., Imaizumi, M., Hirose, K., Miyasaka, T. (2018). Tolerance of perovskite solar cell to high-energy particle irradiations in space environment. IScience, 2, 148–155. https://doi.org/10.1016/j.isci.2018.03.020

[12] Caprioglio, P., Stolterfoht, M., Wolff, C. M., Unold, T., Rech, B., Albrecht, S., Neher, D., On the Relation between the Open-Circuit Voltage and Quasi-Fermi Level Splitting in Efficient Perovskite Solar Cells. Adv. Energy Mater. 2019, 9, 1901631. https://doi.org/10.1002/aenm.201901631

[13] Hooper, K. E., Lee, H. K., Newman, M. J., Meroni, S., Baker, J., Watson, T. M., Tsoi, W. C. (2017). Probing the degradation and homogeneity of embedded perovskite semiconducting layers in photovoltaic devices by Raman spectroscopy. Physical Chemistry Chemical Physics, 19(7), 5246–5253. https://doi.org/10.1039/c6cp05123e

[14] Lakhiani, H., Dunlop, T., De Rossi, F., Dimitrov, S., Kerremans, R., Charbonneau, C., Watson, T., Barbé, J., Tsoi, W. C. (2019). Variations of infiltration and electronic contact in mesoscopic perovskite solar cells revealed by high‐Resolution Multi‐mapping techniques. Advanced Functional Materials, 29(25), 1900885. https://doi.org/10.1002/adfm.201900885

[15] Pistor, P., Ruiz, A., Cabot, A., Izquierdo-Roca, V. (2016). Advanced raman spectroscopy of methylammonium lead iodide: Development of a non-destructive characterisation methodology. Scientific Reports, 6(1). https://doi.org/10.1038/srep35973

[16] Ferrari, A. C., & Robertson, J. (2004). Raman spectroscopy of amorphous, nanostructured, diamond–like carbon, and Nanodiamond. Philosophical Transactions of the Royal Society of London. Series A: Mathematical, Physical and Engineering Sciences, 362(1824), 2477–2512. https://doi.org/10.1098/rsta.2004.1452

[17] Sara Bonabi Naghadeh, Som Sarang, Amanda Brewer, A'Lester Allen, Yi-Hsuan Chiu, Yung-Jung Hsu, Jhen-Yang Wu, Sayantani Ghosh, and Jin Z. Zhang , "Size and temperature dependence of photoluminescence of hybrid perovskite nanocrystals", J. Chem. Phys. 151, 154705 (2019) https://doi.org/10.1063/1.5124025

[18] Howard, J. M., Tennyson, E. M., Barik, S., Szostak, R., Waks, E., Toney, M. F., Nogueira, A. F., Neves, B. R., Leite, M. S. (2018). Humidity-induced photoluminescence hysteresis in variable CS/Br Ratio Hybrid perovskites. The Journal of Physical Chemistry Letters, 9(12), 3463–3469. https://doi.org/10.1021/acs.jpclett.8b01357

[19] Lee, H.K.H., Stewart, K., Hughes, D., Barbé, J., Pockett, A., Kilbride, R.C., Heasman, K.C., Wei, Z., Watson, T.M., Carnie, M.J., Kim, J. and Tsoi, W.C. (2022), Proton Radiation Hardness of Organic Photovoltaics: An In-Depth Study. Sol. RRL, 6: 2101037. https://doi.org/10.1002/solr.202101037

[20] Selesnick, R.S., Young, S., & Winter, L.M. (2015). Estimating Solar Proton Flux at LEO From a Geomagnetic Cutoff Model. Air Force Research Laboratory Report found at https://apps.dtic.mil/sti/pdfs/AD1045883.pdf

[21] Logan, J. V., Short, M. P., Webster, P. T., Morath, C. P., Steenbergen, E. H. (2019). Impact of proton-induced transmutation doping in semiconductors for space applications. Journal of Materials Chemistry C, 7(29), 8905–8914. https://doi.org/10.1039/c9tc02995h

[22] Kraan, A. C. (2015). Range verification methods in particle therapy: Underlying physics and Monte Carlo Modeling. Frontiers in Oncology, 5. https://doi.org/10.3389/fonc.2015.00150

[23] Ziegler, J. F., Biersack, J. P. (1985). The stopping and range of ions in matter. Treatise on Heavy-Ion Science, 93–129. https://doi.org/10.1007/978-1-4615-8103-1_3

[24] NIST, Stopping Power and Range Tables For Protons. Physical Measurement Laboratory. Retrieved August 7, 2021, from https://physics.nist.gov/PhysRefData/Star/Text/PSTAR.html

[25] Matveev, V.I., Makarov, D.N. Nonperturbative shell correction to the Bethe-Bloch formula for the energy losses of fast charged particles. Jetp Lett. 94, 1 (2011). https://doi.org/10.1134/S0021364011130133

[26] L. E. Porter and Hong Lin , "Methods of calculating the Barkas‐effect correction to Bethe‐Bloch stopping power", Journal of Applied Physics 67, 6613-6620 (1990) https://doi.org/10.1063/1.345094

[27] R.M. Sternheimer, M.J. Berger, S.M. Seltzer, Density effect for the ionization loss of charged particles in various substances, Atomic Data and Nuclear Data Tables, Volume 30, Issue 2, 1984, Pages 261-271, ISSN 0092-640X, https://doi.org/10.1016/0092-640X(84)90002-0.

Chapter 5

Temperature Stability of Perovskite Solar Cells Under Mimic Low Earth Orbit Thermal Conditions

5.1 Introduction

As detailed in Section 1.3, the external conditions found in space and in a LEO pose a variety of different problems when looking at the continued performance of perovskite solar cells. One such conditions is the varying temperature that orbiting bodies experience. This temperature variation can be affected by the distance from the sun, period of orbit and the orbital altitude. Objects in direct sunlight are hotter due to the increase in solar radiation, often resulting in the need for heat shields to reduce the temperature of onboard systems. One such example is the James Webb Telescope that has 5 layers of heat shields to protect the telescope equipment.[1] As space solar requires direct sunlight to operate at maximum efficiency, the solar cells used in space arrays need to be thermally stable, otherwise they will degrade during optimal performance conditions. Current PV technology used in space applications, such as Si and III-V are inorganic and are thermally stable.[2] However, as PSCs are an organic-inorganic hybrid with organic/inorganic extraction layers, the thermally stability is a concern for lifetime operations such as CubeSats which can have an operational lifetime of >8 years.

This chapter looks at the thermal stability of the PSCs used throughout this thesis, including the use of characterisation techniques such as Raman spectroscopy and photoluminescence spectroscopy. It is presented that the limiting factor to thermally stable PSCs is the inclusion of the spiro-OMeTAD HTL, specifically the dopants used, and an alternative HTL is suggested in the form of P3HT.

5.1.1 Low Earth Orbit Thermal Conditions

As discussed in Section 1.2.2, the temperature range within the Earth's atmosphere increases with altitude above the Kármán Line, with the only heat coming from solar irradiation in the form of photons. This means that heat transfer through conduction or convection is normally impossible. Therefore, most objects can only release energy through emitting infrared radiation. The overall temperature of an object is when it is at thermal equilibrium between the solar irradiation heating and radiative heat transfer. When a satellite orbits an object, it will enter the objects shadow. This result in thermal cycles as the incident solar radiation decreases as the objects enter the objects shadow, before increasing again when it exits the shadow.[3]

Due to LEO satellites having an orbital period faster than GSO, they experience an increased number of thermal cycles, in which the temperature increases and decreases between two values. For example, the ISS completes a full orbital period every 90 minutes, resulting in 16 temperature cycles.[4] From -100 to +100 °C, this requires a thermal ramp of 4.4 °C/min. One example of a LEO application that is gaining increased attention is CubeSats, such as StarLink™.[5] The measured temperature range for a CubeSat in LEO is -70 < T < 80 °C.[6] The difference in temperature ranges between CubeSats and the ISS is due to the difference in size, with the ISS being bombarded with more photons. Taking boundary limits around this measure range to encompass most LEO applications, the thermal cycling range was chosen to be -100 < T < 85 °C. This temperature range also encompasses the analytical temperature range for the ISS (-100 < T < +78 °C).[6] The range is analytical as there are no temperature readings for the solar cells onboard the ISS and therefore needs to be calculated. For the ramp rate, to maximise time efficiency with measurements, a value of 30 °C/min was chosen. This ramp speed is equivalent to 1 cycle every ~12 minutes for the chosen range. Comparing to LEO, this equates to 10 cycles every 2 hours which is equivalent to 120 cycles per day.

5.2 Results and Discussions

5.2.1 NIP Perovskite Solar Cells

5.2.1.1 J-V Performance Under Mimic LEO Conditions

Using the thermal measurement set-up shown in Chapter 2, the planar PSCs with the device stack of Glass/ITO/SnO_2/$Cs_{0.05}(FA_{0.87}MA_{0.13})Pb(I_{0.83}Br_{0.13})_3$/Spiro-OMeTAD/Au with glass-on-glass encapsulation were thermal cycled between -100 and +85°C under vacuum. The vacuum pressure was $1x10^{-2}$ mbar ($1x10^{-5}$ bar). During the thermal cycle, the devices were measured for the first 2 cycles and then measured during the last cycle. This allowed for an investigation into any early performance changes, and to investigate the long-term stability of the devices. During measurements, the cells were illuminated at 1 Sun AM0 for 2.5 minutes before running the JV measurement to simulate being in LEO. The normalised results of 10 thermal cycles are shown in Figure 5.1. Here the thermal cycling data for a m-CPSC as seen in Chapter 4 is also included.

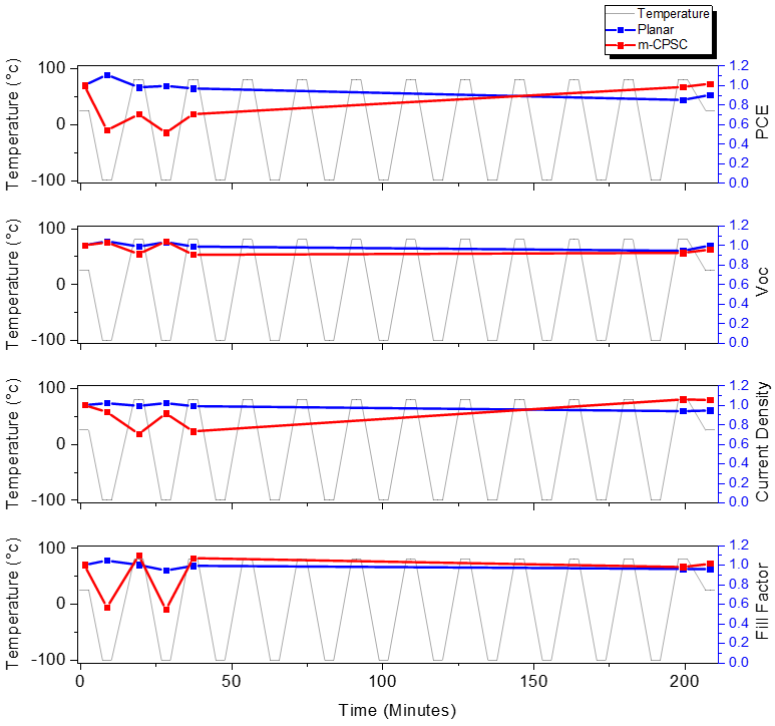

Figure 5.1 Normalised 1 Sun AM0 PV parameters under thermal cycling (-100 <-> +85) °C for a PSC with a spiro-OMeTAD HTL, and a m-CPSC.

Comparing the initial and final measurements after 10 cycles, the PCE of the m-CPSCs increases by 1.7% overall after the thermal cycling. This further showcases the superior stability of the m-CPSC compared to other perovskite architectures. The increase in PCE is due to a 100% retention of FF after cycling, and a 5% absolute increase in the J_{sc}. However, there is a 4% absolute decrease in the V_{oc}. In comparison, the planar PSCs undergoes a 10% absolute decrease from 13% to 11.7% at 25 °C. This decrease in PCE is due to a 6% decrease in Jsc from 22.89 to 21.63 $mAcm^{-2}$, and a 4% decrease in FF from 0.51 to 0.49. The V_{oc} remains stable with a 0.3% decrease after 10 cycles, with a value of 1.08 V. These results showcase the thermal stability of the m-CPSCs, but also a limitation in the planar devices. In the literature, Tumen-Ulzii et al. observed an 80-90% decrease in PSCs using spiro-OMeTAD after ~15 hours of device heating at 85 °C.[8] This is equivalent to a time of 900 minutes of thermal heating (90 cycles), with a linear decrease in PCE observed. Using a linear line of best fit ($y = mx + c$), the calculated time taken for the PCE in Figure 5.1 to decrease to 80% of its initial value (T_{80}) is 301.5 minutes which is equivalent to 15 cycles. From the linear fitting, at T_{80}, the FF, J_{sc}, and V_{oc} will be 0.48, 20.8 $mAcm^{-2}$, and 1.04 V respectively. Using the equivalency that the cycles performed here are 5x faster than those experienced by an object in LEO, then the T_{80} time is equivalent to 1 days in LEO. The average lifetime of a LEO satellite is 8 years, meaning that the spiro-OMeTAD cells degraded by 20% in ~ 0.0003% of a LEO satellites orbital lifetime when looking at T_{80}.[9] For a CubeSat, the average lifetime is 1 year, therefore the spiro-OMeTAD cells reach T_{80} in ~0.003% of a CubeSats lifetime. However, extrapolating from the work of Tumen-Ulzii et al, the decrease in device performance is unlikely to be directly proportional to cycle number, but the time spent at the high temperature limit.

In the literature, the decrease in performance for spiro-OMeTAD HTL PSCs has been attributed to the high temperature instability of the organic HTL.[10-14] To further assess how temperature impacts the J-V performance of PSCs utilising a spiro-OMeTAD HTL, PSCs were cycled between 25 °C (room temperature) and increasing or decreasing temperature steps up to ±180 °C. This larger range was chosen to understand how the high and low temperature cycling components impact device stability, and to find the temperature limit for efficient device performance for future

space missions. The PCE stability of a planar PSC cycled between 25 °C and -100 °C in 10 °C steps up is shown in Figure 5.2a. The PCE stability cycled between 25 °C and -180 °C in 10 °C steps is shown in Figure 5.2b. The V_{oc}, FF, and J_{sc} results are shown in Appendix C.

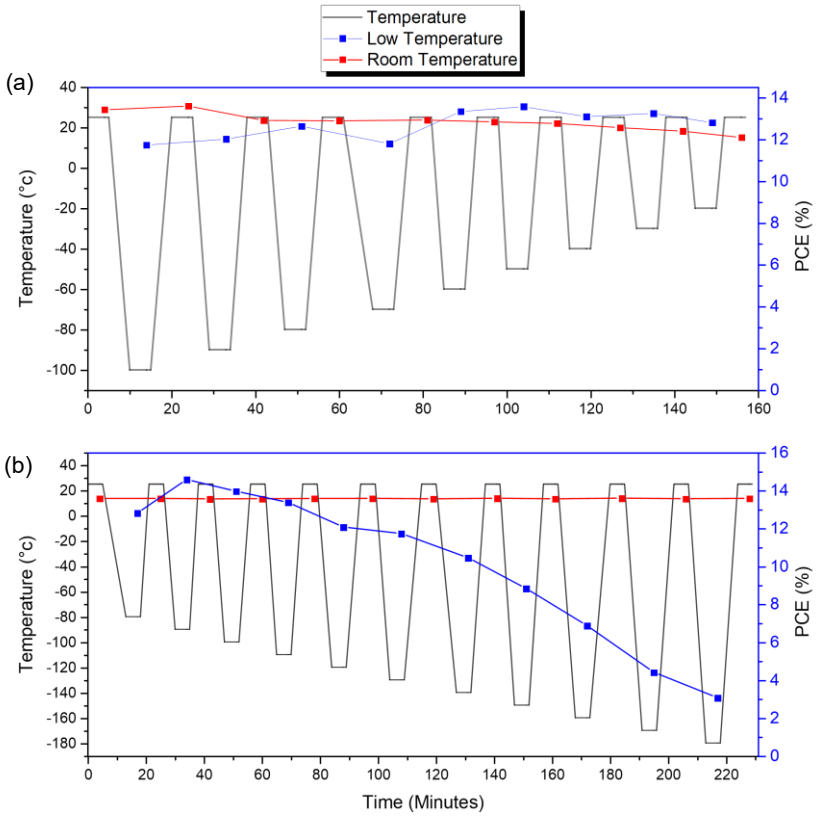

Figure 5.2 a) 1 Sun AM0 PCE as a function of temperature stepping for room and low temperatures (≥-100 °C) b) 1 Sun AM0 PCE as a function of temperature stepping for room and very low temperatures (≥-180 °C).

The low temperature cycling was performed to investigate any performance degradation that may occur during the cycling such as strain on the perovskite, physical or phase changes, and possibly thermal tension (shock). From Figure 5.2a, when the PSC is stepped between -100 °C and 25 °C, at -100 °C the PCE is ~87% of the initial value (11.73%). When the PSC was returned to 25 °C after the -100 °C measurement, the PCE was ~101% of the initial value and suggests that the degradation in device performance due to low temperature testing is reversible. At the final 25 °C measurement, which is -20 °C back to 25 °C, the PCE is ~90% of the initial room temperature value. This decrease is due to a 9% decrease in Voc, and 6% decrease in Jsc. The overall decrease in PCE at room temperature is suggested to be

the result of accumulated cycling, which increases the tensile strain on the perovskite. The reversibility of low temperature degradation is more apparent when looking at Figure 5.2b where the temperature range is increased. Here the devices were cycled between room temperature and incrementally lower temperatures to a minimum of -180 °C. When the devices were returned to room temperature the PCE remains stable with 100% PCE retention across all cycles. When comparing the change in performance at the different cold temperatures, there is a decrease in PCE from temperature ≤-110 °C. The most notable decrease in performance because of the decreasing temperature is the J-V performance difference between -180 °C and 25 °C. This decrease is due to a ~57% reduction in FF, with the V_{oc} and Jsc both decreasing by 15% and 36%, respectively (Appendix C). The J-V curves as a function of temperature are shown in Figure 5.3.

Here J-V curves show an increase in J_{sc} for the -100 and -120 °C measurement. However, as the temperature continues to lower the Voc begins to decrease. While the V_{oc} decreases with decreasing temperature, the Jsc increases at -120 and -150 °C when compared to 25 °C. This behaviour in the V_{oc} and J_{sc} has also been observed under HAPS conditions.[15] In Barbe at al., the decrease in V_{oc} is attributed to a decrease in the shunt resistance and variations in the perovskite band-gap.[15] It has also been shown in the literature that the perovskite active layer undergoes a phase change at ~-111 °C.[16] This phase change results in the formation of carrier traps within the perovskite that reduce charge extraction.[17] Therefore, the large (~36%) decrease in J_{sc} correlates well to the observed reduced charge extraction properties of the Spiro-OMeTAD layer in the literature with decreasing temperature and the formation of carrier traps within the perovskite, which is responsible for the large (~57%) decrease in FF.[18] Little to no work has been published looking at Si and GaAs solar cell performance under the temperatures investigated here (<-150 °C). However, around 100 k (-173.15 °C) there is carrier freeze-out in silicon.[19] This is a phenomenon where at very low temperatures the electrons do not have enough energy to jump to the conduction band and are bound to their donors. Therefore, it can be assumed that at -180 °C (93.15 K) Si PV will also exhibit low performance.

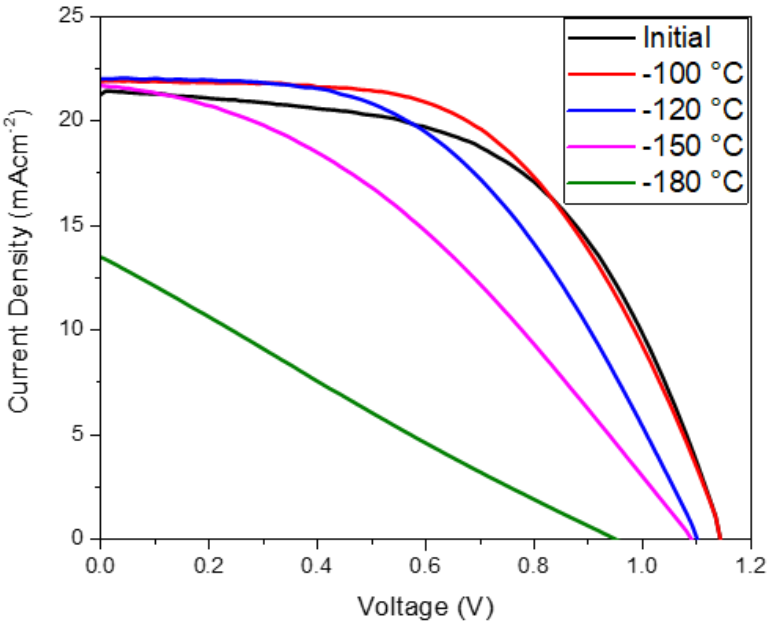

Figure 5.3 J-V curves as a function of temperature for the low temperature stepping shown in Figure 5.2b.

From the low temperature stepping results, it is apparent that the thermal stress the devices experience because of the temperature cycling from cold to room temperature does not affect performance. This is also important for LEO applications as the PSCs will need to be stable at low temperatures. However, further work will be needed to investigate the Low Intensity Low Temperature (LILT) performance of perovskite solar cells for their adaptation into deep space missions. The next step was to assess the high temperature stability. This stability is more important as this corresponds to when the PSCs are in direct sunlight and in operation. The PCE stability of a PSC cycled between 25 °C and 80 °C in 10 °C steps is shown in Figure 5.4a. The PCE stability cycled between 25 °C and 180 °C in 10 °C steps is shown in Figure 5.4b. The V_{oc}, FF, and J_{sc} results are shown in Appendix C.

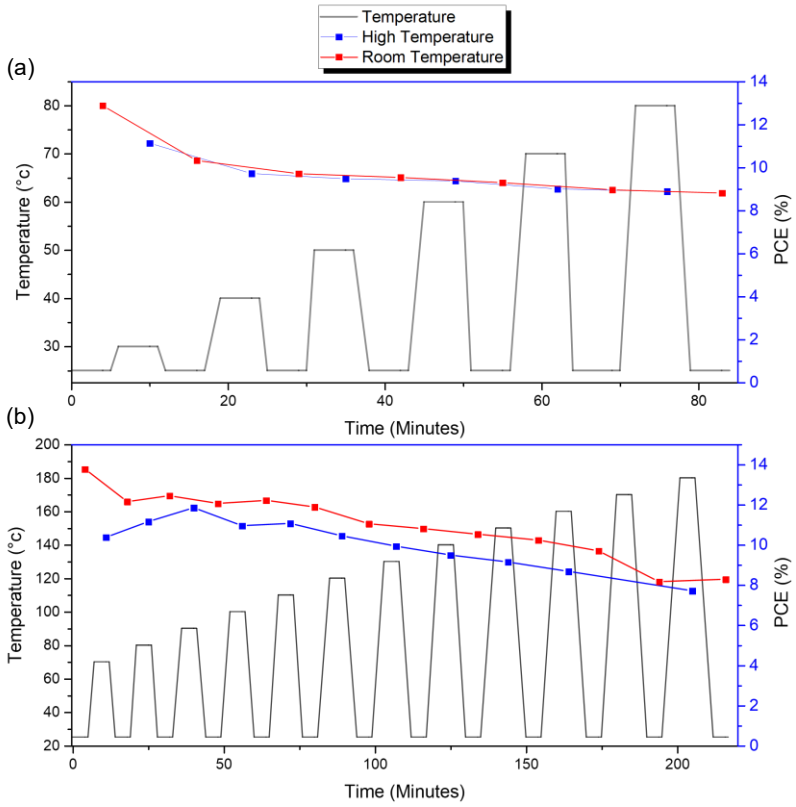

Figure 5.4 a) PCE as a function of temperature stepping for room (25 °C) and high temperatures (≤80 °C) b) PCE as a function of temperature stepping for room (25 °C) and very high temperatures (≤180 °C).

It is clear from Figure 5.4a that as the cells are heated with increasing temperature, the PCE decreases. However, more importantly, the PCE does not recover when returned to 25 °C. The initial 25 °C PCE of ~12.87% decreases to ~8.81% after the cycles when measured again at 25 °C, which is a 32% decrease in performance. As seen in Appendix C, this decrease in performance is driven by a ~8%, ~19%, and ~8% decrease in the V_{oc}, FF, and J_{sc} respectively. The decrease in V_{oc} is expected as it has been shown that at higher temperatures ionic conductivity in triple cation perovskite is increased, leading to increased recombination.[19] For the extreme high temperature performance shown in Figure 5.4b, the PSCs once again do not recover after returning to room temperature. In comparison to the initial 25 °C measurement, at 180 °C the PCE decreased by 44% due to an 8%, 22%, 22% decrease in FF, Voc, Jsc respectively. At the final 25 °C measurement, the device had degraded from the initial PCE of 13.77% to 8.28%, which is a 40% decrease in PCE. This decrease is 20% larger than the decrease observed at 80 °C in Figure 5.4b. From

the J-V curves shown in Figure 5.5, the decrease in PCE is due to the continued decrease in J_{sc}, V_{oc}, and FF as a function of increasing temperature. The decrease in J_{sc} is attributed to the degradation of the spiro-OMeTAD layer, reducing charge extraction. The decrease in V_{oc} correlates to a change in the perovskite band-gap, which results in a higher charge carrier concentration and charge accumulation at the interfaces.[20][21] This charge accumulation will result in an increase in recombination, and therefore a reduced V_{oc}. However, as the V_{oc} does not recover when returned to room temperature, the degradation indicates chemical degradation.

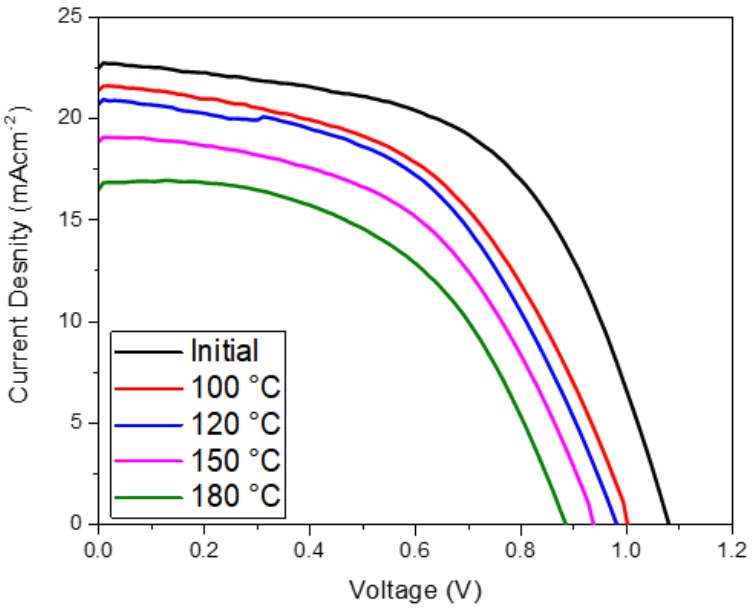

Figure 5.5 J-V curves as a function of temperature for the 'extreme' high temperature stepping shown in Figure 5.4b. Initial here refers to the first 25 °C measurement before the thermal stepping.

To further assess the thermal stability of the PSCs utilising a spiro-OMeTAD HTL, PSCs were held at 85 °C for 1 hour with J-V measurements being taken every 10 minutes. This was to simulate the stability of the PSCs at the maximum temperature during a light cycle with a time equivalent close to that of a LEO application (~45 minutes). The normalised PV parameters are shown in Figure 5.6. Here, the PV parameters were normalised to the initial value to investigate any changes in performance as a function of time held at 85 °C.

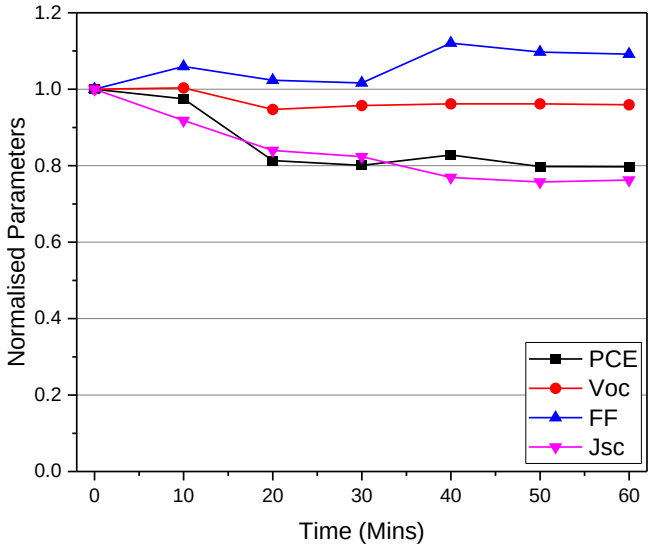

Figure 5.6 Normalised J-V parameters at 85 °C as a function of time for spiro-OMeTAD-based PSCs.

The PCE of the PSCs held at 85 °C decreases with increasing time, with the PCE decreasing by ~20% after 60 minutes at 85 °C. This decrease in PCE is a result of a ~24% decrease in J_{sc} and ~4% decrease in V_{oc}. Interestingly, the FF increases as a function of heating time. After 40 minutes, the FF increased by 12%, and after the full 60 minutes the FF was ~10% higher than the initial measurement. The increase in FF due to heating PSCs has been observed and is suggested because of proper PbI_2 formation acting as passivation centre to reduce the recombination of photo-induced carriers in the perovskite film.[22] In comparison, here the FF remains higher than the initial value for the total duration of heating time. Therefore, within the measurements timescale the increase in FF correlates with PbI_2 being formed to act as passivation centres. Due to the limited heating time (1 hour) however, it is suggested that dispersed PbI_2 was not formed and therefore does not bring about defect states which hinders charge transfer and increases recombination.[22]

From the J-V measurements for the PSCs utilising a spiro-OMeTAD HTL, the PSCs exhibit good low temperature stability, with the PCE returning to pre-cooling performance even when cooled to -180 °C. For high temperature measurements, the PCE does not recover to the pre-heating performance. This decrease in performance was attributed to the spiro-OMeTAD HTL degrading under heating.

Further characterisation techniques were needed to properly confirm that the reduction in performance was due to the degradation of the spiro-OMeTAD HTL. To probe any changes in chemical structure or optical properties, Raman spectroscopy and photoluminescence (PL) measurements were used respectively. To characterise any change in electrical properties, Transient Photovoltage and Photocurrent (TPV/TPC) were used.

5.2.1.2 Raman Spectroscopy and Photoluminescence

To probe the stability of the spiro-OMeTAD HTL during thermal cycling, the first set of Raman and PL measurements were performed during a thermal cycle between -100 and +85 °C. Firstly, the Raman spectra of the spiro-OMeTAD HTL was measured at 25 °C before cycling, at -100 and 85 °C, and then at 25 °C after cycling to probe any reversibility in any measured changes. The averaged spiro-OMeTAD Raman spectra as a function of temperature are shown in Figure 5.7. To help associate peaks with vibrations, the Raman spectrum of spiro-OMeTAD was simulated using ORCA and is shown in Figure C.4.

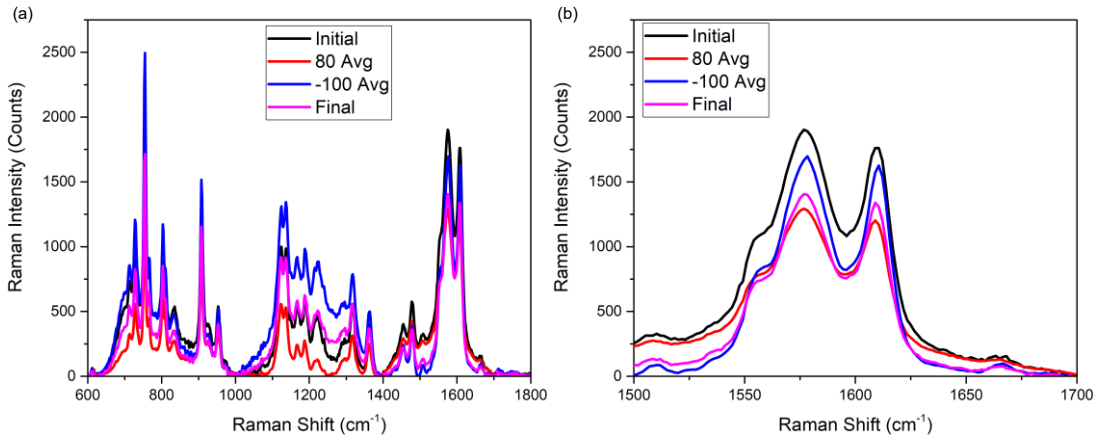

Figure 5.7 a) Averaged Raman spectra of the spiro-OMeTAD HTL as a function of temperature b) Averaged Raman spectra of the spiro-OMeTAD HTL as a function of temperature focussed on the carbon bond peaks. Initial is the first 25 °C measurement, and final is the 25 °C measurement after cycling.

As a function of temperature, there is an observed decrease in the average Raman intensity at -100 °C, 85 °C, and at 25 °C after cycling. As the Raman signal does not completely recover to the initial measurement after cycling, it indicates that

there is degradation within the spiro-OMeTAD layer. This has been seen previously in Chapter 3 under proton bombardment where a degrading spiro-OMeTAD layer correlated well with the observed decrease in Jsc and PCE. In Figure 5.7b, the carbon single bond (C-C) and double bond (C=C) peaks in the aromatic ring are measured at 1576 and 1610 cm^{-1} respectively. The C=C bond is important for organic semiconductors and the source/position of these peaks were confirmed through the Raman simulation. Here the Raman intensity of the C-C peak decreased by 26% and the C=C peak decreased by 24% at 25 °C after cycling compared to the initial value. As both peaks only decreased by 10% on average at -100 °C, the overall decrease after cycling is most likely due to the 85 °C cycling time (~50 minutes). The average 85 °C Raman shows a 32% decrease for both the C-C and C=C peaks. The reduced Raman signal during the high temperature measurements and the final 25 °C measurement correlates well with the overall reduced J_{sc} during the thermal cycling. To probe the effect of temperature on the optical properties of the perovskite during the thermal cycle, PL measurements were taken at each cycle and averaged as a function of temperature. The averaged PL as a function of temperature is shown in Figure 5.8.

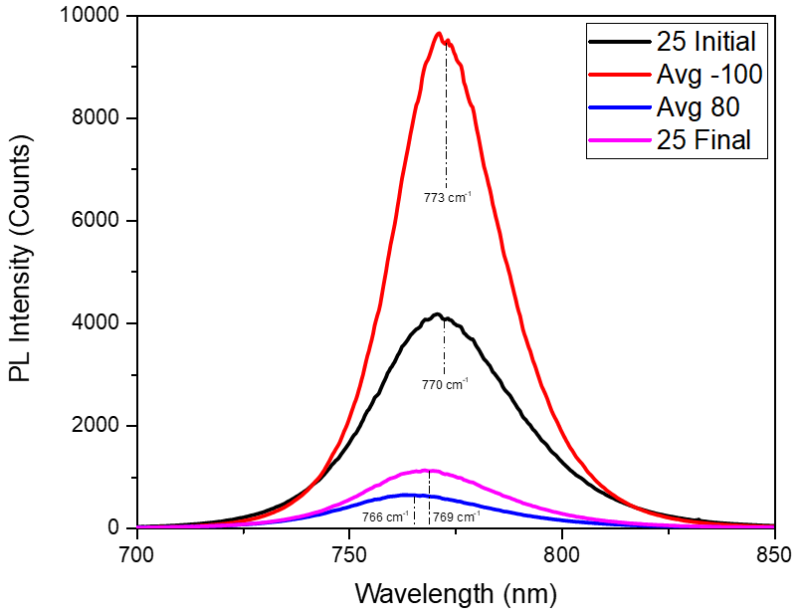

Figure 5.8 Averaged PL response of the perovskite as a function of temperature.

With a peak centre value of 770 cm-1 at 25 °C, there is a 3 cm-1 red shift in the PL response at -100 °C. This shift is expected as in the literature it has been shown

that perovskite has a reverse band structure, which results in the band gap narrowing at low temperatures.[23] The 138% increase in PL intensity compared to the initial 25 °C measurement also suggests that there is an increase in radiative recombination within the perovskite at -100 °C. The opposite is true for the average 85 °C peak, with a 4 cm^{-1} blue shift observed due to the band gap increasing with temperature.[23] However, the PL is quenched by 85% compared to the initial 25 °C measurement. This quenching correlates well with the decrease in Raman intensity at 85 °C and the decrease in J_{sc}. Additionally, the PL intensity does not recover after cycling, with the 25 °C measurement after cycling exhibiting a 73% decrease in intensity. This indicates that the degradation because of the thermal cycling is not completely reversible. This trend has been seen before in Chapter 3, in which the PL was quenched due to the spiro-OMeTAD HTL degrading, which resulted in recombination at the perovskite/spiro interface. To further understand the effect of 85 °C treatment on the optical properties, the Raman and PL measurements were repeated for a device held at 85 °C for 60 minutes.

For the 85 °C holding measurements, the first layer probed was the perovskite active layer. As mentioned previously, PbI_2 can form under heating and if there was an increase in formed PbI_2 because of continued heating, there should be a notable increase in the PbI_2 Raman signal. The average perovskite Raman spectra and normalised average perovskite Raman spectra as a function of thermal holding time is shown in Figure 5.9.

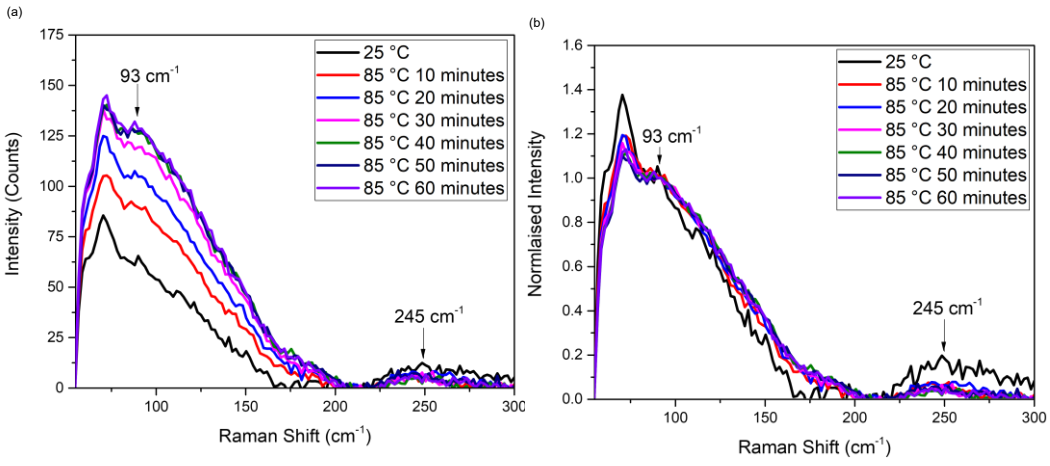

Figure 5.9 a) Averaged perovskite Raman spectra as a function of 85 °C heating time b) Normalised average perovskite Raman spectra as a function of 85 °C.

For the perovskite Raman measurements, the samples were measure through the glass substrate. From the Raman spectra shown in Figure 5.9a, there are 2 main peaks that appear at 93, and 245 cm^{-1}. These peaks correspond to PbI_2, and a MA torsional mode respectively.[21][19][24] Here, the intensity of the 245 cm^{-1} peak is consistent across all measurements, indicating no change in the torsional mode of the MA. The increased intensity of the PbI_2 peak could confirm the increase in PbI_2 formation within the perovskite. The PbI_2 peak intensity increases by 106% when comparing the initial 25 °C measurement to the final measurement after 85 °C heating for 60 minutes, strongly suggesting that there is an increase in PbI2 formation due to the 85 °C heating. In Figure 5.9b, the Raman spectra's have been normalised to the PbI_2 peak (93 cm^{-1}) to probe any shift in peak position. While the increase in PbI_2 correlates well with the increase in FF, the decrease in Voc and Jsc suggests that there are additional degradation mechanisms that correlate to the decreasing PCE.

The second layer to be probed was the spiro-OMeTAD HTL. Here the same measurement conditions for the perovskite layer were used, however the measurements were taken through the spiro-OMeTAD layer rather than the glass. As the carbon-double bond is important for organic semiconductors, the average spiro-OMeTAD carbon-double bond (C=C) Raman spectra as a function of thermal holding time is shown in Figure 5.10.

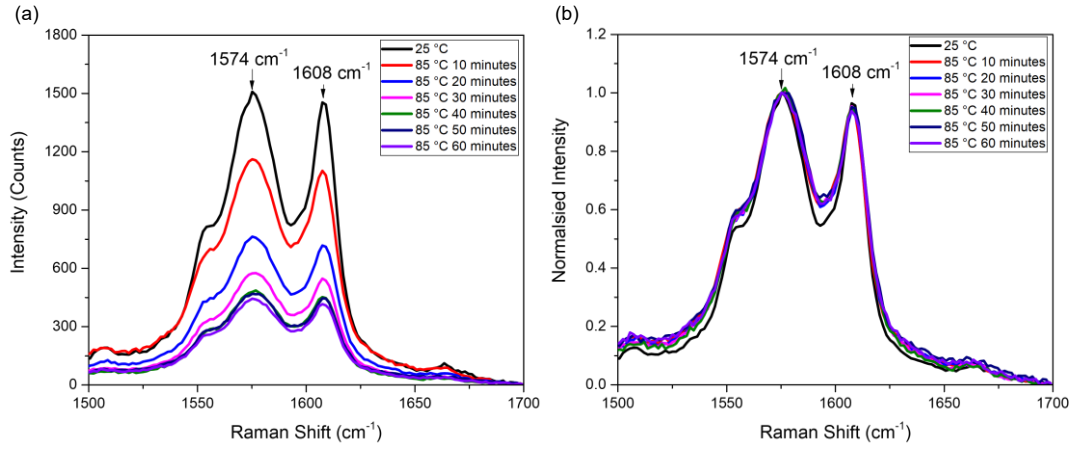

Figure 5.10 a) Averaged spiro-OMeTAD C=C Raman spectra as a function of 85 °C heating time, b) Normalised Average spiro-OMeTAD C=C Raman spectra as a function of 85 °C heating time.

It can be seen in Figure 5.10a, that as the 85 °C heating time increases, the Raman intensity for the carbon bond peaks (1574 and 1608 cm^{-1}) decrease. It has been shown in Chapter 3 that decreasing Raman intensity for spiro-OMeTAD indicates degradation of the layer, which reduces charge extraction and therefore reduces device performance. This suggests that during the operation time of the solar cell in direct AM0 1 Sun intensity for 60 minutes, the increasing temperature of the cell will cause the device performance to decrease during operation. In comparison, the 85 °C holding measurements exhibit a 20% decrease in Jsc as seen in Figure 5.6, while in Figure 5.1 the Jsc decreased by 6% after 10 cycles between -100 and +85 °C. During the thermal cycle, the total time at 85 °C across all cycles is 50 minutes, which suggests that the degradation of the spiro-OMeTAD layer can be slightly reversed under low temperatures, but not completely. This is also seen in the Raman and PL measurements in Figure 5.7 and Figure 5.8 respectively. Figure 5.10b is normalised to the 25 °C intensity for the 1574 cm^{-1} peak and maintains the same intensity ratio across all heating time, indicating that the peaks decrease in intensity at the same rate. To further investigate the decrease in intensity, the carbon bond peak intensity values were plotted as a function of heating time and are shown in Figure 5.11.

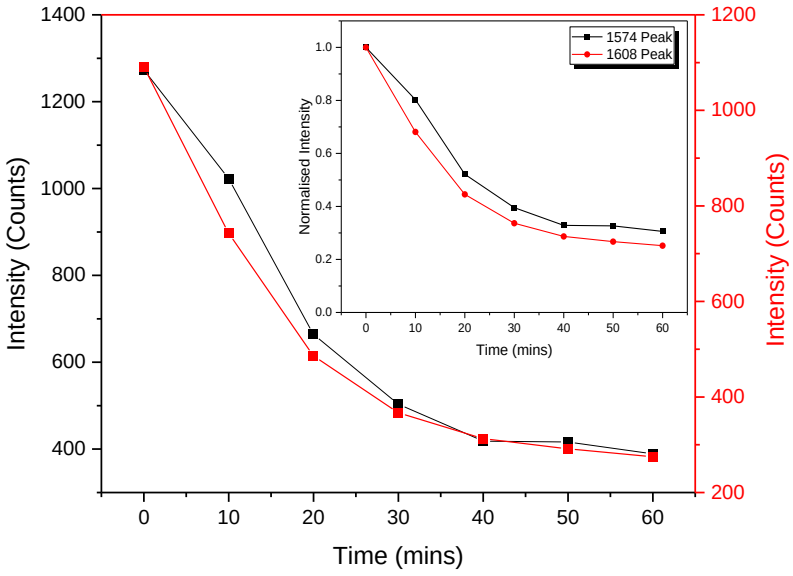

Figure 5.11 Peak intensity of the 1574 and 1608 cm^{-1} carbon bond peaks as a function of heating time at 85 °C. Insert normalised peak intensity as a function of 85 °C heating time.

In Figure 5.11, the intensity of the 1574 and 1608 cm^{-1} peaks decrease at a similar rate, with the 1574 cm^{-1} peak intensity decreasing by 69% and the 1608 cm^{-1} peak decreasing by 75% in comparison to the 25 °C measurement. The reduction in intensity has been attributed to the degradation of the spiro-OMeTAD layer. This correlates with the reduction in J_{sc} and PCE shown in Figure 5.6a. The reduction in Jsc could also correlate to the reduction in V_{oc} as the reduced charge extraction will result in increased recombination. However, this would need to be proved through electrical characterisation measurements.

After Raman spectroscopy was performed on the perovskite active layer and the spiro-OMeTAD HTL, PL was performed on the perovskite active layer to investigate how the thermal holding affected the optical properties of the PSCs. Here, the PL measurements were taken through the glass substrate. The averaged PL as a function of heating time is shown in Figure 5.12.

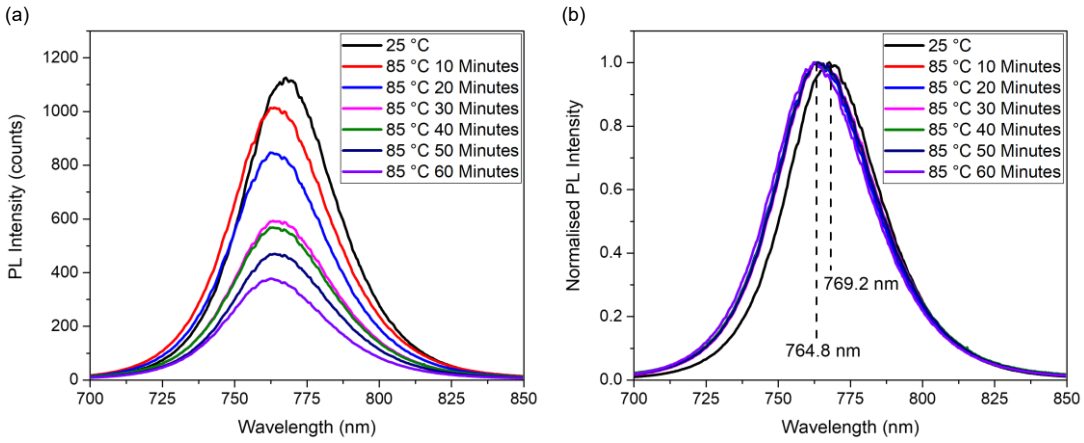

Figure 5.12 a) Averaged PL spectra for a PSC utilising a spiro-OMeTAD HTL as a function of heating time at 85°C, b) Normalised PL peaks as a function of heating time. The initial 25 °C (right) and final 85 °C (left) peak position have been labelled for the normalised plot.

Like the radiation induced degradation in PL intensity seen in Chapter 4, there is a continuous decrease in PL intensity as a function of heating time. The exhibited quenching in PL correlates well with the decreasing Jsc, indicating poor charge extraction and increased non-radiative recombination. After 60 minutes of 85 °C heating, the PL intensity decreases by 67%.[25] Additionally, it is shown that the PL is quenched with increasing heating time. Coupled with the reduction in Jsc, it is

suggested that the reduction in effective charge extraction because of the spiro-OMeTAD HTL degrading results in non-radiative recombination at the spiro-OMeTAD/perovskite interface due to charge accumulation or defects in the spiro-OMeTAD layer. This would also agree with the reduction in V_{oc} shown in Figure 5.6a as a function of thermal holding time. In Figure 5.12b, there is an observed blue shift in the PL peak position from an initial 25 °C measurement position of 769 nm to 765 nm after 60 minutes at 85 °C. The blue shift in the PL peak indicates an increase in high energy band to band recombination in the perovskite and this blue shift in PL has been observed and calculated for MAPI and perovskite QDs.[26][27] To further investigate the effect of 85 °C heating on the PL spectra of the PSCs, the peak position, intensity and FWHM were measured and are presented in Figure 5.13.

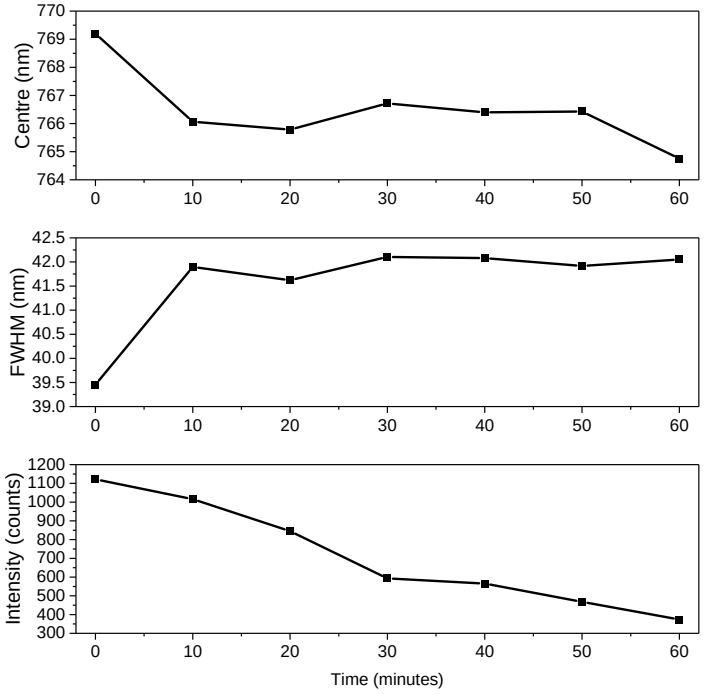

Figure 5.13 PL peak position, FWHM, and intensity as a function of thermal holding time at 85°C for PSCs utilising a spiro-OMeTAD HTL.

As mentioned previously, the PL peak position blue shifts from 769 nm to 765 nm after 60 minutes of heating time. Here, the PL peak position blue shifts by 3 nm between 0 and 10 minutes, with a further shift of 1 nm between 10 and 60 minutes. As the spectral resolution of the measurement system is 1 nm, it is suggested that within 10 minutes the device has reached thermal equilibrium and is stabilized.

As shown in the Raman spectra of the spiro-OMeTAD HTL, here the FWHM increases with increasing thermal holding time. The increase in FWHM, and the broadening of the PL peak can be an indication of increased disorder within the perovskite active layer.[28][29] Following a very similar trend, the FWHM increases by 2 nm (6%) after 10 minutes, but by less than 1 nm between 10 and 60 minutes at 85 °C. This increase in FWHM as a function of temperature has been seen in perovskite QDs and is related to an increase in carrier-phonon coupling, which reduces carrier mobility and increases non-radiative recombination.[30] This is in good correlation with the observed decrease in the V_{oc} as a function of heating time, indicating an increase in non-radiative recombination. An increase in charge accumulation at the interfaces due to poor charge extraction will leads to an increase in non-radiative recombination, such as Auger, which quenches the PL.[31]

5.2.1.3 Electrical Characterisation Measurements

While the Raman and PL measurements corelate well with the observed J-V measurements, additional electrical characterisation techniques were required to further investigate how the 60 minute 85 °C holding affected the devices. For this, Transient Photovoltage/Current (TPV/C) measurements were performed on spiro-OMeTAD HTL PSCs.

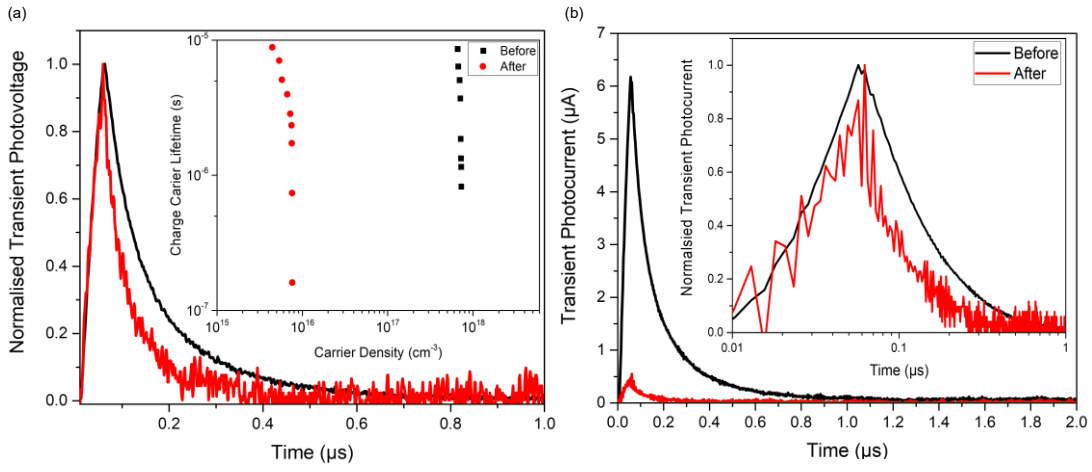

Figure 5.14 a) Normalised TPV decay at equivalent 1 Sun light intensity. Insert charge carrier lifetime vs carrier density b) TPC decay at equivalent 1 sun intensity. Insert normalised TPC decay.

In these measurements the cells were initially measured, and then heated at 85 °C for 60 minutes before being remeasured again. In Figure 5.14a, the TPV decay lifetime reduces from ~1 μs before to ~0.14 μs after heating. The reduction in lifetime indicates an increase in recombination within the perovskite bulk as the cell returns to the steady state faster.[32] However, as the TPV decay does not follow a double exponential decay as seen in Chapter 3, it is unlikely that interfacial recombination is the sole cause. In Figure 5.14a insert, the carrier density of the spiro-OMeTAD HTL PSC decreases by 100x, showing a reduced carrier density within the perovskite bulk from ~10^{18} to ~10^{16} cm^{-3} after heating. While the cause of this reduction is unknown, one suggestion is the reduction in charge extraction due to the degraded spiro-OMeTAD HTL. As the charge extraction is reduced, the generated carriers accumulate at the interface where the recombine and are unable to be extracted. This is further seen in Figure 5.14b where the generated TPC is reduced by ~90% after the 85 °C heating. A reduction in TPC decay time is associated with an increase in charge extraction, but the area under the TPC curve is an indication of the total charge extracted.[32] Here is it shown that the TPC decay time is reduced from ~2 μs before heating, to ~0.3 μs after. In comparison with the J-V data under 85°C temperature holding, the J_{sc} is reduced with increasing time. Therefore, the reduced generated photocurrent and faster TPC decay is an indication of reduced charge extraction, causing the device to return to the steady state much faster. As the devices were cooled before measuring, the degradation in transient photocurrent and increase in recombination correlates well with the non-reversibility of J-V, Raman, and PL measurements.

Overall, it is concluded that the use of spiro-OMeTAD HTL in a PSC limits the high temperature stability. By degrading under high temperature, and thus reducing the charge extraction, charge build-up at the perovskite/spiro interface causes non-radiative recombination and limits device performance. Therefore, to improve the thermal stability of PSCs under mimic LEO conditions, a suitable replacement for spiro-OMeTAD is required.

5.2.2 Perovskite Solar Cells With P3HT HTL

5.2.2.1 J-V Performance Under Mimic LEO Conditions

P3HT is a is a low band gap (1.9 eV) polymer donor with applications in organic photovoltaics, OLEDs and OFETs.[33] The replacement of spiro-OMeTAD by P3HT in PSCs has been reported, with a large increase in the thermal stability of PSCs at 85 °C.[34] Therefore, it is an attractive material to improve the thermal stability of PSCs under mimic LEO conditions.

Following the same procedure from Figure 5.1, the planar PSCs with the device stack of Glass/ITO/SnO_2/$Cs_{0.05}(FA_{0.87}MA_{0.13})Pb(I_{0.83}Br_{0.13})_3$/P3HT/Au with glass-on-glass encapsulation were thermal cycled between -100 and +85°C under vacuum. The vacuum pressure was $1x10^{-2}$ mbar ($1x10^{-5}$ bar). The results of a 10 thermal cycle are shown in Figure 5.15.

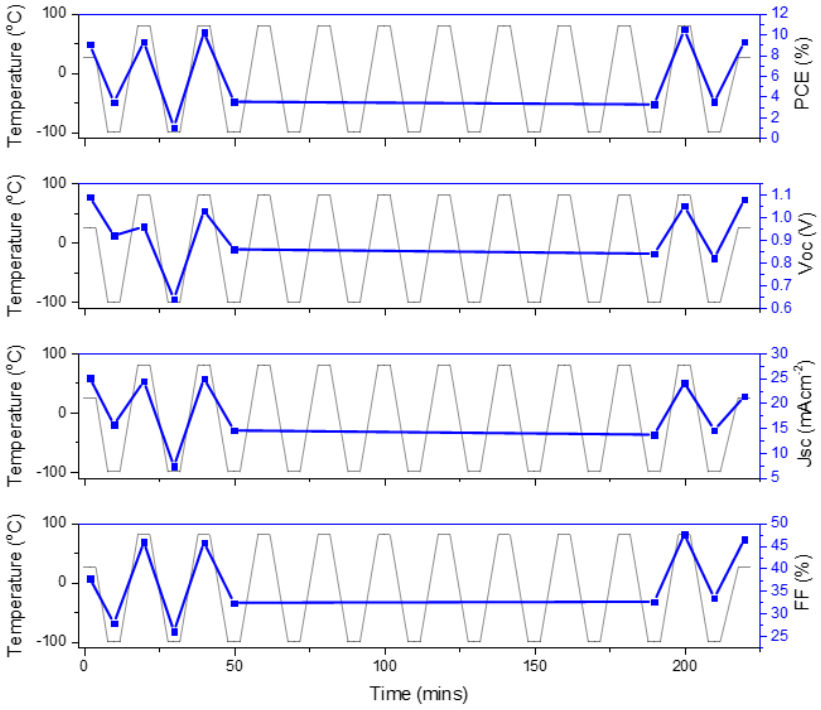

Figure 5.15 PV parameters under thermal cycling between -100 and +85 °C for a PSC with a P3HT HTL under 1 Sun AM0.

Unlike PSCs utilising spiro-OMeTAD as their HTL, the P3HT devices appear much more stable under -100 to +85 °C thermal cycling. After 10 cycles, the PCE of the device increased by 3% overall from 9% to 9.26%. However, despite the increase

thermal cycling stability, the low temperature performance of the P3HT device is lower, with a 78% lower AM0 PCE (3.5%) when compared with the spiro-OMeTAD devices (14%). The reduction in P3HT PSC PCE is due to a 42% and 25% reduction in J_{sc} and V_{oc} at -100 °C, respectively. One possible cause for this reduction is that the hole mobility (μ_0) for P3HT at -100 °C is several orders of magnitude lower than at room temperature. At room temperature, μ_0 for P3HT is ~$3.38x10^{-6}$ $cm^2V^{-1}S^{-1}$, but at -100 °C (173.15 K) μ_0 is ~$1.21x10^{-8}$ $cm^2V^{-1}S^{-1}$, which is 2 orders of magnitudes lower.[35] In comparison, the room temperature μ_0 for spiro is ~$2x10^{-2}$ $cm^2V^{-1}S^{-1}$ and at -100 °C μ_0 is ~$4x10^{-4}$ $cm^2V^{-1}S^{-1}$. While there is a 2-order decrease in μ_0 for spiro, the -100 °C and 25 °C μ_0 is 4 orders larger overall than that of P3HT. This can be seen in the room temperature performance, with the spiro-OMeTAD devices exhibiting a 44% greater PCE (13%) compared to P3HT PSCs (9%). Therefore, at -100 °C P3HT has a hole mobility 4 orders of magnitude lower than spiro-OMeTAD. This suggests that while in a LEO environment P3HT may offer better thermal stability and low temperature performance is not important. Additionally, the overall PCE of the P3HT devices is lower than that of the spiro-OMeTAD PSCs. This is due to a decrease in EQE at wavelengths between 450-750 nm, which is shown in Appendix C. To assess the high temperature stability of P3HT, and to compare it with spiro-OMeTAD, J-V measurements were taken while the device was held at 85 °C for 60 minutes. The normalised PV parameters as a function of heating time are shown in Figure 5.16.

Shown in Figure 5.16, after 20 minutes of heating time the PCE has increased by 12%, along with a 1% increase in V_{oc}, 5% increase in J_{sc}, and a 6% increase in FF. After 60 minutes, compared to the 25 °C measurement the PCE has decreased by 9%, the V_{oc} by 8%, the J_{sc} by 2%, and the FF retains 100% of the initial FF value. the main cause of the decrease in PCE is the 8% decrease in the V_{oc}. One suggestion for the decrease in Voc is that under heating the crystallinity of P3HT increases.[36] Nia et al showed that under heating, XRD patterns show increased intensity and narrowed peak width demonstrating improved crystallinity and indicating that a larger polymer crystal size is achieved. It was also shown that annealing may also influence the perovskite/P3HT interface as the P3HT becomes soft during the annealing process, which effectively increases the contact area, and thus the hole transfer paths. A similar effect could appear here, as after 10 minutes the Voc, PCE, and Jsc increased

before gradually decreasing with increasing heating time. This decrease in Voc could be due to the increased P3HT crystallinity because of the heating time, which would increase recombination at the perovskite/P3HT interface.

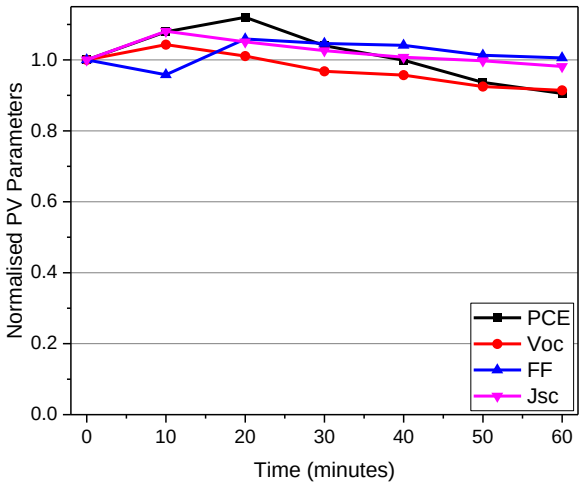

Figure 5.16 a) Normalised J-V parameters at 85 °C as a function of time for P3HT based PSCs.

In comparison to the PSCs with a spiro-OMeTAD HTL, the decrease in J_{sc} is much less severe. Here the J_{sc} decreases overall by 2% after 60 minutes of heating time. For the spiro-OMeTAD devices the J_{sc} decreases by 24%. This further shows the limitation of spiro-OMeTAD for high temperature applications. For the P3HT devices held at 85 °C for 60 minutes, the limitation in device stability is the decrease in the V_{oc} as a function of increasing heating time. As shown in Figure 5.12, during the thermal cycling there is no change in the V_{oc}, suggesting that the low temperature cycling could improve the V_{oc} stability and improves device stability by reversing any changes that occur because of the thermal heating. Overall, under 85 °C temperature holding, PSCs utilising a P3HT HTL are more stable than those with a spiro-OMeTAD HTL. To further investigate any optical changes in the perovskite and P3HT, Raman spectroscopy and PL was performed during a 60 minute 85 °C thermal holding.

5.2.2.2 Raman Spectroscopy and Photoluminescence

Raman spectroscopy was used to probe the chemical structure of the P3HT HTL while devices were held at 85°C for 60 minutes. The measurements were taken through the P3HT layer, and a 35 data point Raman map was taken in 10-minute intervals and averaged to give a Raman spectrum as a function of heating time. The average P3HT

Raman spectra and normalised average P3HT Raman spectra as a function of thermal holding time is shown in Figure 5.17. The Raman mapping of the 1447 cm^{-1} peak intensity as a function of heating time is presented in Figure C.5.

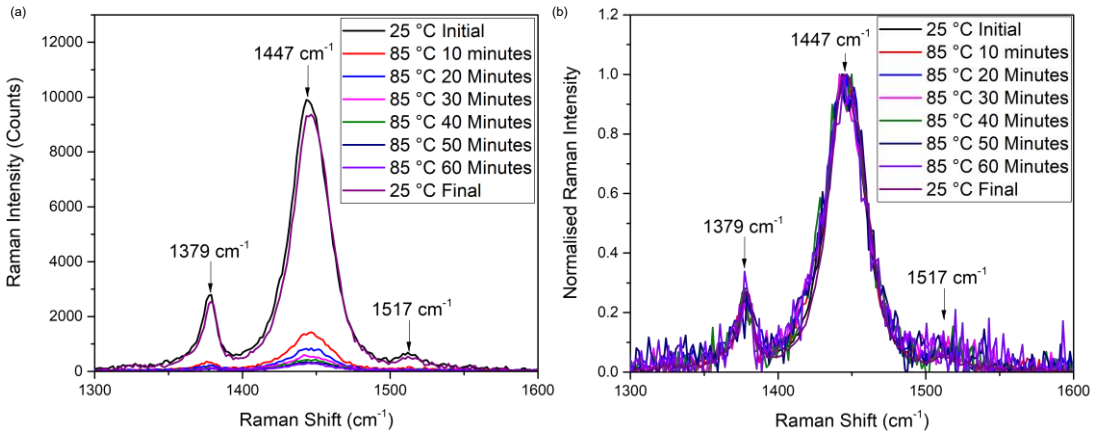

Figure 5.17 a) Averaged P3HT Raman spectra focussed at the 1447 cm^{-1} peak as a function of 85 °C heating time b) Normalised Average P3HT Raman spectra focussed at the 1447 cm^{-1} peak as a function of 85 °C heating time.

The P3HT spectrum shown in Figure 5.17a depicts two major peaks at 1379 cm^{-1} and 1447 cm^{-1}, which are attributed to C–C intra-ring stretching and symmetric C=C stretching vibrations, respectively.[37] There is a less intense peak at 1517 cm^{-1} which is attributed to anti-symmetric C=C stretching.[38] Here it is seen that as the thermal holding time increases, the Raman intensity of the P3HT peaks decreases. However, after the device was cooled for 10 minutes the Raman intensity of the 1447 cm^{-1} peak recovers to 95% of the initial measurement. In comparison, the spiro-OMeTAD Raman intensity in this chapter only recovers to 76% of the initial intensity. Therefore, it is suggested that the chemical changes in P3HT that decrease the Raman intensity under thermal treatment are reversible.

The cause of the decrease in Raman signal is not understood, and the decrease is not in correlation with the measured increase in J_{SC}. One suggestion is that the perovskite/P3HT interface affects the overall crystallinity of the film. It has been shown that in PCBM:P3HT blends, the addition of PCBM causes the P3HT to have mixed amorphous and crystalline phases, and this mixed phase is highly amorphous.[39] The amorphous phase of P3HT exhibits a lower Raman signal under heat treatment, along with improved charge transfer. Both phenomena are exhibited

in this work, with the Raman intensity of the P3HT film decreasing and the J_{sc} of the P3HT devices increasing because of thermal treatment. After 10 minutes of holding time, the Jsc increases by 8% while the 1447 cm^{-1} peak intensity decreases by 86%. To further investigate why there is no correlation between the peak intensity and measured Jsc, the Raman spectra were normalised to the 1447 cm^{-1} peak as seen in Figure 5.17b. Here there is a good overlap at the 1447, 1517 and 1379 cm^{-1} peaks, however the noise of the measurements is more prominent at longer heating times. The changes in 1447 cm^{-1} peak position, FWHM and intensity are presented in Figure 5.18 below. This peak was chosen as it is the most prominent peak and being associated to the C=C bond, which is important for organic semiconductors. The normalised Raman intensity is shown in Figure C.6.

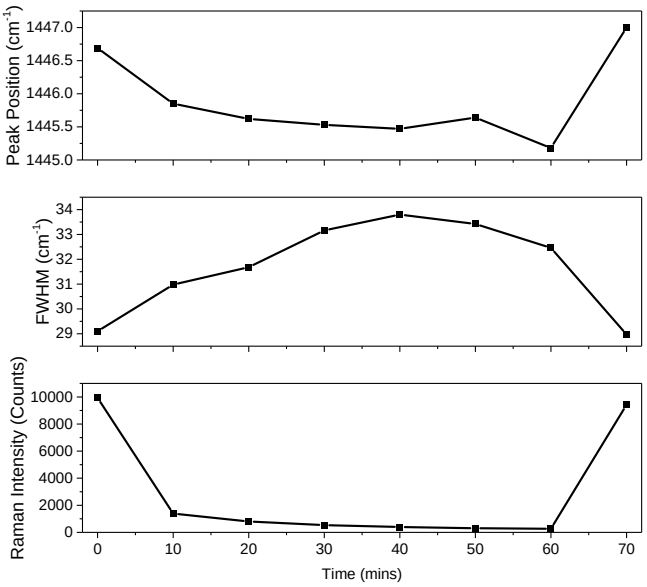

Figure 5.18 Peak position, FWHM, and intensity as a function of thermal holding time for the 1447 cm^{-1} P3HT Raman peak. 70 minutes is the 25 °C measurement after allowing the device to cool.

In comparison to the spiro-OMeTAD devices, the 1447 cm^{-1} peak position shifts to a lower wavenumber rather than a higher value, which is consistent with increase crystallisation, which may also reduce the bandgap.[39] The 1446.7 cm^{-1} peak shifts by 1 cm^{-1} to 1445.5 cm^{-1} after 60 minutes of total heating time, before returning to 1447 cm^{-1} after the device had cooled. Therefore, it appears that the thermally induced change in crystallinity is reversible. However, this will need to be confirmed with additional techniques. The FWHM of the P3HT layer increases with heating time,

as seen previously with the spiro-OMeTAD layer. This suggests an increased disorder within the P3HT layer. One possible cause is the previously mentioned amorphous/crystalline P3HT which is highly amorphous and therefore more disordered.[39] The P3HT film FWHM increases by 4 cm^{-1} (6%), while in comparison the spiro-OMeTAD FWHM increases by 3 cm^{-1} (8%), indicating that there is more disorder for the P3HT. However, as the resolution of the measurements is ~1 cm^{-1}, the FWHM increase is similar for both HTLs. In Figure 5.15, the intensity of the 1447 cm^{-1} peaks decreases with increasing heating time. There is a 97% overall reduction in intensity after 60 minutes at 85 °C. After 10 minutes of cooling time, the peak intensity recover to 95% of the initial 25 °C measurement.

To properly investigate the effects of thermal heating on the P3HT HTL, PL measurements were taken during a 60 minute 85 °C thermal holding experiment, where the PL was measured every 10 minutes. Additionally, a Neutral Density (ND) filter of 1.0 (10% transmittance) was used to reduce oversaturation of the photodetector at longer temperature holding times. The averaged PL spectra as a function of heating time at 85°C are shown in Figure 5.19a, with the normalised averaged PL spectra shown in Figure 5.19b.

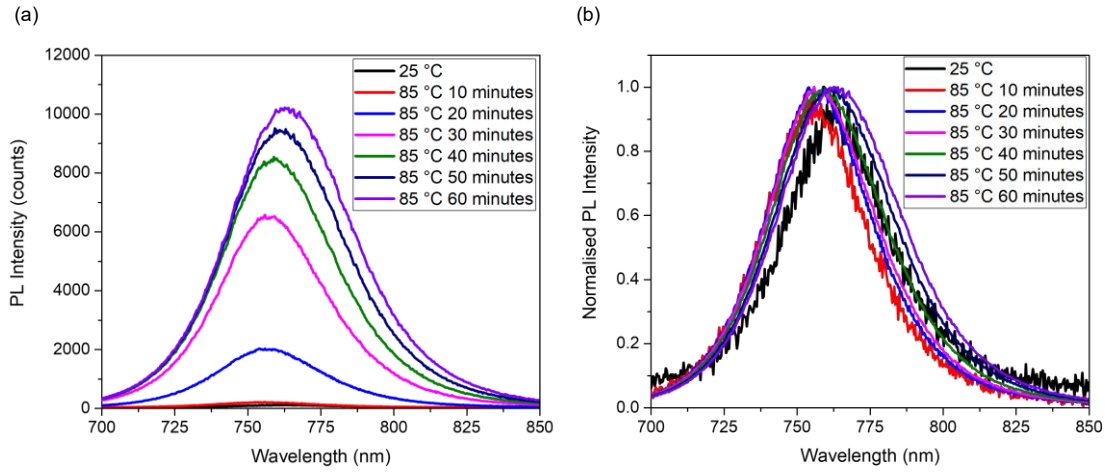

Figure 5.19 a) Averaged PL spectra for a PSC utilising a P3HT HTL as a function of heating time at 85°C, b) Normalised PL spectra as a function of heating time.

The PL intensity for the 25 °C and the 85 °C 10-minute measurement is very low (~80-110 counts), but this is due to the use of the 1.0 absorbance ND filter. Despite this, the trend in PL intensity as a function of heating time is clear. As the

heating time increases, the PL intensity increases significantly, with there being as 124x increase in PL intensity after 60 minutes compared to the measurement at room temperature. The increase in PL indicates a reduction in non-radiative recombination, which is the opposite of what is observed with the spiro-OMeTAD PSCs. Additionally, there is an apparent red-shift in the PL peak position after 60 minutes at 85 °C. Comparing the normalised PL peaks in Figure 5.16b, visually there is an initial blue shift in the PL peak position after 10 minutes at 85 °C, which is attributed to the perovskites reverse band gap and carrier-phonon coupling which increases the band gap with increasing temperature.[28] This was also seen for the spiro-OMeTAD PSCs. This change was initially attributed to an increase in the PL response of the P3HT layer itself. P3HT has its own PL peak centred around 730 nm.[40][41] However, additional PL measurements through the P3HT layer showed the P3HT PL response being oversaturated with the perovskite PL peak. Therefore, the PL of the P3HT is not responsible for the observed PL peak shift, and a different interaction with the perovskite/P3HT layers is responsible. This measurement was performed 3 times to confirm the red shift. This is due to the red-shift not being observed in PSCs with spiro-OMeTAD. To characterise the changes in the PL peak parameters as a function of heating time, the changes in the peak position, FWHM and intensity as a function of thermal holding time is shown in Figure 5.20.

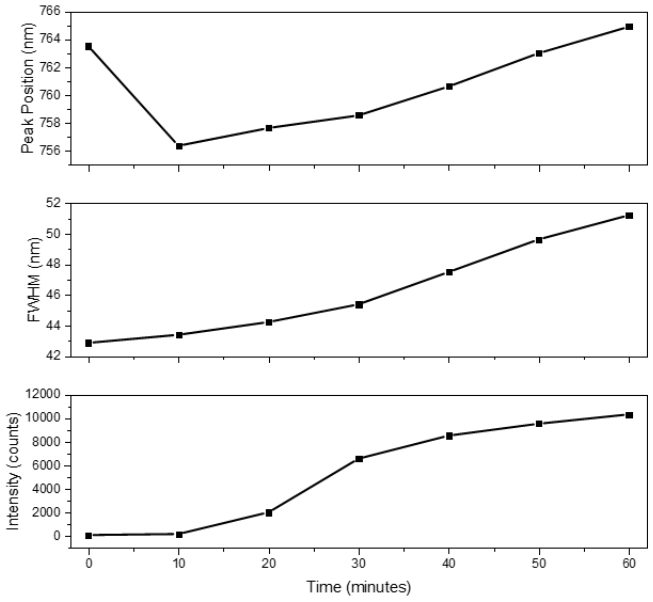

Figure 5.20 PL peak position, FWHM, and intensity as a function of thermal holding time at 85°C for the P3HT PSCs.

As also seen in Figure 5.19b, here the PL peak position first blue shifts before red shifting with increasing holding time. After 10 minutes, the PL peak is blue shifted by 7 nm. The peak position is then red shifted by ≈ 9 nm from 10 to 60 minutes heating time. Overall, the total shift in the peak position after 60 minutes is ≈ 1nm . This shift is equivalent to the spectral limit of the spectrometer, and therefore the redshift in relation to the initial measurement is negligible.

As seen in the PL measurements for the spiro-OMeTAD HTL, here the PL FWHM increases with increasing thermal holding time. Here, the overall increase in the FWHM is ≈8 nm, which is ≈5 nm greater than the FWHM increase observed for the spiro-OMeTAD PSC. This suggests that the perovskite PL response is more disordered with the P3HT HTL. However, in comparison to the spiro-OMeTAD devices the PL is not quenched with increasing 85 °C heating time. Therefore, the induced chemical changes because of the heating correlates to a reduction in non-radiative recombination, however it does lead to an increase in radiative recombination, a reduction in the perovskite optical band-gap, and an increase in the perovskite's PL disorder. Interestingly, the rate of increase of PL intensity as a function of heating time is faster between 0-30 minutes, then between 30-60 minutes of heating time. The change in intensity between 0 and 30 minutes is ~79x greater, while between 30 and 60 minutes the increase is 1.6x greater. The large increase within the first 30 minutes correlates with the increase in device performance within the same time frame. To further characterize any changes that occur in the P3HT devices because of the 85 °C thermal treatment, TPV/C measurements were performed.

5.2.2.3 Electrical Characterisation Measurements

While the Raman and PL measurements suggest that the heat treatment of the P3HT PSCs results in increased crystallinity of the HTL, it also suggested that there is an increase in radiative recombination within the devices. To gain further understanding of the effect of heating, TPV/C measurements were performed on P3HT HTL PSCs. The TPV/C results are shown in figure 5.21.

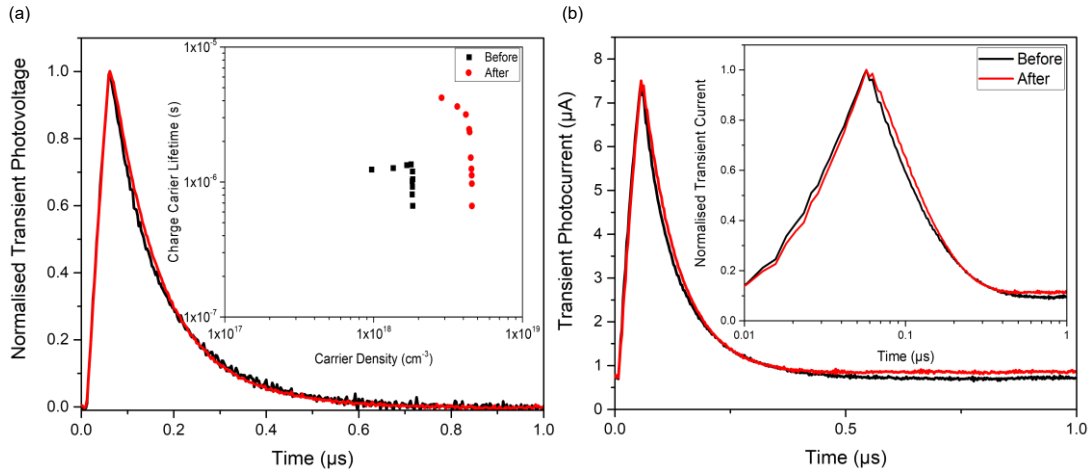

Figure 5.21 a) Normalised TPV decay at equivalent 1 Sun light intensity. Insert charge carrier lifetime vs carrier density b) TPC decay at equivalent 1 sun intensity. Insert normalised TPC decay.

In contrast to the spiro-OMeTAD devices, the before heating TPV decay shown in Figure 21a is almost identical to the decay after heating. The decay time before heating was 0.66 µs, while the decay time after heating was 0.65 µs. This is a 2% overall decrease in TPV lifetime, however in comparison the TPV lifetime in the spiro-OMeTAD devices decreased by 85% after heating. Therefore, the increase in recombination within the device is less so for the P3HT PSCs compared to the spiro-OMeTAD devices. Additionally, the carrier density for the P3HT devices increased 2.5x from ~$1.8x10^{18}$ to ~$4.6x10^{18}$ cm^{-3}, rather than decreasing by ~100x as seen in the spiro-OMeTAD devices. The increase in carrier density can lead to an increase in recombination, however as the PL increases in intensity with heating time, the recombination is more likely radiative than non-radiatively. Additionally, as the dark saturation current is $\propto n_i^2$ (where n_i is the carrier concentration), an increase in the carrier concentration will cause an increase in the dark saturation current and therefore a decrease in V_{oc}.[42] In the TPC decays shown in Figure 5.21b, the TPC decay time after heating is reduced from 0.8 µs to 0.6 µs. As the J_{sc} of the P3HT devices increases with heating time, the faster TPC decay time correlates with the improved charge extraction. However, as the cells were allowed to cool before measuring, the Raman and PL have shown that the thermal activated disorder is reversible. Therefore, while the TPV/C show good stability of the electrical

parameters for the P3HT PSCs, it is unable to probe any electrical changes during the 60 minute 85 °C heating.

5.3 Conclusion

This chapter finds that the thermal stability of planar n-i-P PSCs is heavily reliant on the thermal stability of the HTL, as shown by the degradation of the device performance when utilising spiro-OMeTAD as the HTL at high temperatures (>60 °C). Through J-V measurement and thermal cycling between -100 and 85 °C, it was found that after 10 thermal cycles, the PCE of spiro-OMeTAD PSCs had reduced by 10% due to a decrease in the J_{sc}. To investigate whether the decrease in PCE was due to the cold or hot cycling, spiro-OMeTAD PSCs were cycled from 25 °C to ±180 °C. The cycling PV measurements were presented with the PSCs maintaining 100% of the room temperature PCE when cycled down to -180 °C and back to 25 °C. The high temperature cycling showed decreasing PCE with temperature, and no recovery of performance at room temperature. However, the exact degradation mechanism is unknown and will require further work to investigate. Therefore, it was concluded that the high temperature cycling was the cause of device degradation under mimic LEO conditions.

This chapter finds that the degradation of the Spiro-OMeTAD HTL during high temperature thermal cycling correlates well with a reduction in efficient charge extraction, and therefore an increase in interfacial charge build-up and non-radiative recombination at the spiro/perovskite interface. This reduction in charge extraction correlates well with the observed decrease in the J_{sc} and the observed degradation in the spiro-OMeTAD Raman spectra and PL intensity. Raman spectroscopy measurements showed a reduction in the C-C and C=C bond peak intensity during a thermal cycle and holding the devices at 85 °C for 60 minutes. PL measurements showed a blue shift in peak position because of the perovskite band gap increasing with higher temperatures. In both cycling measurements the Raman intensity and PL intensity did not recover to the pre-heating values after returning the sample to 25 °C. This indicates that the degradation of the spiro-OMeTAD is non-reversible. TPV and TPC measurements confirmed the degradation of charge extraction after heating

and cooling, along with a faster TPV decay indicating an increase in recombination within the device because of holding the devices at 85 °C for 60 minutes.

To improve upon the thermal stability of PSCs, P3HT was suggested as an alternative HTL material due to its reported high thermal stability at 85 °C. J-V measurements performed during a 10 cycled thermal cycle between -100 and 85 °C showed 100% PCE retention after cycling. Raman spectroscopy of the P3HT layer during the 60 minute 85 °C temperature holding showed a decrease in intensity, which did not correlate well to the stable performance. The decrease in intensity is suggested to be due to an interaction at the perovskite/P3HT interface that results in a mixed amorphous/crystalline phase that has been shown to improve device performance in OPVs. However, this will need to be confirmed in further work through in-situ XRD measurements of the P3HT HTL during the 85 °C heating. The Raman spectroscopy also showed an increase in the P3HT FWHM, indicating the polymer becoming more disordered because of the heat treatment. PL measurements of P3HT PSCs showed a 6 nm blue-shift in peak position after 10 minutes of heating at 85 °C, which is due to the perovskites reverse band-gap. However, after 60 minutes of heating the PL peak was red-shifted by 7 nm, indicating a narrowing of the perovskite optical band gap. While the cause of the red-shift is unknown, the PL intensity increase is due to an increase in radiative recombination within the perovskite. The TPV and TPC measurements showed an increase in the carrier concentration, along with a faster photocurrent decay. The increased carrier concentration could be correlated to the decrease in V_{oc} as an increase in carrier concentration increases the dark saturation current, which reduces the V_{oc}. The faster TPC decay correlates well with the increased Jsc because of the 85 °C heat treatment.

It was not possible to perform in-situ XRD measurements on the perovskite layer due to the requirement of the vacuum chamber to mimic the LEO conditions. The aim of the XRD measurement would be to investigate any structural changes in the perovskite layer at 85 °C. The same is true of the TPV and TPC measurements, as in-situ measurements would help further understand the electrical changes due to the heat treatment. Additionally, XPS measurements could be useful in understanding if there is an interaction with the perovskite and P3HT, leading to the

formation of Lewis base interaction with the HTL/ETL and the perovskite layers. Alongside these measurements, Time Resolved PL (TRPL) could also be useful to understand the electrochemical changes within the device.

Overall, the findings in this chapter highlight how spiro-OMeTAD is the limiting factor for thermally stable PSCs in a LEO application, and how P3HT could be a potential replacement. A scientific insight into the chemical and optical changes of both spiro-OMeTAD and P3HT based PSCs was also shown. The findings in this chapter shows how a more thermally robust HTL material is required for PSCs to be a potential PV technology for LEO applications. Overall, it is suggested that the degradation of the spiro-OMeTAD based PSCs is due to limited charge extraction because of thermal degradation of the spiro-OMeTAD layer. The degradation of the layer leads to increased non-radiative recombination within the perovskite layer and could be a result of charge build-up from the reduced extraction. This degradation is non-reversible.

REFERENCES

[1] NASA, “The Sunshield Webb”, Retrieved July 16, 2022, from https://webb.nasa.gov/content/observatory/sunshield.html

[2] Papež, N., Škvarenina, Ľ., Tofel, P., & Sobola, D., “Thermal stability of gallium arsenide solar cells. Photonics”, *Devices, and Systems VII*, 10603, 2017, https://doi.org/10.1117/12.2292673

[3] Pisacane, V. L., “The Space Environment. In Fundamentals of Space Systems”, *Oxford University Press*, pp. 49–74

[4] Garcia, M., “International Space Station Facts and Figures”. Retrieved March 16, 2019, from https://www.nasa.gov/feature/facts-and-figures

[5] ESA, “Cubesats”, Retrieved July 16, 2022, from https://www.esa.int/Enabling_Support/Preparing_for_the_Future/Discovery_and_Preparation/CubeSats

[6] Li, J., Yan, S., Cai, R., “Thermal analysis of composite solar array subjected to space heat flux”, *Aerospace Science and Technology*, 27(1), 84–94, 2013 https://doi.org/10.1016/j.ast.2012.06.010

[7] Ghosh, T., “International Space Station Thermally Induced Solar Array Base Loads”, Retrieved June 16, 2022, from https://web.mscsoftware.com/support/library/conf/auc97/p01997.pdf#page=13&zoom=auto,-226,571.

[8] Tumen-Ulzii, G., Qin, C., Matsushima, T., Leyden, M.R., Balijipalli, U., Klotz, D. and Adachi, C. (2020), Understanding the Degradation of Spiro-OMeTAD-Based Perovskite Solar Cells at High Temperature. Sol. RRL, 4: 2000305. https://doi.org/10.1002/solr.202000305

[9] Yannick Borthomieu, “14 - Satellite Lithium-Ion Batteries”, Editor(s): Gianfranco Pistoia, Lithium-Ion Batteries, Elsevier, 2014, Pages 311-344, ISBN 9780444595133, https://doi.org/10.1016/B978-0-444-59513-3.00014-5.

[10] Jena, A. K., Numata, Y., Ikegami, M., & Miyasaka, T. (2018). Role of spiro-ometad in performance deterioration of perovskite solar cells at high temperature and reuse of the perovskite films to avoid PB-waste. Journal of Materials Chemistry A, 6(5), 2219–2230. https://doi.org/10.1039/c7ta07674f

[11] Jeong, S.-Y., Kim, H.-S., Park, N.-G. (2022). Challenges for thermally stable Spiro-MeOTAD toward the market entry of highly efficient perovskite solar cells. ACS Applied Materials & Interfaces, 14(30), 34220–34227. https://doi.org/10.1021/acsami.1c21852

[12] Kim, S., Bae, S., Lee, S.-W., Cho, K., Lee, K. D., Kim, H., Park, S., Kwon, G., Ahn, S.-W., Lee, H.-M., Kang, Y., Lee, H.-S., Kim, D. (2017). Relationship between ion migration and interfacial degradation of CH3NH3PBI3 perovskite solar cells under thermal conditions. Scientific Reports, 7(1). https://doi.org/10.1038/s41598-017-00866-6

[13] Malinauskas, T., Tomkute-Luksiene, D., Sens, R., Daskeviciene, M., Send, R., Wonneberger, H., Jankauskas, V., Bruder, I., Getautis, V. (2015). Enhancing thermal stability and lifetime of solid-state dye-sensitized solar cells via molecular engineering of the Hole-transporting material Spiro-OMeTAD. ACS Applied Materials Interfaces, 7(21), 11107–11116. https://doi.org/10.1021/am5090385

[14] Hasan, M. S., Alom, J., Asaduzzaman, M., Ahmed, M. B., Hossain, M. D., Saem, A. S. M., Masud, J., Thakare, J., Hossain, M. A. (2022). Recent criterion on stability enhancement of perovskite solar cells. Processes, 10(7), 1408. https://doi.org/10.3390/pr10071408

[15] Tsoi, W. C., Barbé, J., Pockett, A., Stoichkov, V., Hughes, D., Lee, H. K., Carnie, M., Watson, T. (2021). In situ investigation of perovskite solar cells' efficiency and stability in a mimic stratospheric environment for high-altitude pseudo-satellites. Proceedings of the 13th Conference on Hybrid and Organic Photovoltaics. https://doi.org/10.29363/nanoge.hopv.2021.020

[16] Christian Wehrenfennig, Mingzhen Liu, Henry J. Snaith, Michael B. Johnston, and Laura M. Herz , "Charge carrier recombination channels in the low-temperature phase of organic-inorganic lead halide perovskite thin films", APL Materials 2, 081513 (2014) https://doi.org/10.1063/1.4891595

[17] Qin, C., Matsushima, T., Fujihara, T., Potscavage, W. J., Adachi, C. (2015). Degradation mechanisms of solution-processed planar perovskite solar cells: Thermally stimulated current measurement for analysis of Carrier Traps. Advanced Materials, 28(3), 466–471. https://doi.org/10.1002/adma.201502610

[18] Yihua Chen, Shunquan Tan, Nengxu Li, Bolong Huang, Xiuxiu Niu, Liang Li, Mingzi Sun, Yu Zhang, Xiao Zhang, Cheng Zhu, Ning Yang, Huachao Zai, Yiliang Wu, Sai Ma, Yang Bai, Qi Chen, Fei Xiao, Kangwen Sun, Huanping Zhou, Self-Elimination of Intrinsic Defects Improves the Low-Temperature Performance of Perovskite Photovoltaics, Joule, Volume 4, Issue 9, 2020, Pages 1961-1976, ISSN 2542-4351, https://doi.org/10.1016/j.joule.2020.07.006.

[19] Lopez-Varo, P., Amara, M., Cacovich, S., Julien, A., Yaïche, A., Jouhari, M., Rousset, J., Schulz, P., Guillemoles, J.-F., Puel, J.-B. (2021). Dynamic temperature effects in perovskite solar cells and energy yield. Sustainable Energy & Fuels, 5(21), 5523–5534. https://doi.org/10.1039/d1se01381e

[20] Meng, Q., Chen, Y., Xiao, Y.Y. et al. Effect of temperature on the performance of perovskite solar cells. J Mater Sci: Mater Electron 32, 12784–12792 (2021). https://doi.org/10.1007/s10854-020-03029-y

[21] Moot, T., Patel, J. B., McAndrews, G., Wolf, E. J., Morales, D., Gould, I. E., Rosales, B. A., Boyd, C. C., Wheeler, L. M., Parilla, P. A., Johnston, S. W., Schelhas, L. T., McGehee, M. D., Luther, J. M. (2021). Temperature coefficients of perovskite photovoltaics for energy yield calculations. ACS Energy Letters, 6(5), 2038–2047. https://doi.org/10.1021/acsenergylett.1c00748

[22] R.G. Pires, R.M. Dickstein, S.L. Titcomb, R.L. Anderson, Carrier freezeout in silicon, Cryogenics, Volume 30, Issue 12, 1990, Pages 1064-1068, ISSN 0011-2275, https://doi.org/10.1016/0011-2275(90)90208-T.

[23] Yu, C., Chen, Z., J. Wang, J., Pfenninger, W., Vockic, N., Kenney, J. T., & Shum, K. (2011). Temperature dependence of the band gap of Perovskite Semiconductor compound CSSNI3. Journal of Applied Physics, 110(6), 063526. https://doi.org/10.1063/1.3638699

[24] Pérez-Osorio, M. A., Lin, Q., Phillips, R. T., Milot, R. L., Herz, L. M., Johnston, M. B., & Giustino, F. (2018). Raman spectrum of the organic–inorganic halide perovskite CH3Nh3PBI3 From first principles and high-resolution low-temperature Raman measurements. The Journal of Physical Chemistry C, 122(38), 21703–21717. https://doi.org/10.1021/acs.jpcc.8b04669

[25] Quan Wang, Yanmin Zhang, Ran Hu, Daohan Ge, and Naifei Ren , "Structure disorder degree of polysilicon thin films grown by different processing: Constant C from Raman spectroscopy", Journal of Applied Physics 114, 183504 (2013) https://doi.org/10.1063/1.4829667

[26] J. L. Brédas , "Relationship between band gap and bond length alternation in organic conjugated polymers", J. Chem. Phys. 82, 3808-3811 (1985) https://doi.org/10.1063/1.448868

[27] Zhao, X., Kim, H.-S., Seo, J.-Y., Park, N.-G. (2017). Effect of selective contacts on the thermal stability of perovskite solar cells. ACS Applied Materials & Interfaces, 9(8), 7148–7153. https://doi.org/10.1021/acsami.6b15673

[28] Lakhiani, H., Dunlop, T., De Rossi, F., Dimitrov, S., Kerremans, R., Charbonneau, C., Watson, T., Barbé, J., Tsoi, W. C. (2019). Variations of infiltration and electronic contact in mesoscopic perovskite solar cells revealed by high‐Resolution Multi-mapping techniques. Advanced Functional Materials, 29(25), 1900885. https://doi.org/10.1002/adfm.201900885

[29] Tschannen, C. D., Gordeev, G., Reich, S., Shi, L., Pichler, T., Frimmer, M., Novotny, L., Heeg, S. (2020). Raman scattering cross section of confined carbyne. Nano Letters, 20(9), 6750–6755. https://doi.org/10.1021/acs.nanolett.0c02632

[30] Iaru, C. M., Geuchies, J. J., Koenraad, P. M., Vanmaekelbergh, D., Silov, A. Y. (2017). Strong carrier–phonon coupling in lead halide perovskite nanocrystals. ACS Nano, 11(11), 11024–11030. https://doi.org/10.1021/acsnano.7b05033

[31] Jiang, Y., Cui, M., Li, S., Sun, C., Huang, Y., Wei, J., Zhang, L., Lv, M., Qin, C., Liu, Y., Yuan, M. (2021). Reducing the impact of auger recombination in quasi-2d perovskite light-emitting diodes. Nature Communications, 12(1). https://doi.org/10.1038/s41467-020-20555-9

[32] Meng, L., Sun, C., Wang, R., Huang, W., Zhao, Z., Sun, P., Huang, T., Xue, J., Lee, J.-W., Zhu, C., Huang, Y., Li, Y., Yang, Y. (2018). Tailored phase conversion under conjugated polymer enables thermally stable perovskite solar cells with efficiency exceeding 21%. Journal of the American Chemical Society, 140(49), 17255–17262. https://doi.org/10.1021/jacs.8b10520

[33] Holliday, S., Ashraf, R., Wadsworth, A. et al. High-efficiency and air-stable P3HT-based polymer solar cells with a new non-fullerene acceptor. Nat Commun 7, 11585 (2016). https://doi.org/10.1038/ncomms11585

[34] Mu, S., Ye, Q., Zhang, X. et al. Polymer hole-transport material improving thermal stability of inorganic perovskite solar cells. Front. Optoelectron. 13, 265–271 (2020). https://doi.org/10.1007/s12200-020-1041-z

[35] Bagui, A., Iyer, S. S., Increase in Hole Mobility in poly(3-hexylthiophene-2,5-diyl) films annealed under electric field during the solvent drying step, Organic Electronics, 15(7), 1387–1395. (2014) https://doi.org/10.1016/j.orgel.2014.03.042

[36] Yaghoobi Nia, N., Bonomo, M., Zendehdel, M., Lamanna, E., Desoky, M. M., Paci, B., Zurlo, F., Generosi, A., Barolo, C., Viscardi, G., Quagliotto, P., Di Carlo, A. (2021). Impact of P3HT regioregularity and molecular weight on the efficiency and stability of perovskite solar cells. ACS Sustainable Chemistry Engineering, 9(14), 5061–5073. https://doi.org/10.1021/acssuschemeng.0c09015

[37] Rathore, P., Negi, C. M., Verma, A. S., Singh, A., Chauhan, G., Inigo, A. R., Gupta, S. K. (2017). Investigation of the optical and electrical characteristics of solution-processed poly (3 hexylthiophene) (P3HT): Multiwall Carbon Nanotube (MWCNT) composite-based devices. Materials Research Express, 4(8), 085905. https://doi.org/10.1088/2053-1591/aa7dac

[38] Paternò, G., Robbiano, V., Fraser, K. et al. Neutron Radiation Tolerance of Two Benchmark Thiophene-Based Conjugated Polymers: the Importance of crystallinity for Organic Avionics. Sci Rep 7, 41013 (2017). https://doi.org/10.1038/srep41013

[39] Kumar, S., Kumar, M., Rathi, S., Yadav, A., Upadhyaya, A., Gupta, S. K., ; Singh, A. (2018). Study of P3HT/ PCBM morphology using Raman spectroscopy. AIP Conference Proceedings. https://doi.org/10.1063/1.5033010

[40] Mansour, A. E., Valencia, A. M., Lungwitz, D., Wegner, B., Tanaka, N., Shoji, Y., Fukushima, T., Opitz, A., Cocchi, C., Koch, N. (2022). Understanding the evolution of the Raman spectra of molecularly P-doped poly(3-hexylthiophene-2,5-diyl): Signatures of Polarons and bipolarons. Physical Chemistry Chemical Physics, 24(5), 3109–3118. https://doi.org/10.1039/d1cp04985b

[41] Saeed Salem Babkair, Ameer Azam, Kuldeep Singh, Sundeep Kumar Dhawan, and Mohd Taukeer Khan "Synthesis and optoelectrical properties of f-graphene/cadmium selenide hybrid system," Journal of Nanophotonics 9(1), 093048 (13 October 2015). https://doi.org/10.1117/1.JNP.9.093048

[42] Meyer, E. L. (2017). Extraction of saturation current and ideality factor from measuring voc and isc of photovoltaic modules. International Journal of Photoenergy, 2017, 1–9. https://doi.org/10.1155/2017/8479487

Chapter 6

Flexible Thin Film Spray Encapsulation

6.1 Introduction

As detailed in Section 1.3, the external conditions found in space and in a LEO pose a variety of different problems when looking at the continued performance of perovskite solar cells. To reduce the severity of several degradation channels when operating in LEO, solar cells in space are commonly encapsulated with space qualified glass. This glass is used to ensure prolonged high performance by reducing the transmission of UV compared to regular soda lime glass, and by being radiation stable under high energy bombardment.[1] Similar encapsulation techniques are used for solar cells operating on Earth and protect the metal contact side of the device, which normally is in contact with the air. The most common form on encapsulation is soda lime glass, as this provides a stable and long-lasting encapsulation layer. However, for aerospace applications, soda lime glass encapsulation is rigid and heavy. This increases the overall weight of the solar cells and means the devices cannot be flexible. The removal of this thick, solid encapsulation layer allows for lower overall weight for the device, an important factor for space payloads. Therefore, a new encapsulation method must be considered that is flexible and lightweight. The new encapsulation layer should be as light as possible without reducing the stability of the devices.

This chapter looks at improving upon the currently used rigid glass encapsulation method by incorporating spray coating techniques to maximise the protection of PSCs from external stimuli, improve the flexibility of the PSCs, but also reducing the overall weight of the substrate to improve the specific power (power-to-weight ratio).

6.2 Results and Discussions

6.2.1 Currently Used Encapsulation Technique

The most used encapsulation technique for PSCs is soda lime glass, which is normally affixed to the substrate through epoxy. This is known as Glass-Glass Encapsulation.[1] However, as this epoxy can degrade and even dissolve the perovskite active layer, a protective polyimide tape is normally applied on top of the pixels. This incorporates three different materials into one encapsulation process, and each have drawbacks of their own. The protective tape must be applied carefully as once it is placed it cannot be removed without damaging the pixels. The epoxy used can require curing time in which the epoxy solidifies and acts a strong adhesive. This curing process often involves the use of UV light, which as shown in Chapter 1, can cause degradation within the perovskite active layer and/or transporting layers. The application of the encapsulation glass onto the device adds mechanical stress to the PSC, which has been shown to negatively affect device performance.[2] A cartoon of the soda lime glass encapsulation method is shown in Figure 6.1. Here the bottom 4 0.15 cm^2 are covered as these were the pixels that were measured during the testing.

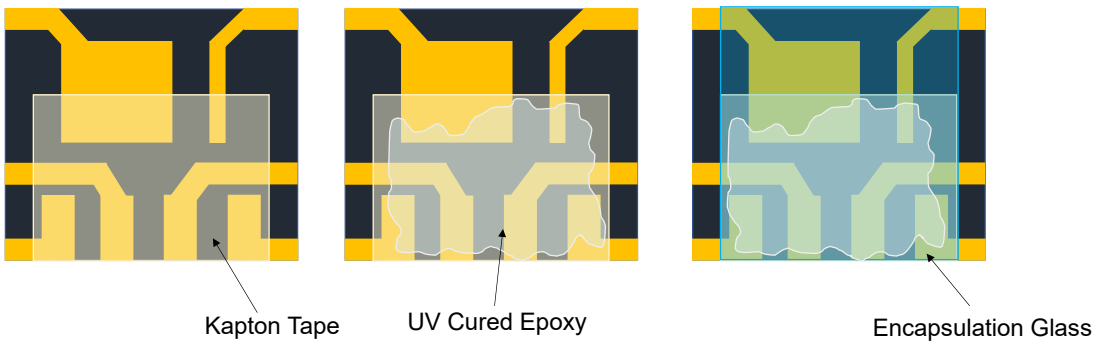

Figure 6.1 Cartoon of the 3 steps involved in the glass encapsulation technique. The Kapton tape is applied over the bottom 0.15 cm^2 pixels, followed by the application of the UV curved epoxy and encapsulation glass.

After the process shown in figure 6.1 is complete, the devices are placed under a UV bulb for 7 minutes to cure and harden the epoxy, completing the encapsulation process. The finished encapsulation process on a PSC following the design shown in Chapter 2 can be seen in Figure 6.2.

Figure 6.2 Perovskite solar cell with the completed glass encapsulation applied.

The glass encapsulation provides adequate protection against external stimuli such as humidity, O_2, and UVB on Earth.[3] In space, the presence of high energy radiation can reduce the optical transmittance of the glass as discussed in Chapter 1, therefore it has limitations in a LEO. However, even when considering only terrestrial application, there is a large drawback when using the glass encapsulation. Shown in this work, there is measured degradation to device performance due to the encapsulation process. This reduction in performance after encapsulation has been recorded for a variety of different encapsulation techniques.[4] The difference in performance between a batch (8 devices) of PSCs before and after glass encapsulation can be seen in Figure 6.3.

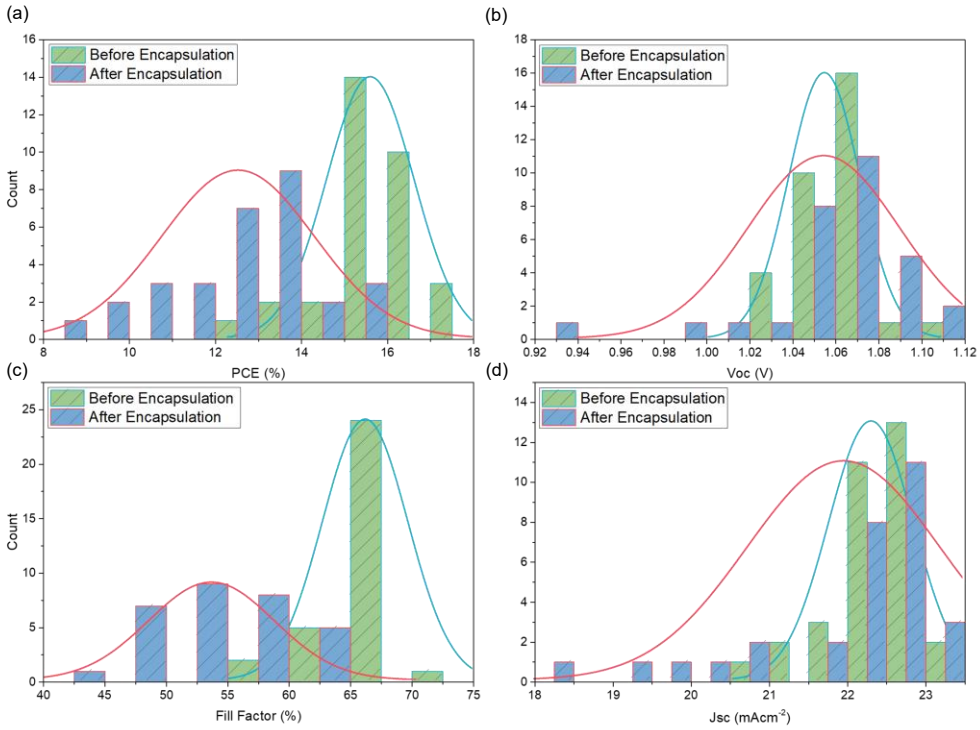

Figure 6.3 Comparison of PSC performance before and after the glass encapsulation process, with a normal curve fitted to each parameter. (a) PCE (b) V_{oc} (c) FF (d) J_{sc}.

From Figure 6.3, the average device performance decreases by 20% after encapsulation. The average J_{sc} decreases by 2%, the average V_{oc} by 0.03%, and the average FF decreases by 19%. Therefore, the largest change is in the FF. It is suggested that the degradation in the FF is caused by fractures that occurs due to the compressive strain from applying the glass encapsulation layer. It has been shown that the heating process of perovskite formulation induces tensile stress when the layer is cooled back to room temperature as the Thermal Expansion Coefficient (TEC) is mismatched between the perovskite and substrate.[2] This tensile stress reduces the fracture energy, the energy required to induce cracks within the layer, meaning the device layers are more susceptible the cracking. The formation of cracks and delamination because of strain has been observed in perovskite films.[5] Incidentally, after the application an encapsulation layer the facture energy has been observed to increase.[6] Indicating that while the encapsulation process degrades the devices, the encapsulation then improves the stability. Therefore, soda lime glass encapsulation, while offering good protection from a variety of different external stimuli, has drawbacks.

6.2.2 Spray Encapsulation Materials

To overcome the degradation of device performance, increased weight, and reduced flexibility that soda lime glass encapsulation offers, personal attention was drawn towards the use of thin film, polymer-based encapsulation techniques.

Three different spray encapsulation materials were chosen to investigate as a potential replacement for soda lime glass. These were silicone (polysiloxane), polyurethane and polymethyl methacrylate (PMMA). Silicone is a well-known polymer sealant, lubricant, adhesive, and insulator material.[7] Polyurethane is commonly used flexible polymer insulator than can be made flexible and is used on furniture to improve durability and wear.[8] PMMA is a well-known polymer material used in a variety of different applications and is often used a substitute for glass. Applications include sheeting, conformal coatings, and aircraft canopies.[9] All three options can be spray coated, improving the coverage over the solar cell and is a more

up-scalable process. These three materials were bought commercially from RS components, already in spray can format.

Initially the different polymer encapsulants were sprayed on bare glass substrates to investigate the wetting of each material and to measure the thickness of a single spray coat. This variation in spray patterns and thicknesses for each of the different? can be seen in Figure 6.4. The images were taken using a digital camera built into the Tencor profilometer.

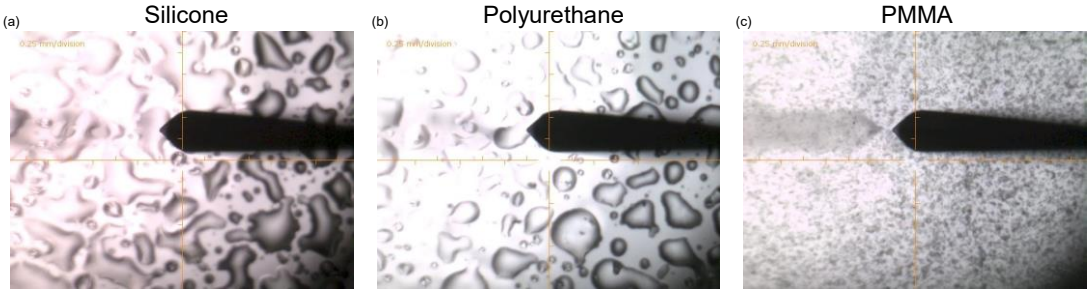

Figure 6.4 KLA Tencor profilometer imagery for 1 coat spray of (a) Silicone (b) Polyurethane (c) PMMA. The measurements were taken after the samples had dried (10 minutes).

As seen in Figure 6.5, the wetting on the glass is inhomogeneous for each material. The droplet size varies between each encapsulation material. However, from the profilometer imagery, the droplet size for the PMMA spray is visually very small and more homogenous in comparison to the silicone and the polyurethane. These samples were then measured with the profilometer to probe the droplet thicknesses for each material. The results are shown in Figure 6.5. Three different measurements were taken across the sample to investigate how the homogeneity of droplet thickness varied across the sample area, and are denoted as Scan 1,2, and 3.

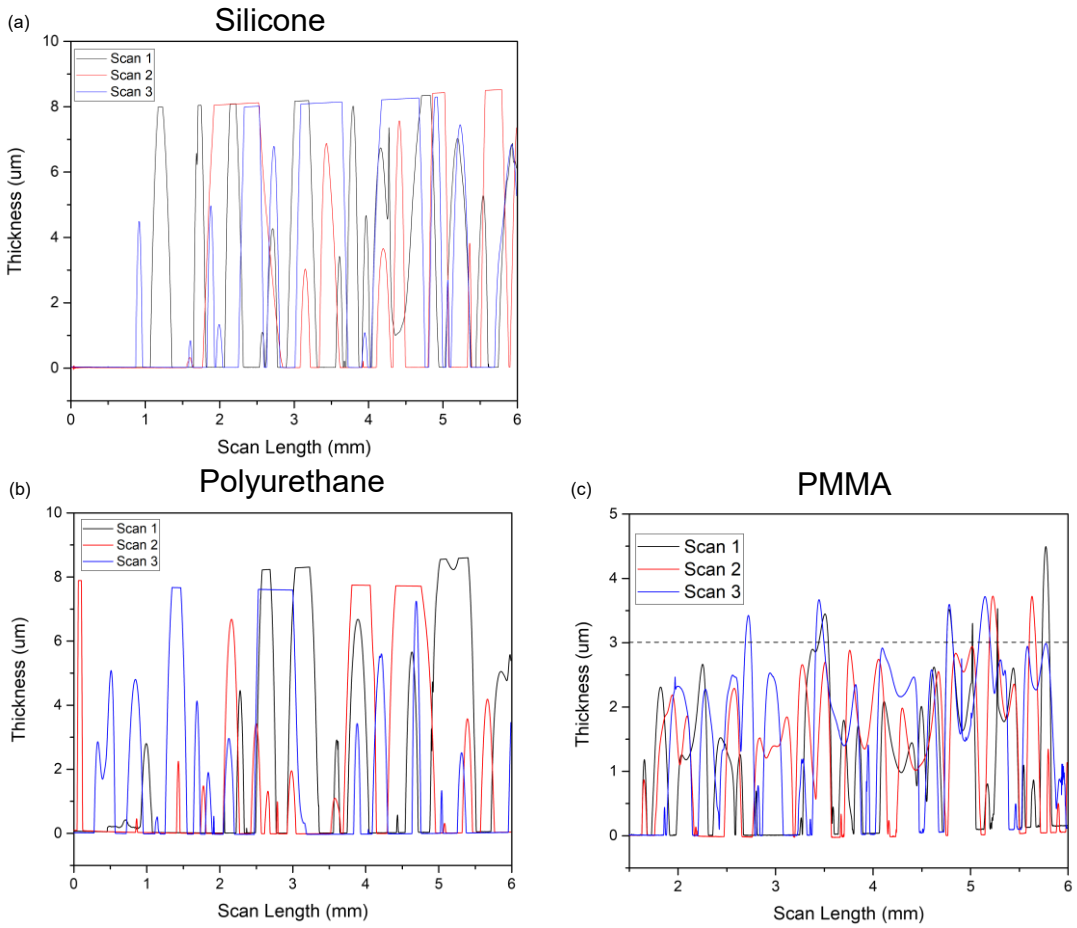

Figure 6.5 Profilometry data for one spray coat of the different encapsulation materials on bare soda lime glass. (a) Silicone (b) Polyurethane (c) PMMA.

From Figure 6.5, both the silicone and polyurethane have a comparable thickness with a maximum droplet thickness of ~8 µm. However, the droplet thickness varies greatly, with some droplets being <1 µm and the overall thickness range for both silicone and polyurethane being 500 nm – 8 µm. For the PMMA spray, the droplet size is significantly smaller, with many of the droplets having a thickness between ~2-3 µm.

Initially, all three encapsulation materials were to be used and their encapsulation properties characterized. However, due to the solvent/solubility for each of the encapsulation materials, it was clear that there would be performance issues spraying directly onto the PSCs used in this thesis. As stated in Section 2.2.1, the spiro-OMeTAD is dissolved in CB. However, it is also easily dissolvable in a variety of different organic solvents. These solvents include toluene, xylene, and ethyl acetate. These solvents are used to dissolve the spray materials, with silicone being

dissolved in xylene, polyurethane in toluene and PMMA in ethyl acetate. These details are shown in Table 6.1, along with the vapour pressure at 25°C for each of the organic solvents. The vapour pressure is a measure of the tendency for a material to change into a gaseous/vapour state. 55°C was chosen due to the PSCs utilising spiro-OMeTAD as an HTL. As seen in Chapter 5, spiro-OMeTAD is thermally unstable at temperatures >60 °C, therefore a temperature lower than 60 °C was required to maximise drying without degrading the devices.

Table 6.1 Encapsulation materials, the organic solvent used in the spray, and the vapour pressure of each solvent at room temperature and 55 °C.[10]

Encapsulation Material	Spray Solvent	Vapour Pressure at 25 °C (mm Hg)	Vapour Pressure at 55 °C (mm Hg)
Silicone	Xylene	6.5	41
Polyurethane	Toluene	28	112.5
PMMA	Ethyl Acetate	94.7	346.6
Water	H_20	25	118

Comparing the vapour pressure of each of the solvents, xylene has a much lower value than water, meaning that it will evaporate at a much slower rate. Whereas, both toluene and ethyl acetate are higher. Toluene evaporates slightly faster than water, and ethyl acetate evaporates ~4x faster than water at 25 °C. At higher temperatures, the vapour pressure increases, however ethyl acetate still evaporates at a much higher rate, with toluene and xylene evaporating slower than water. Given that the cells are limited by the heating temperature due to the spiro-OMeTAD HTL, the best candidate to test and characterise was PMMA due to its fast solvent evaporation and lower boiling point (77.1 °C).[11]

6.2.3 PMMA Layer Thickness Measurements

Once PMMA was chosen as the preferred encapsulation candidate moving forward, the layer thickness would need to be determined to understand encapsulation properties, such as the Water Vapour and Oxygen Transfer Rate (WVTR & OTR respectively). These rates are the measure of permeability to water vapour and oxygen and was an important factor in optimising layer thickness and coverage.

As mentioned above, the process for spray coating devices would need to incorporate low temperature heating to evaporate the ethyl acetate to minimise any degradation to the spiro layer. As referenced in Chapter 5, spiro-OMeTAD can undergo thermal degradation at temperatures as low as 60 °C, so a lower temperature would be needed to reduce any degradation from the heating process as well. The chosen temperature was 55 °C. Once the temperature was chosen, masks were fabricated that allowed for the pixels to be spray coated, but also for the ITO and Au contacts to still be connected, due to PMMA being an insulator. The spraying technique used to encapsulate the PSCs with PMMA is shown in Figure 6.6.

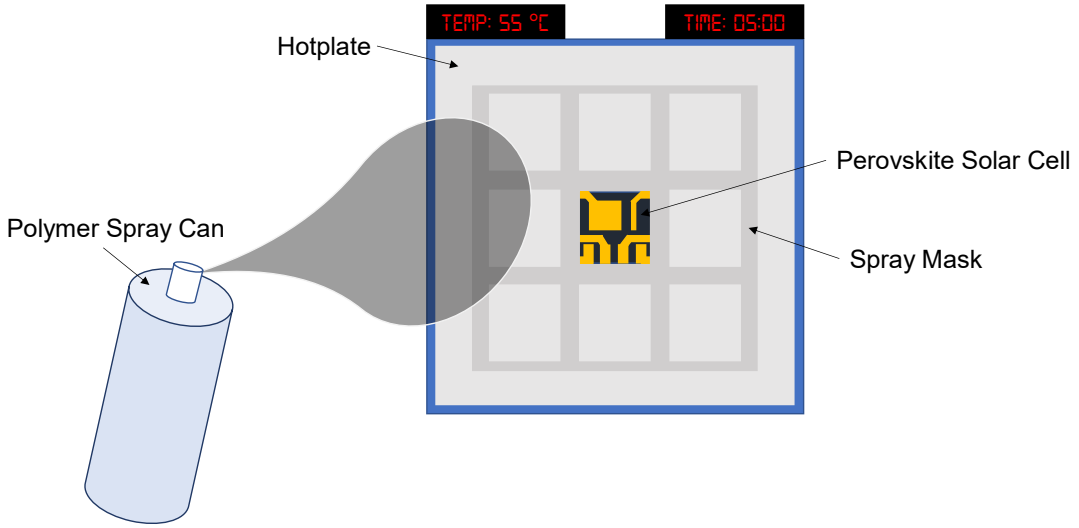

Figure 6.6 Cartoon of the experimental set-up for the deposition of the thin film PMMA encapsulation layer. Here the hot plate is set to 55 °C (top left) and the samples are left for 5 minutes to dry after coating (top right).

In the spray set-up, the cells and mask are placed onto a hotplate set to 55°C and left to reach thermal equilibrium (5 minutes). The spray can is moved across the device and back again, this is defined at 1 coat. Therefore 2 coats is 4 passes, 3 coats is 6 etc. Once the device has been coated, it is left on the hotplate for 5 minutes to evaporate the ethyl acetate. Then the devices and mask are removed from the hotplate and left to cool (5 minutes). After this 5-minute cooling period, the devices are encapsulated.

After spray encapsulating a PSC, profilometer measurements were taken to investigate the PMMA encapsulation thickness on-top of the device rather than on a

glass substrate. The results are shown in Figure 6.7. In these measurements, the profilometer is set to measure outside the encapsulation area initially, before passing over the PMMA layer. This is to account for the roughness of the spiro-OMeTAD layer and set a baseline.

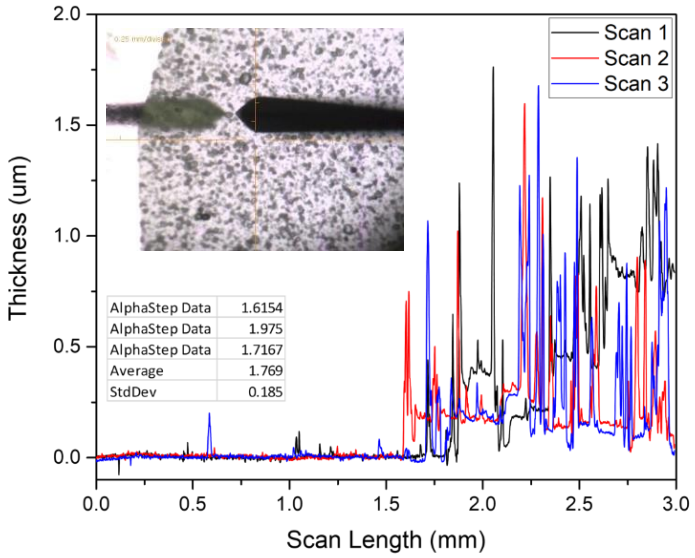

Figure 6.7 Profilometer data over 3 scans with the average and standard deviation included. Insert is the profilometer camera image of the PMMA layer on the spiro-OMeTAD HTL.

From Figure 6.7, one coat of PMMA gives a very rough layer and as seen previously when spray coated on glass, the droplet size is small (~0.125 mm). This large variation and roughness indicated that more spray coats would be needed to get a layer thickness that is more uniform. While this is a real result, the layer thickness is noisy and non-uniform. This is an issue when looking at parameters such as WVTR as it is affected by layer thickness.[12] Therefore, it was decided to repeat the measurements with more coatings. Three coats of PMMA spray encapsulation was applied to a PET flexible substrate using the same spray mask as the PSCs. The profilometry measurement for this 3-coat film is shown in Figure 6.8. The substrates were changed from glass to PET in this case as these films were also used for bend testing measurements, which are shown in Section 6.2.5.4.

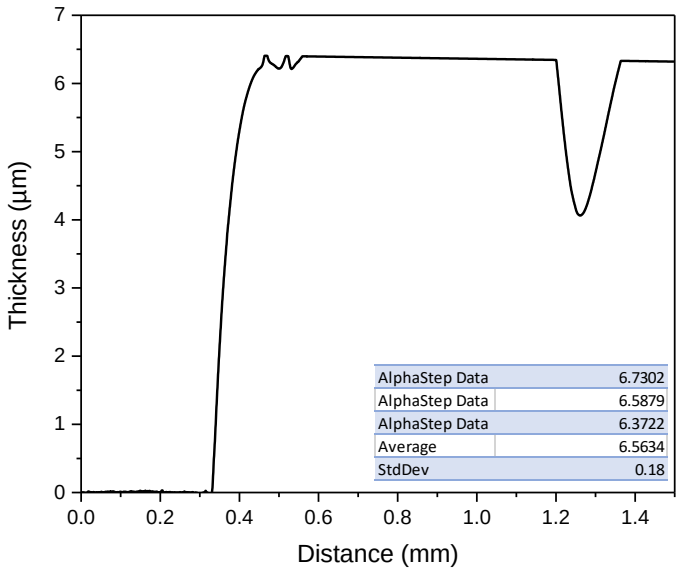

Figure 6.8 Averaged profilometer measurement for 3 coats of PMMA on a PET substrate. The three different measurements were taken at different locations around the encapsulation layer.

In the case of PMMA on PET substrates, multiple PMMA spray coats give a much more uniform film and decreases the roughness of the encapsulation layer. The variation in droplet size and thickness is also reduced and the average layer thickness of ~6.56 ± 0.18 µm is mostly consistent. However, as observed in Figure 6.8, there are still troughs that appear in the encapsulation layer, meaning the layer is not complete homogenous. While the layer underneath the PMMA encapsulation is different, the 3 coat measurements on PET are for more uniform compared to Figure 6.7. Assuming a linear increase in thickness with increasing number of coats, the thickness of 1 coat PMMA is ~2.17 µm. However, the profilometry measurements in Figure 6.7 an average thickness of 1.77 µm meaning that the increase in thickness is not linear. Therefore, a different technique was needed to characterise the thickness of a 1 coat PMMA layer.

In the literature, it has been shown that for a variety of different materials, such as graphite and transparent polymers, the Raman spectra can be used to determine layer thickness.[13] In this case, the Raman intensity is directly proportional to the layer thickness and therefore increases with increasing thickness. By measuring the Raman signal of the PMMA film on the PET substrates and correlating that to the profilometry measurements, the intensity ratio between the different

coating numbers would allow for an estimated layer thickness. The Raman spectra of a bare PET substrate was also measured in case there were any overlapping peaks with the PMMA signal.

The Raman signal from the PMMA/PET samples can be found in Figure D.1. The Raman signal from the PET almost perfectly overlaps the PMMA signal. Therefore, the Raman signal measured for the PMMA films may also include signal from the PET as the PMMA is transparent. Additionally, if there is any non-uniformity in the layer this could cause the laser to directly probe the PET. The inability to disassociate one from the other means that the results from these measurements are unreliable and inaccurate. To rectify this issue, the same procedure was performed on crystalline silicon (c-Si) substrates.

C-Si has a well-known single Raman peak at 520 cm^{-1}, therefore there should be no other overlap with the PMMA. In addition to the 1 and 3 coat samples, a 2-coat sample was also prepared as this would help with understanding how multiple sprays affect the overall thickness of the encapsulation layer. The averaged Raman spectra from these measurements is shown in Figure 6.9 and the mapping results can be found in Figure D.2.

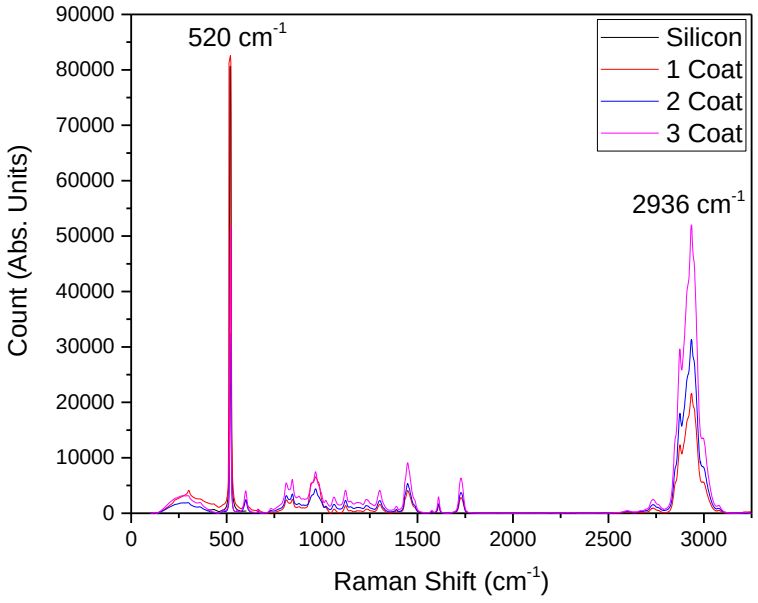

Figure 6.9 Averaged Raman spectra for a bare c-Si along with the averaged Raman spectra for 1,2, and 3 coat c-Si/PMMA samples.

As expected, the c-Si has a peak at 520 cm^{-1}. In comparison to the PET/PMMA Raman signal, the peak at 3081 cm^{-1} is no longer visible, indicating that the laser was able to penetrate to the PET layer and its highly likely the spectra in Figure D.1 is from the PET. However, there is peak at 2936 cm^{-1} attributed to the vibration of the C-H bonds that was used to estimate the 1 coat and 2 coat layer thickness.[14] By taking the ratio of the peak intensity, the thickness of 1 coat was calculated to be ~2.7 µm and the thickness of 2 coat was calculated to be ~3.9 µm. While the 3 coat profilometry measurement is on PET not silicon, the calculated thickness are a reasonable estimation as the PMMA is spray coated. The difference between the Raman calculated 1 coat layer thickness and the 3 coat profilometer measurement suggests that there is not a linear relationship between the number of spray coats and the resultant layer thickness. Assuming homogeneity in the PMMA thickness, the estimated thickness of 2.7 µm is ~400x thinner that the 1.1 mm encapsulation glass used in the current glass encapsulation technique. In terms of the weight of overall substrates, the spray encapsulated device weighs ~60mg while the glass encapsulated device weighs ~1.7g. This is a ~283x reduction in weight (~1.64g difference).

Now that the spray encapsulation layer thickness was known, testing and characterisation of the encapsulation was required. This included the variation in device performance before and after encapsulation; the thermal stability of the encapsulation layer as this is relevant to the operation of the devices in a LEO environment; and the dark storage stability and humidity stability as the cells would need to maintain performance while they are stored before they are launched into orbit.

6.2.4 Performance Before and After Encapsulation

As mentioned in Section 6.1.1, it is suggested that the use of glass encapsulation negatively affects device performance due to the delamination of the perovskite and HTL layer from compressive strain. This is shown in Figure 6.3. An important test for the spray encapsulation is how the application affects the device performance, especially due to the organic solvents used in the spraying process. Therefore, the

devices were measured before and after the application of the PMMA encapsulation layer. The results of this comparison are presented in Figure 6.10.

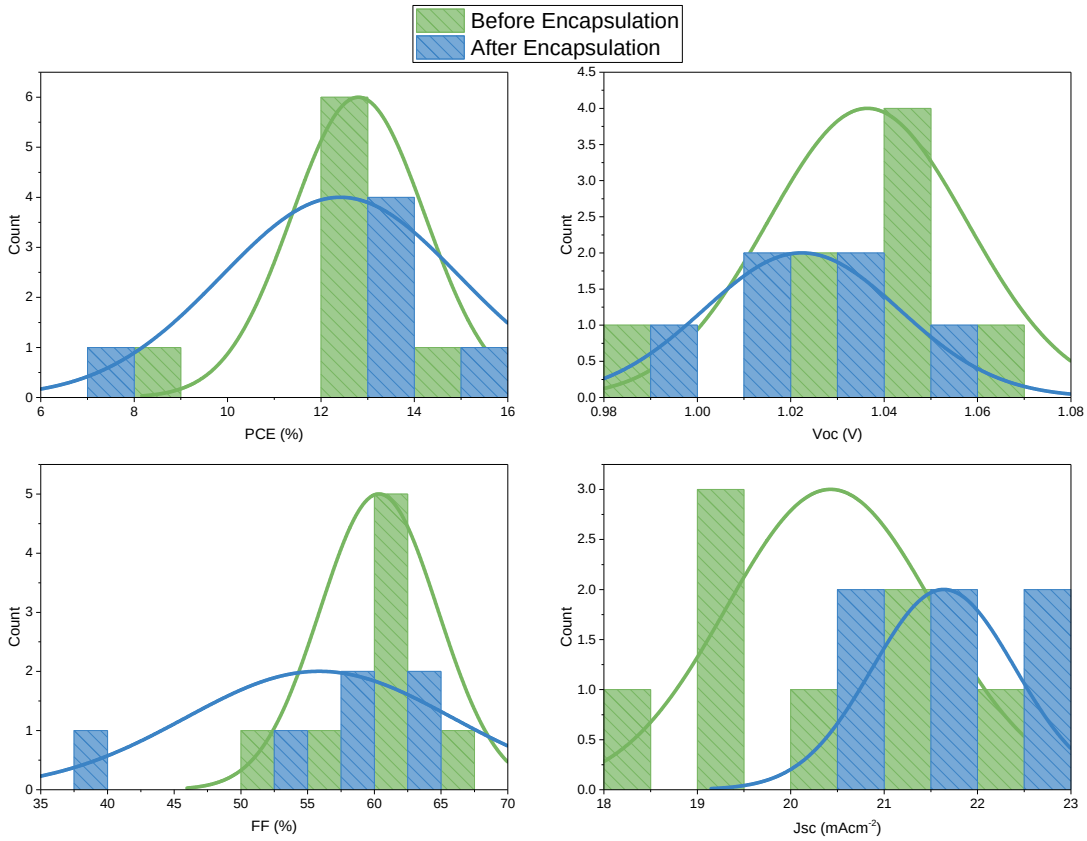

Figure 6.10 PV Parameters for PSCs before and after PMMA spray encapsulation. The results shown are for a 1 coat encapsulation process to investigate how a single coat affected device performance.

After encapsulation, it appears the overall PCE of the devices remains largely unchanged. Here the average PCE after encapsulation is 12.42%, which is slightly decreased from the initial average of 12.81% (~3% decrease). Due to issues of shadowing from the spray mask, the pixel count after encapsulation was reduced. This showcases the importance of the mask, as the encapsulation layer is a good insulator and can easily stop contact being made to the electrodes. In comparison with the glass encapsulation, the PCE decreases from an average of 15.63 to 12.54% (~20% decrease). The V_{oc} remained very consistent, with the average Voc before encapsulation being 1.04 V, and after encapsulation it decrease to 1.02 V (~1% decrease). In comparison with the glass encapsulated device, the V_{oc} remains unchanged. The fill factor is significantly reduced with a 10% absolute decrease in

one pixel; however, this is not mirrored across all measurements and excluding this outlier the average FF decreases by 1% from 60.35 to 59.78% after encapsulation. There is a considerable shift in J_{sc} from 18-22 $mAcm^{-2}$ before encapsulation, to 21-23 $mAcm^{-2}$ after. The improvement in performance is unlikely to be due to PMMA layer itself as it is an insulator and will not improve the conductivity of the electrodes. Further work will be needed to investigate the mechanisms behind this increase.

6.2.5 PMMA Encapsulation Heat, Humidity, and Bend Stability

6.2.5.1 Thermal Stability

As showcased in Chapter 5, the thermal stability of PSCs is paramount to their inclusion in aerospace applications, and especially space applications. Therefore, it was very important that the durability of the PMMA encapsulation layer was tested under the same thermal cycling procedure. The PMMA spray is only certified within the temperature range of -40°C to 60°C, therefore the thermal cycling will be applying much higher thermal stress onto the encapsulation layer. Additionally, comparing the thermal cycle performance against a non-encapsulated device and a glass encapsulated device will assist in separating degradation of the spiro-OMeTAD from the PMMA. If the thermal stability of the PMMA encapsulated and glass encapsulated device was similar, any decrease in performance would be attributed to the spiro-OMeTAD layer as degradation is expected at the temperature range of -100 to +85 °C, as shown in Chapter 5.

The 1 coat, unencapsulated and glass encapsulated thermal cycling stability testing results are shown in figure 6.12. Here the devices were thermally cycled in the dark and exposed to 1 Sun AM0 light intensity during measurements. The vacuum level during these measurements was ~$9x10^{-2}$ mbar as described in Section 2.5.3.

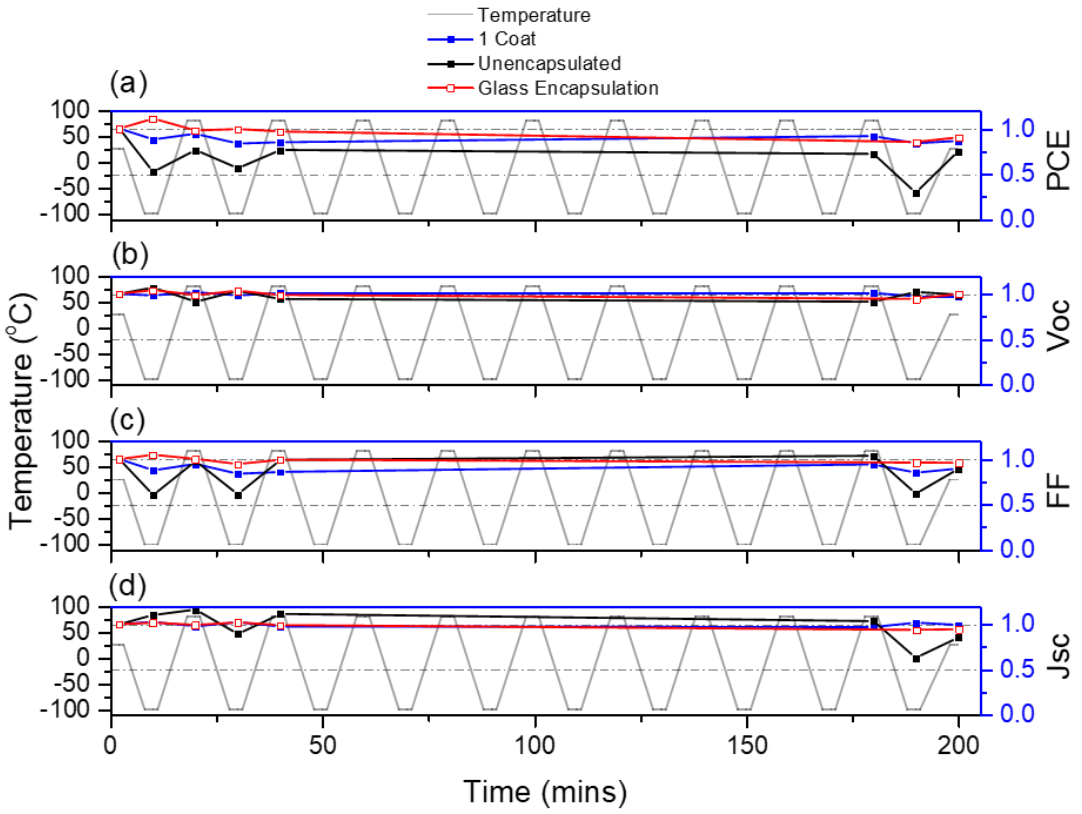

Figure 6.11 Normalised PV parameter comparison for the 1 coat, unencapsulated and glass encapsulated PSCs under thermal cycling from -100 to +85 °C. Shown top to bottom (a) PCE (b) V_{oc} (c) Fill Factor (d) J_{sc}

From Figure 6.11, the normalised PV parameters show that the 1 coat spray encapsulated device stability is comparable to the glass encapsulated device. Comparing the final PCE after the thermal cycling, the unencapsulated device PCE decreasing to 75% of its initial PCE. The 1 coat and glass encapsulated devices PCE decreased to 86% and 90% respectively. The main cause of the unencapsulated device's PCE decrease is a 15% decrease in the J_{sc}. This is attributed to the degradation of the spiro-OMeTAD HTL, with the 1 coat maintaining 99% of it's initial J_{sc}, with the glass encapsulated device maintaining 94%. The Jsc retention for the encapsulated devices is attributed to the increase of the fracture energy because of the encapsulation.[15] If the encapsulation is rigid or has a similar TEC to the layer, more energy is required to create fractures because of thermal stress. However, the 1 coat device shows a decrease in FF (89% of initial) compared to the glass encapsulated device (96% of initial FF value). In terms of the V_{oc}, the difference is

negligible with the 1 coat device retaining 97% and the glass device retaining 99% of their initial values.

The difference in stability between the unencapsulated device, and both the spray and glass encapsulated PSCs, showcases how the inclusion of encapsulation improves upon the thermal stability of the PSCs by increasing the fracture energy. However, the thermal degradation of the spiro-OMeTAD HTL is still apparent. It is also observed that the encapsulated perform better at -100 °C compared with the unencapsulated device. Therefore, here it is suggested that the inclusion of the encapsulation reduces the tensile strain due to the contracting film under cold temperatures.

Under mimic vacuum and temperature conditions, the PMMA spray encapsulation is comparable to that of the glass encapsulation and successfully operates outside of the listed temperatures. This is a very important result as if the PMMA performed worse than not encapsulating the devices, the encapsulation layer would be unsuitable and would need to be replaced. Overall, the 1 coat PMMA is encapsulating the PSCs well and the thermal cycling stability is comparable to glass.

6.2.5.2 Dark Storage Stability

The next step was to probe the dark storage stability. There is a long waiting period between the fabrication of the solar cells, the creation of the solar array, and the payload launch. While the cells are stored in a dry (nitrogen) environment, the ambient condition stability of PMMA encapsulated PSCs is still important for terrestrial applications.

For the stability measurements of the PSCs, they were stored in dark under ambient conditions. These conditions were at a temperature of 22-25°C and the relative humidity between 30-50%. These conditions are like those detailed in the dark storage measurement standard ISOS D-1, in which the cells are kept at room temperature with a relative humidity of 50%.[16] In these measurements, the devices were left in a drawer and were measured one week and one month (~730 hours), respectively, after the spray encapsulation was applied. The cells were also measured before the spray encapsulation was applied. The results of this experiment can be seen in Figure 6.12. Unencapsulated and glass devices were not studied for a

comparison. This is because there is already a large amount of work looking at the ambient stability of PSCs, so the work here was compared to the literature.[4][17][18]

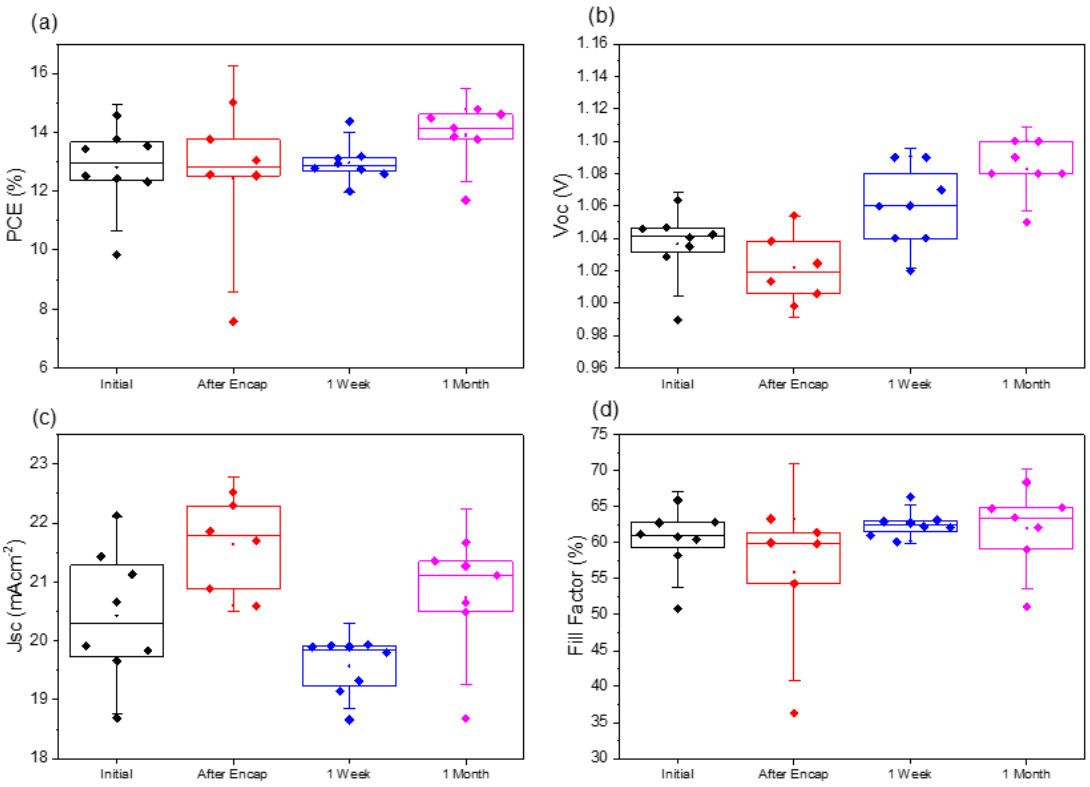

Figure 6.12 Box plot of the PV parameters measured during the dark storage stability testing for 1 coat encapsulated PSCs. The parameters shown are (a) PCE (b) Voc (c) Jsc (d) FF.

Initially, as seen in Figure 6.13, the PCE remains after the spray encapsulation is applied. After 1 week the PSCs show change in the PCE distribution. The distribution narrows, increasing the average PCE from 12.42% after encapsulation, to 13% after one week of dark storage. After 1 month in dark storage, the average PCE increases to 13.9%. This increase in PCE is attributed to the increase in the V_{oc} with increasing with the time spent in dark storage. In the analysis of Figure 6.13. However, as seen in Figure 6.13c, the average Jsc only increases after the initial encapsulation (21.64 $mAcm^{-2}$), before deceasing after 1 week (19.57 $mAcm^{-2}$) and then returning to similar values compared to before encapsulation (20.43 $mAcm^{-2}$) after 1 month in dark storage (20.75 $mAcm^{-2}$). The most noticeable trend is the continued increase in the Voc as the time in storage increases. Before encapsulation, the average Voc was 1.03 V, after 1 month in dark storage the average Voc was

measured to be 1.08 V. This is an increase of 5%. One potential reasoning is the presence of moisture inside the PSC as the PMMA has a WVTR. Moisture has been shown to increase PSC performance and the V_{oc} by promoting a reaction between PbI_2 and organic salts.[19][20] Another potential reason is increasing oxidation of Spiro-OMeTAD HTL. This increases the charge transfer at the perovskite/Spiro-OMeTAD/gold interfaces, decreasing the series resistance (R_s). Consequently, the fill factor is affected by Rs.[18] This reasoning is discussed further in Section 6.2.5.3.

In comparison to the literature, the 1 coat spray encapsulation performs better than not encapsulating the devices. A 60% decrease in PCE after 15 days of ambient storage has been observed in unencapsulated perovskite devices.[4] This degradation has also been confirmed through XRD measurements.[21] In comparison to glass encapsulation, the ambient humidity stability of the PMMA encapsulation is greater in some cases, as the type of epoxy used affects the stability.[4] Using the same glass-glass encapsulation method shown in Figure 6.1, PSCs have shown 90% PCE retention after 1000 hours.[22] With this decreasing to 70% retention after 4000 hours.[23] As the 1 month measurements are equivalent to 730 hours under ambient conditions, the PMMA encapsulated devices exhibit similar if not greater ambient stability than the glass-glass encapsulation method. Here is it concluded that 1 coat PMMA offers a good baseline in terms of dark storage conditions, however further work is needed to assess the stability over much longer time frames, and with a thicker PMMA layer.

6.2.5.3 Relative Humidity Stability in Ambient Air

Further testing was needed to probe the stability of the PMMA encapsulation under different relative humidity's. While this does not directly affect space-based PV, if the PMMA encapsulation provided excellent humidity stability it would also be appealing for terrestrial applications.

Firstly, a baseline was needed to allow a further investigation into what humidity was detrimental to perovskite devices and if the spray encapsulation would improve upon the stability. This was achieved using the humidity set-up shown in Chapter 2. Here, an unencapsulated, 1 coat and glass encapsulated PSC were humidity stepped from 10 to 80% RH, with a JV measurement taken at every 10% RH

interval after 5 minutes of wait time. The normalised device parameters as a function of increasing relative humidity are shown in Figure 6.13. The JV curves as a function of relative humidity are shown in Figure D.3.

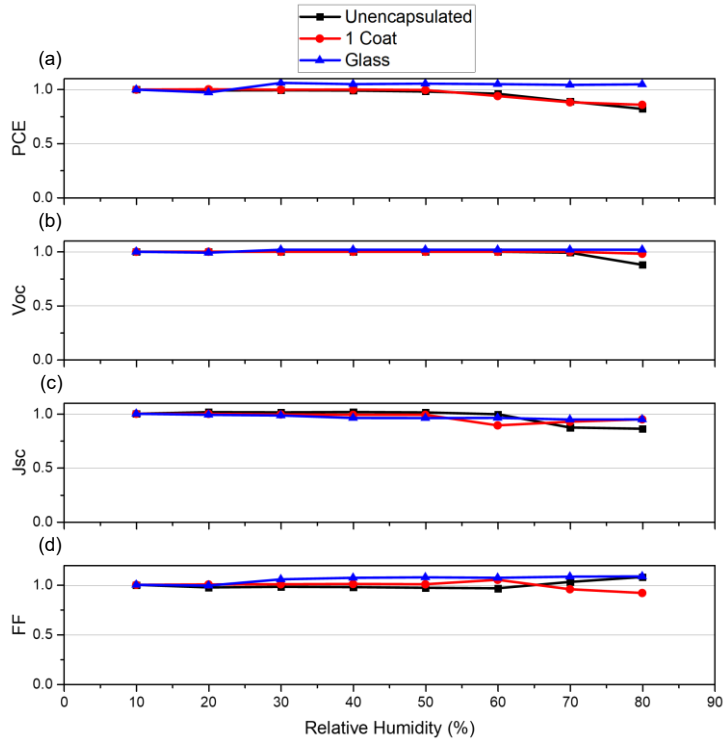

Figure 6.13 Normalised JV parameter for an unencapsulated, 1 coat and glass encpasulated device (a) PCE (b) Voc (c) Jsc (d) FF.

The glass encapsulation devices maintains a normalised PCE of 1.05 up to 90% RH and showcases the protection the glass encapsulation offers. This increase in PCE is due to a 9% increase in FF and 2% increase in V_{oc}. The Jsc decreases by 5%. In comparison, both the unencapsulated and 1 coat encapsulated devices show a sharp decrease in PCE after reaching 50% RH. The unencapsulated device encounters a PCE decrease of 4% at 50% RH, before degrading further at 80% RH with a 18% decrease in PCE. The 1 spray coat device exhibits a 1% decrease in PCE at 50% RH, but further declines to a 15% PCE loss at 80% RH. This loss in PCE is driven by the 5% and 8% reduction in the J_{sc} and FF respectively. The unencapsulated device undergoes a 14% decrease in J_{sc} at 80% RH. Unexpectedly, the FF increases at higher % RH, but as seen in Figure D.3, the JV shape is heavily distorted and has three potential V_{oc} values. This indicates that the measured FF value is incorrect and should be much lower, meaning

the PCE should be much lower for the unencapsulated devices as well. For the 1 spray encapsulated devices, the J_{sc} decreases by 5% and the FF decreases by 8% at 80% RH respectively. Same as in the case of the unencapsulated device, the JV line shape of the 1 coat PSC begins to distort from 50% RH and higher. The large decrease in PCE for the 1 coat spray encapsulated device compared to the glass encapsulation provides a large stumbling block for the use of the PMMA spray in terrestrial conditions. To understand why this decrease occurred at the same % RH as the unencapsulated device, the Water Vapour Transfer Rate (WVTR) for PMMA was considered.

WVTR is the measure of how much water vapour permeates through an area of material per unit time, and can be calculated through Equation 6.1:

$$WVTR = \frac{P_o(P_2 - P_1)}{L} e^{\frac{-E_a}{RT}} \quad (6.1)$$

Where P_0 is the permeation coefficient, ($P_2 - P_1$) is the partial pressure difference between the vapour and the material, L is the material thickness, E_a is the activation energy of the material, R is the ideal gas constant and T is the absolute temperature.[24] Normally this value is measured experimentally as there are several standards for measuring the WVTR.[25] However, the estimated WVTR is useful for a guide to further understand the degradation exhibited by the 1 coat encapsulated device. From published experimental data, the activation energy for PMMA is 65 $kJmol^{-1}$ and Po is 1.7 $g{\cdot}mm/m^2{\cdot}day{\cdot}atm$.[26][27] Taking the partial pressure difference to be 1 atm ($1x10^5$ Pa) and the temperature to be 293 k (room temperature), the WVTR of 1 coat PMMA is calculated to be ~16.27 $g/m^2{\cdot}day$. This value will be lower in practise as the partial pressure should be less than 1 atm. Initially, the similar performance between the unencapsulated and 1 coat PSC is counterintuitive as the PMMA film reduces the moisture entering the perovskite and degrading it. However, by correlating the profilometry data of 1 coat in Figure 6.7, there is large variation in film thickness across the encapsulated area. This inhomogeneity increases the WVTR, allowing for the moisture to enter the perovskite more readily. Interestingly, the relative humidity does not affect the WVTR of the material, only the temperature and the thickness. As the temperature of the cells remains the same during the

humidity stability experiments, the film thickness is the deciding factor in the WVTR calculation. Therefore, by making the PMMA film thicker and improving the film homogeneity, the humidity stability should be improved. The WVTR for a 2 and 3 coat PMMA film was calculated to be ~11.26 & ~6.77 g/m^2·day respectively. The reduction in the WVTR for the thicker films is as expected, and the stability should begin to correlate more with the decreasing WVTR. Due to the 1 coat PSC degrading >50% RH, the humidity stability experiment was repeated with the humidity held at 50% RH for 3 hours. JV measurements were taken every 10 minutes to investigate the change in the PV parameters over time. The normalised JV parameters over the 3 hours are presented in Figure 6.14. The J-V curves are shown in Figure D.4.

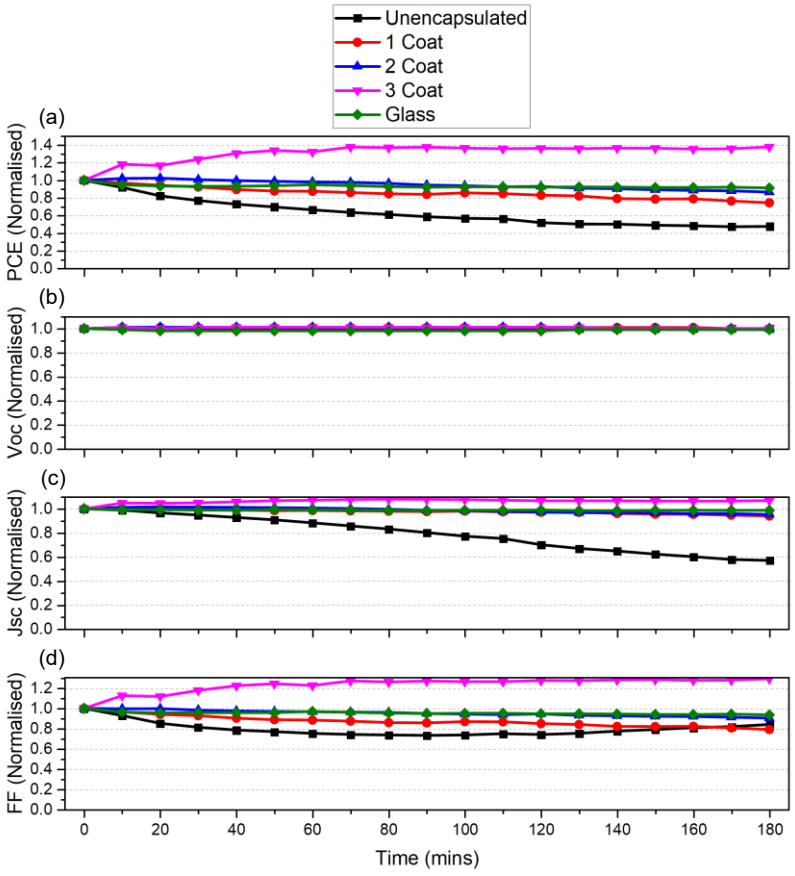

Figure 6.14 Normalised JV parameter for an unencapsulated, 1 coat, 2 coat, 3 coat, and glass encpasulated device (a) PCE (b) Voc (c) Jsc (d) FF

The inclusion of encapsulation significantly increases the device stability under the testing conditions as seen in Figure 6.15. The performance of the unencapsulated cell decreases to ~42% of its initial starting performance after 3 hours. This degradation is mainly driven by the reduction in the Jsc (43% reduction)

and FF (20% reduction). There is an increase in FF for the 1 coat device after 90 minutes of humidity holding. The cause of this increase is not currently known. As the devices are fabricated onto glass substrates, the moisture should enter the PSC through the Au face and therefore will encounter the perovskite at the perovskite/spiro interface. This means that the perovskite at the interface will begin to degrade first, which could affect the charge extraction, indicating the reduction in the J_{sc}. The Voc remains stable for the unencapsulated device across the 3-hour test. For the glass encapsulated device, the device performance degrades by 8% in the first 20 minutes and is then stable for the remaining 160 minutes (92% retained PCE). This decrease is due to a slight decrease in the FF (93% retained FF). The Voc and Jsc remain stable with 99% and 99% retention respectively.

For the PMMA encapsulated devices, the 1 coat encapsulated device follows a similar trend to the unencapsulated device, with a slow decrease in FF (79% retention) over the 3 hours (0.12 %/min), and a small decrease in J_{sc} (94% retention). The 1 coat device retains 74% of its initial PCE after 3 hours. The 2 coat PSC shows good FF retention (90%), good Jsc retention (95%), and retains 87% of its initial PCE after the experiment. As the J_{sc} decreases in the 1 and 2 coat devices, moisture must still be passing through the PMMA layer due to the inhomogeneity and high WVTR. However, the J_{sc} variation is minimal in comparison to the unencapsulated device. From Figure 6.15a and Figure 6.15h, the 3-coat device offers the best stability and performance under the testing conditions. The 3-coat device undergoes a 30% increase in PCE within the first hour of testing, and this increase is maintained throughout the remaining testing time. The V_{oc} remains unchanged during the humidity holding, with a 100% retention after 3 hours. The J_{sc} and FF undergo a 7% and 30% increase during the holding respectively. The increase in both the PCE of the 2 coat and 3 coat devices suggests a positive effect of the humidity holding. It has been shown that the inclusion of H_20 can improve performance of triple cation PSCs by improving the crystallinity of the perovskite.[28] To further probe why the devices improved with 3 coat encapsulation, Raman and PL measurements were taken on an unencapsulated, 3 coat, and glass encapsulated device while being held at 50% RH. The PL results are shown in Figure 6.15.

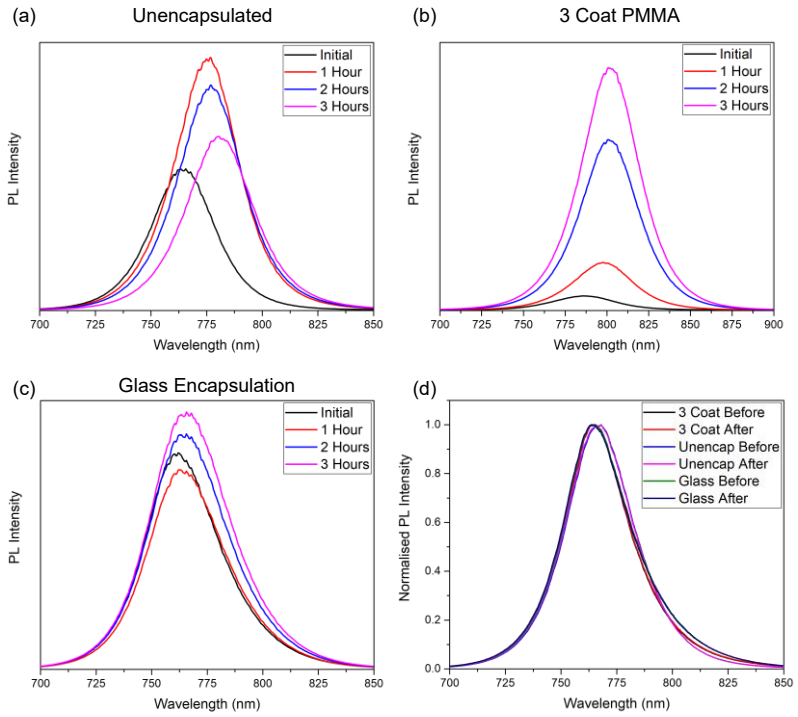

Figure 6.15 Averaged photoluminescence measurements at 50% RH as a function of time for (a) unencapsulated PSC (b) 3 coat encapsulated PSC (c) glass encapsulated PSC. (d) normalised averaged photoluminescence measurements at 40% RH before and after 3 hours under 50% RH for unencapsulated, 3 coat PMMA, and glass encapsulation.

Under 50% RH, there is an observed increase in PL intensity for all 3 samples. For the unencapsulated PSC, there is a 136.63% increase in intensity after 3 hours. There is a 23.25% and 2342.86% increase for the glass and 3-coat PMMA device respectively. This increase in PL under humidity treatment has been seen in Howard et al, which showed that the presence of moisture increases the radiative recombination, increasing the PL intensity. This is due to the passivation of surface defect states, which increases the carrier lifetime.[29] It is also mentioned that continued humidity treatment results in degradation of the perovskite, causing new surface trap states. This behaviour explains the increase and decrease in PL intensity for the unencapsulated PSC. Therefore, the increase in the PL for the 3-coat PMMA PSC is due to the passivation of surface defects due to the moisture treatment, however as the PMMA encapsulation limits the concentration of moisture entering the perovskite layer, there is no decrease in the PL. Additionally, the passivation and

increased carrier lifetime could be responsible for the increased J_{sc}, and FF observed in Figure 6.4. This behaviour was also observed in the proton bombardment in Chapter 3. The increase in PL intensity for the glass encapsulated device is unintuitive due to glass not having a WVTR, however moisture could enter the device through the areas no encapsulated by the glass. The observed PL red-shift is attributed to a change in the perovskite phase and increased halide migration.[29] However, as seen in Figure 6.15d, the induced redshift in the PL peak position is reversible. Here the PL was measured at 40% RH, held at 50% RH for 3 hours, before returning the 40% RH and remeasured. For all samples, the PL peaks perfectly overlap after returning 40% RH, indicating that the moisture induced phase change and halide migration is reversable. To further investigate any change in the optical properties of the devices peak position, FWHM and calculated optical band gap shown in Figure 6.16.

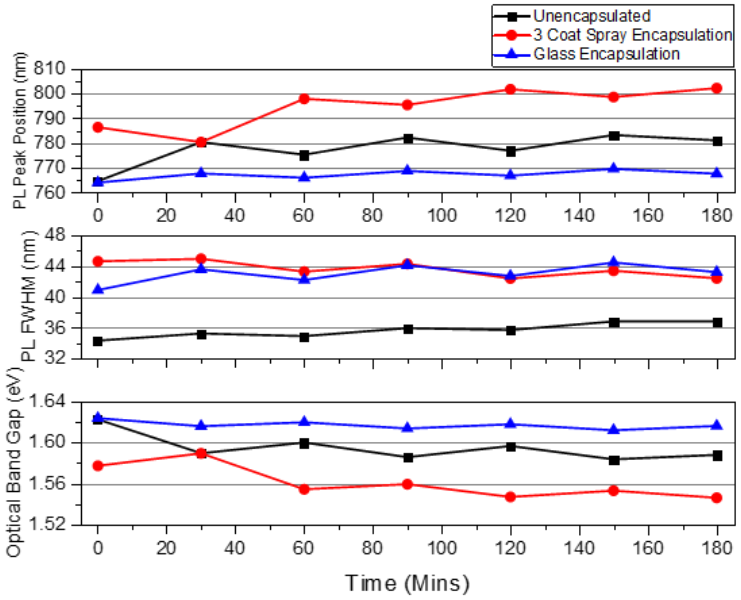

Figure 6.16 Changes in PL peak position, FWHM and band gap for the unencapsulated, 3 coat spray encapsulated, and glass encapsulated PSCs.

By comparing the initial PL peak positions, the application of the 3-coat spray encapsulation influences the optical properties of the perovskite. The mechanism behind this is unknown, however the 3-coat PSC has an initial PL peak position of 786.29 nm. Both the unencapsulated and glass encapsulated device have similar initial PL peak positions of 764 and 764.5 nm respectively. After 3 hours, the glass encapsulated device has a redshift ~5nm, while the unencapsulated and 3 coat

redshift by ~17 and ~16 nm respectively. This suggests that the glass encapsulation provides much better phase stability from moisture than the PMMA encapsulation due to having no WVTR. The PL FWHM is larger for the glass encapsulated and 3-cat PMMA devices compared to the unencapsulated device, indicating that the presence of both encapsulation methods increases the disorder of the PL. However, the FWHM fluctuates for both the unencapsulated, and glass encapsulated device but decreases for the 3-coat. It is reported that the increase in FWHM is linked to an increase in disorder within the device, as the line shape shift from a Lorentzian to gaussian with increasing disorder.[30] The optical band gap values were calculated via the equation:

$$E_g^{opt}(eV) = \frac{1240}{Peak\ Wavelength\ (nm)} \tag{6.2}$$

Where the peak wavelength is the PL peak wavelength value. As shown in Chapter 5, the optical bandgap is related to the electrical band gap via the equation:

$$E_g^{Elec} = E_g^{Opt} + E_B \tag{6.3}$$

Where E_B is the exciton binding energy. Using Equation 6.2, the 3-coat PMMA device optical band gap decreases by 0.04 eV. For the unencapsulated and glass encapsulated devices, the optical band gap decreases by 0.04 and 0.01 eV respectively. Comparing the calculations to the J-V measurements, in Figure 6.14 the Voc for all devices measured during the humidity holding J-V experiment does not change by more than ~1%. For the 3-coat and unencapsulated devices, assuming E_B does not change, the observed change in the optical band gap is equivalent to a 4%. However, it has been shown that as the perovskite band-gap becomes narrower, the J_{sc} increases.[31] Here it is suggested that this is the cause of the increase in the J_{sc} for the 2 and 3-coat PMMA devices.

Raman spectroscopy measurements were also performed at 50% RH for 3 hours. These measurements were performed to investigate any changes in the perovskite during the humidity holding. The normalised averaged Raman spectra for all 3 samples are shown in Figure 6.17.

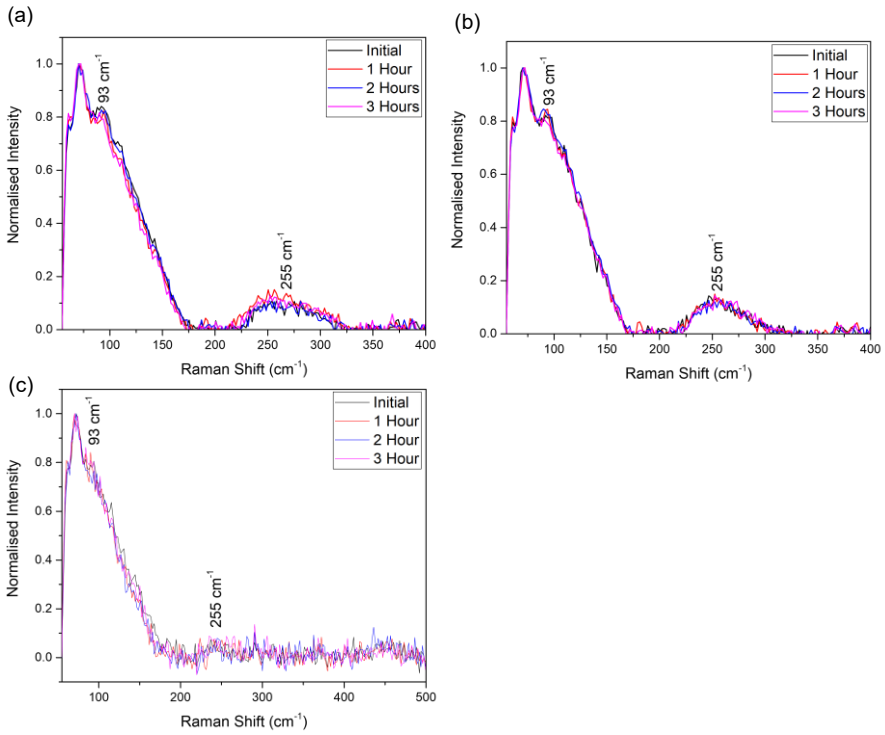

Figure 6.17 Normalised averaged Raman spectroscopy as a function of time for PSCs before and after the 3-hour humidity holding experiment. (a) unencapsulated (b) 3 coat PMMA (c) glass encapsulated.

From the Raman measurements, there are 2 distinct peaks that related to the perovskite. The first peak at 93cm^{-1} is attributed to Pb-I stretching.[32] For the unencapsulated and 3-coat PMMA encapsulated PSC, this peak is quite prominent and shows no decrease and/or shift after the 3 hours of humidity holding. However, this peak is not visible in the glass encapsulation measurements. Therefore, the presence of the peak at 93 cm^{-1} is likely related to the presence of moisture within the unencapsulated and 3 coat PMMA PSCs. The second perovskite peak is seen at 255 cm^{-1} and is attributed to MA.[33] As there are no peaks forming at 110 and 168 cm^{-1}, which are related to moisture degradation of perovskite, it can be assumed that the area being probed by the Raman has not undergone humidity degradation or was not severely dihydrated.[34]

6.2.5.4 Flexion Testing

The remaining mechanical test was to probe the flexion (bending) stability of the film. PMMA spray encapsulation was applied to PET films and bent around different

diameters to probe the formation of any cracks within the encapsulation layer. A cartoon of the experimental process is shown in Figure 6.18.

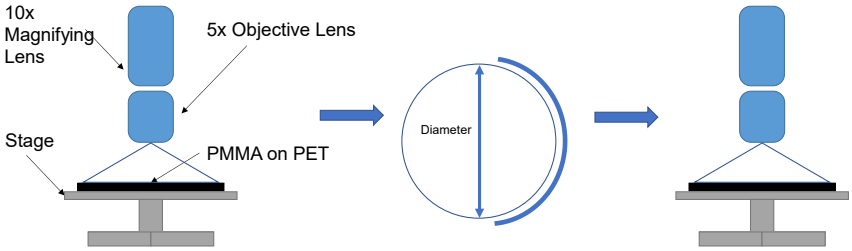

Figure 6.18 Cartoon of the experimental process to probe crack formation in the PMMA encapsulation under flexion testing

The experimental process consisted of using the 10x magnifying lens and 5x objective lens to image the PMMA film before flexion, bending the film around plastic tubing of different diameters, and then re-imaging the films to probe the formation of any cracks within the PMMA layer. The PMMA film was bent around a variety of diameters from 7.5 cm to 6 mm. The optical images of the films after the bend testing can be seen in figure 6.19.

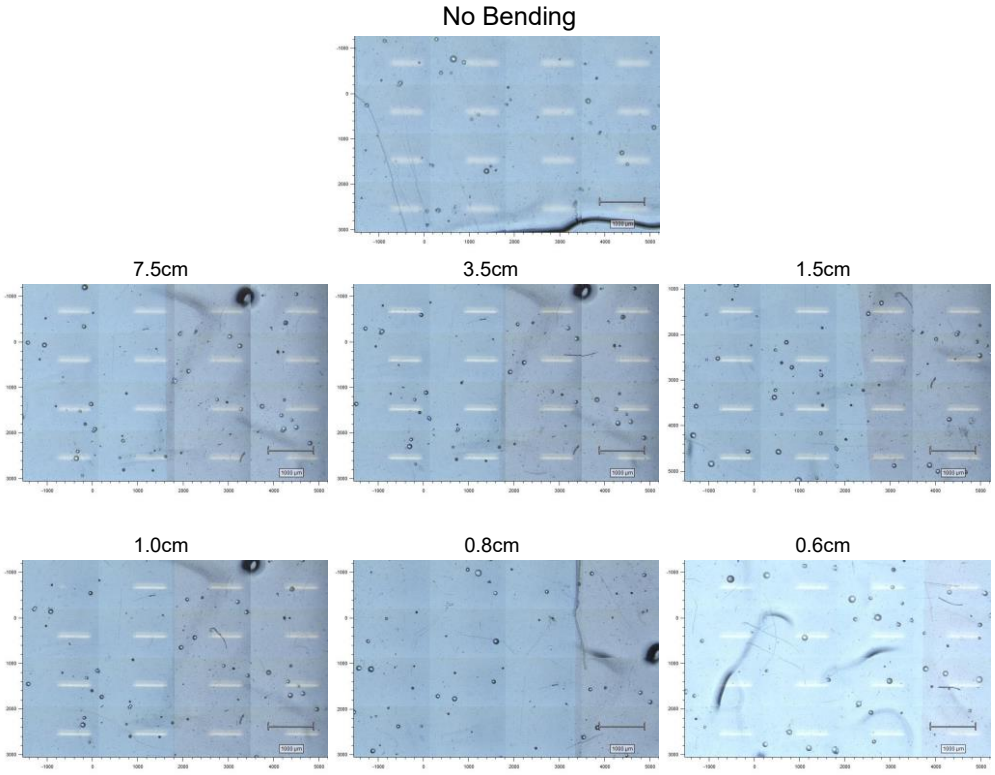

Figure 6.19 Optical microscope images of the PMMA film after being flexed around the labelled diameters.

From the flexion images, there are no clear cracks within the PMMA layer when compared to the control image. Most noticeably in the 0.6 cm image, there are long features that appear throughout the film. These features are most likely variation in the PMMA thickness as seen in the bottom of the control sample image. Additionally, across all images there are small "bubble-like" features. These features are not a result of the bending, and therefore are a result of the encapsulation process. One potential cause is dust or defects on the PET surface, therefore affecting the roughness and eventual PMMA thickness. The same PMMA film was used for all 6 measurements, therefore increasing the stress on the same film to properly assess the mechanical stability of the encapsulation films. In this case the PMMA film was a 1 coat encapsulation as crack propagation in PMMA increases with material thickness.[35] Therefore, if the film cracked or deformed at 1-coat then the probability of deformation at higher coats would be much greater.

6.2.6 Proton Hardness Simulation

To link the PMMA encapsulation to all work shown in this thesis, SRIM simulation was also performed for PMMA to assess the stopping power of the film and the target depth that one could expect in the presence of 150 keV protons. The results of the SRIM simulation are shown in Figure 6.20.

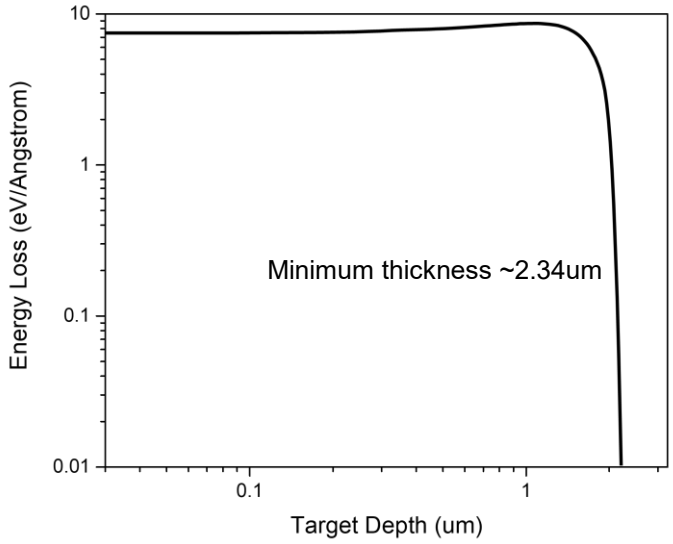

Figure 6.20 SRIM simulation of PMMA under 150 keV proton bombardment.

In the same instance of the mesoporous carbon electrode SRIM simulation in Chapter 4, the PMMA layer has a target depth less than the material thickness. As shown in this chapter, the PMMA thickness for 1 coat is calculated to be 2.7 µm, therefore any 150 keV protons incident on the PSC will stop within the PMMA encapsulation layer at a target depth of 2.34 µm. Additional work would need to be undertaken to assess the proton stability of the PMMA layer as it is a polymer, but the SRIM simulation is promising for the use of PMMA as a protective layer from proton radiation.

6.3 Conclusion

This chapter finds that PMMA spray encapsulation could be beneficial in improving the stability of PSCs while reducing the weight of the devices. The weight of the 1-coat PMMA encapsulation was measured to be ~60 mg, while the encapsulation glass was measured to be ~1.4 g, therefore reducing the encapsulation weight by ~96%. It was found that the PCE and FF of glass encapsulated PSCs decreases after encapsulation and could be linked to tensile strain and fracture during the encapsulation process. From a selection of different commercially available spray encapsulants, PMMA in ethyl acetate was deemed to be the least likely to dissolve the spiro-OMeTAD HTL and perovskite active area. The PMMA spray was less harmful to the device's performance than glass encapsulation, with the overall PCE decreasing by 3% compared to the 20% for glass. PMMA/Silicon was used to properly identify the PMMA peaks and using the ratio between peak intensity of the different thickness, the PMMA film was found to be 2.7 µm for 1 coat spray encapsulation.

Thermal cycling between -100 °C and +85 °C was performed on a 1 coat PMMA encapsulated device and confirmed that the inclusion of encapsulation improved the stability compared to unencapsulated devices. The PMMA device stability is comparable to the glass encapsulation, showing that the PMMA encapsulation works well under mimic LEO thermal cycling.

Dark storage measurements under the ISOS-D1 standard found that after 1 month the performance of the PSCs with 1 coat spray encapsulation were unchanged and had improved. Under humidity testing at ≥50% RH, the device performance with one coat spray encapsulation decreased at the same rate as the unencapsulated PSC.

To investigate the cause, the WVTR of PMMA was calculated and found that the WVTR should decrease with increasing PMMA thickness. Three PSCs with different PMMA thicknesses were held at 50% RH and it was found that 3-coat PMMA offered the best humidity stability as expected from the WVTR calculations. For the 3-coat PMMA device the PCE increased by 30%. Non-destructive techniques were employed to investigate any changes in the molecular or optical structure due to the humidity testing. PL spectroscopy measured at 50% RH found that there was considerable redshift of 15 nm for the PMMA encapsulated layer compared with the 5 nm shift for the glass encapsulated devices. The estimated changes in the V_{oc} were consistent with the experimental V_{oc} values, indicating no degradation from the band-gap shift. However, the decreasing band gap is suggested to be responsible for the 7% increase in J_{sc} observed for the 3-coat device. Raman spectroscopy was performed at 50% RH and found that after 3 hours there was an increase in the PbI_2 response for the unencapsulated and 3-coat devices, indicating a change in the chemical structure due to the humidity treatment. However, due to the minimal response at 110 and 164 cm^{-1}, the Raman spectroscopy measurements agree with no strong dehydration of the perovskite.

Flexion testing of a 1 coat PMMA film on PET was performed to assess relevant mechanical stress stability. At a diameter of 6 mm, no cracks in the PMMA were observed highlighting the mechanical stability of the spray encapsulation. Lastly, SRIM simulation was performed for PMMA and found that a minimum stopping distance of 2.34 µm is required to stop 150 keV protons, which is less that the 1 coat spray thickness. Therefore, here it is proposed that PMMA spray coated encapsulation is a scalable, stable encapsulation material for use in aerospace applications.

Additional optimisation of spray parameters and layer characterisation will need to be performed to assess the role of spray defects and inhomogeneity on stability. An investigation into different solvents and solution concentrations would also be beneficial to further improve film wettability and homogeneity. As thin film encapsulation is required to reduce the PSC weight and improve the specific power, the findings in this chapter highlight the PMMA encapsulation's thermal and humidity stability.

REFERENCES

[1] Yalcin, S., Aktas, B., Yilmaz, D. (2019). Radiation shielding properties of cerium oxide and erbium oxide doped obsidian glass. Radiation Physics and Chemistry, 160, 83–88. https://doi.org/10.1016/j.radphyschem.2019.03.024

[2] Boyd, C. C., Cheacharoen, R., Leijtens, T., McGehee, M. D. (2018). Understanding degradation mechanisms and improving stability of perovskite photovoltaics. Chemical Reviews, 119(5), 3418–3451. https://doi.org/10.1021/acs.chemrev.8b00336

[3] Ramasamy, E., Karthikeyan, V., Rameshkumar, K., Veerappan, G. (2019). Glass-to-glass encapsulation with ultraviolet light curable epoxy edge sealing for stable perovskite solar cells. Materials Letters, 250, 51–54. https://doi.org/10.1016/j.matlet.2019.04.082

[4] Corsini, F., Griffini, G. (2020). Recent progress in encapsulation strategies to enhance the stability of organometal halide perovskite solar cells. Journal of Physics: Energy, 2(3), 031002. https://doi.org/10.1088/2515-7655/ab8774

[5] Ramirez, C., Yadavalli, S. K., Garces, H. F., Zhou, Y., Padture, N. P. (2018). Thermo-mechanical behavior of organic-inorganic halide perovskites for solar cells. Scripta Materialia, 150, 36–41. https://doi.org/10.1016/j.scriptamat.2018.02.022

[6] Park, K. H., Kim, D. B., Lee, D. E., Park, K. S., Cho, Y. S. (2022). Effect of transparent polymer encapsulation overlayers on bending fracture behavior of flexible organic lead halide perovskite thin films. Journal of Alloys and Compounds, 908, 164607. https://doi.org/10.1016/j.jallcom.2022.164607

[7] LeVier, R. (1995). What is silicone? Journal of Clinical Epidemiology, 48(4), 513–517. https://doi.org/10.1016/0895-4356(94)00207-7

[8] Gama, N., Ferreira, A., Barros-Timmons, A. (2018). Polyurethane foams: Past, present, and future. Materials, 11(10), 1841. https://doi.org/10.3390/ma11101841

[9] Ali, U., Karim, K. J., Buang, N. A. (2015). A review of the properties and applications of Poly (methyl methacrylate) (PMMA). Polymer Reviews, 55(4), 678–705. https://doi.org/10.1080/15583724.2015.1031377

[10] DDBST GmbH. (n.d.). Saturated vapor pressure. Vapor Pressure Calculation by Antoine Equation. Retrieved May 10, 2022, from http://ddbonline.ddbst.com/AntoineCalculation/AntoineCalculationCGI.exe

[11] BrandTech Scientific. (n.d.). Solvent boiling points chart. BrandTech Scientific Inc. Retrieved May 10, 2022, from https://brandtech.com/solventboilingpointschart/

[12] Abbas, G. A., Papakonstantinou, P., Okpalugo, T. I. T., McLaughlin, J. A., Filik, J., Harkin-Jones, E. (2005). The improvement in gas barrier performance and optical transparency of DLC-coated polymer by silicon incorporation. Thin Solid Films, 482(1-2), 201–206. https://doi.org/10.1016/j.tsf.2004.11.174

[13] Li, S.-L., Miyazaki, H., Song, H., Kuramochi, H., Nakaharai, S., Tsukagoshi, K. (2012). Quantitative Raman spectrum and reliable thickness identification for atomic layers on insulating substrates. ACS Nano, 6(8), 7381–7388. https://doi.org/10.1021/nn3025173

[14] Thomas, K. J., Sheeba, M., Nampoori, V. P., Vallabhan, C. P., Radhakrishnan, P. (2008). Raman spectra of polymethyl methacrylate optical fibres excited by a 532 nm diode pumped solid state laser. Journal of Optics A: Pure and Applied Optics, 10(5), 055303. https://doi.org/10.1088/1464-4258/10/5/055303

[15] Cheacharoen, R., Rolston, N., Harwood, D., Bush, K. A., Dauskardt, R. H., McGehee, M. D. (2018). Design and understanding of encapsulated perovskite solar cells to withstand temperature cycling. Energy & Environmental Science, 11(1), 144–150. https://doi.org/10.1039/c7ee02564e

[16] Khenkin, M. V., Katz, E. A., Abate, A., Bardizza, G., Berry, J. J., Brabec, C., Brunetti, F., Bulović, V., Burlingame, Q., Di Carlo, A., Cheacharoen, R., Cheng, Y.-B., Colsmann, A., Cros, S., Domanski, K., Dusza, M., Fell, C. J., Forrest, S. R., Galagan, Y., … Lira-Cantu, M. (2020). Consensus statement for stability assessment and reporting for perovskite photovoltaics based on ISOS procedures. Nature Energy, 5(1), 35–49. https://doi.org/10.1038/s41560-019-0529-5

[17] Idígoras, J., Aparicio, F. J., Contreras-Bernal, L., Ramos-Terrón, S., Alcaire, M., Sánchez-Valencia, J. R., Borras, A., Barranco, Á., Anta, J. A. (2018). Enhancing moisture and water resistance in perovskite solar cells by encapsulation with ultrathin plasma polymers. ACS Applied Materials Interfaces, 10(14), 1187–11594. https://doi.org/10.1021/acsami.7b17824

[18] La Ferrara, V., De Maria, A., Rametta, G., & Delli Veneri, P. (2021). The effect of storage cycle on improvement in the photovoltaic parameters of planar triple cation perovskite solar cells. Materials Advances, 2(16), 5396–5405. https://doi.org/10.1039/d1ma00345c

[19] Fan, W., Deng, K., Shen, Y., Bai, Y., Li, L. (2022). Moisture accelerated precursor crystallization in ambient air for high-performance perovskite solar cells toward mass production. Angewandte Chemie. https://doi.org/10.1002/ange.202211259

[20] Liu, K., Luo, Y., Jin, Y., Liu, T., Liang, Y., Yang, L., Song, P., Liu, Z., Tian, C., Xie, L., Wei, Z. (2022). Moisture-triggered fast crystallization enables efficient and stable perovskite solar cells. Nature Communications, 13(1). https://doi.org/10.1038/s41467-022-32482-y

[21] Wilderspin, T. J., De Rossi, F., Watson, T. M. (2016). A simple method to evaluate the effectiveness of encapsulation materials for perovskite solar cells. Solar Energy, 139, 426–432. https://doi.org/10.1016/j.solener.2016.09.038

[22] Aranda, C. A., Caliò, L., Salado, M. (2021). Toward commercialization of stable devices: An overview on encapsulation of hybrid organic-inorganic perovskite solar cells. Crystals, 11(5), 519. https://doi.org/10.3390/cryst11050519

[23] Castro-Hermosa, S., Top, M., Dagar, J., Fahlteich, J., Brown, T. M. (2019). Quantifying performance of permeation barrier-encapsulation systems for flexible and glass-based electronics and their application to perovskite solar cells. Advanced Electronic Materials, 5(10), 1800978. https://doi.org/10.1002/aelm.201800978

[24] Hülsmann, P., Weiß, K.-A., Köhl, M. (2012). Temperature-dependent water vapour and oxygen permeation through different polymeric materials used in photovoltaic-modules. Progress in Photovoltaics: Research and Applications, 22(4), 415–421. https://doi.org/10.1002/pip.2273

[25] Suzuki, A., Takahagi, H., Uehigashi, A., Hara, S. (2015). Development of reliable technique for evaluating the properties of water vapor barriers. AIP Advances, 5(11), 117204. https://doi.org/10.1063/1.4935341

[26] Vingaard, M., de Claville Christiansen, J. (2011). Activation energy of poly(methyl methacrylate) from rheometry and polymer welding. Journal of Materials Science, 46(13), 4660–4666. https://doi.org/10.1007/s10853-011-5372-4

[27] Keller, P. E., Kouzes, R. T. (2017). Water vapor permeation in plastics. https://doi.org/10.2172/1411940

[28] Zhang, W., Xiong, J., Li, J., Daoud, W. A. (2019). Mechanism of water effect on enhancing the photovoltaic performance of triple-cation hybrid perovskite solar cells. ACS Applied Materials & Interfaces, 11(13), 12699–12708. https://doi.org/10.1021/acsami.8b20264

[29] Howard, J. M., Tennyson, E. M., Barik, S., Szostak, R., Waks, E., Toney, M. F., Nogueira, A. F., Neves, B. R., Leite, M. S. (2018). Humidity-induced photoluminescence hysteresis in variable CS/Br Ratio Hybrid perovskites. The Journal of Physical Chemistry Letters, 9(12), 3463–3469. https://doi.org/10.1021/acs.jpclett.8b01357

[30] Goetz, K. P., Taylor, A. D., Paulus, F., Vaynzof, Y. (2020). Shining light on the photoluminescence properties of metal halide perovskites. Advanced Functional Materials, 30(23), 1910004. https://doi.org/10.1002/adfm.201910004

[31] Tong, J., Jiang, Q., Zhang, F., Kang, S. B., Kim, D. H., Zhu, K. (2020). Wide-bandgap metal halide perovskites for tandem solar cells. ACS Energy Letters, 6(1), 232–248. https://doi.org/10.1021/acsenergylett.0c02105

[32] Silva Filho, J. M., Borrero, N. F., Viana, G. A., Merlo, R. B., & Marques, F. C. (2020). Lead iodide thin films via RF sputtering. Crystal Growth & Design, 20(3), 1531–1537. https://doi.org/10.1021/acs.cgd.9b01250

[33] Pistor, P., Ruiz, A., Cabot, A., Izquierdo-Roca, V. (2016). Advanced raman spectroscopy of methylammonium lead iodide: Development of a non-destructive characterisation methodology. Scientific Reports, 6(1). https://doi.org/10.1038/srep35973

[34] Hooper, K. E., Lee, H. K., Newman, M. J., Meroni, S., Baker, J., Watson, T. M., Tsoi, W. C. (2017). Probing the degradation and homogeneity of embedded perovskite semiconducting layers in photovoltaic devices by Raman spectroscopy. Physical Chemistry Chemical Physics, 19(7), 5246–5253. https://doi.org/10.1039/c6cp05123e

[35] Loya, J. A., Villa, E. I., Fernández-Sáez, J. (2010). Crack-front propagation during three-point-bending tests of polymethyl-methacrylate beams. Polymer Testing, 29(1), 113–118. https://doi.org/10.1016/j.polymertesting.2009.09.012

Chapter 7

Conclusions and Further Work

While PSCs are beginning to reach the threshold for viability in terms of device efficiency, device stability remains a barrier to adoption for aerospace applications. Research efforts have focussed on the AM1.5G stability such as moisture and light soaking of perovskite active layers, leaving the AM0 stability and Low Earth Orbit (LEO) environment stability unclear.

Chapter 3 investigates the proton radiation stability of PSCS utilising an AZO TCO, and how the role of different device layers affect the overall stability of PSCs. Triple cation perovskite solar cells were shown to undergo a severe performance decrease under 150 keV proton bombardment at fluences >1x10^{13} protons/cm^2. Device degradation of the PSCs was due to degradation of the J_{sc}, with a 99.99% decrease at a fluence of 1x10^{15} protons/cm^2. SRIM simulation showed proton penetration through the full device stack, and most of the protons stopping within the AZO revealing the significance of the role of the TCO in PSC radiation stability. Remarkably, at a fluence of 1x10^{15} protons/cm^2, the triple cation perovskite showed excellent radiation stability confirmed through XRD measurements. Through Raman spectroscopy, there was a measured decrease of the spiro-OMeTAD signal indicating degradation of the HTL. This was confirmed through PL measurements that showed quenching as a function of increasing fluence and through TPV measurements. The TPV measurements showed that at fluences >1x10^{13} protons/cm^2 a double exponential fitting was required, showing an increase in interfacial recombination at the spiro/perovskite interface. When quartz/AZO samples were bombarded under 150 keV, no change in transmittance was observe, showcasing the proton stability of the quartz substrate and the AZO TCO. These results show that good radiation stability of the HTL is necessary for good PSC radiation stability.

Chapter 4 explores how the radiation stability of mesoporous carbon-based PSCs (m-CPSCs), with attention to the radiation stability of the carbon electrode. It

was found that m-CPSCs retain 100% PCE under 150 keV proton bombardment up to a fluence of $1x10^{15}$ protons/cm^2. Raman spectroscopy on the active area showed no change in chemical structure. However, measurements performed on the carbon electrode exhibited signal from dehydrated MAPI. As the perovskite in the electrode is part of the capping layer, the moisture degradation did not affect the device performance. The Raman signal from the carbon D and G-bands showed no change in the chemical properties of the carbon as a function of the proton irradiation; the signal of the D band varied between samples independently from proton fluence. This suggests that the screen-printed carbon electrode is not uniform across the printing area, or there are areas within the print that are defect rich. Photoluminescence measurements of the active area showed PL quenching as a function of proton fluence, this correlates well to the J_{sc} increase with the same trend. Therefore, the PL quenching is suggested to be indicative of better charge extraction. Additionally, the decrease in PL intensity correlates to a V_{oc} loss of 12 meV. PL measurements of the carbon electrode showed both blue and red-shift in the peak position. The measured blue shift is attributed to the poly-disperse nature of the perovskite, while the red-shift is due to the moisture degradation of the perovskite in the capping layer. SRIM simulations of 150 keV proton bombardment into different electrodes showed that the stopping power of the carbon electrode is lower than Au and it revealed that the carbon thickness (~12 µm) is responsible for the m-CPSC radiation stability. Additional simulations were performed by solving the Bethe-Bloch equation across a large range of proton energy values (0.1 – 10000 MeV). The simulation confirmed the SRIM results. However, when the mass-stopping power was simulated to remove the effect of the density, the carbon electrode exhibited the greatest stopping power across the different materials. These results show the superior radiation stability of m-CPSCs, and that the radiation stability is not limited to just PV but can be applied to other electronic systems as well.

In Chapter 5, the thermal stability of PSCs was investigated to study the stability under mimic LEO conditions. PSCs with a spiro-OMeTAD and P3HT HTL were thermal cycled for 3 hours between -100 and +85 °C. After 3 hours, the spiro-OMeTAD PSCs had degraded by 10% while the P3HT PSCs retained 100% of their initial PCE. 1 hour 85 °C thermal holding showed that the PCE decrease for the spiro-

OMeTAD devices was due to a reduction in J_{sc}. Through Raman spectroscopy and PL measurements, the decrease in Jsc is suggested to due to the degradation of the HTL, increasing non-radiative recombination. The Raman spectroscopy during thermal cycling showed a decrease in the C-C and C=C bond peaks, which do not recover after finishing the cycling and returning the cells to 25 °C. The PL showed a large blue shift and quench with increasing heating time. The blue shift is due to the increase in thermal energy within the perovskite, and the reverse band-gap. The quenching correlates well with the decrease in J_{sc}, suggesting an increase in non-radiative recombination which correlates well with the degradation of the spiro-OMeTAD HTL. TPV and TPC measurements showed a large decrease in carrier concentration (100x) and much faster TPV decay indicating an increase in recombination. The reduced TPC generation suggests worse charge extraction. Alternatively, the same measurements performed on the P3HT PSCs showed the decrease in Raman intensity was reversible, and it was suggested that an interaction at the perovskite/P3HT interface could lead to an amorphous/crystalline phase. The PL measurements showed an increase in intensity and a red shift. Coupled with the TPV and TPC results, the increase PL is attributed to an increase in carrier density, resulting in more recombination within the perovskite. However, the cause of the PL redshift is unknown and will require further investigation.

Chapter 6 focused on spray coated thin film encapsulation. Firstly, the effect of glass encapsulation on PSC performance was investigated. It was found that after the application of polyimide/epoxy/glass encapsulation, there is a 20% reduction in PCE. This degradation is attributed to defect creation within the perovskite layer because of strain generation greater than the fracture energy of the layer. PMMA was chosen as a replacement material, which was spray coated onto PSCs at 55 °C. After the spray encapsulation, the PSCs retained 97% of their initial efficiency. Profilometry measurements and Raman spectroscopy were coupled to estimate the thickness of the PMMA encapsulation for multiple coatings. The thickness after 1 coat was estimated to be 2.7 μm. Following the same thermal cycling measurement as Chapter 5, the PMMA encapsulated devices exhibited similar stability to the glass encapsulated devices, showing the potential for LEO applications. Additionally, the PMMA encapsulated devices retained their PCE after 1 month in ISOS-D1 standard

dark conditions. Then the humidity stability of the PMMA encapsulation was investigated, firstly by stepping the %RH from 10 to 80%, then by holding the devices at 50% RH for 3 hours. For >50% RH both unencapsulated and 1-coat PMMA encapsulated devices degrade, which for the PMMA encapsulated device was attributed to the WVTR of the PMMA and inhomogeneity of the film. For the 50% RH holding experiment, the 3-coat PMMA encapsulated PSC showed exceptional stability in comparison to thinner coatings, while also showing a 30% improvement in PCE. Through PL measurements, the increase in PCE is suggested to be due to the reduction in the band gap of the perovskite, increasing the J_{sc}. Finally, flexion testing was performed down to a diameter of 0.6 cm. Through optical imaging, no crack formation was seen showcasing the mechanical stability of the PMMA encapsulation. These results show the potential for spray encapsulated PMMA in both terrestrial and space applications.

In the work concerning the proton radiation hardness in Chapters 3, it was found that the gold metal electrode initially increases in sheet resistance after the proton bombardment, and then begins to decrease with increasing fluence. It is suggested that due to Au being an FCC structure that generated vacancies relax at their nearest neighbour, and it has been shown that the bond length can change after bombardment increasing the conductivity. Further work could be undertaken to better understand why the sheet resistance initially increases after proton bombardment. Additionally, it is suggested that further work be undertaken to fully investigate the role of the TCO under proton bombardment. Methods such as XRD could be useful to investigate any structural changes in the TCO because of proton irradiation.

For the m-CPSCs in Chapter 4, Raman spectroscopy was performed on the carbon electrode. Since the intensity ratio between the D and G peaks shows a large increase in disorder for the $1x10^{12}$ protons/cm^2 sample but not the $1x10^{15}$ protons/cm^2, further work to assess how low energy proton bombardment affects the D peak in sp2 carbon systems could be performed. For example, sheet resistance and photocurrent mapping could provide insight into how the proton bombardment affects conductivity and charge extraction.

In Chapter 5, it was found that the correlation between the decreasing device performance at high temperatures was the degradation of the spiro-OMeTAD HTL. The degradation led to a reduction in charge extraction. To further investigate the degradation of the spiro-OMeTAD, DFT could be performed to simulate the Raman spectra at different temperatures. It would be interesting to perform transient photovoltage and photocurrent measurements in-situ to investigate the charge carrier density and lifetime for both spiro-OMeTAD and P3HT PSCs during the 85 °C heating, along with XRD of the P3HT HTL in-situ.

The increasing of specific power is an area of current research interest. In Chapter 6, some preliminary results of spray coated PMMA encapsulated are shown. Here, the PMMA encapsulation reduces the overall encapsulation weight by 96% and improves the performance retention after encapsulation. However, many of the presented results are for 1 coat PSCs when 3 coats was shown to be the most stable. Following the same methods, additional work should be undertaken to further investigate the stability of 3-coat PMMA encapsulation.

The work presented in this thesis establishes relationships between the choice of HTL and encapsulation technique with material/device stability under mimic LEO conditions. Namely how the choice in HTL can lead to reduced proton bombardment or thermal stability, and how the encapsulation method can have an adverse effect on device performance. These are crucial for addressing the feasibility of future PSCs under mimic LEO conditions, thereby paving the way toward achieving long-term stability of PSCs for space applications.

Appendix A

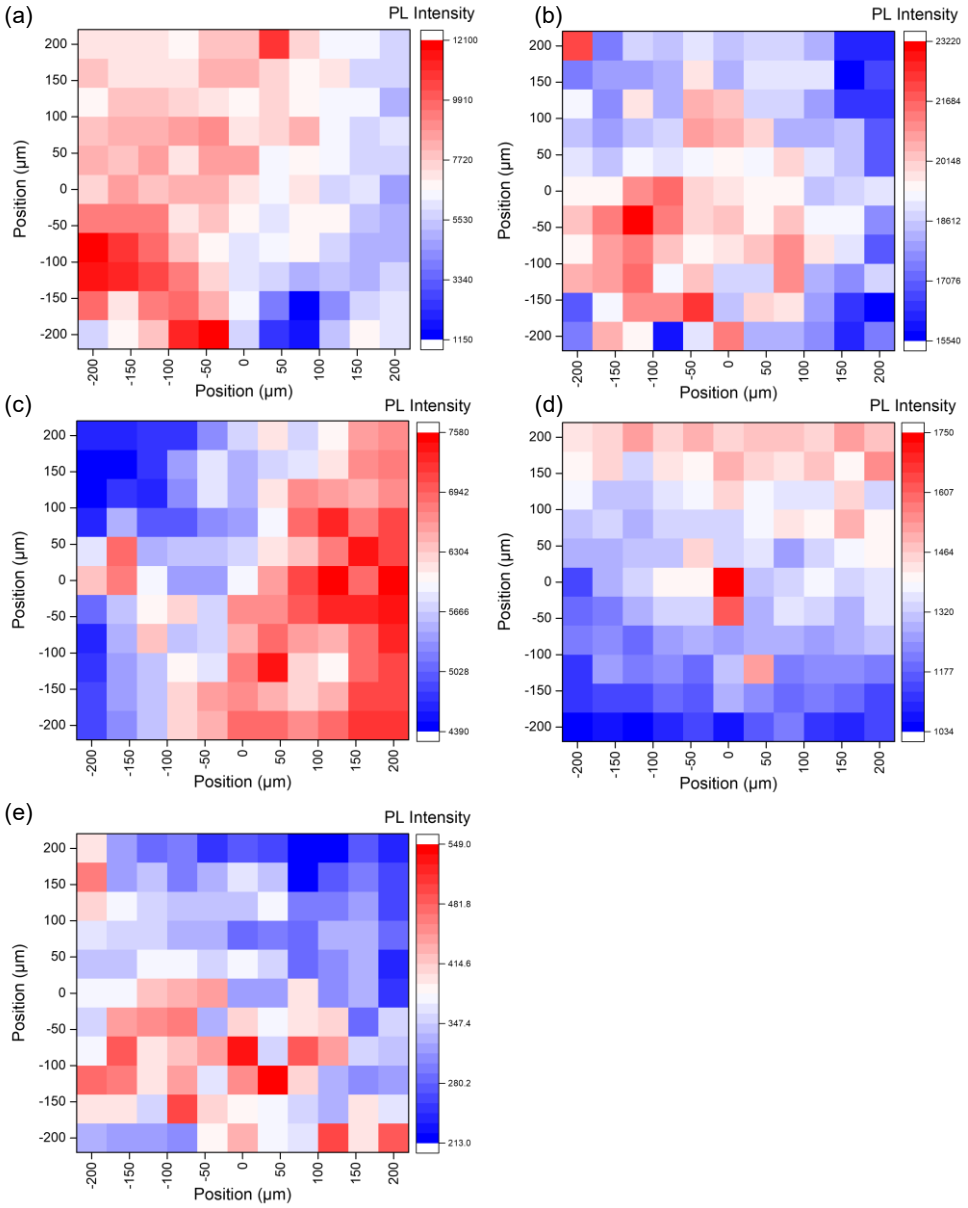

Figure A.1 PL mapping at the peak position as a function of proton fluence. (a) Control (b) $1x10^{12}$ protons/cm^2 (c) $1x10^{13}$ protons/cm^2 (d) $1x10^{14}$ protons/cm^2 (e) $1x10^{15}$ protons/cm^2.

Table A.1 AM1.5G PV parameters for every pixel before proton bombardment and colour coded for their allocated proton fluence.

Pixel Number	PCE (%)	Voc (V)	Fill Factor (%)	Jsc ($mAcm^{-2}$)
1	12.22	1.11	65.49	16.84
2	11.02	1.09	63.91	15.79
3	8.78	1.05	59.68	13.98
4	14.75	1.12	68.70	19.18
5	13.76	1.11	62.69	19.84
6	12.90	1.10	59.97	19.59
7	12.26	1.09	58.07	19.40
8	14.95	1.10	69.94	19.41
9	12.46	1.07	61.79	18.77
10	11.38	1.07	59.88	17.77
11	10.96	1.07	52.45	17.98
12	12.60	1.03	57.17	22.50
13	11.84	1.07	56.07	19.70
14	12.49	1.04	55.11	21.31
15	8.53	1.03	54.93	15.09
16	8.28	0.94	40.43	22.23
17	9.30	0.99	50.78	18.53
18	12.4	1.06	55.84	17.84
19	10.59	1.04	51.97	23.03
20	9.56	1.05	53.85	16.88
21	9.26	1.02	47.72	19.05
22	10.68	1.08	54.19	18.31
23	13.19	1.09	65.20	18.56
24	12.73	1.08	64.55	18.25
25	12.81	1.09	66.72	17.57
26	11.18	1.05	61.65	17.26
27	10.49	1.08	59.91	16.19
28	10.18	1.07	57.58	16.50
29	9.51	1.07	54.84	16.20

Control $1x10^{12}$ p/cm^2 $1x10^{13}$ p/cm^2 $1x10^{14}$ p/cm^2 $1x10^{15}$ p/cm^2

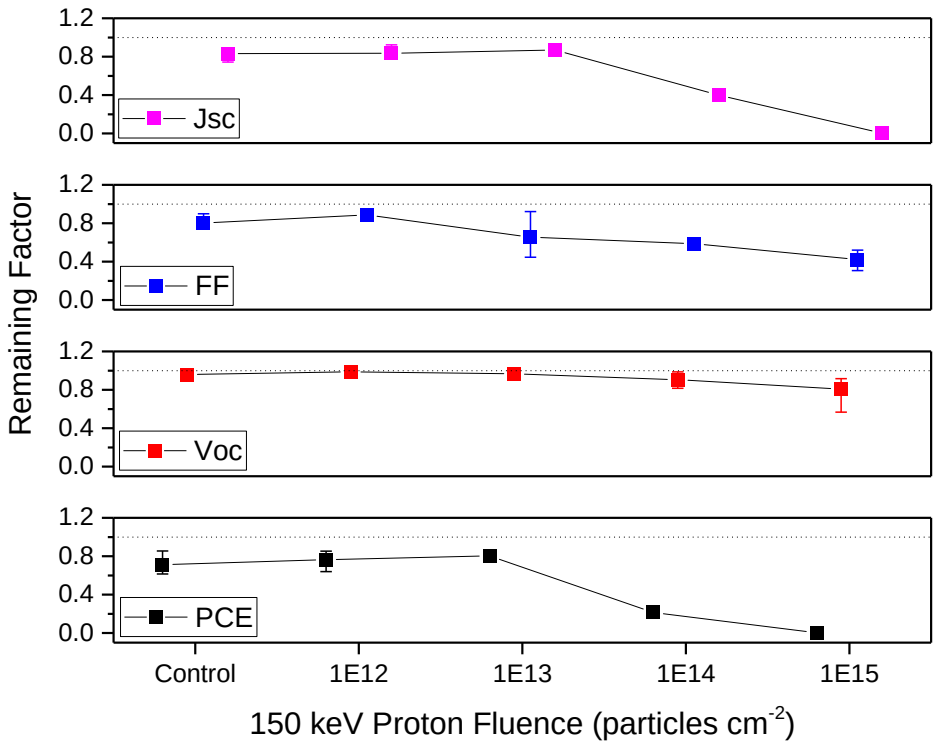

Figure A.2 Changes of photovoltaic characteristics (J_{sc}, FF, V_{oc}, and PCE) of perovskite solar cells under 1 Sun AM0 illumination as a function of proton fluence.

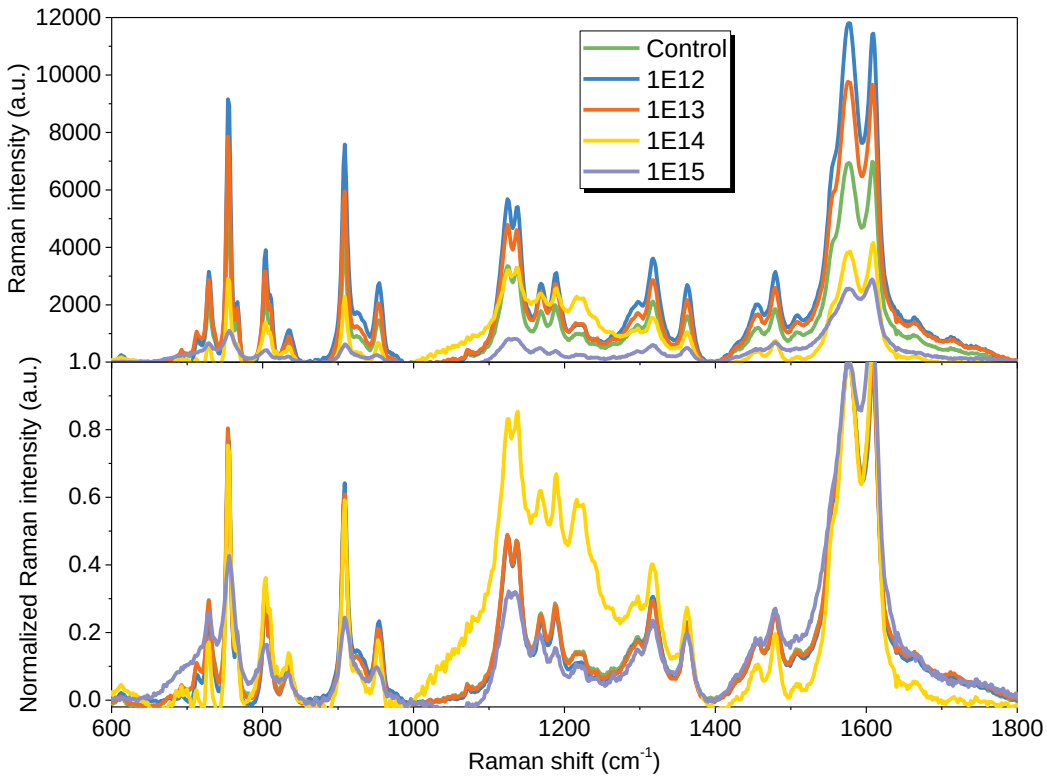

Figure A.3 Raw Raman spectra as a function of proton fluence. The normalised spectra has also been included for comparison.

APPENDIX B

Table B.1 1 sun AM0 PV parameters for every pixel pre- and post- proton bombardment.

Fluence (Protons/ cm^2)	Pre PCE (%)	Post PCE (%)	Pre V_{oc} (V)	Post V_{oc} (V)	Pre J_{sc} (mA/cm^2)	Post J_{sc} (mA/cm^2)	Pre FF (%)	Post FF (%)
Control	10.35	10.06	0.88	0.82	25.14	26.19	60.92	60.53
Control	10.17	9.58	0.88	0.86	24.58	25.61	60.25	56.50
$1x10^{12}$	9.85	9.72	0.89	0.85	24.08	25.84	59.75	57.38
$1x10^{12}$	9.04	8.58	0.87	0.83	24.73	22.13	58.94	59.49
$1x10^{13}$	10.15	9.08	0.87	0.86	26.63	24.77	56.81	55.78
$1x10^{13}$	9.22	8.78	0.86	0.82	24.65	23.8	56.46	58.58
$1x10^{14}$	10.46	10.36	0.87	0.84	25.15	26.01	62.32	61.66
$1x10^{14}$	10.15	9.51	0.85	0.81	25.73	25.04	60.07	60.49
$1x10^{15}$	7.56	10.23	0.85	0.82	21.62	26.50	53.59	52.91
$1x10^{15}$	10.17	10.01	0.88	0.79	25.00	24.47	60.33	59.80

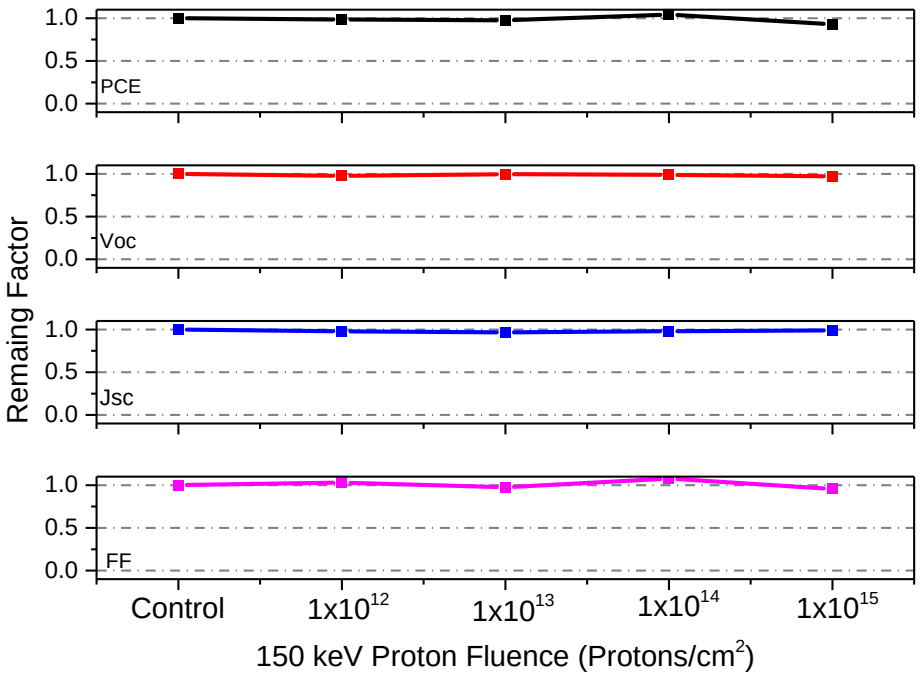

Figure B.1 Remaining Factor of PCE, V_{oc}, J_{sc}, and FF (under 1 sun AM1.5G illumination) versus proton fluence of m-CPSC (including the control device).

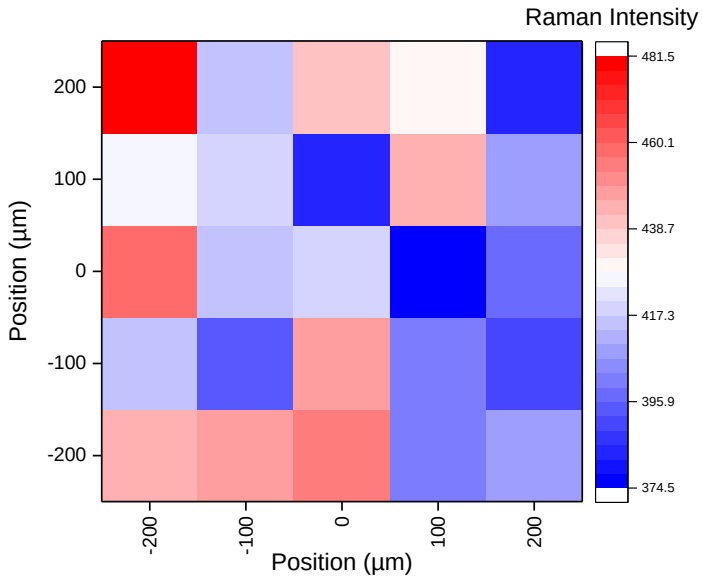

Figure B.2 Mapping of the perovskite peak at 100 cm^{-1} for the control sample. Raman measurements are sensitive to focus, and the roughness of the mesoporous layers cause intensity variation over small areas.

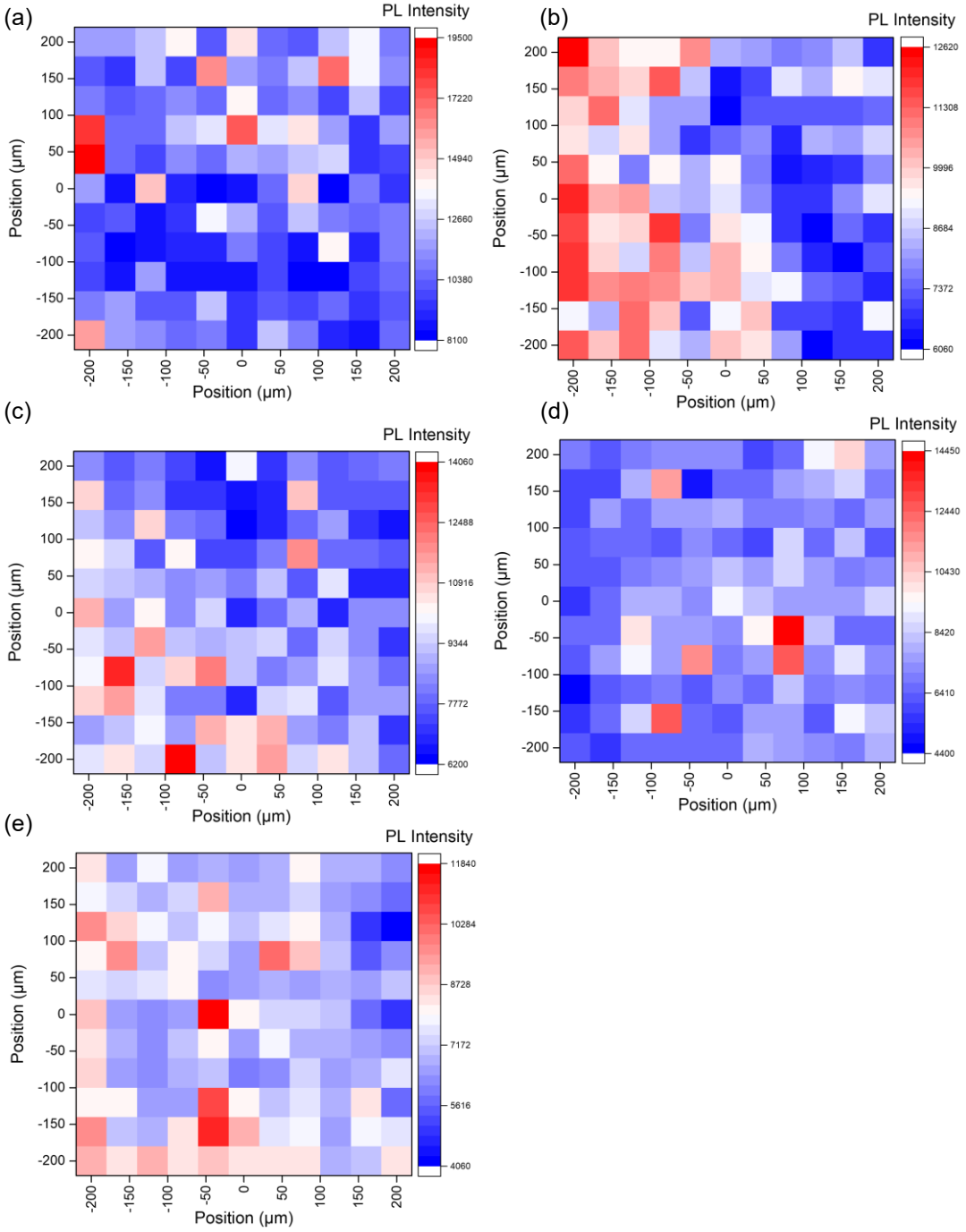

Figure B.3 PL mapping of the perovskite within the active area through the glass substrate. These measurements were taken as a function of proton fluence. (a) Control (b) $1x10^{12}$ protons/cm^2 (c) $1x10^{13}$ protons/cm^2 (d) $1x10^{14}$ protons/cm^2 (e) $1x10^{15}$ protons/cm^2

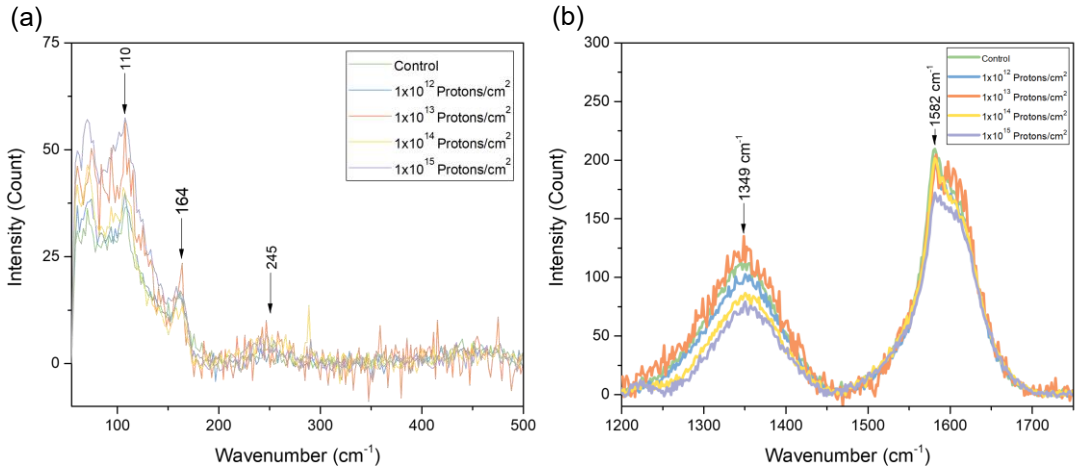

Figure B.4 Raman spectra of the perovskite solar cells (a) 50 and 500 cm^{-1} as a function of proton fluence (b) 1200 and 1750 cm^{-1} as a function of proton fluence.

APPENDIX C

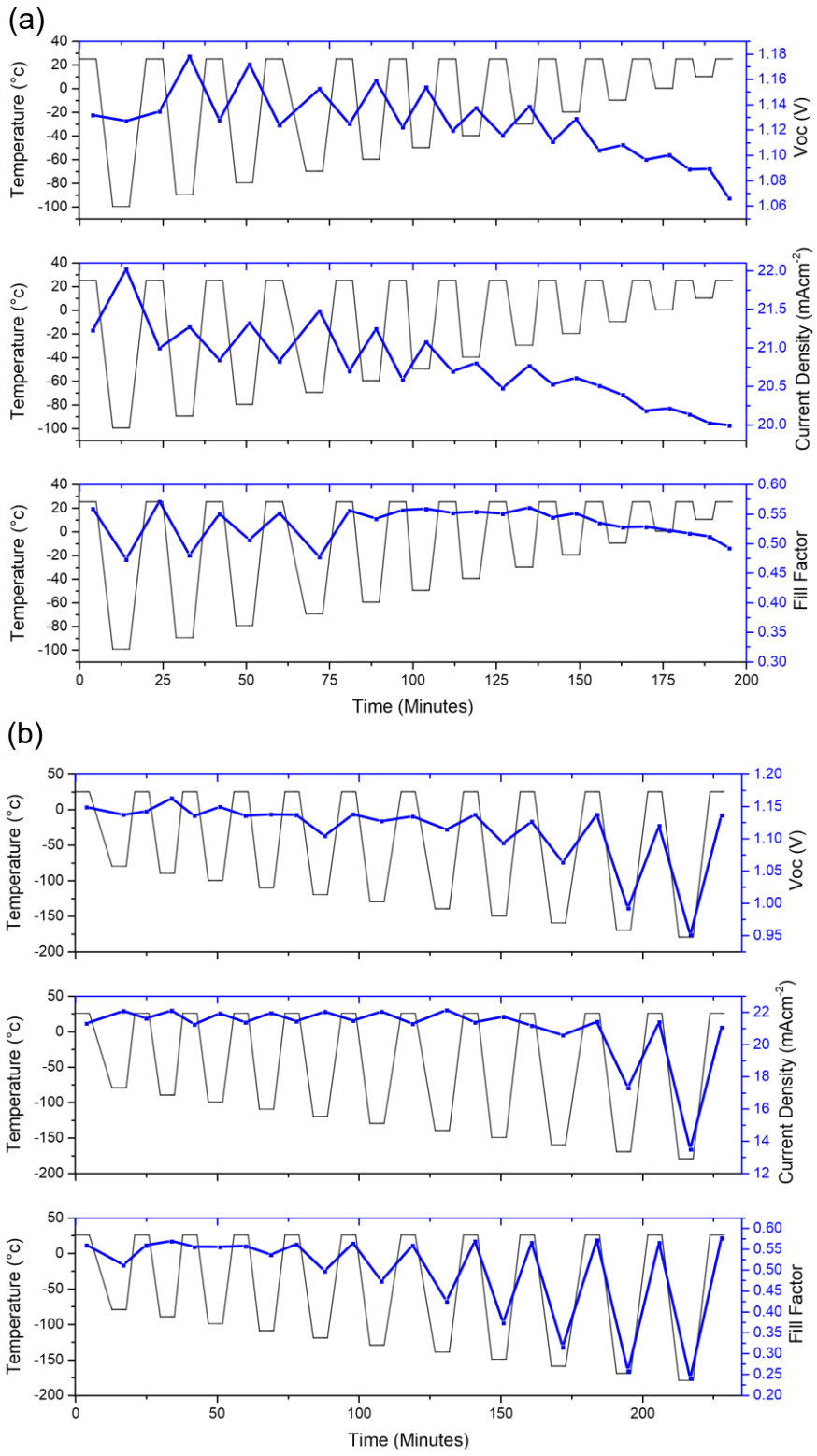

Figure C.1 PV parameters as a function of temperature stepping for room and low temperatures (≥-100 °C) b) PV parameters as a function of temperature stepping for room and very low temperatures (≥-180 °C).

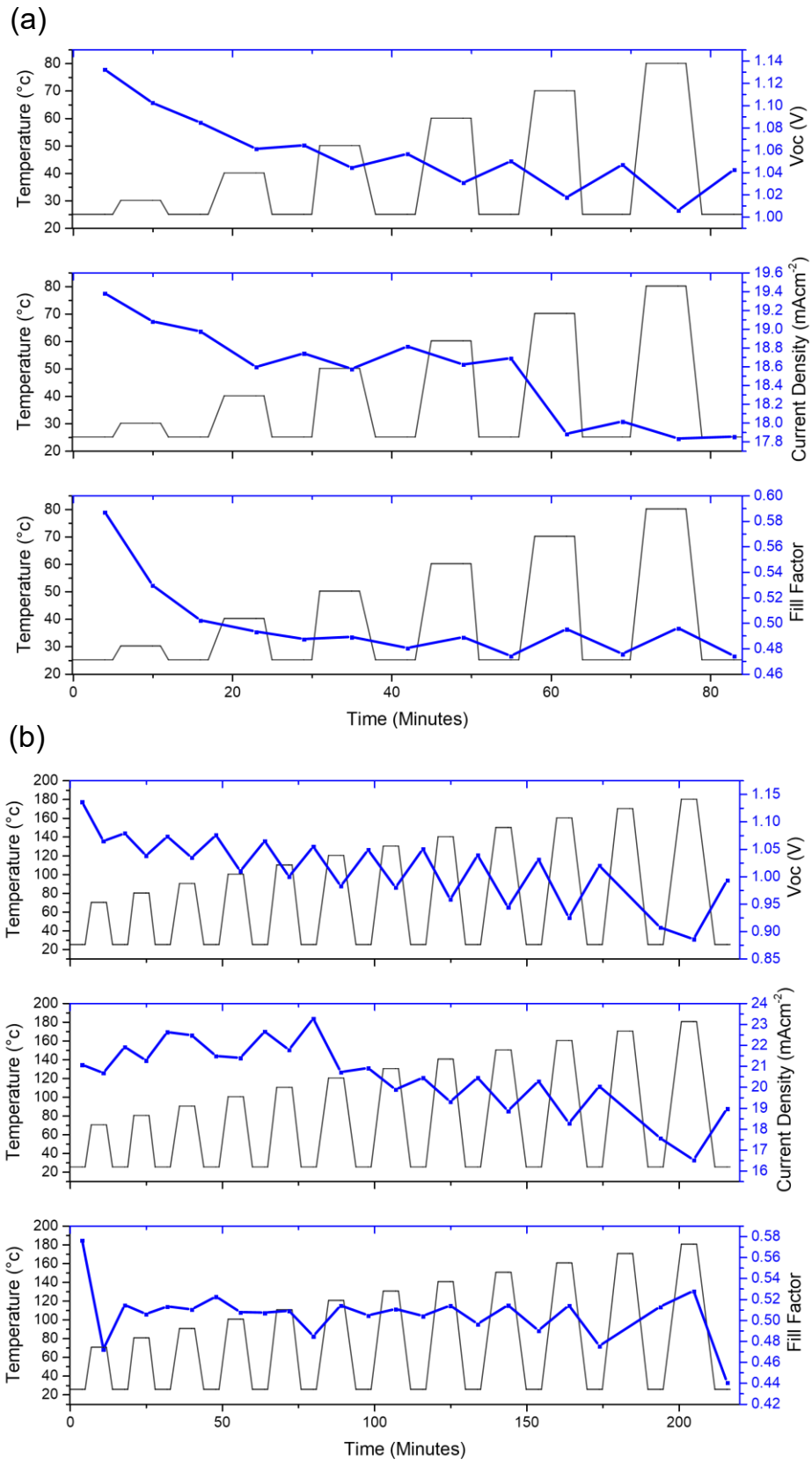

Figure C.2 a) PV parameters as a function of temperature stepping for room and high temperatures (≤80 °C) b) PV parameters as a function of temperature stepping for room and very high temperatures (≤180 °C).

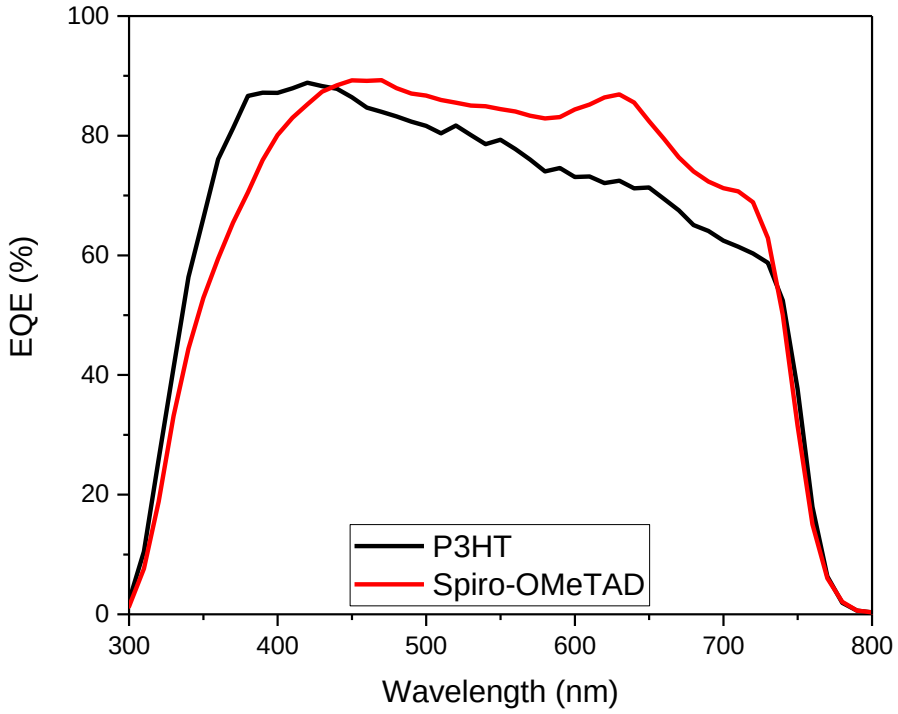

Figure C.3 EQE response for PSCs with a P3HT and spiro-OMeTAD HTL.

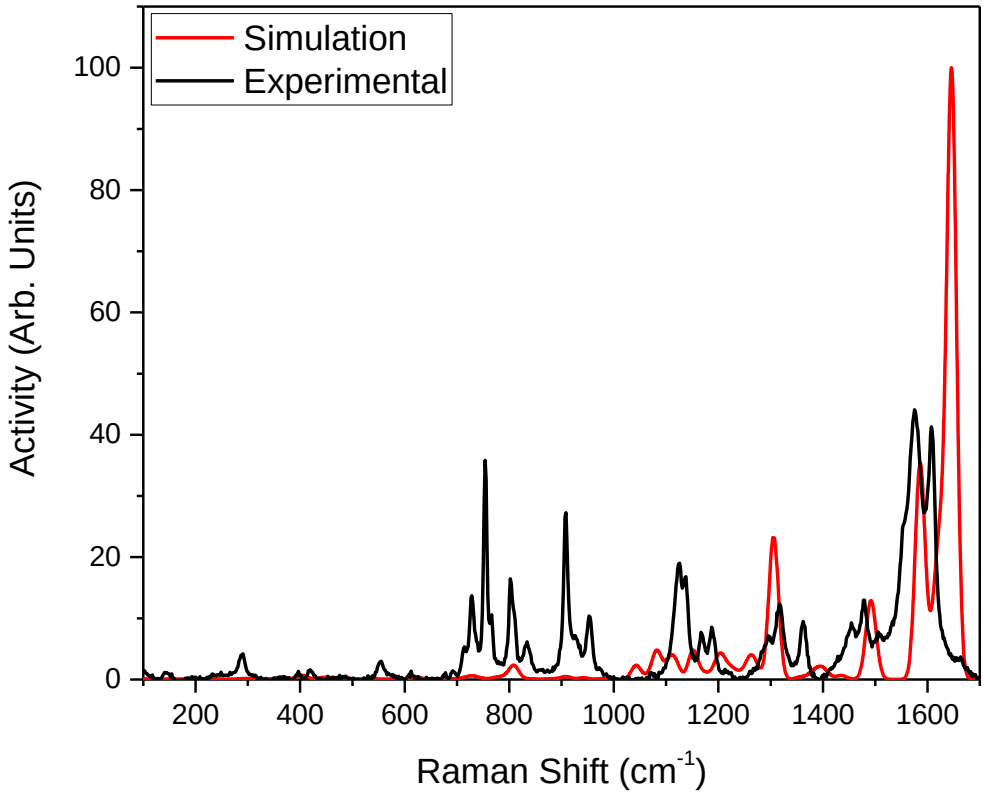

Figure C.4 (a) DFT Raman simulation of pristine spiro-OMeTAD using ORCA and Avogadro.

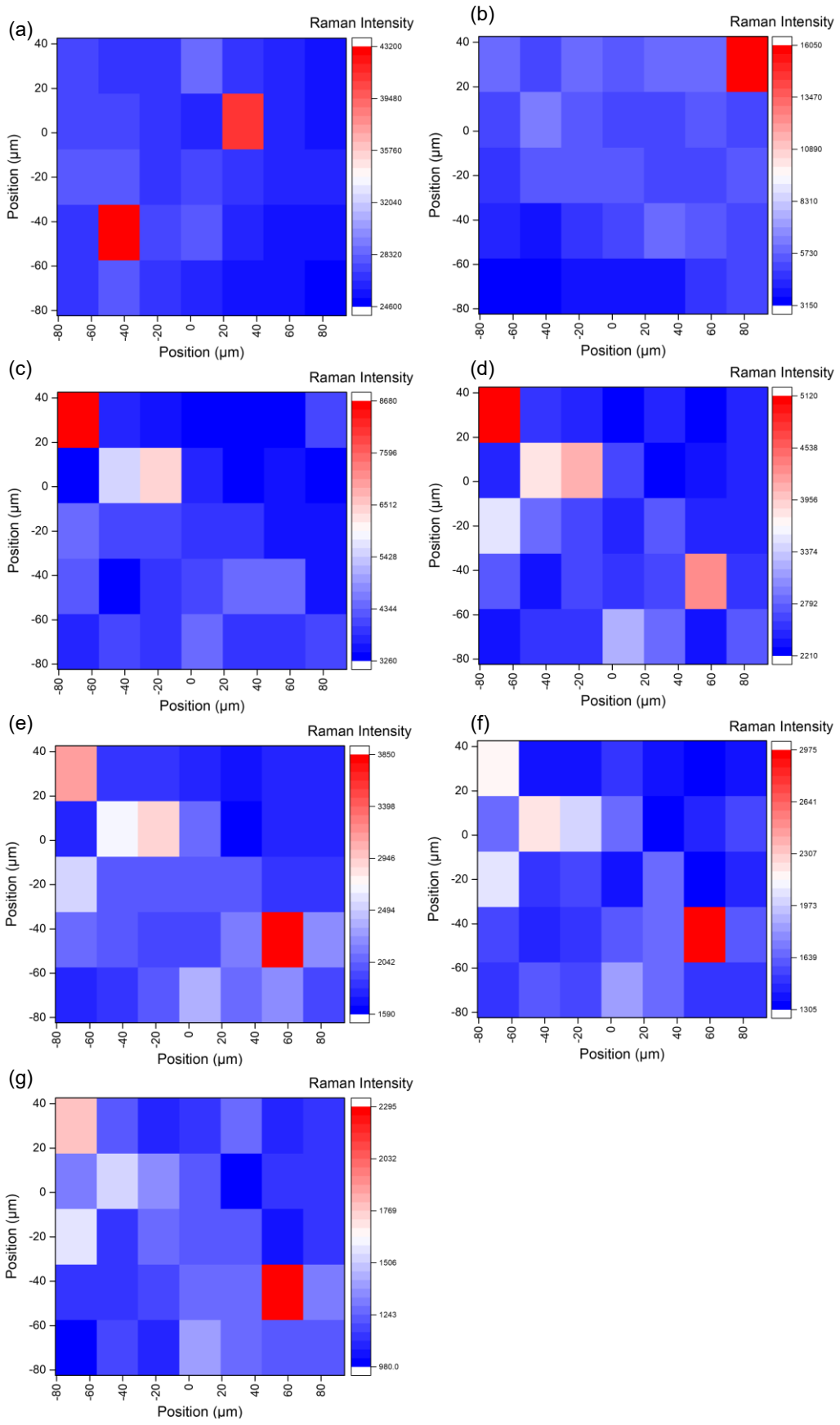

Figure C.5 Raman intensity of the 1447 cm^{-1} peak for P3HT as a function of 85 °C heating time in minutes. (a) 0 (b) 10 (c) 20 (d) 30 (e) 40 (f) 50 (g) 60

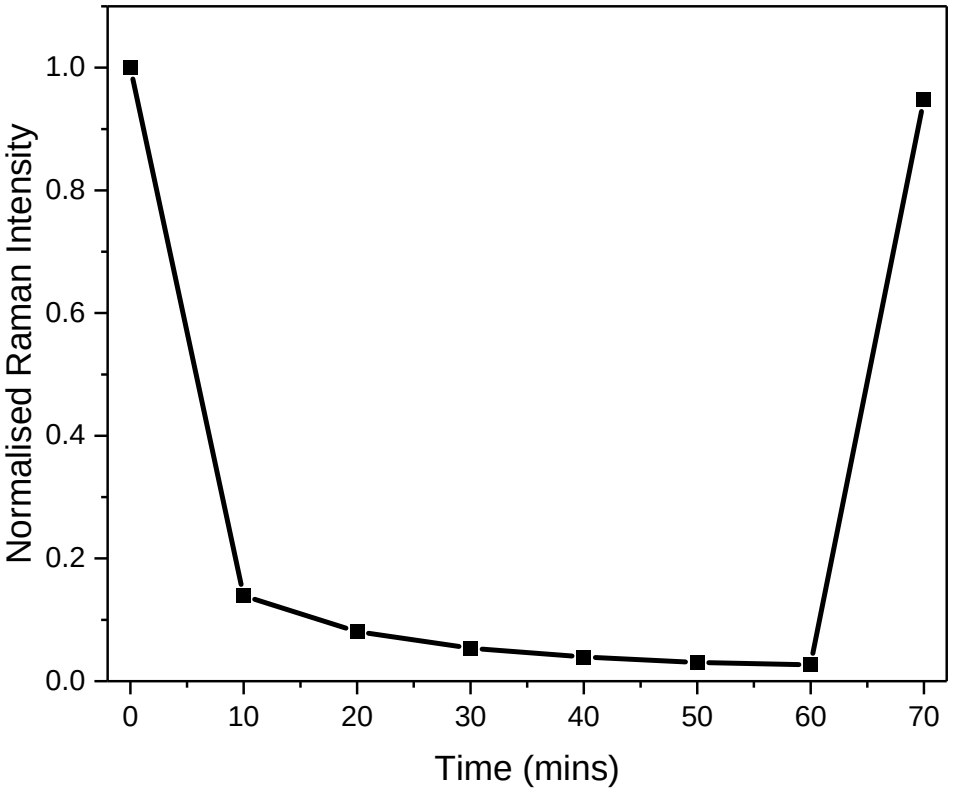

Figure C.6 Normalised 1447 cm-1 P3HT peak intensity as a function of heating time.

APPENDIX D

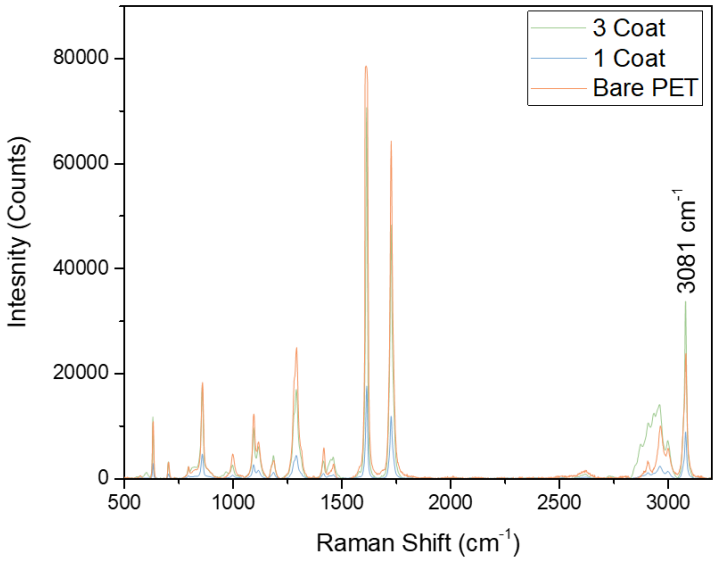

Figure D.1 Averaged Raman spectra for a 1 and 3 coat PMMA spray on PET substrates. The Raman spectra of a bare PET substrate is included to act as a control measurement.

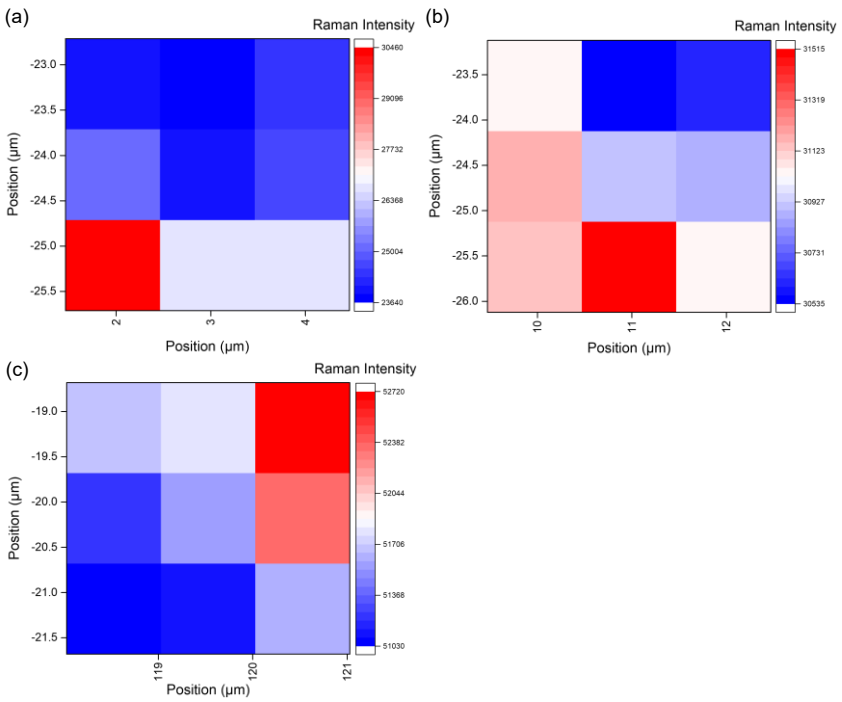

Figure D.2 PMMA Raman mapping of the 2936 cm^{-1} peak intensity. (a) 1 coat (b) 2 coat (c) 3 coat. For both the 2 and 3 coat measurements, the difference between the maximum and minimum values is ~1000 counts. For the 1 coat measurements it's ~10000.

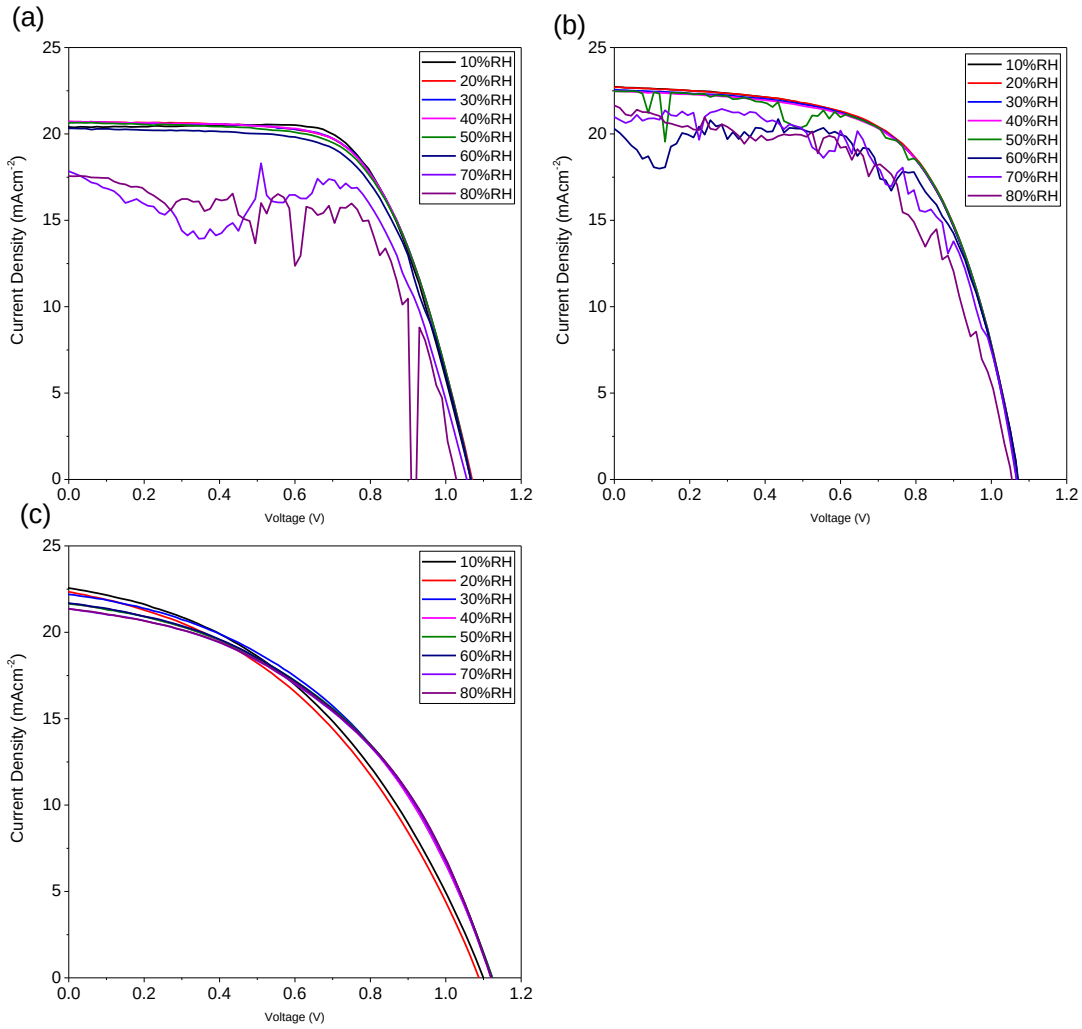

Figure D.3 J-V curves for the different encapsulation methods under humidity stepping from 10-80% RH. (a) unencapsulated (b) 1 coat PMMA (c) glass encapsulation

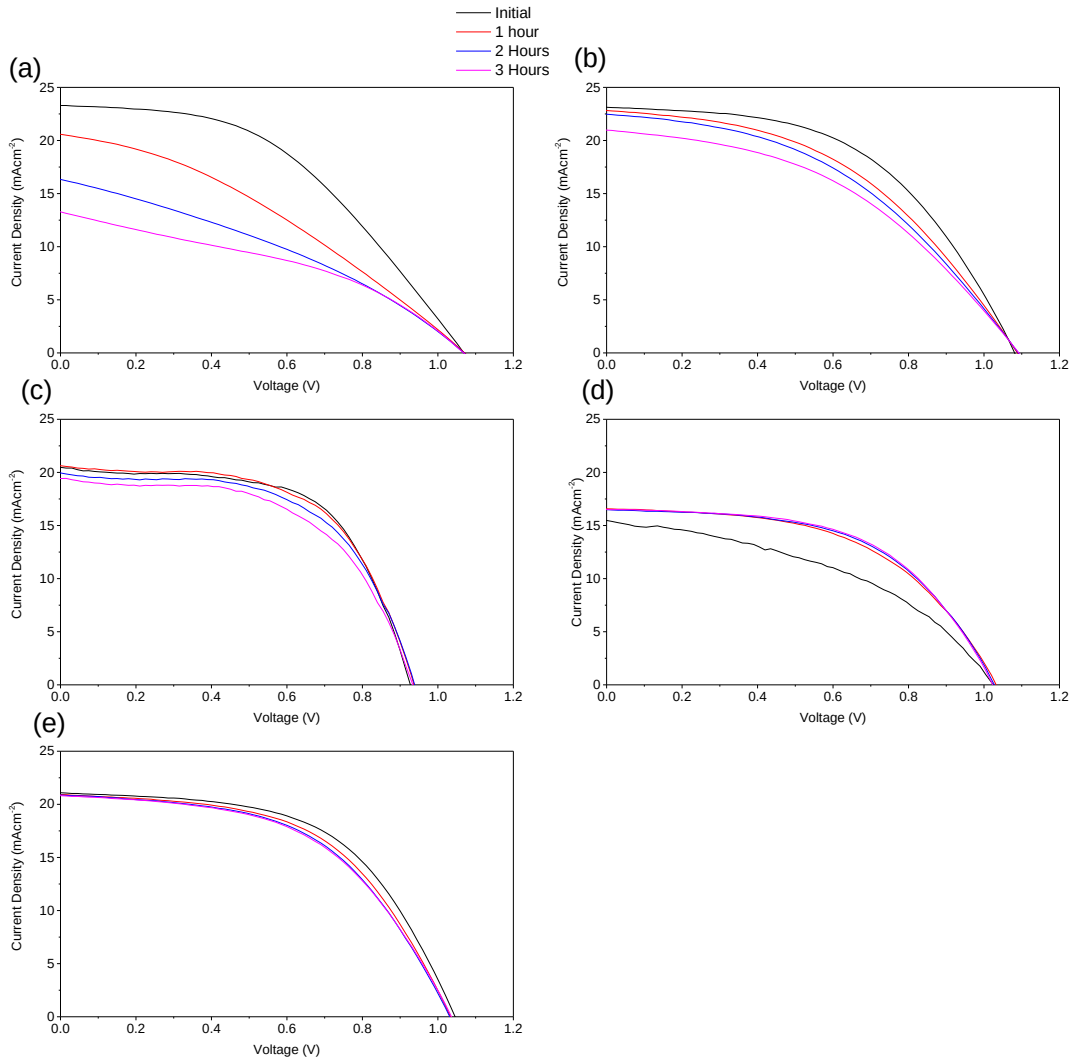

Figure D.4 J-V curves for the different encapsulation methods under humidity 50% RH for 3 hours. (a) unencapsulated (b) 1 coat PMMA (c) 2 coat PMMA (d) 3 coat PMMA (e) glass encapsulation.

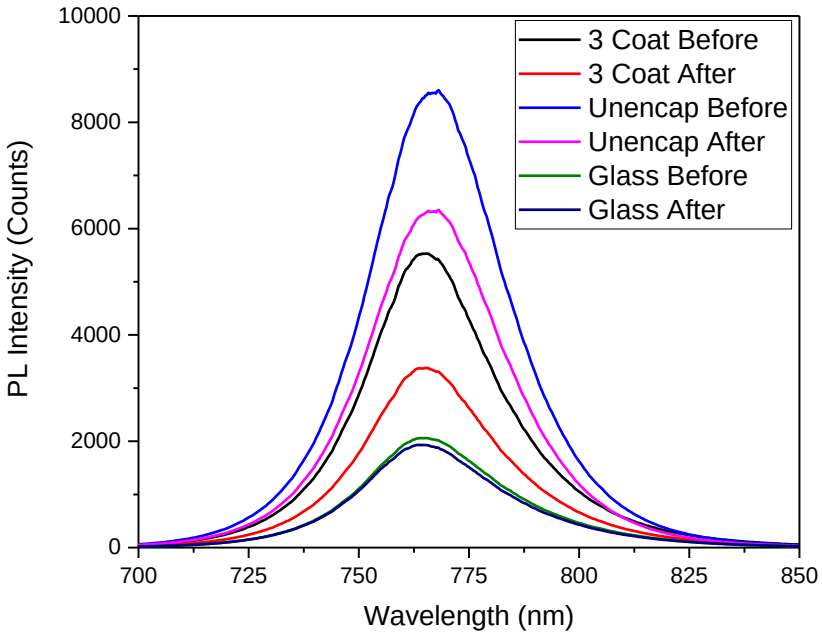

Figure D.5 Averaged PL intensity at 40% RH for the encapsulated samples before and after 3 hours holding at 50% RH.